

SILICON NANODEVICE QUBITS BASED ON QUANTUM DOTS AND DOPANTS

ANASUA CHATTERJEE



SUBMITTED IN PARTIAL FULFILMENT OF
THE REQUIREMENTS FOR THE DEGREE OF
DOCTOR OF PHILOSOPHY

DEPARTMENT OF PHYSICS AND ASTRONOMY
UNIVERSITY COLLEGE LONDON

JANUARY 2017

© Copyright Anasua Chatterjee, 2017.

All rights reserved.

I, Anasua Chatterjee, confirm that the work presented in this thesis is my own. Where information has been derived from other sources, I confirm that this has been indicated in the thesis.

A handwritten signature in black ink, appearing to read 'Anasua Chatterjee', with a stylized, cursive script.

Anasua Chatterjee

Abstract

Silicon Nanodevice Qubits Based on Quantum Dots and Dopants

Anasua Chatterjee

Quantum physics applied to computing is predicted to lead to revolutionary enhancements in computational speed and power. The interest in the implementation of an impurity spin based qubit in silicon for quantum computation is motivated by exceedingly long coherence times of the order of seconds, an advantage of silicon's low spin orbit coupling and its ability to be isotopically enriched to the nuclear spin zero form. In addition, the donor spin in silicon is tunable, its nuclear spin is available to be employed as a quantum memory, and there are major advantages to working with silicon in terms of infrastructure and scalability. In contrast, lithographically patterned artificial atoms called quantum dots have the complementary advantages of fast electrical operations and tunability.

Here I present our attempts to develop a scalable quantum computation architecture in silicon, based on a coupled quantum dot and dopant system. I explore industry-compatible as well as industrial foundry-fabricated devices in silicon as hosts for few-electron quantum dots and utilise a high-sensitivity readout and charge sensing technique, gate-based radiofrequency reflectometry, for this purpose. I show few-electron quantum dot measurements in this device architecture, leading to a charge qubit with a novel multi-regime Landau-Zener interferometry signature, with possible applications for readout sensitivity. I also present spin-to-charge conversion measurements of a chalcogen donor atom in silicon. Lastly, I perform measurements on a foundry-fabricated silicon device showing a coupling between a donor atom and a quantum dot. I probe the relevant charge dynamics of the charge qubit, as well as observe Pauli spin blockade in the hybrid spin system, opening up the possibility to operate this coupled double quantum dot as a singlet-triplet qubit or to transfer a coherent spin state between the quantum dot and the donor electron and nucleus.

Acknowledgements

It is a truth universally acknowledged, that a graduate student in possession of a finished thesis must have a large number of people to thank. First on that very long list would be my advisor John, who has been extremely supportive, and very patient about my many non-traditional¹ ideas and plans. His understanding, tolerance for stupid questions and late-night panicky emails² and calm demeanour mean that I always regain some perspective after a meeting with him. His remarkable and wide ranging scientific knowledge and intuition, as well as his dedication to forming and maintaining fruitful collaborations has given me so much to learn from.

The London lab gang have been sources of commiseration, empathy and a lot of laughter over these years. Cheuk, one of the first people I met when I arrived, has been a rock of support through all my experiments, and the horrors of silicon device fabrication (where his knowledge is unparalleled, as is his uncannily steady hand with tweezers). Matias, the other half of the fridge duo, has taught me so much about low-noise cryogenic measurement³, as well as the importance of keeping calm (it helps if you whistle, however annoyingly), cultivating healthy detachment (I think it's safe to say I've failed at this), and reading the arXiv everyday. Jarryd set high standards for everything in the lab, while Gary and Roberto were very patient with someone who'd never even seen a spectrometer before. In the small amount of time I had with Vasileia, Stephanie and Richard, I received a lot of advice and help from them and I wish them the best. Naitik and Philipp have been great friends despite my constant whining to them, while John Mansir and Simon will be worthy successors to Bender the fridge. Salahuddin's antics bring some much needed laughter to the lab, and Eva, with her readiness to help with matters scientific and otherwise, will be greatly missed,

¹British for "crazy". In the same vein, "very interesting" is likely to mean "that is utter nonsense", and "minor comments" indicates you need to rewrite everything.

²and being almost murdered on a ski slope by a flailing beginner...

³Also that you need to microwave flaming shots before you set them on fire...not in the lab of course!

as will the F10 lab itself (though not the treacherous pipes). Christoph and HeeJin haven't yet learnt that as postdocs they should be ordering us around, and spend their time helping us instead; don't change, guys! To the new cohort (Simon, James, Gavin, Pierandrea and David): may the little blue minifridge never be empty (though chartreuse is clearly superior to beer).

I've been fortunate enough to be a part of the London Centre for Nanotechnology, which I have seen go from strength to strength over these four years. My colleagues at the LCN have all fostered an atmosphere of collaboration and scientific inquiry; I would like to thank especially Mark Buitelaar, my second supervisor, for his support and expertise, Jeroen Elzerman, Jonathan Burnett (and everyone from Warburton group) and especially Andrew Fisher for his unstinting mentorship and willingness to listen to researchers.

To the Cambridge crowd, thanks for putting up with me for six whole months; I really enjoyed my time at the Cavendish (some of it due to the excellent coffee machine!). In particular, Fernando's depth of knowledge about reflectometry has been extremely educational for me, and I have benefited from his strong support and thoroughness in all matters scientific⁴. Nick's depth of knowledge about microwave engineering and most things physics is almost frightening; though he is the exact opposite as a landlord⁵. Andrew Ferguson, Alessandro Rossi, Andi Betz, Adam Esmael, James Haigh, have all made my stay at Cambridge fruitful and fun. At Southampton, Feras and now Liam have kept the silicon MOS flag flying high, and it's great to see devices result from all our collective hard work. In my month and a half at Copenhagen I have experienced a wonderfully well-run lab where it is such a pleasure to do science⁶, and I have to thank Charlie and Ferdinand for welcoming me and giving me free rein on a precious dilution fridge, as well as Christian, Filip, and

⁴and culinary; "chorizo in everything...but never in paella!"

⁵written in expectation of more excellent baked goods

⁶the fact that it is the first lab I've worked in that isn't dark and underground also helps, as does the glorious coffee machine!

Frederico for their help and companionship. Karl, whom I seem to be following around the world, has been as helpful as he was in Princeton, and remains scarily efficient as always. Pettalab (and of course Princeton itself) has had a great hand in making me the researcher I am, and I'd like to thank my first advisor Jason Petta, who continues to be a true mentor and friend, and who set me on the path to a PhD in experimental condensed matter when I was a young undergraduate susceptible to the charms of theoretical physics. Lastly, I'd like to thank CEA-LETI for the excellent devices they made for us, and continue to make.

For feeding and housing me in the expensive sinkhole for money that is London⁷, I would like to thank the EPSRC, as well as the UCL Dean's Prize, the UNDEDD grant, and the Yusuf Ali travel grant.

I'd like to thank my huge rambunctious family who are a welcome relief from the academic bubble and a reality check that good things exist outside the lab. Their support and love has been unconditional and plentiful, even during the times when I disappear into experiments and forget to call (or treat vacations like writing retreats). To my father who gave me the Feynman lectures when I was way too young and kickstarted this whole painful process, I say a grudging but heartfelt thank you. I thank my mother for always unconditionally taking my side whenever I vent to her; and yes I do like physics more than biology (her subject).

Lastly, to the long-suffering Sroyon, who has made these four years the happiest in my life, thank you so much. For following me around to different cities at the drop of a hat, for putting up with my worst-case scenarios and long absences in the lab, quelling my late-night panic attacks ("yes I'm sure you turned off that one valve"), and for generally looking at the world with eternal surprise.

⁷though I would like to thank the city for its excellent 24-hour night buses that have saved my life after many a late night in the lab

To my dadu, who taught a little girl to read.

Contents

Abstract	5
Acknowledgements	7
List of Tables	13
List of Figures	14
1 Background and Motivation	17
1.1 Silicon spin qubits for quantum computation	18
1.2 Donor spins in silicon	19
1.3 Quantum dots in semiconductors	22
1.4 The dopant-dot hybrid qubit	22
1.5 Thesis outline	24
2 Quantum Dots	27
2.1 Single and double quantum dot devices	27
2.2 Coulomb blockade and charge sensing	29
2.3 Charge qubits	34
2.4 Landau-Zener interferometry	36
2.5 Spin qubits and Pauli spin blockade	43
2.6 Dopant spins in silicon	49
3 Experimental Techniques	55
3.1 Electrically Detected Magnetic Resonance	55
3.2 Measurement setup and techniques	58
3.3 Gate-based RF-reflectometry	63
3.4 Fabrication of nanoscale silicon devices	68
3.5 CMOS foundry silicon-on-insulator devices	77

4	Gate-based charge sensing of a double quantum dot in a silicon nanowire	82
4.1	Primary thermometry	84
4.2	Microwave sensing	92
4.3	Multi-regime Landau-Zener Stückelberg interferometry in a double quantum dot	95
4.4	LZS results and discussion	101
4.5	Theoretical description	106
4.6	Outlook and conclusion	113
5	Electrically Detected Magnetic Resonance of Selenium Donors in Silicon	115
5.1	Introduction: deep double donors in silicon	115
5.2	Sample design and measurement Setup	126
5.3	EDMR spectrum	129
5.4	Temperature and power dependence of the EDMR signal	130
5.5	Effects of laser and broad-wavelength illumination	136
5.6	Analysis	139
6	A Hybrid Dopant-Dot Double Quantum Dot in Silicon	149
6.1	Device and measurement setup	150
6.2	Double quantum dot behaviour	150
6.3	Microwave spectroscopy	155
6.4	Charge relaxation	158
6.5	Spin blockade	161
6.6	Conclusions	163
6.7	Methods for coherent control	164
7	Conclusion and Outlook	168
7.1	Outlook and future work	172
A	Fabrication Listings	175
B	Measurement Notes	181
	Bibliography	191

List of Tables

3.1	Test structures for the silicon fabrication platform	75
5.1	Experimental values for donors in silicon	120
A.1	Silicon MOS fabrication process flow	175
A.2	CEA-Leti die, postprocessing and stripline fabrication	178
A.3	EDMR interdigitated contact fabrication	180

List of Figures

1.1	Device implementations of donor, quantum dot, and coupled systems	21
2.1	Device implementations of quantum dot systems	28
2.2	Transport through a single quantum dot	31
2.3	Double quantum dots and the stability diagram	33
2.4	Triple points in double quantum dot transport	35
2.5	A tunnel coupled charge qubit	36
2.6	Evolution of the energies during Landau-Zener interferometry	37
2.7	Charge qubit manipulation through Landau-Zener Interferometry	40
2.8	Effect of decoherence on the Landau-Zener interferometry pattern	42
2.9	Spin blockade in quantum dot systems	43
2.10	Spin qubit manipulation	46
2.11	Donor wavefunction in silicon	50
2.12	Breit-Rabi diagrams of donors	53
3.1	ESR and EDMR setup	57
3.2	DC line anchoring and filtering	60
3.3	On-PCB copper powder and RC filtering	61
3.4	Fridge printed circuit board	63
3.5	RF reflectometry setup	64
3.6	RF-resonance from a loaded tank circuit	65
3.7	Regimes of gate-based reflectometry	66
3.8	Silicon device fabrication platform	70
3.9	The stages of Metal-Oxide-Semiconductor lithography.	71
3.10	Fabricated devices	73
3.11	Device tests and design progression	78
3.12	Foundry-fabricated FD-SOI devices	80

4.1	Gate-based reflectometry of a quantum dot	85
4.2	Device and reflectometry setup	87
4.3	Peak shape, FWHM and amplitude with mixing chamber temperature	91
4.4	RF-drive broadening and gate lever arm	93
4.5	Microwave effects and simulations	96
4.6	Stability diagram in transport and reflectometry	100
4.7	Phase response of the resonator under Landau-Zener interferometry	102
4.8	Frequency dependence of the LZS interferometry pattern	105
4.9	Circuit model, stability diagram and energy levels of the double quantum dot	107
4.10	Multiple-passage regime	109
4.11	Single-passage regime	110
4.12	Double-passage regime	111
4.13	Landau-Zener interferometry in a four-level system	112
5.1	Shallow and deep donors in silicon	117
5.2	Selenium hyperfine transitions	119
5.3	Ionization energies and donor species populations with temperature	121
5.4	EDMR sample and measurement setup	126
5.5	EDMR spectrum of ^{28}Si : ^{77}Se device	130
5.6	Power dependence of EDMR and ESR signals	132
5.7	Peak-to-peak linewidth	134
5.8	Temperature dependence of the EDMR Signal	135
5.9	Modulation frequency	136
5.10	Effect of white light and laser illumination	137
5.11	Change in photocurrent at resonance	138
5.12	Spin dependent recombination	142
6.1	Dopant-dot device and setup	151
6.2	Double dot stability diagram	152
6.3	Charge assignment of dopant and dot transitions	153
6.4	Magnetic field dependence of donor transition	154
6.5	The dopant-dot hybrid system	155
6.6	Microwave spectroscopy	157
6.7	Charge relaxation measurement protocol	159
6.8	Charge relaxation time	160

6.9	Pauli Spin Blockade	162
6.10	Electron Spin Resonance	165
6.11	Coplanar Waveguide for ESR measurements	166
7.1	Qubit configurations for silicon nanowire finFETs	170
A.1	EDMR spectrum prior to surface treatment	180
B.1	Room temperature RF setup	183
B.2	Additional dopant-dot device measurements	186
B.3	Microwave simulations for a dot-to-lead transition	187
B.4	Coplanar waveguide model	190

Chapter 1

Background and Motivation

Quantum physics, when applied to computing, is projected to lead to revolutionary enhancements in computational speed and power. This thesis focuses on quantum information and quantum computing, specifically through quantum architectures built from hybrid systems, which can couple distinct qubit implementations with complementary advantages. In traditional computing, “Moore’s law” observes that the number of FETs (field effect transistors) on an integrated circuit doubles approximately every two years to enable traditional semiconductor-based computing systems to grow in speed and processing power. However, we appear close to a limit to Moore’s Law, since MOSFETs are reaching a physical scalability limit[1] in the sense that they cannot be made much smaller, or be packed in much more densely. However, quantum computing is projected to bring as regime-changing an upheaval as the first transistor, with exponential speedups in many processes such as codebreaking[2] and quantum simulation[3] that are just too computationally intensive today.

There are indeed challenges commensurate to these rewards. The building blocks of such a quantum computer, called qubits, have to be resistant to environmental disturbance; they need to hold information encoded in them for long periods as well as be easy to control. This is unfortunate, since often these two qualities are somewhat antithetical; if something is easy to interact with and control, this often means that the environment is also able to interact with it in ways that affect the coherence of information stored in it. As a result quantum physicists are increasingly looking towards hybrid systems today. Combining a system with high resistance to environmental interference with one that is easier to control and engineer is a promising approach for building an effective quantum computing architecture. This work seeks to explore just such a novel, hybrid building

block; the quantum dot coupled to an impurity spin in silicon. In doing so, we also aim to gain understanding into the physical system composed of a natural atom (the dopant atom in the silicon crystal) coupled to an artificial atom (the gate-defined quantum dot).

1.1 Silicon spin qubits for quantum computation

Silicon, as the material of choice of the semiconductor industry, is ubiquitous in hardware for classical computation and consequently in all our consumer electronic devices. It turns out that silicon also has quite a few advantages over other materials as a quantum computing platform as well, which we can evaluate in terms of the DiVincenzo criteria[4], a set of five requirements for qubits suitable for quantum computation. These can be briefly summarised as: the qubit must be scalable and well characterised, it must be able to be initialised, as well as manipulated, by a universal set of quantum gates, it must not decohere quickly, and it should be able to be read out with high fidelity. Any quantum technology built on silicon is inherently more scalable, having the semiconductor industry and its fabrication skill and technology to draw upon. Silicon is also an excellent semiconductor vacuum for spin (i.e. a low magnetic-decoherence causing environment), containing only a very few decoherence centers in the form of the (spin-1/2) ^{29}Si isotope, so that qubits in silicon are protected from many sources of noise that decohere other qubits. Moreover, silicon can be isotopically purified to the (spin-0) ^{28}Si isotope, giving extraordinary gains in the coherence of stored quantum information. In terms of the DiVincenzo criteria, we are now left with the requirements of initialisation, manipulation and high-fidelity readout, which we explore in the next section (and in the rest of this thesis).

1.1.1 The semiconductor industry

Our interest in silicon provides a secondary motivation for the experiments performed in this thesis. In its quest for faster and more powerful computers, the semiconductor industry has strongly embraced miniaturization. However as we have discussed, this scaling down process has a limit and we are indeed now very near it; around a gate length of ~ 5 nm. The proximity of the source and drain electrodes can now lead to short-channel effects such as punch through and atomistic variations across chips. However, while this is a problem for the semiconductor industry, it provides a motivation for the disruptive technology that is quantum computation. In addition it is worth underlining that this process of miniaturiza-

tion also provides us with a resource that this thesis aims to take advantage of; high quality few-nm sized devices, produced with great reliability in ultra-clean environments with integrated control electronics, which are capable of harbouring both few electron quantum dots and dopant atoms and therefore a hybrid system. Through the experiments performed in this thesis, we have tried to develop a silicon architecture that is truly compatible with the silicon industry, by exploring quantum dot behaviour that is well-explained by theory, but established in large-scale foundry-made devices.

1.2 Donor spins in silicon

Silicon is a mainstay of the electronics industry, but along with it are impurity atoms called dopants embedded in the crystal lattice which are essential for microelectronics. Of these, “donors” are atoms with an extra electron to donate to the semiconductor, typically from Group V (P, As, Sb, or Bi) in the periodic table, occupying substitution sites in the silicon lattice. These are typically “shallow” donors, with the single electron ground state ~ 50 meV below the conduction band edge (though we will explore a “deep” donor, from Group VI, in a later chapter). At low temperatures (< 50 K) these atoms have a bound electron and a nucleus, both of which have a spin degree of freedom that can be probed and manipulated using established methods such as Electron Spin Resonance (ESR).

1.2.1 State of the art for donor qubits in silicon

Research in the field of dopant atoms in semiconductor materials has been conducted for more than fifty years, well before the conception of quantum information. In 1998, however, interest in these donors as the physical implementations of qubits took off with the publication of the Kane proposal[5], which proposed a computer consisting of arrays of qubits made up of the spin state of donor nuclei. Below are some developments in donor spin qubits that contribute to the realisation of a Kane computer:

- **Readout and control of donor spins** The reading out of the spin state of the qubit is an extremely important first step. In 2010, the single-shot readout of the electron spin of a phosphorus atom in silicon using spin-to-charge conversion was reported[6]. This readout method was then combined with coherent control to achieve a single spin-qubit in silicon[7] with a coherence time of $200 \mu\text{s}$ (with an architecture shown in Fig. 1.1(a)). This was followed by the readout and control of a nuclear spin qubit in

silicon[8] with a coherence time of 60 ms. Soon after, a substrate with an isotopically purified Si-28 epilayer was used to replicate these results but with great gains in coherence times (30 s for the nuclear spin, and 0.5 s for the electron spin[9]), setting a benchmark for solid state qubits.

- **Donor placement** The Kane computer requires near-atomic precision of donor placement in the silicon lattice, about 10 nm apart. Ion implantation[7, 8, 10] using lithographically opened windows as well as scanning probe microscopy[11] methods have been employed for this purpose. The latter provides the near-atomic precision required for the Kane proposal.
- **Spin-selective addressing** Electron spin resonance (ESR) manipulation is usually used to control donor spins; however this is typically a global method, and the Kane proposal requires a way of addressing individual spins. The Stark shift using electric tuning through gate voltages has been proposed for this purpose and has been demonstrated in ensembles of donors[12, 13], as well as recently in devices[14].
- **Two-qubit gates and the nuclear spin** Single and two-qubit gates form a universal set of quantum gates, required for any quantum computer. Kane's original proposal envisaged using controllable electron-mediated exchange coupling between adjacent nuclear spins, requiring fine control over the inter-electron wavefunction overlap. This is difficult to engineer over any large distance, and also in part because of oscillations in the exchange due to interference in the electron wavefunction by the six-fold degenerate conduction band minima of silicon[15]. In general, the coupling and interaction of neighbouring nuclear spins is quite a difficult question for a donor-based quantum computer, a challenge recognised in Kane's original proposal. While the donor electron's spin is easier to address (and the coherent transfer of a quantum state between the electron and nuclear spin has been demonstrated[16]), this is also not trivial.

From the above discussion, there emerges a need for a fast method of manipulation that will enable us to entangle nearby donor electron or nuclear spins. Additionally, donors in silicon also have the drawback of being low in tunability compared to artificial atoms, in particular the electrostatically defined quantum dot.

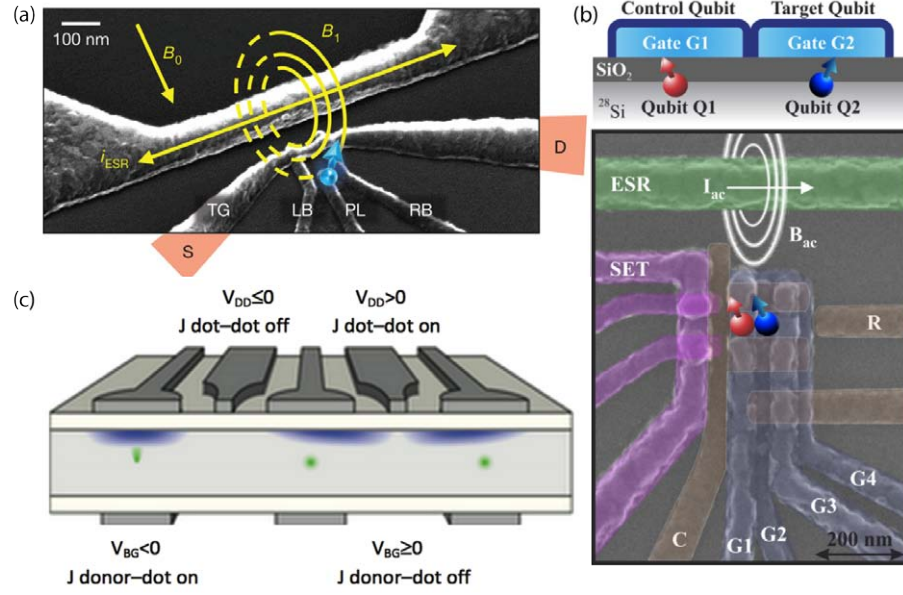


Figure 1.1: Device implementations of donor, quantum dot, and coupled systems, as described in the text. (a) Donor spin qubit architecture, implemented in Refs. [6–8]. The top gate (TG) draws up electrons into the channel from the source (S) and drain (D) reservoirs, and left (LB) and right (RB) barrier gates create tunnel barriers isolating a pool of electrons forming a single electron transistor (SET) used as a charge sensor. The plunger (PL) or donor control gate tunes the energy levels of the donor, ion-implanted under it. Spin dependent tunneling of the donor electron into and out of the SET is the readout mechanism. Coherent control is achieved through ESR using the coplanar waveguide (CPW) at the top of the image. (b) Double quantum dot (DQD) architecture in silicon[17, 18]. An SET (left) is used as a charge sensor for the DQD. An ESR antenna (top) is used to achieve control of the dot electron spins. (c) A coupling scheme[19] to achieve entanglement of two donor electrons mediated by a double quantum dot. Gate voltages (V) tune the exchange couplings (J) between the two dots, and between each dot and its corresponding donor.

1.3 Quantum dots in semiconductors

In the same year as the Kane proposal, Loss and DiVincenzo[20], proposed another kind of qubit, the quantum dot. Semiconductor quantum dots are typically gate-confined regions of a substrate, typically tens of nanometers in size, which can be used to form potential wells in which to trap electrons and form artificial atoms with discrete, quantized energy levels. The quantum dot as a qubit has providentially complementary attributes to the donor atom; potentially not as long-lived, but comparatively easy to engineer as well as tune. These qubits also provide fast control of spin states through electrical voltages (which are much easier to apply, especially locally, than magnetic fields). They are able to be fabricated using silicon as the substrate, a material which can also host our donor atoms for a hybrid architecture. In terms of scalability, arrays of quantum dots are also easier to fabricate than those of donors, since this typically involves a repeating lithography pattern, whereas for single donors, precise single-ion implantation techniques are required. In silicon (more specifically, in a SiGe heterostructure), a linear array of 9 quantum dots was recently implemented[21]. In Chapter 2 we present in detail the background, theory and measurement of semiconductor quantum dots, with particular emphasis on silicon.

Fig. 1.1(b) shows an architecture in silicon recently used to isolate a double quantum dot (the high degree of control available through precisely engineered overlapping gates is notable). Quantum dots patterned on silicon in general have shorter coherence times than donor atoms; recent experiments[17] on a device based on a silicon substrate with an isotopically purified ^{28}Si epilayer have found a coherence time of $T_2 \sim 28$ ms (a value measured using the CPMG pulse sequence; using the same sequence, $T_2 \sim 560$ ms was found for a donor electron spin and $T_2 \sim 35.6$ s for an ionised donor nuclear spin[9]). However, in this quantum dot device, one-qubit gates and the recently demonstrated two-qubit gates (essential operational steps for the implementation of universal quantum computation) can be performed in a time that allows for 10^5 two-qubit gates within one T_2 [18]. This fast operation time is what makes these quantum dots attractive as computational units.

1.4 The dopant-dot hybrid qubit

An apparent next step would be to harness the complementary advantages of these two systems, by placing them in close proximity and coupling them together to exchange information. This thesis explores ways in which this kind of coupling can be achieved, as well

as tries to find optimum dopant and dot systems for which this can be implemented. We are also interested in implementing this dopant-dot coupling in a scalable silicon device architecture. A hybrid architecture with a quantum dot coupled to a donor atom, forming a novel kind of double quantum dot could take advantage of fast spin manipulations using gate voltages to form a hybrid singlet-triplet qubit. The system would also have access to the long-lived quantum memory offered by the nuclear spin of the donor atom, the natural field gradient from which could also be used to drive spin rotations. Another potential application could be the creation of spin buses with quantum dots chains to mediate quantum information stored in donor qubit over long distances[22]. Additionally, in a hybrid architecture, entangled states could be operated upon in a double quantum dot, and could then be transferred to the long-lived nuclear spins of two donors, the memory element.

An important step is to achieve quantum state transfer between the donor and the dot. Two possible ways to achieve this are mentioned below.

Electron shuttling

One way of accomplishing the transfer of spin information is to physically transfer the electron carrying the spin information from the dot to the dopant. To explore transfer of a quantum state, we start out with a lithographically defined double quantum dot (DQD) in a triplet ground state (at a small magnetic field), as well as a dopant in the positively charged D^+ state. By pulsing gate voltages, we can shuttle the electron from one of the quantum dots into the dopant, wait some time, and shuttle back into the QD. The probability of the singlet state (zero in the absence of any spin flips) will indicate if the electron can be transferred between the QD and dopant in a spin-conserving way. The singlet state can be measured using a quantum capacitance measurement[23] using gate based charge sensing or alternatively, a proximal RF-SET charge sensor. Coherent transfer by adiabatic passage (CTAP)[24, 25] has been suggested to achieve electron shuttling. However, the coherent transfer of information by physically moving electrons is acknowledged to be difficult, though the physical shuttling of electrons across three quantum dots has been recently achieved[26].

Exchange coupling

A second perhaps more feasible method, aims to create a dopant-dot singlet triplet qubit, with greater tunability and spin coherence expected than in the shuttling approach since

there is no physical movement of the quantum systems. The essential ingredient is an exchange coupling (ideally electrostatically controlled) between one of the dots and the dopant. Fig. 1.1(c) shows an architecture where electrostatically tunable exchange couplings (“J dot-dot”, J_{DQD} and “J donor-dot”, J_{DD}) would facilitate a memory SWAP operation[19]. A starting point would be a DQD in the (1,1) singlet state and a dopant in the neutral D^0 spin-down state, with the coupling J_{DD} switched off. Then, with an appropriately timed voltage pulse, J_{DD} would be turned on to entangle the donor and quantum dot spins so that the DQD would have some probability of being in the triplet state. Varying the J_{DD} pulse length would induce oscillations in the DQD triplet population, enabling a measurement of the dopant-dot exchange coupling and operation of the hybrid system as a singlet-triplet qubit. When this is performed on both halves of the double quantum dot with two singly-coupled donors, it would pass an entangled state from the DQD to the two donor electron spins (which could then be extended to the even longer-lived donor nuclear spins).

In recent times, coupling of a dopant to a dot has been an area of focused research. Spectroscopy of dopant states in the coulomb blockade regime of a quantum dot has been shown[27, 28]. In a silicon nanowire device, a hybrid dopant-dot device has been reported and explored as a charge qubit, and the observation of Pauli spin blockade has also been reported. These results are presented in Chapter 6 of this thesis and in published form in Ref. [29]. Very recently, in a gate-defined metal-oxide-semiconductor quantum dot with a dopant implanted nearby, nuclear-spin driven singlet-triplet rotations were reported[30].

1.5 Thesis outline

This thesis describes experiments geared towards the development of a dopant-dot hybrid system in silicon. We concentrate largely on a foundry-fabricated silicon nanowire qubit architecture, as well as the development of said architecture into one suitable for scalable quantum dots. We present the fabrication of nanoscale silicon devices as well as a low-temperature measurement setup, using which we study non-invasive gate-based reflectometry as a very sensitive charge sensing technique. We then present quantum dot measurements in a CMOS-silicon device. We study a donor from the chalcogen family, selenium, that has been predicted to have several characteristics making it useful for integration into coupled devices. Finally, we present a hybrid dopant-dot system and explore its potential as a charge and spin qubit. This thesis is organised into the following chapters:

Chapter 2 deals with the relevant theoretical background for this thesis. The theory of single and double quantum dots is presented, and they are examined as charge and spin qubits in the light of recent experimental studies. Finally, we present a review of the dopant atom in silicon, its level spectrum, and its detection and coherent manipulation using ESR.

Chapter 3 presents the experimental techniques used for this thesis. The experimental setup for electron spin resonance (ESR) studies as well as for those carried out in a dilution fridge at millikelvin temperatures are presented and we discuss the wiring and filtering of such an apparatus. We then present a review of the main measurement technique used in this thesis, gate-based reflectometry and discuss the radiofrequency reflectometry setup required for this sensitive method of charge-sensing. For the fabrication of our coupled system, we have chosen the proven Metal-Oxide-Semiconductor fabrication process, common to microelectronics industry cleanrooms and we present the development of a versatile fabrication platform established at University College London as well as the University of Southampton. Lastly, we present the devices used for many of the experiments in this thesis; nanometer-scale fin-FET devices produced by the industrial foundry at CEA-Leti. The formation of quantum dots in these devices and their measurement is also briefly discussed.

Chapter 4 reports measurements that establish quantum dot behaviour in the foundry-fabricated silicon nanowire FET device architecture presented in the previous chapter, and shows the sensitivity of our gate-based RF-reflectometry technique by performing charge-sensing measurements. We show dispersive readout of a double quantum dot and explore new multi-regime physics of Landau-Zener-Interferometry. We also present gate-based thermometry experiments as well as microwave-amplitude detection. In this Chapter we explore the double quantum dots that are one component of our hybrid architecture. These experiments were performed at the University of Cambridge, at the Hitachi Cambridge Laboratory and at the Department of Microelectronics, in conjunction with Dr. M. F. González-Zalba.

In **Chapter 5** we move to the other component of our hybrid system, donors in silicon, and present experiments performed on selenium donors. The chalcogens in silicon have very high binding energies and selenium in addition has a strong hyperfine coupling (which could mean that the coherent evolution of our hybrid singlet-triplet qubit could be driven at GHz frequencies) and a (predicted) low Stark shift, characteristics that make it valuable for high-temperature operation and for device integration. We present electrically detected magnetic resonance (EDMR) measurements and observe spin-dependent transport from a “deep” dopant in silicon.

Chapter 6 brings the above two systems together, presenting measurements taken on a silicon finFET device similar to those presented in Chapter 4, but with a doped channel. In this device we see the first evidence for a dopant coupled to a quantum dot, together forming a double quantum dot. We explore this system as a charge qubit and study its charge dynamics. We also show Pauli spin blockade in this coupled system, which opens up perspectives for a hybrid dopant-dot spin qubit. We further report on methods developed to perform coherent control of such a system.

In **Chapter 7** we summarize the key outcomes of this thesis, and we also suggest possible directions for future work in this field.

Chapter 2

Quantum Dots

In the previous chapter we presented our motivations for the development of a hybrid spin qubit architecture with donor spins in silicon coupled to quantum dots. Since our coupled system in its most basic form is still essentially a double quantum dot, albeit one consisting of electrons located on one “natural” and one “artificial” atom, we are able to use the theory of double quantum dots for the description for this coupled system. We discuss here the general theory of dot behaviour and signatures in transport and charge sensing measurements, as well as charge and spin qubits made out of quantum dots.

2.1 Single and double quantum dot devices

Quantum dots are submicron structures containing a small number of free charge carriers. The spatial extent of the dot in all three dimensions is limited so that the energy levels are quantized[31], like an atom (leading to them being called “artificial atoms”). Level quantization sets in when the size of the system is comparable to the Fermi wavelength; for metals, this is only a few nm, while for semiconductors (especially low effective mass ones like GaAs and InAs), this can be ~ 100 nm. The formation of a dot is associated with a weak tunnel coupling to the external environment (a conductance small compared to that of a single channel), and an electrostatic charging energy that is large compared to $k_B T$, where k_B is Boltzmann’s constant. The measurement of a quantum dot by transport relies on tunnel barriers opaque enough to form the dot, yet transparent enough to allow measurable transport through the device. This can be achieved using local gate electrodes to tune the occupation. For a double quantum dot in series, the complexity increases since one now needs to tune three tunnel barriers independently of the occupations of the two

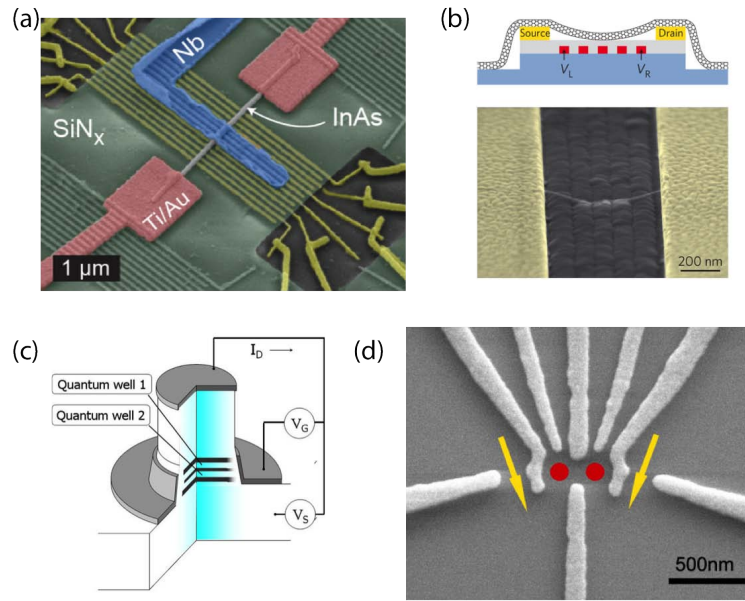


Figure 2.1: Device implementations of quantum dot systems. (a) An indium arsenide (InAs) nanowire double quantum dot, gated using bottom gates below the nanowire[32]. (b) A carbon nanotube quantum dot, with the nanotube suspended from the contacts. The gate can therefore affect the nanotube both mechanically and electrically[33]. (c) A vertical and compact quantum dot made out of quantum wells[34]. (d) A gate-confined gallium arsenide (GaAs) double quantum dot[35].

dots. Therefore, there are many different ways of designing a quantum dot in a physical system, with associated advantages and disadvantages; some of these are shown in Fig. 2.1.

2.2 Coulomb blockade and charge sensing

The most basic measurements for a single or double quantum dot are transport measurements, where the current from source to drain is measured while gates are tuned, in a regime where the system temperature is small compared to the size of the dot (or rather, the dot energy levels set by the latter). In the “Coulomb blockade” regime of transport, the ground state of the system relies on a fixed occupancy of electrons in each dot. The electrons in the quantum dots energetically cannot tunnel to the leads, while to add electrons from the leads, one would require more energy in order to occupy the next available quantum dot state. Therefore, transport can only occur when the internal states of the quantum dot align with the Fermi level of the source and drain leads. This leads to peaks in the conductance measured through the quantum dot; these signatures of single electron tunneling are known as Coulomb blockade peaks.

2.2.1 The constant interaction model

To understand the physics of quantum dot systems better, we consider them in the simple and intuitive constant interaction model[31, 36, 37] which takes into account (a) the Coulomb repulsion and the energy required to overcome it when adding an electron to the dot as well as (b) the quantised single particle energy levels due to the confinement. The model assumes that the Coulomb interaction is parametrised by a constant capacitance $C = C_s + C_d + C_g$ for the source, drain and gate respectively. It also does not consider second order effects and assumes that the single-particle energy spectrum is unaffected by the interactions. In this model, the ground state energy ($U(N)$) of an N electron dot is approximated by

$$U(N) = [e(N - N_0) - C_g V_g - C_s V_s - C_d V_d]^2 / 2C + \sum_N E_n \quad (2.1)$$

where $N = N_0$ at $V_g = 0$, e is the electron charge, and V_s , V_d and V_g are voltages on the source, drain and gate. The last term E_n is a sum over the energies of the N occupied single-particle states. The electrochemical potential of the dot can therefore be defined as

$\mu(N) = U(N) - U(N - 1)$ and given by

$$\mu(N) = (N - N_0 - 1/2)E_C - \frac{e}{C}(C_g V_g + C_s V_s + C_d V_d) + E_N \quad (2.2)$$

Adding an electron to the dot will now change the electrochemical potential by the addition energy

$$\Delta\mu(N) = \mu(N + 1) - \mu(N) = E_C + \Delta E \quad (2.3)$$

where $E_C = e^2/C$ is the charging energy and ΔE is the single particle spacing arising from the quantum mechanical confinement of the electrons within the dot. The model, along with electronic transport signatures predicted by it, are shown in Fig. 2.2.

Low bias regime

In the low bias regime, where the source-drain voltage difference is low compared to ΔE and E_C , electrons can tunnel on and off the dot one by one, but only when its electrochemical potential lies between that of the source and drain, i.e. $\mu_s > \mu(N) > \mu_d$. When $\mu(N) < \mu_d$ and $\mu(N + 1) > \mu_s$, there can be no transport and this situation is called Coulomb blockade.

High bias regime

In the high bias regime, multiple levels can lie in the bias window and so-called “bias spectroscopy” can be performed, since the current through the dot increases when an additional level enters the dot. In this case either $eV_{sd} > \Delta E$ or $eV_{sd} > E_C$ and typically at high enough biases transport paths open up for excited states, allowing us to obtain information about the energy spectrum of the quantum dot.

2.2.2 Double quantum dots

In this thesis, we are concerned with double quantum dots and we therefore extend the model presented in the previous section to the case of quantum dots in series[36]. The double quantum dot can be seen as an “artificial molecule” compared to the single dot which is more like an atom. In this case, the “interatomic” bond character is defined by the tunnel coupling (possibly controlled by a gate) and it can be tuned from an ionic character (with electrons localised on both dots) to a more covalent-like system with electrons delocalised over both dots. We will discuss this model in the next section.

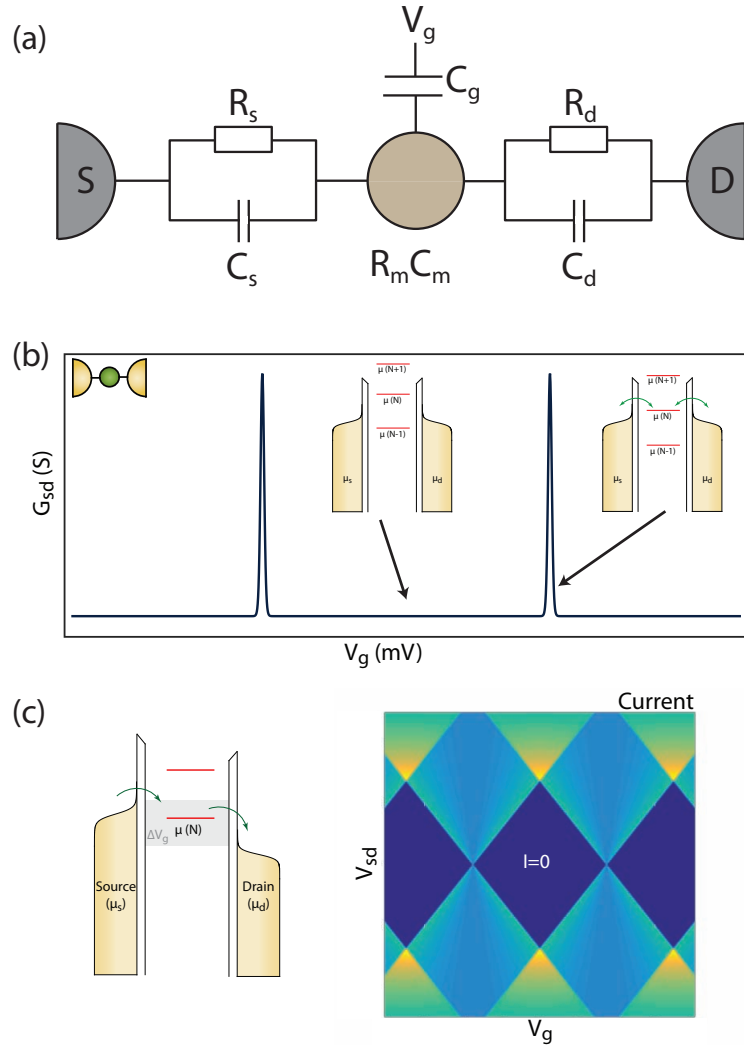


Figure 2.2: Transport through a single quantum dot. (a) Circuit diagram showing resistive and capacitive couplings to the source and drain, and the capacitive coupling to the gate. (b) The linear conductance with gate voltage shows Coulomb blockade, with current allowed to flow only when the dot level is aligned with the leads at zero bias. (c) At finite bias, there is an expanded window of gate voltage where current may flow, causing diamond-shaped regions of blockade (shown on the right). At high enough applied bias, multiple charge states may lie within the window and current can flow through multiple channels. Figures adapted from [36] and transport simulated in Matlab.

In the constant interaction model applied to the double quantum dot, the system of conductors can be expressed as matrices (instead of constant as before), where the charges at each node are linear function of the potentials, $\mathbf{Q} = \mathbf{C}\mathbf{V}$, where \mathbf{C} is the capacitance matrix. Proceeding as in the previous section, but with the matrix method, we find for the electrochemical potential of dot 1

$$\mu(N_1, N_2) = (N_1 - 1/2)E_{C1} + N_2E_{Cm} - \frac{1}{|e|}(C_{g1}V_{g1}E_{C1} + C_{g2}V_{g2}E_{Cm}) \quad (2.4)$$

E_{C1} is the change in the potential of dot 1 when (with gate voltage fixed), N_1 is changed by 1, and is called the addition energy of dot 1, with E_{C2} the addition energy of dot 2. The mutual charging energy E_{Cm} gives the change in the energy of one dot when an electron is added to the other. These energies are given by

$$\begin{aligned} E_{C1} &= \frac{e^2}{C_1} \frac{1}{1 - \frac{C_m^2}{C_1 C_2}} \\ E_{C2} &= \frac{e^2}{C_2} \frac{1}{1 - \frac{C_m^2}{C_1 C_2}} \\ E_{Cm} &= \frac{e^2}{C_m} \frac{1}{1 - \frac{C_1 C_2}{C_m^2 - 1}} \end{aligned} \quad (2.5)$$

In practice it is useful to define the reduced gate voltage $n_g = C_g V_g / |e|$, the polarization charge applied by the gate in electron units. If n_g is some integer N , the dot obtains N electrons, while for a half-integer value of n_g , electrons can move on and off the dot (the single-electron tunneling state). Coulomb blockade for a double quantum dot (when N is an integer) results in lines of stable charge configurations which change in shape depending on the interdot tunnel coupling. Fig. 2.3 shows the shape of the transport configurations against the individual dot gate voltages for the limiting cases of weak coupling ($C_m = 0$) and strong coupling ($C_m/C_{1(2)} \rightarrow 1$), as well as for the typical case where the coupling is intermediate. The charge stability diagram is then made up of hexagonal regions of fixed charge, leading to the so-called honeycomb charge diagram. In this situation in the low bias regime, transport through the double dot is permitted where the boundaries of three hexagonal regions meet, called “triple points”; this is where the potentials of the two dots are aligned with the potentials of the leads. In the high bias regime the triple points now become triangular regions, where two dot levels can lie in the bias window, as shown in Fig. 2.4. Lastly, considering that the dot levels are quantised, for large voltages, ground

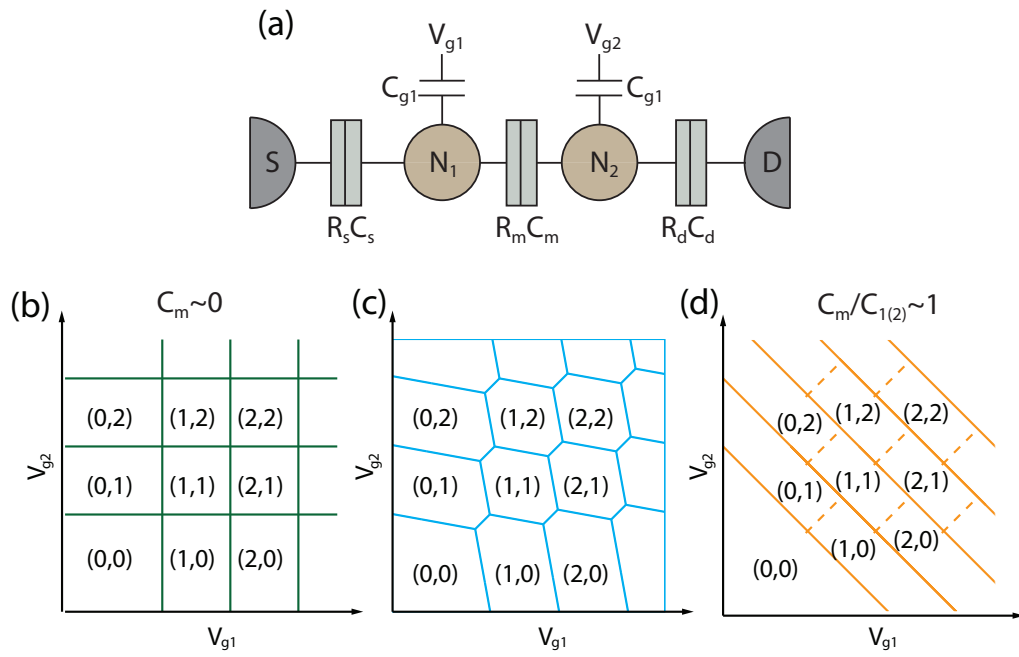


Figure 2.3: Transport through a double quantum dot. (a) Circuit model for a double quantum dot, now showing the mutual resistive and capacitive couplings of the two dots. (b)-(d) Charge stability diagrams, showing the electron numbers in dots 1 and 2 (N_1 , N_2), for a double quantum dot in the (b) weak, (c) intermediate and (d) strong coupling regimes. Figure adapted from Ref. [36].

states as well as excited states contribute to the transport. The successive alignment of ground and excited states contributes to resonances within the bias triangles. Transport measurements are useful for estimating charging energies, dot configurations and tunnel rates (the bending of the edges of the stability diagram with strong tunnel couplings, for example, is useful for this). However, transport requires the exchange of dot electrons with leads, and therefore is inherently an invasive method. Qubit occupation can alternatively be determined by the technique of charge sensing, where the capacitance or resistance of a proximal charge sensor, sensitive to electrons tunnelling into and out of the dot is monitored. Quantum point contact (QPCs), single electron transistors (SETs) as well as quantum dots are typically used for charge sensing. In addition, gate-based charge sensing, a method that has become popular over the last few years, can be used and is described in Chapter 3.

We now discuss two kinds of two level systems or qubit candidates that are described in this thesis and that can be realised using double quantum dot systems. The first kind is the charge qubit.

2.3 Charge qubits

We have discussed how the ionic and covalent type states form in the weak and strong limits of the tunnel coupling in a double quantum dot[38]. The one-electron charge states $(0,1)$ and $(1,0)$, i.e. whether the electron is on the right dot or the left, form the basis states $|0\rangle$ and $|1\rangle$ of a charge qubit, shown in Fig. 2.5. We define the “detuning”, ϵ , as the gate voltage parameter which takes us across the $(1,0)$ and $(0,1)$ interdot charge transition (ICT) and sets the energy splitting. Therefore we have the diagonal matrix element of the Hamiltonian, $\mathcal{H} = \frac{\epsilon}{2}\sigma_z$. The tunnel coupling ($t_c = \Delta/2$) gives the off-diagonal terms in the Hamiltonian, leading to a full Hamiltonian of the form

$$\mathcal{H}_i(t) = -\frac{\Delta}{2}\sigma_x - \frac{\epsilon}{2}\sigma_z \quad (2.6)$$

and a splitting between the eigenenergies of $\Omega = \sqrt{\epsilon^2 + \Delta^2}$ at the avoided crossing near zero detuning.

For charge qubits, by preparing a state with the electron in one dot (say, the left, at $\epsilon_0 < 0$) followed by a pulse on the drain to zero detuning, one can make the system undergo coherent state mixing. When the device is switched back to ϵ_0 , the electron charge state

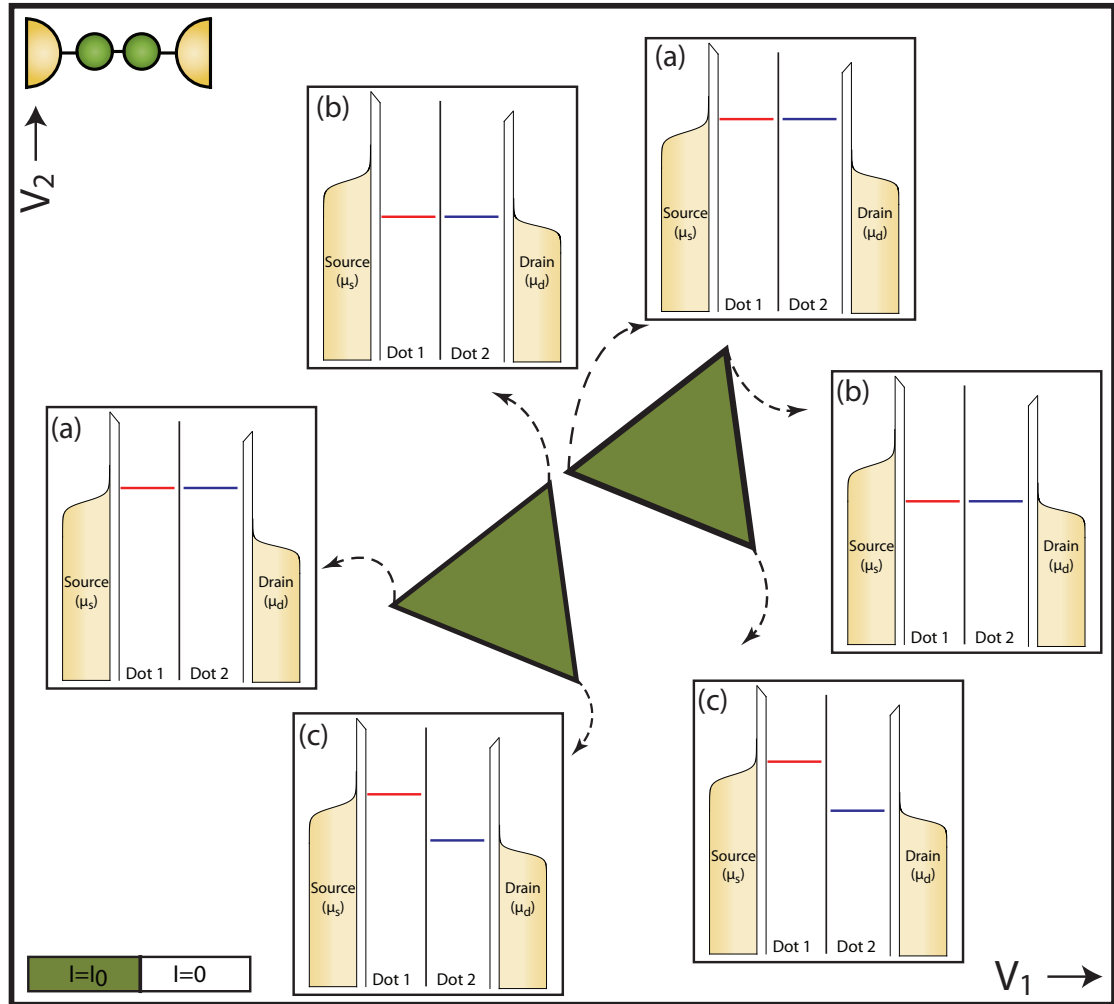


Figure 2.4: Triple points in double quantum dot transport. Transport can occur when at least one energy level, for both the left dot and right dot lie in the bias window. The energy level of the left dot also has to be lower(higher) than that of the right dot at positive(negative) bias. The corners of the triangular points, as shown, correspond to situations where (a) both dot levels are in resonance with the source, (b) both dot levels are in resonance with the drain and (c) the left dot level is in resonance with the source, and the right dot level with the drain. Figure adapted from Ref. [36].

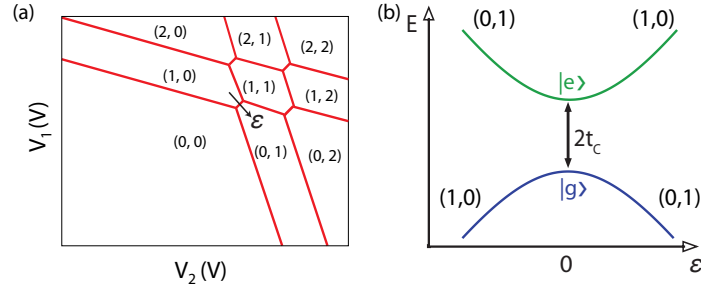


Figure 2.5: A tunnel coupled charge qubit. (a) Charge stability diagram showing the charge qubit that can be formed in the detuning direction (indicated by ϵ), using the (0,1) and (1,0) states. (b) Band diagram for a double quantum dot as a charge qubit, showing the tunnel coupling between the two states.

can be measured by looking for the signature of the electron tunneling out to the source, which will indicate it is in the right dot[39].

Microwave spectroscopy

Applying microwaves to the gate electrode, we can observe coherent oscillations between the electron charge states at detuning values where the energy splitting matches that of a single photon[40], i.e. following the relation $\Omega = \sqrt{\epsilon^2 + \Delta^2} = h\nu$, where ν is the microwave frequency. This is called photon assisted tunneling (PAT)[36], and by tracking the PAT peaks with detuning and microwave frequency, the energy levels of the system can be accurately mapped out. Tuning the frequency to match the energy splitting at zero detuning also leads to resonant driving, and the half width at half maximum of this resonance gives an approximate value for the coherence time T_2^* ; however a value measured in this way is typically broadened by slow and time averaged charge fluctuations. By chopping microwaves, the charge state relaxation time can be mapped out[41, 42]. These techniques will be used in Chapter 6 for our dopant-dot charge qubit.

2.4 Landau-Zener interferometry

We now take a look at the theory of Landau-Zener Interferometry; we will perform a Landau-Zener interferometry experiment in a silicon double quantum dot in Chapter 4. The analysis presented in this section closely follows that presented in Ref. [43]. We con-

sider our charge qubit as a strongly and periodically driven two level system (TLS), with energy bias or detuning $\epsilon(t)$ and tunnelling amplitude Δ , where the latter in our system is fixed. For such a TLS, the Hamiltonian in terms of the Pauli matrices $\sigma_{x,z}$ can be written as

$$\mathcal{H}_i(t) = -\frac{\Delta}{2}\sigma_x - \frac{\epsilon(t)}{2}\sigma_z \quad (2.7)$$

We also assume periodic driving with amplitude A , angular frequency ω and offset ϵ_0 , such that

$$\epsilon(t) = \epsilon_0 + A \sin \omega t \quad (2.8)$$

The instantaneous eigenvalues of $\mathcal{H}(t)$ are

$$\begin{aligned} E_{\pm}(t) &= \pm \frac{1}{2}\Omega(t) \\ \Omega(t) &= \sqrt{\Delta^2 + \epsilon(t)^2} \end{aligned} \quad (2.9)$$

For a strongly driven TLS, Landau-Zener dynamics are often explored in the literature in terms of the intuitive adiabatic-impulse model[44], where the TLS is repeatedly driven through an avoided crossing. While this theory was originally developed for atomic systems and in the solid state for superconducting qubits, it has been shown to be effective for the case of single-electron charge qubits in GaAs[45]. Following this model, the interference of two quantum states during a double passage through an avoided level crossing solely relies on the mutual coupling and is independent of the exact time evolution of the two states in the vicinity of the avoided crossing. The energy eigenstates in the adiabatic

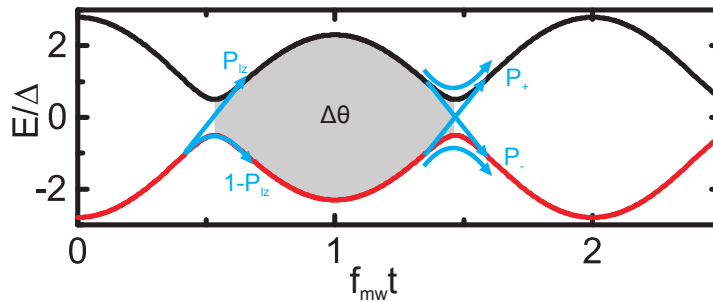


Figure 2.6: Evolution of the energies during Landau-Zener interferometry. The ground (red) and excited (black) state energies evolve as a function of time when periodically driven through the anti-crossing, with P_{LZ} the probability of a Landau-Zener transition. The dynamical phase $\Delta\Theta$ is given by the area in gray, and for a double passage is equivalent to the Stückelberg phase. Figure taken from Ref. [46].

basis change very fast around the avoided-crossing region, and remain more or less constant away from the crossing; we therefore intuitively expect that the system evolves adiabatically away from the avoided crossing. However, the evolution becomes nonadiabatic near the anticrossing. Instead of making an arbitrary boundary between the nonadiabatic and adiabatic regimes, it is mathematically simpler to consider adiabatic evolution everywhere except at zero detuning, where a sudden mixing in the populations of the two energy levels is modelled. This picture is called the adiabatic-impulse approximation, which emphasizes the two-stage model and the instantaneous nature of the non-adiabatic transitions across the avoided crossing.

Single Passage: The full derivation of the Landau-Zener probability is given in Ref. [43], and we do not reproduce it here but discuss the results in different regimes. If we assume that the system initially occupies the lower energy level, the transition probability from the lower to the upper level during a single sweep across the avoided crossing can be described within a quasiclassical approximation[47] (we will consider the effects of decoherence later), and the probability that the system ends up in the upper energy level is given by

$$P_+ = P_{LZ} = \exp \left[-\frac{\pi \Delta^2}{2\omega \sqrt{A^2 - \varepsilon_0^2}} \right], \quad (2.10)$$

where P_{LZ} is the probability of a Landau-Zener transition. For small Δ this implies that the probability rapidly changes along the lines $|\varepsilon_0| = A$, and is constant in between. The inclination of these lines can be compared with experiment for the calibration of microwave amplitude. Defining the driving velocity $v = \omega \sqrt{A^2 - \varepsilon_0^2}$ leads us to see that as we vary v from 0 in the adiabatic limit to ∞ in the sudden-change limit, the probability of the state transitioning from the lower to upper level P_+ goes from 0 to 1. As we will discuss next, this feature can be exploited by varying v such that the transition acts as a 50/50 beam splitter for the electron wavefunction.

Double Passage and the Stückelberg Phase: We now consider now the double-passage problem, where we traverse the avoided crossing region twice at the same speed (or drive back and forth across the crossing), completing one full driving cycle of the periodic drive. The probability of the system ending up in the upper basis can now be given by

$$P_+ = 4P_{LZ}(1 - P_{LZ}) \sin^2 \Phi_{St}, \quad (2.11)$$

which comes out to be

$$P_+ \simeq 2\pi \frac{\Delta^2}{A\omega} \left(1 - \frac{\varepsilon_0^2}{A^2}\right)^{-1/2} \sin^2 \Phi_{\text{St}}, \quad (2.12)$$

$$\Phi_{\text{St}} = -\frac{\varepsilon_0}{\omega} \arccos \frac{\varepsilon_0}{A} + \frac{A}{\omega} \left(1 - \frac{\varepsilon_0^2}{A^2}\right)^{1/2} - \frac{\pi}{4}. \quad (2.13)$$

where Φ_{St} is the Stückelberg phase[48, 49]. This situation is shown in Fig. 2.6. The probability of the system being excited into the upper state after two consecutive passages through the avoided crossing is therefore an oscillating function of this phase, the two components of which are acquired during the adiabatic evolution and non-adiabatic (impulse) transition. Without interference, the averaged probability is $\langle P_+ \rangle = 2P_{\text{LZ}}(1 - P_{\text{LZ}})$. However, the quantum mechanical interference between the different LZ transitions means that the total excitation probability after both passages ranges from 0 for destructive interference to $\langle P_+ \rangle = 4P_{\text{LZ}}(1 - P_{\text{LZ}})$ for constructive interference, similar to the Mach-Zehnder interferometer[50, 51].

This kind of double-passage experiment presents a way to perform coherent charge state manipulation. Fig. 2.7 shows the steps involved in such an experiment. Choosing an initial state (0,1), the ground state at $\epsilon > 0$, we adiabatically sweep across zero detuning. Now the ground state is (1,0). For a non-adiabatic sweep, the population mostly remains in the initial state (1,0). The speed of the pulse across zero detuning can be set such that the resulting qubit state contains 50% of (1,0) and (0,1); this analogous to an optical 50/50 beam splitter for light. This can be quantified by the Landau-Zener formula for single passage (Eq. 2.10).

After the beam-splitting pulse, the qubit can precess effectively in the x-y plane of the Bloch sphere (with the Larmor frequency proportional to Ω until a refocusing pulse across the anticrossing takes it back to the initial state (0,1)). The probability of finding the qubit in the initial state will now show a Mach-Zehnder type interference pattern with the qubit states as the light paths, and coherent manipulation can be achieved by the tuning of pulse lengths[51, 53].

Multiple Passage: The characteristic speckled LZS interference pattern is one that arises from a multiple passage experiment, where the system is swept across the avoided crossing periodically. Some relevant timescales here for a visible interference pattern are (a) the time between subsequent tunneling events, which is of the order of half of the driving period ($T/2 = \pi/\omega$) and (b) the phase coherence of the system, for which we

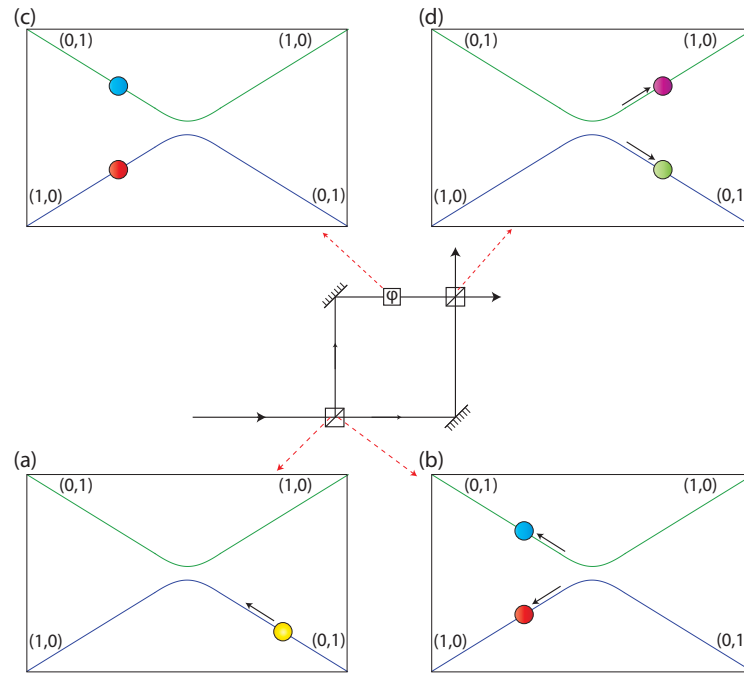


Figure 2.7: Charge qubit manipulation in a Mach-Zehnder type of experiment. (a) The qubit is initialised in the $(0,1)$ and (b) swept non-adiabatically across the anticrossing with a 50/50 probability of finding the electron in either charge state; this process is like a 50/50 beam splitter for light. (c) The state is allowed to precess in the x - y plane by waiting for a certain free evolution time, then (d) pulsed back across the avoided crossing. A charge sensing measurement can be performed, and an interference pattern observed as for light. Figure adapted from Ref. [52].

consider the dephasing time T_2 . The characteristic Landau-Zener time ($t_{\text{LZ}} \sim \frac{2}{\Delta} \frac{\Delta^2}{4\omega\sqrt{A^2 - \varepsilon^2}}$) for the duration of a transition should therefore be $t_{\text{LZ}} < T/2 < T_2$, such that consecutive LZ events cannot overlap, and that the phase coherence of the system is preserved.

The interference patterns observed can be vastly different depending on this characteristic Landau-Zener time; in the two opposite limits where the individual crossings are slow (such that they are almost adiabatic, and $P_{\text{LZ}} \ll 1$), or fast. In both cases, there is a resonance condition which determines whether there will be an interference pattern between the upper and lower states. In the LZS experiment explored in Chapter 4, we are in the fast passage regime

$$\Delta^2/A\omega \ll 1, (1 - P_{\text{LZ}}) \ll 1 \quad (2.14)$$

and therefore we concentrate on the description of this regime (the slow passage regime is described further in Ref. [43]). The resonance condition here can be analytically calculated; it reduces to $\varepsilon = k\omega$ for integer k . Changing the system parameters (ε_0 or ω), we pass through different k -photon resonances; this can give us a valuable energy scaling as well. Additionally, to calibrate the microwave power applied, one can use the separation between the minima or maxima in the interference pattern (Fig. 2.8, described later, shows some LZS patterns).

In the analysis before, we have ignored decoherence (or rather, assumed $T/2 \ll T_2$). From the full calculations including the relaxation and dephasing times T_1 and T_2 (these are performed in the rotating wave approximation using the Bloch equations for the reduced density matrix, detailed in [43], Appendix B), the steady state solution for the time-averaged upper-level probability in the strong-driving regime is:

$$P_+ = \frac{1}{2} \sum_k \frac{\Delta_k^2}{\Delta_k^2 + \frac{T_2}{T_1} (|\varepsilon_0| - k\hbar\omega)^2 + \frac{\hbar^2}{T_1 T_2}}, \quad (2.15)$$

where $\Delta_k = \Delta J_k(A/\hbar\omega)$, and J_k is the k -th order Bessel function. This formula is a good approximation everywhere except for the vicinity of $\varepsilon_0 = 0$ (however it is still qualitatively illuminative in this region, as we will see in our simulations in Chapter 4). It is worth noting that this formula additionally describes the single and double passage cases, with the effect of decoherence included.

Decoherence and the Landau-Zener problem

For LZS interferometry, it is useful to consider a fast-driven TLS where we start with incoherent driving (slow compared to T_2) and gradually increase the coherence time of the system[43]. We look at the effect of coherence on the steady-state populations of the two levels. With strong decoherence, no interference occurs between the different Landau-Zener transitions. In this case, going back and forth through the avoided crossing, we give a small impulse (uncorrelated to impulses from all the other sweeps) to the state populations, which adds up to a steady state where the two states have equal populations of the two energy levels (the exact ratio depends on thermal excitation and relaxation rates). This is shown in Fig. 2.8(a). We now increase the coherence time to a point where the two transitions in a single driving period (i.e. driving back and forth) are separated by a time smaller than T_2 . However, the transitions induced by two different driving *cycles* are separated by more than T_2 , and these are then independent impulses. There are therefore two interfering transitions per cycle, and if the phase accumulated between these corresponds to destructive interference, at the end of a full driving period there will be no mixing. There will now be lines in the previously incoherent map, as shown in Fig. 2.8(b). We can now increase T_2 even more, such that we can interfere between transitions from a few successive driving cycles. The resonance lines now start forming; indicating that the mixing between the two states is suppressed whenever the resonance condition presented in Section 2.4 is not satisfied (Fig. 2.8(c)).

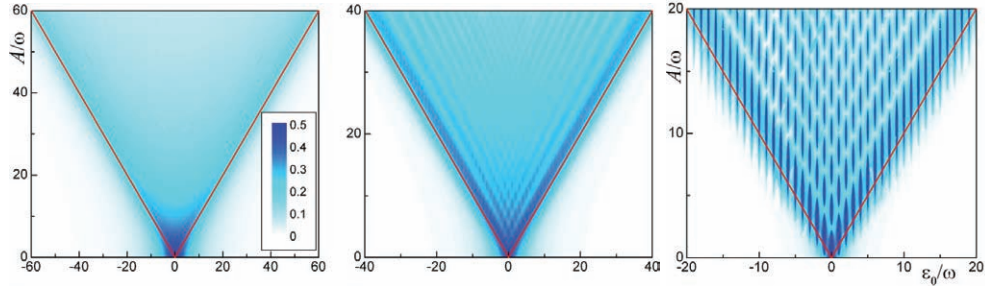


Figure 2.8: Effect of decoherence on the Landau-Zener interferometry pattern. LZS interferometry with high-frequency driving is shown, including the effects of decoherence, by numerically solving Eq. 2.15, with the upper level steady state probability plotted. The dephasing time T_2 is given by $\omega T_2/(2\pi) = 0.1$ in (a), 0.5 in (b) and 1 in (c), while the relaxation time is given by $\omega T_1/(2\pi) = 10^3$ for all plots. Figure adapted from Ref. [43].

In Chapter 4 we will revisit the LZS formulas, with some modifications due to the technique of gate-based reflectometry and the measurement via the quantum capacitance.

2.5 Spin qubits and Pauli spin blockade

We now move on to one- and two-electron spin states in quantum dots, and the spin qubits that can be represented using them. For a single electron, the magnetic moment is an extremely small quantity ($\sim 57.8 \mu\text{eV/T}$) and its direct detection is correspondingly extremely difficult[54, 55]. As such, measurements of the spin state are typically made through projection into another more easily measurable quantity, for example the charge, which is accessible by transport and charge-sensing measurements. Therefore, spin-to-charge-conversion has become the standard way to read out quantum dot spin states[6, 23, 56, 57]. With the addition of this technique, the electron spin in a quantum dot is a promising candidate for a qubit, especially over the charge qubit, since it couples less easily to the environment in the solid state and has longer coherence times, but can still be read out and shuttled using electric signals, via the charge of the electron.

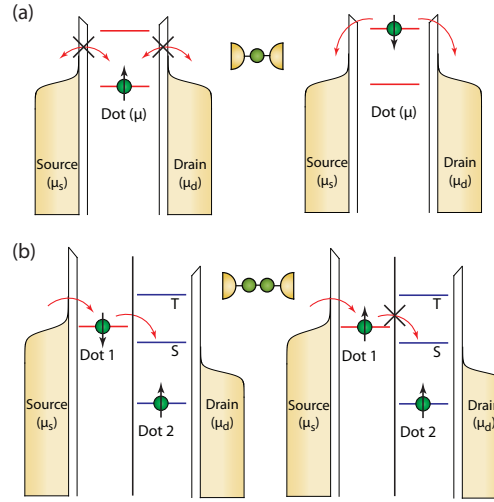


Figure 2.9: Spin blockade in quantum dot systems for (a) a single dot and (b) two dots in series. At low temperatures and with a small magnetic field applied to split the spin states, the lower energy spin state is trapped in the quantum dot. However, the high energy spin state is free to tunnel out of the quantum dot and this can be detected through transport, or through a proximal charge sensor.

2.5.1 Single electrons and the Loss-DiVincenzo qubit

We first discuss the case of a single electron in a quantum dot. This was the basis of the original Loss-DiVincenzo proposal, where two single-electron spins in adjacent quantum

dots formed two qubits, with each two level system formed of the $|\uparrow\rangle$ and $|\downarrow\rangle$ spin states split by the Zeeman energy (E_Z) in a large external magnetic field B_0 (~ 1 T). This kind of qubit relies on a kind of spin blockade; when the quantum dot is tuned correctly, the energy difference between the two spin states under B_0 means that tunneling is allowed for one orientation of the spin, and blocked for the other (Fig. 2.9). Manipulation of the spin can be accomplished using Electron Spin Resonance, or ESR. For example, microwave pulses at resonance ($h\nu = E_Z$) can be applied to an on-chip transmission line to create an AC magnetic field B_1 , driving rotations between $|\uparrow\rangle$ and $|\downarrow\rangle$. In 2006, this technique was first demonstrated by Koppens *et al.*[58] in a GaAs quantum dot that had a microwave stripline fabricated on top, shown in Fig. 2.10(b).

For double quantum dots, a two qubit logic gate has been performed in silicon[18], using a similar technique. A microwave stripline addresses two adjacent spins in a double quantum dot, with a small frequency difference of 40 MHz that is electrically tuned via the Stark shift. In this case, the readout is hysteretic; tunneling of dot 1 to the reservoir is via dot 2, leading to hysteresis as a function of the sweeping direction since there is a finite mutual charging energy. Dot 1 can only tunnel to dot 2 and then to the reservoir when the dot levels are aligned, leading to a charge-sensing signal that is maximised in this situation.

ESR has also been demonstrated using an oscillating electric field applied to a gate electrode[59]. This method is preferable since it avoids the fabrication of a separate stripline, which is typically large compared to the quantum dot dimensions and therefore affects scalability. However, this method generates the effective AC B_1 field by moving the electron wavefunction using the AC-electric field in an external magnetic field gradient. Such a gradient can be generated using a micromagnet[60, 61] or by random variations in the nuclear magnetic field[62], or alternatively by spin orbit coupling[59] (giving rise to Electron Dipole Spin Resonance or EDSR). In our experiments in Chapter 6, we show that another method of generating a gradient could be built into our hybrid dopant-dot system, since an electron localised on the dopant feels the contact hyperfine interaction from the nuclear spin, which it does not while localised on the dot. Measurements hinting at this process, with rotations driven using the natural field gradient due to a phosphorus atom have recently been reported[30].

In single-spin quantum dots, the DiVincenzo[20] criteria have largely been met, in silicon as well as in other materials. However, the schemes above have the disadvantage that they require high magnetic fields to provide high Zeeman splittings, which can affect coherence in certain systems[63] which operate better at low magnetic fields. In addition,

micromagnets and coplanar striplines are difficult to scale up, and silicon has a very weak spin-orbit coupling as well as a lack of a strong fluctuating nuclear magnetic field. An alternative method therefore focuses on two-electron spin states, and is outlined below.

2.5.2 Two electrons and the singlet-triplet qubit

For two electrons, we have the following four two-spin states, the antisymmetric singlet

$$|S\rangle = (|\uparrow\downarrow\rangle - |\downarrow\uparrow\rangle)/\sqrt{2} \quad (2.16)$$

with $S = 0$ and the symmetric triplets

$$\begin{aligned} |T_+\rangle &= |\uparrow\uparrow\rangle \\ |T_0\rangle &= (|\uparrow\downarrow\rangle + |\downarrow\uparrow\rangle)/\sqrt{2} \\ |T_-\rangle &= |\downarrow\downarrow\rangle \end{aligned} \quad (2.17)$$

with $S = 1$ and $S_z = 1, 0$, and -1 , which are degenerate at zero field but split by the Zeeman energy in an external magnetic field (~ 100 mT). In the two-electron spin system, the basis states typically used to represent a qubit are the singlet S and the triplet T_0 with $m_s = 0$. Originally proposed by Levy[64], this qubit basis was proposed as it could render the qubit immune to spatially uniform magnetic field fluctuations. In the (1,1) charge state¹, the overlap between the electron wavefunctions is very small. However, if the two electrons are on the same dot (the (2,0) or (0,2) configurations) then due to the antisymmetrization condition on the total wavefunction there is a large exchange splitting E_{ST} between the singlet and triplet states as shown in the energy diagram in Fig. 2.10(a). The effective exchange between the singlet and triplet states in a hybridised situation, with $t_c > 0$, given by J , is now detuning dependent, and can be controlled using gate voltages. This exchange splitting is typically dot size dependent, and can be made very large compared to $k_B T$ (up to several meV) and can be used to drive rotations around the z-axis (parallel to the external magnetic field). There are also regions in detuning where the singlet state maps to the charge state (0,2) while the triplet remains in the (1,1) state, leading to spin-to-charge conversion that can be detected.

¹where given a charge assignment (N_L, N_R), N_L for example signifies the excess charge on the left dot.

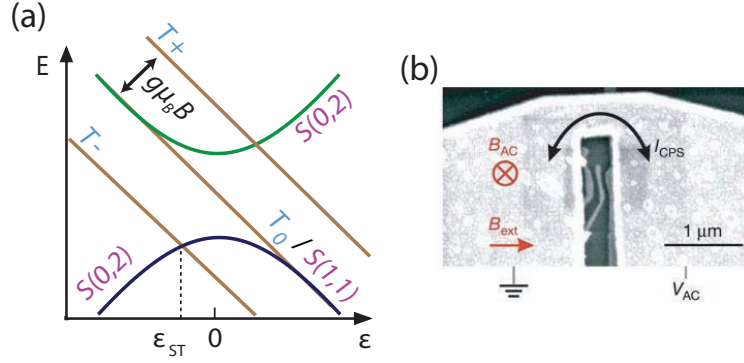


Figure 2.10: (a) The energy level diagram of a singlet-triplet qubit with detuning, seen at a transition such as the (1,1) to (2,0). The triplet states are split by an applied magnetic field (assuming a positive g -factor). (b) The device structure used by Koppens *et al.*[58] comprises a microwave stripline fabricated directly above a quantum dot (visible below).

Qubit manipulation

Given a singlet-triplet qubit defined as above, a spin-sensitive measurement can then be performed by:

- Initialization into either the singlet[66] or triplet[58] state (via the detection of spin blockade, for example) by starting with both electrons in the same quantum dot. Here the exchange splitting J of the (2,0) charge state, which is large ($\sim 100\mu\text{eV}$ for GaAs), is substituted for the Zeeman splitting of a single spin.
- Separation of the two spins into the (1,1) state by tilting the potential so that J is turned off.
- State evolution; by (a) waiting at the evolution point[57, 63], (b) performing single spin rotations[58] or (c) two-spin operations[66].
- Projection into the (2,0) charge state. If the state is a singlet, the spins can be tilted into the same quantum dot. However, if the state is a triplet, they will be in spin blockade due to the exchange splitting.

We now come to x -axis rotations. In GaAs, where these have been demonstrated, there is an effective hyperfine field, which fluctuates on a timescale of a few μs and is therefore different for the two quantum dots. This field ΔB_N sets the σ_z matrix element, where the Hamiltonian is now given by $\mathcal{H} = \frac{J(\epsilon)}{2}\sigma_z + \Delta B_N\sigma_x$, and we now have two axes of control

for our qubit[66]. In other systems such as silicon, where there is a much smaller hyperfine field arising from the ^{29}Si isotope (and no hyperfine field for isotopically purified ^{28}Si) methods such as a coplanar stripline need to be used for this purpose[18].

Nuclear spin polarization

The last topic we touch upon for singlet-triplet qubits is the technique of nuclear spin polarization. At the $S - T_-$ crossing shown in Fig. 2.10(a) ($S - T_+$ for GaAs due to its negative g-factor), the effective exchange matches the Zeeman energy and any nuclear spin gradient mixes the two states. This kind of transition is important for our proposed hybrid dopant-dot spin qubit, as explored in Chapter 6. At such a mixed crossing, an $S - T_-$ transition results in an electron spin flip; angular momentum conservation now requires a simultaneous spin ‘flop’, coming from a neighbouring nuclear spin in GaAs or in natural Si, while for a dopant-dot hybrid qubit in ^{28}Si , the dopant nuclear spin flip can be induced in this way. Repeated transitions followed by exchange of electrons with the leads can then build up a nuclear spin polarization[67]. Such polarization techniques have been shown to strongly increase the inhomogeneous coherence time T_2^* [68] and in our system can be explored as a way to access the dopant nuclear spin.

Lastly, we mention the exchange-only qubit[69, 70], which has been proposed for three spins in a triple quantum dot architecture. Rotations in such a qubit are mediated in both x- and z-directions by the exchange interaction and this eliminates the need for direct or indirect magnetic control via micromagnets, striplines, or spin-orbit coupling and EDSR. While this system has been explored in GaAs quantum dots, it is yet to be implemented in silicon.

2.5.3 The silicon material system

In this section, we briefly describe the silicon semiconductor as host for quantum dot qubits as described above, as compared with other systems such as GaAs heterostructures and InAs nanowires. In Chapter 1 we have presented silicon as an attractive host for a qubit architecture due to the presence of a multi-billion dollar semiconductor industry that is able to make small scale silicon devices, complete with control electronics, with repeatability and ease. However, apart from these scalability considerations, silicon as a semiconductor host for quantum dots has some specific advantages in terms of qubit relaxation and coherence, which we now discuss.

Spin-orbit interaction

The decay of coherent Rabi oscillations, a measure of information loss, can be attributed to processes categorised as relaxation and decoherence. The relaxation timescale T_1 is strongly correlated with the spin-orbit coupling in the host material.

For a charge qubit, relaxation to the ground state is often mediated by phonons[31]. However, for pure spin states, a spin-flip process is required, which phonons cannot cause since they carry no angular momentum. However in practice, the pure spin states we use to describe spin qubits are not totally ‘pure’ due to the presence of spin-orbit coupling, which couples the spin degree of freedom to the orbital levels[71]. The spin orbit coupling arises from the stretched lattice Coulomb potential (and consequently an effective magnetic field) seen by the relativistically moving conduction band electrons[72, 73]. This can be decomposed into Dresselhaus[74] and Rashba[75] processes. The former, also called bulk inversion asymmetry, comes from the atomic cores of the host lattice, while the latter, also called structure inversion asymmetry, consists of the macroscopic electric field into which gate potentials also contribute. The spin-orbit interaction couples the pure spin states to the orbital levels, so that the spin and orbital quantum numbers are not good anymore. Phonons can now therefore participate in the relaxation process without the selection rules imposed earlier. Silicon has a weak spin-orbit coupling[76], due to its low atomic number and its monoatomic lattice, and this results in spin-orbit induced relaxation rates that are predicted to be at least two orders of magnitude smaller than for GaAs[77].

Hyperfine interaction

Decoherence of the spin qubit is described by T_2 , the time taken to lose coherent phase information. Hyperfine-induced decoherence is a major contributor to the lower coherence times of GaAs spin qubits (where Rabi oscillations quickly decay on a scale of tens to hundreds of nanoseconds) as compared to silicon[62, 66]. The Zeeman splitting of a nuclear spin is typically much lower than realistic values of $k_B T$, since the g-factor has a value that is 10^3 times lower. The direction of the nuclear spin is constantly fluctuating, leading to a total hyperfine field that is a Gaussian distribution. Due to this fluctuating nature, the Larmor frequency also fluctuates, leading to decay of the Rabi oscillations that decay as e^{-t^2/T_2^2} where $T_2 \propto \Delta B_N$. To improve T_2 , apart from refocusing pulse sequences such as CPMG[66], one can move to a host material with fewer nuclear spins. Silicon has a low concentration of nuclear spins arising from the low-abundance ^{29}Si isotope (only 5%),

and it can be further isotopically purified to the ^{28}Si isotope, which results in a kind of “semiconductor vacuum” for spin.

One disadvantage, however, which should be mentioned at this point is that the ~ 3 times larger effective mass of silicon as compared to GaAs leads to a need for scaling down already small gate configurations in order to form quantum dots with adequate orbital level spacings (by a factor of about ~ 2.5 for a typical depletion-gate geometry as shown in Fig. 2.1(d)). We discuss this fabrication challenge, and a potential solution to it, in more detail in the following chapter.

Lastly, we discuss a final obstacle for silicon, its six-fold degenerate valleys. These are six equivalent conduction-band minima located on the Δ lines, at $k \approx 0.84k_0$ toward the six X-points of the Brillouin zone[78]. Due to confinement in the z-direction and/or uniaxial tensile strain at the interface, the valleys perpendicular to the interface have a much smaller energy than those in the plane of the interface. The two z-valleys can be further coupled by a sharp interface, with a valley-orbit coupling Δ which is sample and interface dependent (for example for Si/SiGe and Si/SiO₂)[77]. A large valley splitting is desired since the degenerate system then reduces to a single-valley qubit, a nuclear-spin free version of the very successful GaAs system. On the other hand, for smaller valley splittings, the energy scale is no longer set by the confinement but by the valley splitting and it can become difficult to observe spin blockade since it can be lifted by the valley degree of freedom.

In the next section, we discuss the other component of our hybrid qubit, the dopant spin in silicon.

2.6 Dopant spins in silicon

Up to now we have discussed quantum dots in the solid state. In this section, we present a few aspects of the physics of dopant atoms, and especially their spins, in silicon. In particular, electron spin resonance has been used for decades to measure and manipulate dopant spins in silicon, and is a technique we will apply in the measurements presented in the later chapters of this thesis.

For the sake of simplicity, we consider the ^{31}P donor in silicon, which can be conceptualised as a hydrogen atom in a solid state matrix. It has the excess charge of the phosphorus nucleus as compared to the silicon nuclei, creating a Coulomb potential that can bind an extra electron in the neutral donor (D^0) charge state. The nucleus has a spin $I = 1/2$ (this

can be different for other donors, with several interesting consequences²), while the extra electron also has a spin $S = 1/2$. A single donor atom is therefore, as discussed in Chapter 1, a two-qubit system in itself.

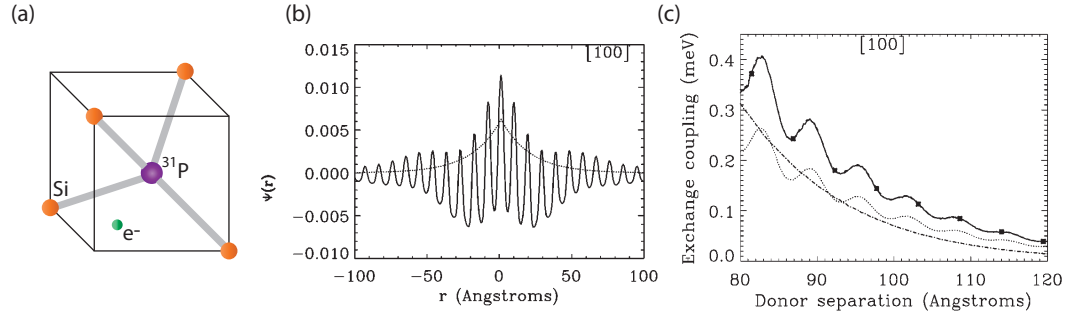


Figure 2.11: (a) Silicon crystal with a phosphorus donor occupying a substitutional site, with an extra electron. (b) Kohn and Luttinger solution for the donor electron wavefunction. (c) Corresponding oscillations in the exchange between two proximate donors, with asterisks denoting lattice sites. Latter two figures from Ref. [78] (in which the calculations for the solid line in (c) were performed, while the dotted line is a comparison with Ref. [15]. The dotted-dashed line is calculated using a simple 1s hydrogenic orbital form.).

2.6.1 Level spectrum and energies

In the Kane model for a quantum computer, the nuclear spins encode the qubit, while the donor electron wavefunction mediates single and coupled gate operations and is crucial[5]. Kohn and Luttinger were the first to go beyond simple hydrogenic approximations for the electron wavefunction and include the effect of the silicon lattice. In 1955 they applied effective mass theory to calculate the donor electron wavefunction, expanded in the basis of the Bloch functions for silicon[80].

The coefficients $F(k)$ are obtained by substituting in to the Schrodinger equation, with a Hamiltonian given by $H_0 - U(r)$, where H_0 is the Hamiltonian for the silicon lattice and $U(r)$ the donor potential. This results in hydrogenic wave functions, scaled by the silicon dielectric constant $\kappa = 11.9$ and the effective mass³. The six independent equations give us wavefunctions spread over multiple lattice sites, which oscillate rapidly with the lattice periodicity and are modulated by a slower-varying envelope function. We commented upon

²For example, the so-called “clock transitions” in Bismuth, with $I = 9/2$ for ^{209}Bi lead to dramatically increased coherence times[79].

³Spherical conduction band minima at the Brillouin zone origin are assumed, and an effective mass averaged over the perpendicular and parallel directions is used.

the sixfold-degenerate valleys in the bandstructure of silicon in the previous section; these have consequences for the energy spectrum of the donors in silicon, and taking valley-orbit coupling into account accounts for much of the discrepancy observed between the Kohn-Luttinger energy levels (28.95 meV) and the experimental values (45.5 meV). Further refinements, bringing the energy levels into agreement with the experimental values, were made using local empirical pseudopotential methods[15].

However, for the purposes of the Kane model of quantum computer, we are interested in the donor wavefunction. Fig. 2.11 shows the wavefunction calculated in Refs. [15, 78] and the consequent calculated exchange energies versus donor separations. We can make the observation that the exchange coupling is extremely sensitive to the relative orientation of the two phosphorus donors and oscillates rapidly with distance. This sets stringent requirements on the placement of donors for quantum computation architectures reliant on the exchange interaction between two such atoms. As such, interfacing with other systems to mediate interactions between dopants, instead of relying on interdonor exchange couplings, is an attractive option.

Interface effects and the D^- state

Two electron states for shallow donors have very small binding energies in bulk silicon, of the order of a few meV[81]. However, the binding energy of the donor is very much affected by the interface, and quantum confinement strongly increases the binding energy, for example in the case of the silicon nanowires studied in this thesis. For an As donor in strong electric field applied in a silicon transistor, not only was the D^- shifted into a more bound configuration, a D^- excited state, thought not to exist for donors in bulk silicon, was observed[82].

A second interesting consideration is that of effects seen when a donor is close to an interface. While at low fields the electron is confined by the donor's Coulombic potential, at higher fields (but before ionization) there is a potential well at the interface pulling the donor electron up and away from the donor. However, even in this regime the electron is confined laterally by the donor potential. Proposals have been made to exploit this effect for quantum computation.

2.6.2 The donor spin system

We now discuss the spin system of the donor using a spin Hamiltonian approach. This is crucial for understanding the excitation spectra in ESR experiments.

Using \mathbf{S} and \mathbf{I} as the donor electron and nuclear spin respectively, we can write down the spin Hamiltonian as follows[83]

$$\mathcal{H} = \mathcal{H}_Z + \mathcal{H}_\mathcal{H} + \mathcal{H}_{SS} + \mathcal{H}_{SO} \quad (2.18)$$

where the terms going into the Hamiltonian are the Zeeman, hyperfine, spin-spin interaction, and spin-orbit interaction energies.

The Zeeman term can be written (in frequency units) as follows:

$$\mathcal{H}_Z = \gamma_e \mathbf{B}_0 \cdot \mathbf{S} - \gamma_n \mathbf{B}_0 \cdot \mathbf{I} \quad (2.19)$$

where $\gamma_e = g_e \mu_B / \hbar$ is the electron gyromagnetic ratio, defined as positive, with g_e is the electron g-factor and \mathbf{B}_0 the static magnetic field. Similarly, $\gamma_n = g_n \mu_n / \hbar$ is the nuclear gyromagnetic ratio, with g_n the nuclear g-factor and μ_n the nuclear magneton, three orders of magnitude smaller than that of the electron. The Landé g-tensor \mathbf{g} entering into Eq. 2.19 is generally anisotropic in crystals and is a consequence of spin-orbit coupling; since silicon has very weak spin-orbit coupling, we can take $g \approx 2$ for electrons in silicon. Silicon also has a sixfold degenerate valley structure, and the difference in effective mass results in different values of g within a valley. However, the valleys are equally populated in the ground state and the electron sees an average of the g-factors, so that no anisotropy is expected. However, this is important for silicon heterostructures (SiGe) and possibly for confined nanostructures.

The second term is the Hyperfine term, or the Fermi contact hyperfine interaction, arising from the overlap of the electron wavefunction with the donor nucleus. This term is given by

$$\mathcal{H}_\mathcal{H} = \mathbf{S} \cdot \mathbf{A} \cdot \mathbf{I} \quad (2.20)$$

where \mathbf{A} is the hyperfine tensor, which is mostly isotropic for the 1s state, and is proportional to the electron wavefunction at the nuclear site. This wavefunction can be tuned electrically and can in turn tune the hyperfine interaction, forming the basis of the A-gate in the Kane architecture[5]. We discuss the different donor hyperfine splittings and their consequences in later chapters.

The third term in Eq. 2.18 is the spin-spin term, coming from the interactions between nearby electron spins, mainly the dipole-dipole coupling and the exchange interaction. We have already discussed the exchange interaction and its oscillations in the previous section. The dipolar term is given by $\mathbf{S}_1 \cdot \mathbf{D} \cdot \mathbf{S}_2$ where D is a dipolar term depending on the spatial separation of the donors. The last term in the spin Hamiltonian is the spin-orbit coupling

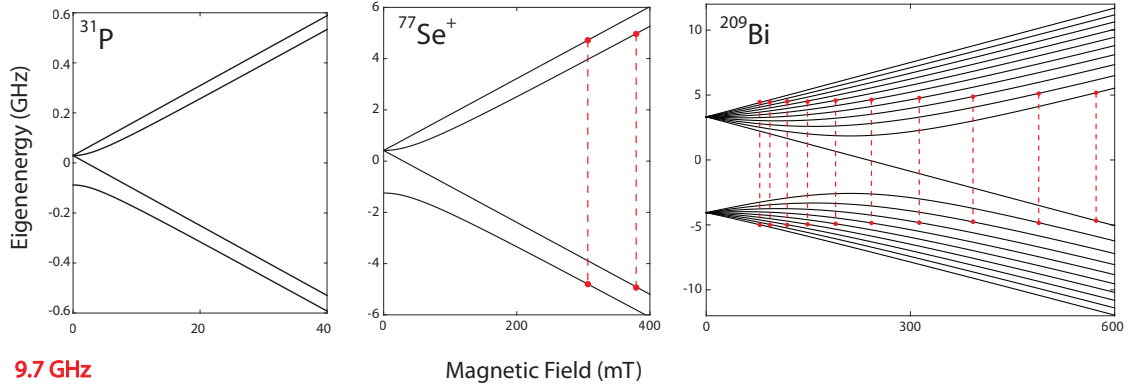


Figure 2.12: Breit-Rabi diagrams of donors, eigenenergies plotted as a function of magnetic field. The red dashed lines represent allowed ESR transitions driven by microwaves at 9.7 GHz (for selenium and bismuth; phosphorus transitions are not visible at this scale). Phosphorus (^{31}P) and Selenium ($^{77}\text{Se}^+$) have nuclear spins of $1/2$, but different hyperfine strengths, leading to quantitative differences. Bismuth (^{209}Bi), on the other hand, has a nuclear spin of $9/2$ and is shown with its ten allowed ESR transitions.

term,

$$\mathcal{H}_{SO} = \lambda \mathbf{L} \cdot \mathbf{S} \quad (2.21)$$

characterised by the spin-orbit length λ . This term is quite important in quantum dot systems, such as GaAs heterostructures and InAs nanowires. It is made up of the Dresselhaus (or bulk anisotropy) term and the Rashba (or surface anisotropy) term, with the latter arising from asymmetries of the potential in the direction perpendicular to the interface (which could be important for gated or confined donors close to the interface). The Dresselhaus term is not present in silicon, due to its bulk inversion symmetry.

For ESR of isolated donors, the two most important terms are the Zeeman and the Hyperfine, and we can write the simplified Hamiltonian as

$$\mathcal{H} = \gamma_e B_0 S_z - \gamma_n B_0 I_z + A I_z S_z \quad (2.22)$$

where A is assumed to be isotropic. This Hamiltonian is isotropic and can be exactly solved for the eigenstates, the eigenenergies for which come out to be:

$$\begin{aligned}
 E_{\downarrow\uparrow} &= \frac{-\sqrt{(\gamma_+ B_0)^2 + A^2} - A/2}{2} \\
 E_{\downarrow\downarrow} &= \frac{-\gamma_- B_0 + A/2}{2} \\
 E_{\uparrow\downarrow} &= \frac{\sqrt{(\gamma_+ B_0)^2 + A^2} - A/2}{2} \\
 E_{\uparrow\uparrow} &= \frac{\gamma_- B_0 + A/2}{2}
 \end{aligned} \tag{2.23}$$

where $\gamma_{\pm} = \gamma_e \pm \gamma_n$ and where the arrows indicate the orientation of the electron (\uparrow) and nuclear (\uparrow) spin, and the energies are in frequency units. Fig. 2.12 shows the above eigenenergies versus magnetic field, plotted for the donors relevant to the experiments presented in this thesis, ^{31}P and ^{77}Se (both with nuclear spin $1/2$), as well as the allowed ESR transitions when applied microwaves of 9.7 GHz (X-band ESR) are used to generate the oscillating AC magnetic field B_1 . We also include the energy spectrum of ^{209}Bi , which has a nuclear spin of $9/2$, to illustrate its rich Hilbert space which is relevant for the experiments explored in Chapter 6.

In the remainder of this thesis, we present our experimental setup, as well as our efforts towards choosing a quantum dot architecture, selecting suitable donors, and finally, forming a dopant-dot hybrid qubit.

Chapter 3

Experimental Techniques

In this Chapter, we introduce the main experimental techniques used to perform the measurements in this thesis. First, we discuss the measurement of dopant spins via spin-to-charge conversion using the technique of electrically detected magnetic resonance, which we carry out in a cryostat that goes down to 4 Kelvin. Quantum dots and dopant spins coupled to them typically require temperatures in the millikelvin range for their measurement, so that the relevant energy scales (such as the dot charging energies) are greater than $k_B T$. For these transport and charge sensing measurements, millikelvin temperatures are achieved in a dilution fridge. We introduce the cryogenic setup, and the techniques of DC transport as well as fast, sensitive gate-based RF-reflectometry. We also briefly present the fabrication of silicon quantum dot and dopant devices as well as the development of a flexible fabrication platform for making silicon devices with a high-quality interface. Lastly, we present one of the cornerstones of the results presented in this thesis, CMOS-silicon devices fabricated in an industry compatible foundry, and discuss their design, the mechanics of quantum dot formation, and some aspects of performing measurements upon them.

3.1 Electrically Detected Magnetic Resonance

Electrically Detected Magnetic Resonance (EDMR) is a technique used to detect spin-dependent transport in the solid-state that can be orders of magnitude more sensitive than ESR, and is capable of detecting ensembles of fewer than 100 donors[84][85]. It has been a forerunner in the study of spin-to-charge conversion mechanisms such as spin-dependent tunneling which have been instrumental in the integration of dopants into devices. We now discuss the measurement setup of EDMR used in the measurements shown in Chapter 5.

3.1.1 Electron Spin Resonance

ESR is a technique that can probe the spin degree of freedom for donors in silicon. The spin Hamiltonian of a donor electron in a silicon crystal was presented in Chapter 2. Given a static magnetic field B_0 , and ignoring the hyperfine coupling and other higher order terms, we find the resonance condition $h\nu = g\mu_B B_0$ [83]. For the donors in silicon, which have Landé g -factors close to 2, microwave photons can drive spin resonance for Zeeman fields of a few Tesla. The magnetic field component of this oscillatory microwave field is perpendicular to B_0 and is conventionally called B_1 .

In a typical ESR setup like the one shown in Fig. 3.1, a single-mode resonant microwave cavity (a cylindrical TE_{011} in our case) is inserted between the Helmholtz coils of an electromagnet, and typically also immersed in a helium flow cryostat for cooling down to 4.2 K. Microwaves are generated by the microwave bridge, and the signal is split into two components. One is sent in to the sample and out through a circulator to be detected via a Schottky diode, while the second component is used as a reference for the demodulation. When the resonance condition given in the previous paragraph is satisfied, the sample absorbs microwaves and this translates to a signal on the spectrometer. A field modulation technique is used to improve the signal-to-noise ratio. The magnetic field in a typical ESR (and EDMR) measurement is superimposed with an ac magnetic field B_{mod} , with a modulation frequency f_{mod} typically 10–100 kHz, and the signal channel detects signals at this ac frequency only, via a lock-in technique. Our measurements are carried out in a Bruker Eleksys E680 spectrometer with an X-band resonator (X-band measurements are carried out at microwave frequencies of 9–10 GHz and fields of ~ 0.35 T), shown in Fig. 3.1(a).

One limitation of the EPR technique is the requirement for a large ensemble of spins (the limit is about 10^{10} for X-band), due to the small Zeeman energy of an individual spin (as well as the diodes used for detection). The fundamental advantage of EDMR is that due to the switch to measuring electrical transport, we are no longer limited by the small Zeeman energy for many mechanisms or by the detection diode sensitivity. This is mainly because while the bare magnetic moment of a single electron is a very small quantity and therefore hard to measure, charge sensing and the detection of electrical transport are much easier, even for very small ensembles and single electrons.

- The sample should be mounted such that it is positioned at the center of the cavity, where B_1 is the largest and E_1 is the smallest.
- Single-mode microwave cavities enhance B_1 by the loaded Q-factor, so the resonator should be tuned carefully to maximise Q (typically ~ 6000 for our resonator).
- EDMR signals are reported in literature as the fractional change in current or resistivity on and off resonance. Under magnetic field modulation, the recorded EDMR signal is:

$$\text{Signal} \propto \frac{\partial}{\partial B} \left(\frac{\Delta \rho}{\rho_0} \right) B_{\text{mod}} \quad (3.1)$$

where B_{mod} is the modulation amplitude.

- For the above description to be meaningful, B_{mod} must be lower than the linewidth of the EDMR signals measured with respect to B_0 ; however, too low an amplitude will lead to a loss of signal intensity. For best results, B_{mod} should be picked to match the smallest linewidth of the signal.
- The modulation frequency should be chosen to be slower than any transient effects expected from the device.
- The magnetic field step should be smaller than at least a tenth of the linewidth measured.

While Chapter 5 deals with EDMR experiments carried out using the techniques above, most of the experiments in this thesis were carried out at millikelvin temperature ranges in a dilution refrigerator, in nanoscale silicon devices. In the next section we summarize this setup and mention some best practices.

3.2 Measurement setup and techniques

To resolve very small energy scales (the charging energy of a quantum dot, for example, can be in the low meV range) and currents, we often need to cool down a system to the millikelvin range of temperature, since temperature will otherwise typically be the dominant energy scale. In this Chapter, we describe measurement techniques used to carry out the different experiments in the next few chapters. Most of these were carried out in a dilution

fridge, and this involved the wiring and setup of DC, pulse and microwave lines as well as an RF-reflectometry setup at milliKelvin temperatures.

To this end, several measurements described in this report were performed in a cryogen-free, top-loading Oxford Triton 200 dilution refrigerator with a stable base temperature of 30 mK and with high-homogeneity and horizontal (± 3 T main coil, ± 0.1 T sweep coil) superconducting magnets. The rest of this section describes a few essential features of this refrigerator and some extended wiring and filtering work performed on it¹. At all stages, effort has been taken to design a simple, plug-and-play enabled system which is easily modifiable. The rest of the cryogenic experiments were carried out at the University of Cambridge, in a Kelvinox K400 dilution refrigerator with a base temperature of 35 mK, the wiring of which was already installed (and is described in detail elsewhere[89]).

DC lines

Equipped with 24 DC lines, our fridge has an RF reflectometry setup as well as several stages of filtering. The filtered DC lines consist of an enmeshed copper loom with 12 twisted pairs and are connected to the sample PCB (described later) via a simple plug-and-play PCI connector² into which the PCB slots. At the mixing chamber stage, six of these 24 wires are copper, chosen to apply larger currents (for example to the source and drain of the device under measurement), while the rest are manganin, chosen to minimize the heat load to the mixing chamber. All wires are thermally anchored to the fridge by making thermal contact to the fridge plates at various stages. Additionally at the mixing chamber plate, the loom is wound several times around a copper bobbin anchored to the plate, with each layer wrapped with Eccosorb³ as shown in the left panel of Fig. 3.2, to minimize radiation. The Eccosorb is also part of the filtering stages, described below.

Filtering

The DC wires extend from the device at millikelvin temperatures to the measurement electronics at room temperature, so they need to be carefully filtered and heat-sunked to avoid heating up the sample (the electron temperature can be elevated due to electrical noise

¹We do not describe the stages of the fridge in detail since by now such wiring is fairly standard. Theses by Alex Johnson[87] or Leonardo Di Carlo[88] provide good methods and rationales for wiring a dilution fridge from scratch.

²PCI Express connector, FCI 10039755.

³Eccosorb microwave absorber material, LS24 0.25 inch wide absorbent foam sheet, Emerson and Cunnning Microwave Products Inc., available at <http://www.eccosorb.com/>

from the leads). Several stages are required at different temperatures and frequencies. At room temperature, the wires are connected to a fixed fridge ground through switches and embedded in a breakout box. At various stages in the fridge (50K, 4K, 800mK, 100mK), Eccosorb is wrapped around the loom using nylon thread. This material is a lossy microwave absorber and has been used with success in cryogenic systems for absorption of high-frequency radiation (1-26 GHz). Such a stage is shown in Fig. 3.2.

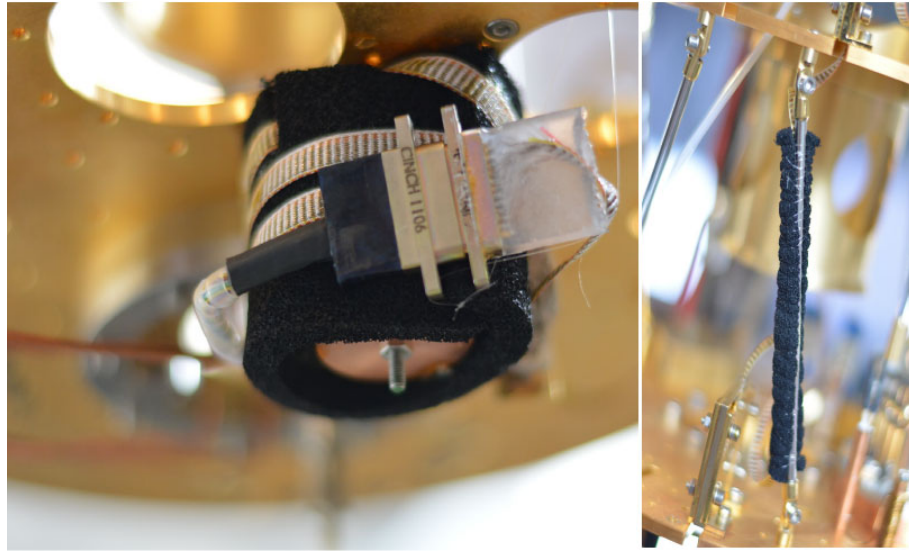


Figure 3.2: Left, mixing chamber stage showing thermal anchoring of the loom (DC lines) using a copper bobbin and Eccosorb. Right, loom filtering with Eccosorb, duplicated at different stages in the dilution fridge.

To get rid of further high-frequency noise, copper powder filters are utilized. These are well-established in cryogenic systems and consist generally of powdered copper suspended in epoxy into which the wires to be filtered are embedded. In our home-built filtering system, instead of a box with physical wires coiled inside and fixed inside the fridge, we utilise a PCB with 24 gold traces each $100\mu\text{m}$ wide that meander to a total length of 1.5m, covered with Stycast 1266 clear epoxy[90], connectorized inside a copper box. The epoxy has been mixed with copper powder of $3\mu\text{m}$ average diameter. The PCB based design makes the entire assembly plug-and-play by making use of D-connectors on both ends, and it allows us to integrate the next stage of filtering on it as well: RC filters.

To remove the remaining low frequency noise, we add RC filters to the remaining part of the wires on the PCB. This is done by soldering surface-mount resistors and capacitors onto each line and to ground. By using replaceable SMD resistors and capacitors, we can

change the cut-off frequency of these RC filters (for example, to have different cut-offs for source-drain versus gates) at each cooldown as required. Fig. 3.3 shows the the filter PCB along with its frequency response with gold meander, Eccosorb and the copper powder epoxy treatment.

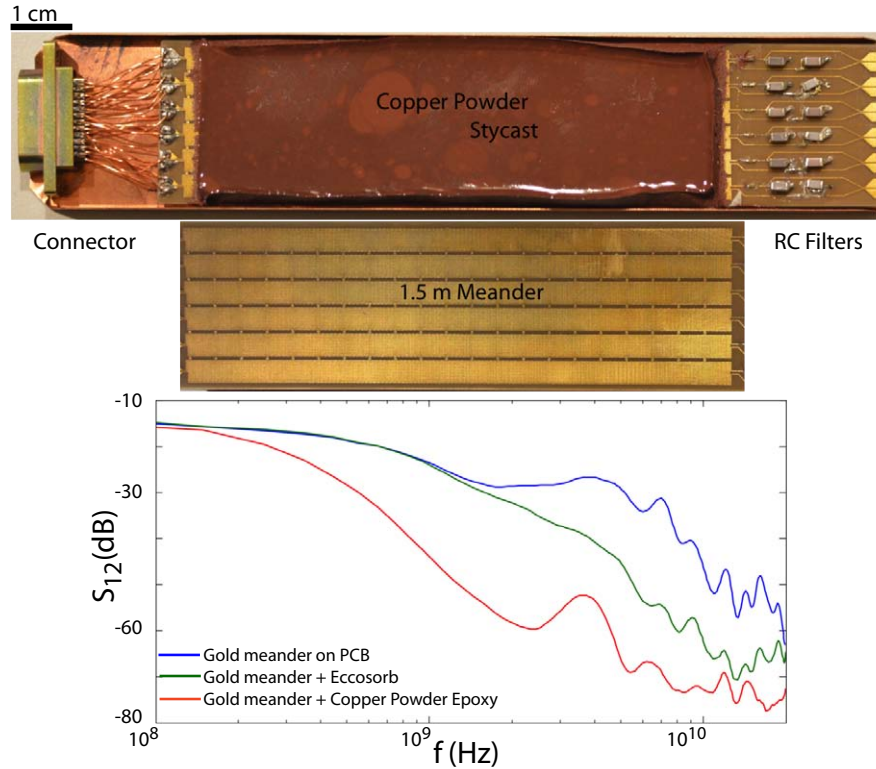


Figure 3.3: Above, Copper Powder and RC filter system showing 1.5 m meandering gold traces under the copper powder/Stycast epoxy. Below, filter response at room temperature with meander alone (blue trace), with Eccosorb (green trace), and with the copper powder filter (red trace).

High frequency lines

In our system coaxial cables are used to send fast voltage pulses and microwaves, and are in three parts across the stages of the fridge; copper or tin, connected by stainless steel or titanium-niobium. They are anchored at 50K, 4K, 800mK and 100mK. XMA brand cryogenic attenuators, typically at least -20 dB per line are used to thermalize the inner conductor of the coax at different stages⁴. At the sample PCB, the coaxial cable plugs

⁴Recent experiments have noted a noise source specific to pulse tube cooled cryogen-free dilution fridges, where pulse tube vibrations couple in to qubit measurements through the triboelectric effect; in a future

into an SMP connector⁵, which is then connected to a copper trace coated with silver from which we can bond to the chip (this sample PCB is described in the next section).

Measurement PCB

For connecting the microscopic world of the device to the macroscopic world of the measurement system, we have developed a PCB which houses the chip and from which we can wirebond to the leads of the sample. The PCB material is Rogers 4003C laminate on FR4, (400 μ m wide), selected for its superior high-frequency operation and because of its similar thermal expansion coefficient to copper and its low dielectric constant which minimises parasitic capacitance. This material lets us design low-loss high frequency traces which is important for our pulsed, ESR and RF lines. These traces are connected to the coaxial cables via an SMP connector (mentioned above) that enables right-angled connections. These traces also include slots for surface mounted inductors, capacitors and resistors which can together form easily replaceable bias tees as well as a tank circuit for the RF line. Vias randomly spaced throughout the PCB connect the top and bottom ground planes and minimize crosstalk between lines. As mentioned before, the DC wires coming to the PCB make connection to the traces when the PCB is plugged into a PCI connector at one end. A silver instead of gold finish ensures that the magnetic material nickel, often included as a layer in a gold deposition on commercial PCBs, is not present on our PCB. In a later design, a cutout was added to access the back of the sample with a laser or other optical excitation, as well as a connectorized copper box encapsulating the PCB.

Dip-probe and optical access

Miscellaneous parts of the lab measurement system that have been developed include a dip-probe that can be used for preliminary measurements, at room temperature and at 4K in liquid helium (it can be used in either an Oxford Instruments CF-935 optical flow cryostat for the Bruker spectrometer system, or in a helium dewar, having a system to adjust its height). The dip-probe has the same PCI connector as the fridge PCB, which makes the PCB usable on either system, enabling multiple samples to be tested at 4K before selecting one for cooling to dilution temperatures. Apart from this, the Oxford Triton dilution fridge

setup, cables used should be tested for such effects. In general, jacketed cables were found to have better characteristics[91].

⁵SMP-MOLEX-73415-3320 connectors, specified up to 40 GHz.

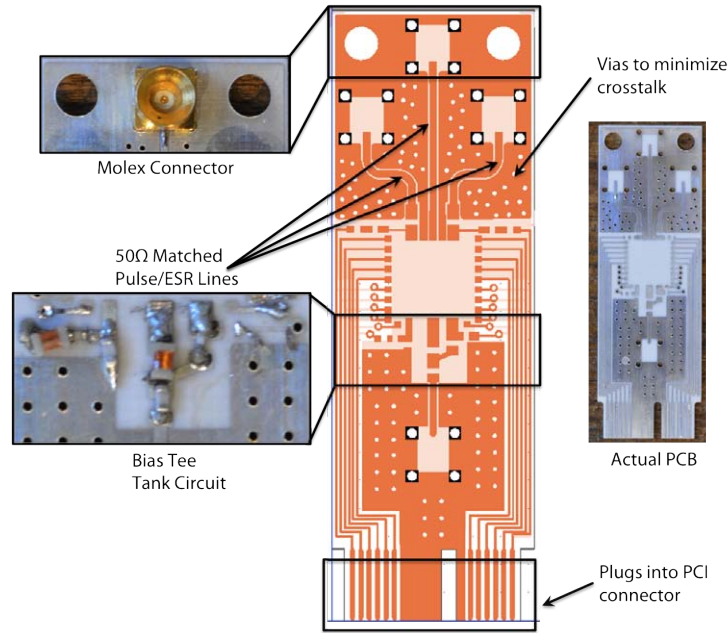


Figure 3.4: Measurement PCB, designed in-house (width is 2.5 mm) with tank circuit, bias tee, DC lines, and impedance matched lines indicated. The device being measured is to be positioned in the central square region.

is equipped with a set of shields that are fitted with aligned optical windows, which allow us to access the sample space with a free-space laser.

Lastly, we describe the radiofrequency reflectometry setup developed in the fridge, which is the basis for most of the experiments in this thesis, as well as the specific reflectometry technique used.

3.3 Gate-based RF-reflectometry

Radiofrequency (RF) reflectometry is a high-sensitivity charge detection and measurement technique that has become very popular for low-noise measurements, especially in regimes where direct transport is not possible. Gate based RF reflectometry simplifies design fabrication since it eliminates the need for a separate SET charge sensor (whether measured by RF or transport). The measurement is also high frequency and high bandwidth, and not limited by $1/f$ noise as in conventional DC transport[92]. The capacitive coupling essential for this kind of charge sensor requires a strong gate lever arm which is a design feature incorporated into the devices measured for this thesis (explained in the last section of this

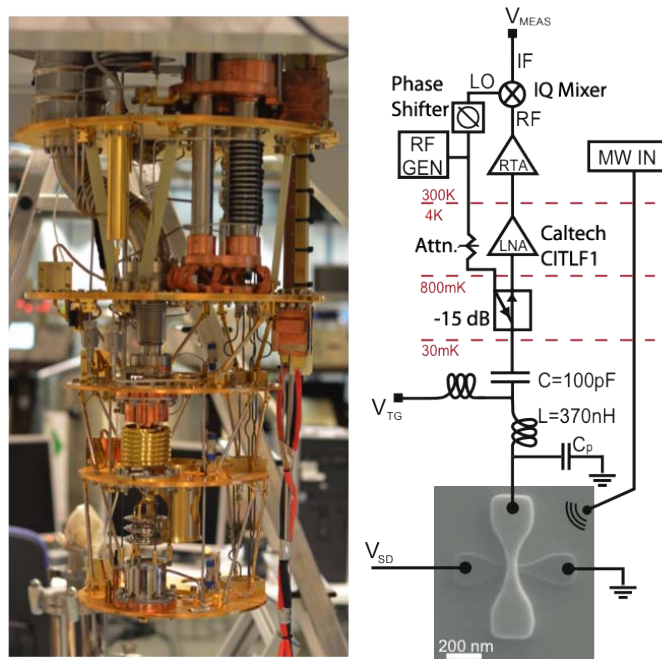


Figure 3.5: Left, all fridge stages. Right, schematic of RF setup with a typical sample.

chapter), but is also easy to achieve, for example, in nanotube or nanowire quantum dot systems using high-k gate dielectrics.

In our dilution fridge we have implemented an RF setup for gate-based charge-sensing, the main mechanics of which are shown in Fig. 3.5. An RF signal (typically with frequency $\sim 300 - 400$ MHz and power ~ -90 dBm at the sample) is sent through a directional coupler and stages of -20 dB attenuators to a tank circuit, composed of a surface mount inductor (typically 370-390 nH), a parasitic capacitance to ground (around 1 pF), and a device capacitance (typically a few pF). As shown in Fig. 3.4, an on-board bias tee is usually used to apply both RF and DC voltages on the measurement gate. The reflected signal is amplified by ~ 35 dB through a low noise amplifier (a Caltech CITLF1, 0.1–1 GHz) anchored at 4K. Finally, the signal is further amplified at room temperature and demodulated using the reference signal through an IQ demodulator implemented through an evaluation board (a Polyphase Microwave AD0105B card) which enables us to read both I and Q channels after further room temperature amplification. A phase shifter is used to adjust the signal between the orthogonal I and Q channels. Along with the RF setup, a microwave antenna is connected to a high frequency line which lets us apply microwaves close to the device under measurement. Fig. 3.6 shows RF amplitude traces taken with our measurement setup,

showing a resonance at 324 MHz, which shifts with back gate (this behaviour is discussed in Appendix B). We now turn to a description of the gate-based RF-reflectometry technique

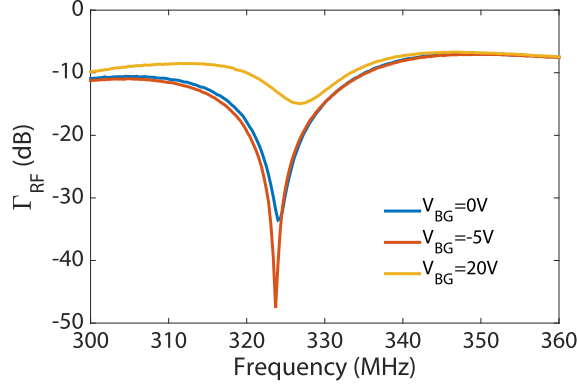


Figure 3.6: Resonance from a loaded tank-circuit at the base temperature of 40 mK. Changes in the device (for example, the back gate as shown here) can have strong effects on the resonance, showing the need for in-situ tuning.

used for most of the measurements in this thesis, using the setup described above, following previous work[93–95]. We consider a typical measurement in a quantum dot device; we embed the device into the resonator by coupling through a gate electrode, typically the top gate, by wirebonding on to it from the end of the inductor in our tank circuit. We then measure the reflected RF signal. At the resonant frequency, the amplitude (A) and phase (ϕ) components of the reflected signal are sensitive to changes in the complex admittance of the device. This admittance depends on the tunnel rate (Γ_0), the RF drive frequency (ω_0) and the temperature of the electrons in the lead (T_e)[96]. A is affected by changes in the power dissipation in the system, while changes in ϕ are due to dispersive tunneling or quantum capacitance changes. These changes can be understood in terms of electron transitions in a tunnel-coupled two-level system that is driven with a fast RF excitation, with the dynamics given by a master equation[96, 97] (detailed in Chapter 4). The rate equations can be solved in different regimes based on a comparison of the tunnel rates with the drive frequency (as well as a comparison of the lifetime broadening with the temperature). In these regimes, resonances arising from quantum dot-to-lead transitions can have appreciably different lineshapes and signal amplitudes depending on tunnel rates, temperature and drive frequency. Low-temperature measurements as shown in Refs. [93, 95], reproduced in Fig. 3.7, illustrate these different regimes, discussed in the next section.

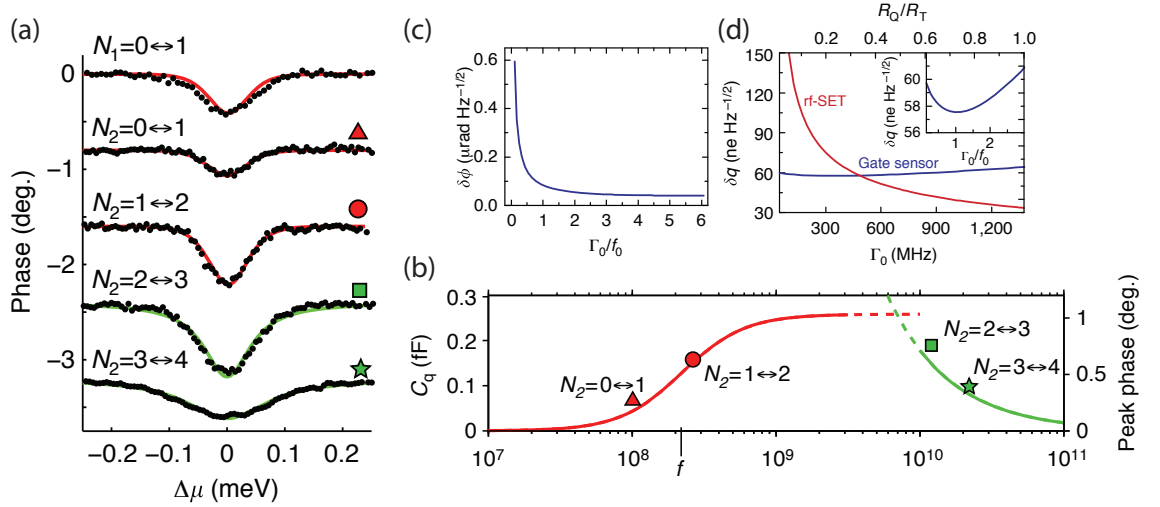


Figure 3.7: Tunnel rates and their effect on gate-based reflectometry sensitivity and resonance linewidths. Data from gate-based reflectometry experiments described in Refs. [93, 95]. (a) Phase response of electron transitions as a function of the potential of a quantum dot relative to the Fermi level of lead ($\Delta\mu$, while N_1 and N_2 distinguish between the two quantum dots), tuned using gate voltages. Red curves are fits to Eq. 3.2 for thermally broadened transitions, green curves are lifetime broadened and fit to Eq. 3.4. Symbols correspond to panel (b) where the predicted capacitance response is shown vs tunnel rates for high tunnel rates (green curve, Eq. 3.4) and low tunnel rates (red curve, Eq. 3.2), compared to thermal broadening. Plots are from [95], with measurements performed on a Si:P device. (c) Phase sensitivity and (d) dissipative charge sensitivity for an RF gate-based sensor compared with a typical RF-SET, both plots versus tunnel rates (Γ_0), from Ref. [93] where the device is a nanoscale silicon transistor as described in Section 3.5.

3.3.1 Detection regimes based on tunnel rates

Considering the case of a quantum dot coupled to a lead, the RF reflectometry signal typically shows a peak at the degeneracy point in the dissipative and dispersive responses as we tune the two levels. However, we need to look at traces taken well away from any triple-point charge degeneracies to avoid cotunneling effects.

Low tunnel rates

At low tunnel rates, i.e. $k_B T_e \gg \hbar \Gamma_0$ the width of the transitions is determined by the electron temperature since the thermal energy is greater than the lifetime broadening due to the interaction with the leads. The rate equations then give us the following relations for the average power dissipation in the device (P) and the averaged phase response (ϕ):

$$\langle P \rangle \approx \frac{(eV_g^{rf}\alpha)^2}{4k_B T_e} \cosh^{-2}\left(\frac{\Delta E(0)}{2k_B T_e}\right) \frac{\Gamma_0}{1 + \Gamma_0^2/\omega_0^2} \quad (3.2)$$

$$\langle \phi \rangle \approx -\frac{\pi Q}{C_p} \frac{(e\alpha)^2}{4k_B T_e} \cosh^{-2}\left(\frac{\Delta E(0)}{2k_B T_e}\right) \frac{1}{1 + \omega_0^2/\Gamma_0^2} \quad (3.3)$$

with V_g^{rf} the gate voltage change produced by the RF-drive, and $\Delta E(0)$ the energy separation of the two level system at zero detuning. A few things to be noted about this regime are, firstly, that at low tunnel rates, the peak quantum capacitance is low, and no additional power is dissipated in the device, since electron tunneling cannot keep up with the drive. Secondly, we note that the peak at the degeneracy point has a \cosh^{-2} dependence, borne out by the experimental results shown in Fig. 3.7. The width of this peak gives us the thermal energy and therefore the electron temperature. Lastly, as seen in Fig. 3.7(c)-(d), Ref. [93] measured the charge sensitivity of this technique and found a very low value of $37\mu e \text{ Hz}^{-1/2}$, outdone only by RF-SETs ($1\mu e \text{ Hz}^{-1/2}$), which perform best at high tunnel rates ($>600 \text{ MHz}$), while the gate based sensor performs well in all regimes, including better than RF-SETs at low tunnel rates ($<500 \text{ MHz}$). Low tunnel rates correspond to highly resistive tunnel barriers, which is usually the situation for few-electron quantum dots.

Tunnel rates comparable to drive frequency

For $\Gamma_0 \sim \omega_0$, we find that maximum power is dissipated since on average, inelastic tunneling happens at the end of the RF cycle, and inelastic tunneling results in an excess dissipated

energy which results in a change in the total reflected power. Significant dissipation is not ideal as it introduces noise into the measurement, but the maximum charge sensitivity of the RF-resonator is also seen when the tunnel rate matches the drive frequency.

However, an encouraging consequence of the above relations is that unlike the power dissipation, the average phase response does not peak at the resonant frequency and then drop again, but goes to a constant value for large Γ_0 . In this limit, the excess power dissipation can be minimised while the phase response is still maximised.

High tunnel rates

If the tunnel rates are considerably faster than the drive frequency, i.e. $\Gamma_0 > \omega_0$, the coupling is capacitive only and electron tunneling occurs out of phase with the driving signal. Electron tunneling is elastic and power dissipation does not occur. In this regime of dispersive readout the parametric capacitance response C_p can be given by

$$C_p \approx \frac{(\alpha V_g^{\text{rf}} e)^2}{\pi} \frac{\hbar \Gamma_0}{(\hbar \Gamma_0)^2 + (\Delta E)^2} \quad (3.4)$$

In this regime, the width of the peak, when fit to the above equation, gives the lifetime broadening, i.e. the tunnel rates. Phase detection is maximised at these tunnel rates, a regime more suitable for systems with transparent tunnel barriers (but performs well at moderate tunnel rates as well). Fig. 3.7(a)-(b) show the predicted change in the phase response and the measured resonance linewidth as the tunnel rates change.

In general, from the above regimes we learn that gate-based reflectometry works for most regimes, but tunnel rates high enough (compared to the drive frequency) to avoid maximum dissipation but low enough to keep tunnel barriers opaque enough for measurement are optimum for quantum dot measurements. Tuning of the tunnel barriers can be achieved typically by barrier gates, or by back gating in the devices described later in this thesis. The resonator frequency can of course also be tuned within a certain range by a suitable choice of components, as well as in situ using tunable inductors or varactors[98].

3.4 Fabrication of nanoscale silicon devices

We present here the design and fabrication of planar-MOS devices on a purpose-built versatile fabrication platform based on silicon. Silicon MOS technology is ubiquitous in con-

sumer electronics today, and this is a large motivator for the development of a quantum computation architecture based on silicon. In the next section we will present some of these industry-fabricated devices, a nanometer-scale subset of which are the basis of most of the measurements in this thesis. However, industry-made devices typically have less flexible timescales and designs and are subject to a myriad of design rules and materials restrictions. As such, for the rapid prototyping and development that research-grade devices require, we developed a fabrication platform and process flow that lets us fabricate various kinds of silicon devices with a fast turnaround time. While the fabrication platform was developed at UCL⁶ and the devices shown here were fabricated at UCL, the completed platform is now implemented on a larger and faster scale by the cleanroom at Southampton University. We show some later work where the devices have been fabricated by this team.

Fabrication platform

The Metal-Oxide-Semiconductor (MOS) fabrication process is ubiquitous in industry, making it attractive for designing qubits that are scalable and compatible with industry processes. It has been used to great effect in recent experiments in both donor [7–9, 14] as well as quantum dot qubit systems [17, 18]. It is therefore a natural and established fabrication procedure to employ in the manufacturing of a device where the end goal is to combine these two systems. In addition, the advantages of silicon as a host material have been discussed in Section 1.1.

Our fabrication efforts, carried out at the London Centre for Nanotechnology (LCN) cleanroom, were twofold, (a) to develop a versatile and reliable platform for the fabrication of silicon nanodevices and (b) the fabrication of nanodevices specifically designed for a quantum dot-donor coupled system. The design of our fabrication platform is shown in Fig. 3.8. It is based on a high-resistivity 100 mm silicon wafer, subdivided into four quadrants, each bearing 56 device regions which can be used to fabricate two devices each, for a total of 448 possible devices per wafer. Each device region is built from the bottom up, complete with bond pads, metal contacts, ohmic regions, as well as regions demarcated for the fabrication of a coplanar waveguide (CPW) in order to carry out ESR measurements. At the end of the process we finish with a flexible platform, with a free central device region

⁶The author wishes to thank Dr. Cheuk Chi Lo for his fabrication and device design expertise, hard work, help and assistance during the fabrication and design process, as well as Dr. Liam Boodhoo at the University of Southampton.

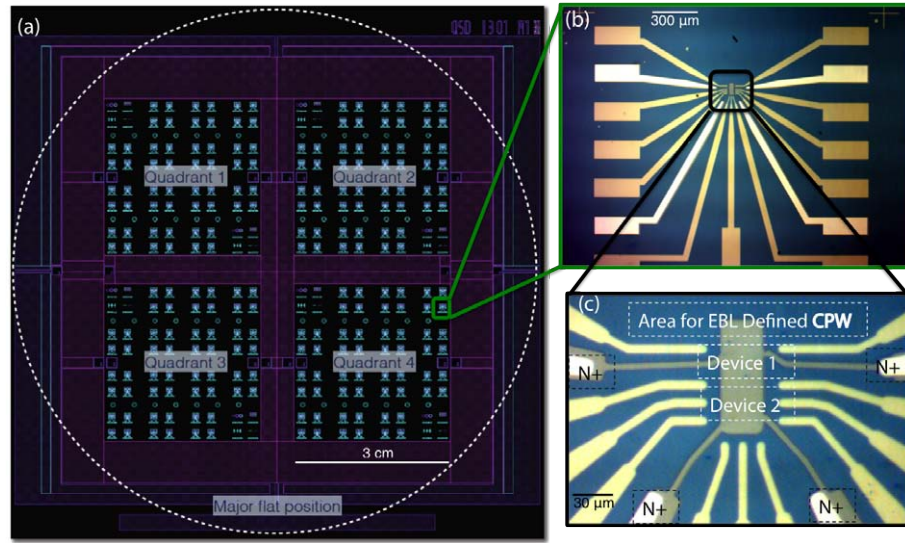


Figure 3.8: Silicon device fabrication platform. (a) Wafer-level schematic of the home-built fabrication platform. (b) Zoom onto one particular device region. (c) Further close up of the active area, with space for a coplanar waveguide, two sets of devices and two sets of heavily doped n+ regions.

suitable for a number of different device designs with varying complexity, which are then patterned using electron-beam lithography as required.

Fig. 3.9 shows pictorially the steps carried out in our MOS fabrication process. These steps are explained in more detail below.

Field oxide and n+ regions

Our fabrication process starts with a clean, high resistance ($>10 \text{ k}\Omega$), float zone, nominally p-type silicon wafer from TOPSIL Semiconductor Materials. A high quality 150 nm field oxide is grown by a wet oxidation process at the University of Southampton. After this, photolithography is performed on a Quintel 4000-6 mask aligner to pattern regions for ohmic contact deposition. These areas are then etched (in a 6:1 buffered oxide etch solution) free of oxide and are sent to the University of Surrey to have phosphorus dopants incorporated through ion-implantation (at a concentration of $2 \times 10^{15} \text{ cm}^{-2}$ with a peak concentration $\sim 20 \text{ nm}$ below the silicon surface, an implantation energy of 40 keV, and a tilt of 7° to avoid channeling effects in crystalline silicon). At the end of this process, the photoresist (HMDS and S1818) acting as the implantation mask is removed.

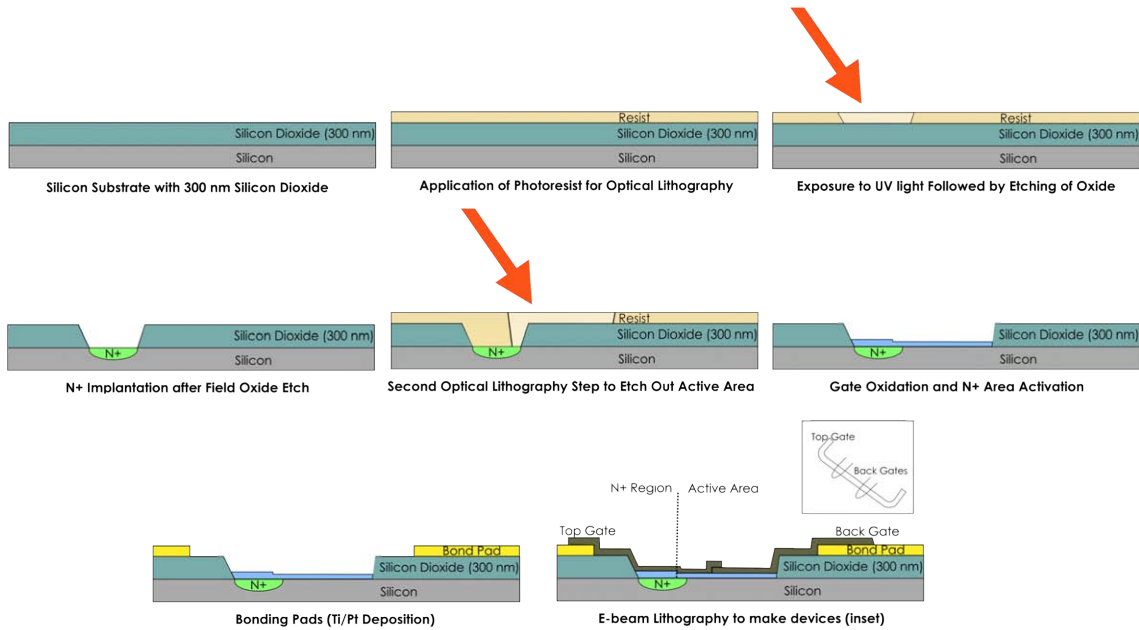


Figure 3.9: The stages of Metal-Oxide-Semiconductor lithography.

Low-dose dopant implantation

Since our aim is to explore dopant spins in silicon, we require a low-dose dopant implantation that provides a low concentration of dopants in our active regions (around 1 every 30–50 nm). Two ways of doing this are possible with our platform. The first method, adopted at the LCN, is achieved by opening up only the active regions with a photolithography step followed by an HF dip to etch away the field oxide. The wafer is then sent to the University of Surrey for a low dose implant (at a concentration of 10^{11} cm^{-2} , and implantation energies depending on the desired depth of dopants; some values used were 10 keV and 19 keV). Arsenic dopants were typically used, to differentiate any single-dopant spin effects from the phosphorus-doped ohmic regions.

The second method available requires a small window (30 nm square) to be opened up in the silicon, so that donors can be implanted at a very low dose in order to have only a few dopants in the small window, obeying Poisson statistics. This window can then be aligned to a “dopant gate” drawn by electron beam lithography in a later stage of the fabrication process. If implantation occurs through an oxide or a device region, an RTA anneal, lasting 5 seconds at 1000°C should be performed. However, if a good quality dry oxide is grown right afterwards at a similarly high temperature, then this can heal implantation damage as well as activate the ohmics.

Device regions and gate oxide

The active regions of the device are now etched free of field oxide, using another photolithography step, followed by another field oxide etch (this will already have been done if the low dose implant is performed at this stage). The active regions are now bare silicon. A high quality 9 nm gate oxide is then grown at the University of Southampton (14 minutes of dry oxidation at 900°C, followed by a 20 minute nitrogen anneal at 950°C). This also has the effect of activating the n+ regions.

Metal contact and bond pad deposition

A third photolithography step is used to deposit aluminium metal contacts through thermal evaporation after etching of the thin oxide. A fourth, and final, photolithography step is used to define alignment marks, device numbering, as well as the large-feature bond pads which will be used to contact the device for measurement. These are deposited by electron beam evaporation and are composed of 8 nm titanium as a sticking layer, followed by ~ 45 nm platinum for visibility under the electron-beam system. The wafer is now ready to be diced into smaller, manageable pieces that are ideal for the smaller-scale precision electron beam lithography to produce a nanoscale device.

Device lithography

Electron beam lithography (EBL) is well-suited to devices at this scale since using an electron beam enables us to overcome the diffraction limit of light, allowing the writing of very small features (of the order of 20–30 nm). We use a Raith 150-TWO EBL tool to write features of the order of tens of nanometers, with a minimum feature size of 30 nm and a pitch of 30 nm achieved. The sample is spin-coated with a ~ 100 nm thick layer of the positive resist polymethyl-methacrylate (PMMA) 950 A2. A typical exposure is at a small (10 micron) aperture and a 20 kV excitation voltage. After exposure, the sample is developed; the exposed PMMA is dissolved and metal deposition through thermal evaporation is carried out, followed by an overnight liftoff immersion in the solvent acetone. This is usually followed by a second device layer, made up of the top gate and a coplanar waveguide for qubit control. Between layers, the aluminium gates are passivated by oxidation; a ~ 3 nm thick aluminium oxide is grown on a hot plate at 150°C for 10 minutes in the cleanroom atmosphere. This process may be repeated multiple times for different device layers in the design, however the ultimate gate stack height is limited by the thickness of the resist since

each layer of gates must wrap around the previous layer without breaks. This, in practice, typically limits us to three metal layers. Lastly, the sample is annealed for 20 minutes at 400°C in N₂(95%)/H₂(5%) to reduce the interface trap density (a forming gas anneal).

Fabricated devices

A few types of devices fabricated using the MOS fabrication protocol detailed above are shown in Fig. 3.10. In general, these devices consist of two layers of aluminium gates. While single electron transistors consisting of two barrier gates and a top gate (for accumulation of electrons) are a first step, plunger gates or side gates (Fig. 3.10(d)) between the barrier gates are an essential complexity, required to tune the coupling between quantum dots as well as between a dot and a donor. In addition, a broadband coplanar waveguide (CPW) as shown in Fig. 3.10(b) is essential to be able to drive ESR transitions and control our qubit. Till date, devices with inter-gate pitch as low as 20 nm have been fabricated.

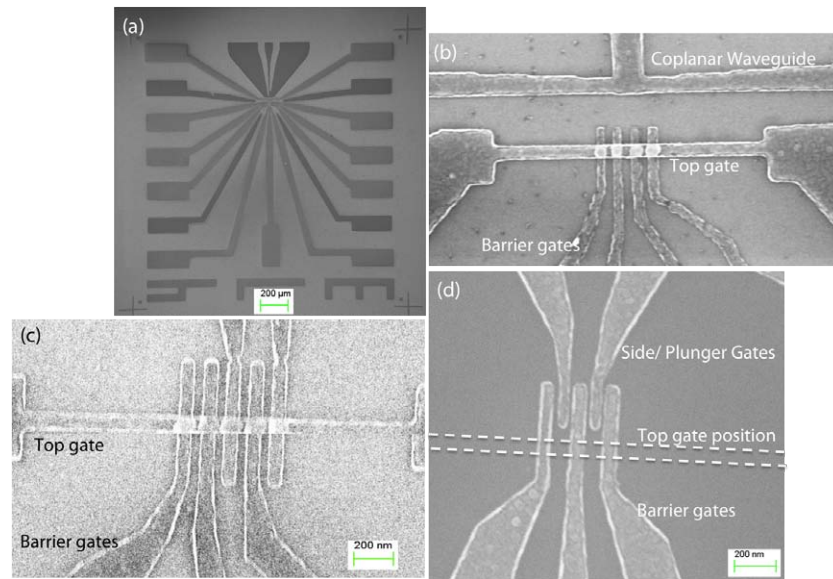


Figure 3.10: A few devices fabricated using the above methods, at the London Centre for Nanotechnology. (a) Completed device region showing a coplanar waveguide at the top, alignment marks and numbering, and bond pads. (b) A device with a proximal coplanar waveguide (CPW) for driving ESR transitions. (c) A device with several gates close together with a 50 nm pitch. (d) A device with plunger or side gates between the barrier gates to provide tunability of quantum dots. A guide to the eye indicates the position of the (not yet deposited) top gate.

Test structures

A final yet crucial component of our fabrication platform is the extensive set of test structures, present at two opposite corners of every quadrant. Our test structures take up eight device regions per quadrant, but are nevertheless essential to the successful fabrication of nanoscale silicon devices. Similarly to GaAs and SiGe heterostructures, where the quality of the heterostructure is possibly the single most important factor in making a few-electron quantum dot, in silicon a high quality interface is key to making nanodevices⁷. To this end, testing the contact resistances, device-to-device leakage, ohmic resistivity, field oxide and (most crucially) gate oxide quality is extremely important before proceeding to the next step; this can save extensive amounts of time.

Some crucial parts of our test structure set are shown in Table 3.1.

Measurements carried out on these structures include assessing the quality of the oxide (both field and gate) through CV measurements, as well as standard MOSFET measurements (I_d - V_d and I_d - V_g) to gauge the quality of the ohmics, the effect of oxide quality on transport, and device-to-device leakage. These measurements were carried out at room temperature and at 4K, using a Keithley Parameter Analyser connected to a cryogenic probe station, as well as in a dip-probe immersed in liquid helium after wirebonding. These measurements are routine and integrated into the fabrication cycle for fast feedback and process evolution.

3.4.1 Device measurements and nanofabrication challenges

Preliminary measurements on nanoscale devices were promising. The devices measured in this section are single-electron transistors (SETs) that can potentially be used to detect single donors in the globally doped silicon[7]. In addition, the formation of a quantum dot in these devices would also enable exchange coupling and/or electron transfer between such a single donor and the quantum dot.

At 4 K as well as in the dilution refrigerator at 30 mK, our MOS devices consistently show turn on and pinch-off behaviours. Measurements on one such device, similar to Fig. 3.10(b,c), are shown below in Fig. 3.11(a). The device turns on with a threshold around 0.6 V. Additionally, setting the top gate to above turn-on, at 0.7 V, we can use the bottom gates (separated from the top gate via the gate oxide of around 10 nm) to pinch off the channel, either singly or together (in which case the pinch off voltage is higher).

⁷As Herbert Kroemer famously said, “the interface is the device”.

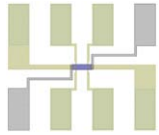
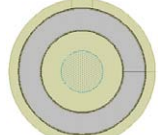
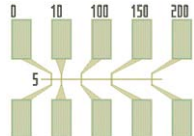
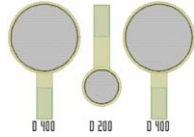
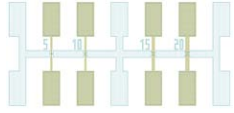
Image	Structure	Use
	Planar MOS-FETs	I-V characteristics, Ohmics, gate oxide quality and gate leakage
	Ring-FETs	Same as above; also ensure current flows from source to drain through channel and not through substrate
	N+ Resistivity	Ohmic region resistivity, implantation dose verification
	CV Structures	Field and gate oxide quality, charge trap density, oxide leakage
	Kelvin Structure	Ohmic contact resistance, top gate metal continuity

Table 3.1: Test structures for the silicon fabrication platform. Colour key: brown indicates n+ regions, green stands for metal contact pads, blue indicates intrinsic areas, and black the top gate layer.

Fig. 3.11(a) also shows the current in the channel near the threshold, showing Coulomb oscillations.

However, a few challenges were encountered in the quest to reach the few-electron quantum dot limit.

- **Oxide quality** The minimisation of leakage and the optimization of oxide quality is essential for silicon devices. Poor oxides lead to scattering and parasitic dot formation in transport, as well as charge fluctuations causing switching and unstable device behaviour during measurements. Typical defects affecting device behaviour are **fixed oxide charges** (surface defects created during oxide that lead to scattering), **interface trapped charge** (silicon dangling bonds or P_b centers, oxidation or implantation-induced), **oxide trapped charges** (holes or electrons trapped in the oxide, can be annealed out at low temperatures), and **mobile ionic charges** (alkali ions such as sodium and potassium; these can be minimised by clean processing, and deep cleaning of furnace tubes and beakers in chlorine)[99–101]. A variety of these issues were encountered, exacerbated by the difficulty of ensuring furnace tubes clean to silicon-grade in a university cleanroom with multiple ongoing research projects.
- **Device-to-device leakage** Mobile charges as well as large trap densities were found to randomly occur in some wafers, due to the same communal processing issues as above. These caused a common problem in silicon MOS device fabrication, that of device-to-device leakage, where current flows under bias between the ohmic regions of different devices, which are (or should be) separated by intrinsic silicon.
- **Channel stoppers** To neutralise the problem of device-to-device leakage after performing extensive simulations[102], channel stopper implants were introduced at the beginning of the process, before the ohmic implantation step. For these, boron (at a concentration of 10^{17} cm^{-3} about 74 nm below the surface) is implanted into a frame around the device regions to prevent current flowing between them.
- **Device dimensions** While substrates exhibiting good gate oxide quality and minimal leakage through the gate oxide were fabricated at the LCN, in nanodevices that were measured (e.g. the one shown in Fig. 3.11(a)) we were unable to reach the few-electron quantum dot regime. The high effective mass of silicon implies that to create a comparable confinement to successful GaAs quantum dot designs, the electron beam pattern would need to be scaled down by a factor of 1.73-2.5[52]. This is at

the very limit of the resolution of the current 30 kV electron-beam-lithography tool at the LCN and this drastically reduced our yield.

- **Dot formation** Lastly, recent developments[17, 103] in the still-nascent field of silicon quantum dots have shown that dot formation in planar silicon as well as in SOI (discussed in the next section) is very different from that in heterostructure-based material systems such as GaAs and SiGe. In silicon planar MOS quantum dots based on aluminium gates on a Si/SiO₂ architecture, strain upon the interface directly under the metal gate means that dots are often formed directly below gates, not between tuned barrier gates as previously assumed. This led to changes in our design.

For the reasons outlined above, fabrication of our silicon-MOS platform itself as well as nanodevices was shifted to the cleanroom located at the University of Southampton as part of our mutual research collaboration. The Southampton cleanroom is a state-of-the-art nanofabrication facility capable of fast wafer-scale processing. This cleanroom is also equipped with a 100 kV JEOL electron beam lithography tool which enables us to reach the smaller dimensions required for few-electron silicon quantum dots. The most basic devices tested based on the new design direction are shown in Fig. 3.11(b)-(c). Parallel gates corral electrons into quantum dots below them, while a confinement gate is used to squeeze the wavefunction of the electrons in the dots. A reservoir gate, shown on the left, is connected to an ohmic and is a source for electrons to tunnel onto the dots. A microwave stripline (or SET for charge sensing) can be located above the structure, while alternatively gate-based charge sensing is used to read out the individual dots.

3.5 CMOS foundry silicon-on-insulator devices

In the previous section, we introduced a silicon-MOS fabrication platform developed as a way to make a scalable qubit architecture that would be compatible with industry but also EBL-compatible. However, while there are some advantages of research-scale fabrication in terms of faster turnaround times and design flexibility, in this section we explore a different approach, which provides large-scale fabrication capabilities along with sophisticated machinery and design capabilities dedicated to silicon nanofabrication.

Over the past few decades, the CMOS electronics industry has been continuously scaling down transistors in size, to increase performance and reduce power consumption. The transistor has now shrunk below tens of nanometers, with the finFET transistor at the 7 nm

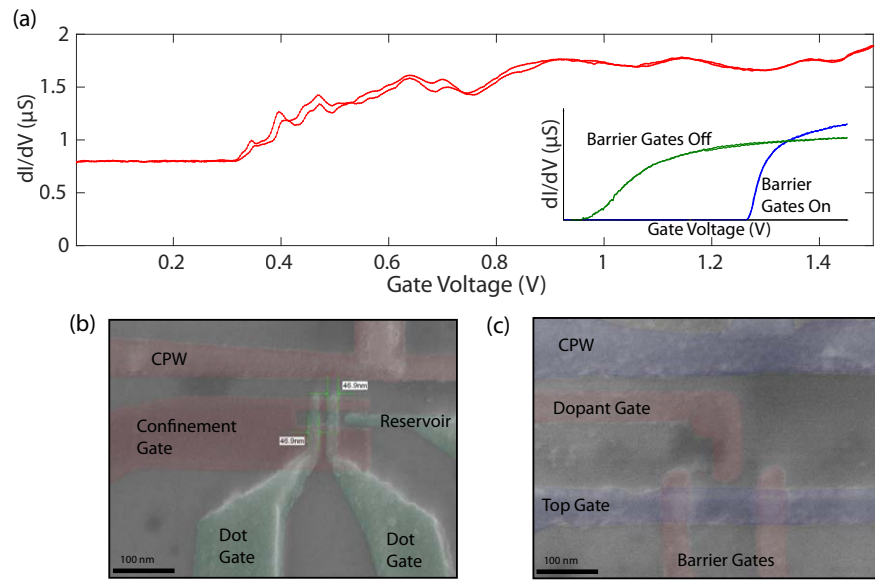


Figure 3.11: Device tests and design progression. (a) Device near turn on showing reproducible conductance oscillations. Inset shows that channel can be pinched off using barrier gates. Measurements taken at 30 mK on a device fabricated at the London Centre for Nanotechnology, as shown in Fig. 3.10(b, c). (b) Double quantum dot design, with dot formation expected under each gate. (c) Dopant-dot device design, requiring local implantation of a dopant under the dopant gate.

node[1]. This means that silicon nanodevices that are small enough to show quantum effects are now routinely produced by industry (while still being extremely hard to make in research laboratories and university cleanrooms)⁸. In addition, these devices, which are produced in commercial, ultra-clean and streamlined CMOS foundries, are much more reliable, robust and able to be made on a large (*e.g.*, 300 mm) wafer scale, qualities very much desirable for research purposes. Most of the measurements in this thesis were performed on such devices, called fully-depleted silicon-on-insulator nanowire transistors (FD-SOI).

As mentioned before, limitations of this approach also exist. Industry processes are not built for very specific, small-scale device designs that can be easily tweaked and added to. As such simple, flexible and reproducible designs have been fabricated that are nevertheless excellent testing grounds for quantum effects. The devices measured in this thesis are single-gate fin-FET devices, and we now describe their fabrication.

3.5.1 Device fabrication

These FD-SOI nanowire devices are made at CEA-LETI⁹ and a typical device is shown in Fig.3.12. Initially, [110] n-type and p-type NW-FETs with a high-k dielectric and metal gate stack were fabricated on [100] SOI wafers with a buried oxide thickness of 145 nm. The silicon film is ~ 11 nm thick. The channel is first implanted before patterning with boron for p-type and phosphorus for n-type devices. The silicon layer is then patterned to create the nanowires using a mesa isolation technique, with the nanowires defined by optical (deep-UV) lithography and resist trimming, achieving nanowires as small as ~ 7 nm wide. The gate stack consists of 1.9 nm CVD HfSiON, 5 nm ALD-deposited TiN and 50 nm polysilicon layers. The gate is wrapped around the channel in an Ω -gate configuration, with gate lengths ranging from 10 nm to $10\ \mu\text{m}$ and nanowire widths ranging from 10 nm to $10\ \mu\text{m}$ as well. After gate etching a nitride spacer of thickness 10 nm is deposited on the sidewalls of the gate. Raised source and drain contacts (18 nm) were then grown to realise low access resistances. A second offset spacer (tetraethyl orthosilicate and nitride layer) was fabricated, followed by self-aligned source/drain implantations, activation spike anneal (a very fast anneal that moves dopants from interstitial to substitutional sites in the silicon lattice) and silicidation for low contact resistances. In the last stage tungsten contacts and

⁸At this size, silicon transistors sit so close to each other that quantum tunneling can occur. This is terrible for digital logic, but opens up new vistas for quantum physicists!

⁹The author wishes to thank Sylvain Barraud at CEA-Leti who made the samples as well as the European TOLOP (www.tolop.eu) project partners who spearheaded the project, especially the Hitachi Cambridge Laboratory who provided us with samples.

copper back-end process flows were used, finishing in $2\ \mu\text{m}$ oxide encapsulation. In some devices, the channel is doped with phosphorus donors at a relatively low concentration of $5 \times 10^{17}\ \text{cm}^{-3}$, enabling us to study dopant physics in this subset of devices[104], as explored in Chapter 6.

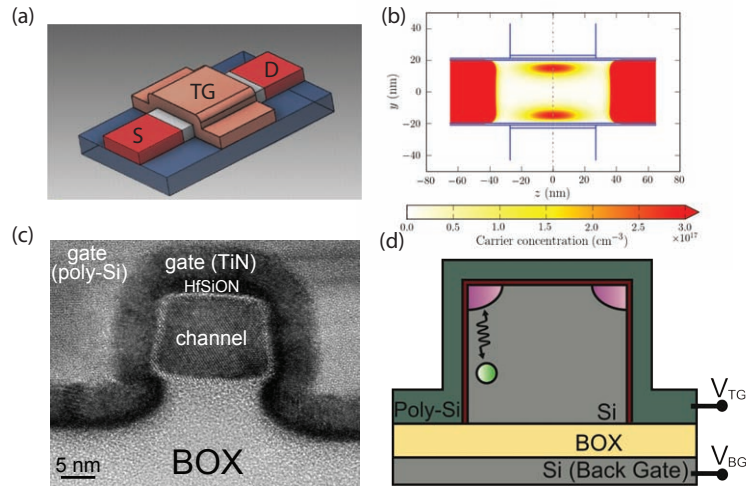


Figure 3.12: Foundry-fabricated FD-SOI devices from CEA-LETI. (a) 3D schematic of wrap-around top gate device such as the ones measured in this thesis. (b) Simulations performed in Ref. [105] showing the formation of corner dots along the channel in this kind of device. (c) TEM cross-section image from the previous reference of a typical device showing channel gate and oxide layers. (d) Schematic form of (c), showing locations of corner dots simulated in (b), as well as showing possible donor location for a device with a doped channel.

3.5.2 Quantum dot formation

Because of the morphology of the wrap-around top gate, the electric field exerted by it is strongest at the topmost corners where the two gate faces meet. This has been called the ‘corner effect’ in fin-FET nanowires. This process has been studied in detail, with simulations showing electron accumulation occurring first at the topmost corners[105]. In addition, as shown in Fig. 3.12, the presence of disorder creates confinement of the corner channels along the transport direction, leading to double dots in parallel. Localization is driven by remote Coulomb charges at the $\text{SiO}_2/\text{HfSiON}$ interface and this attractive potential leads to the formation of small quantum dots in the center of the channel edge, localised around 10 nm. This analysis is borne out by the large charging energies typically seen from

these dots[93][106][29], from the lever arm of the top gate being much higher than that of the back gate, and from the signatures of parallel double quantum dots seen in transport spectroscopy (no precise alignment of the quantum dot levels is seen, a feature required in series transport). This corner effect and the resulting double quantum dot system has been observed by several research groups and is remarkably consistent, even across large wafers.

3.5.3 Measurement

Measurement of these devices is straightforward in some ways, thanks to their simplicity. The top gate, with a strong lever arm to both corner quantum dots, is connected to a tank circuit resonator for gate-based reflectometry of the kind described in Section 3.3. Due to the wrap-around Ω -gate geometry and extremely thin gate dielectric, the coupling of the dots to the gate and therefore to the resonator is extremely strong (lever arms are ~ 0.9), resulting in excellent results using dispersive readout through gate-based reflectometry as described in the previous section. In these devices, this technique has been shown to achieve sensitivities comparable to the best RF-SETs[93]. The other knob available to tune in the simplest single-gate devices is the back gate voltage; the back gate, or the silicon handle wafer (scratched with a diamond scribe and attached to the measurement PCB with a conductive adhesive) is able to be used as a gate by flashing it with an LED to generate charge carriers. In devices where the single wrap around gate is split into two gates facing each other, the two gates can tune each dot independently and the back gate can then be used to tune the tunnel coupling.

In Chapters 4 and 6, we present measurements performed on these devices, to first develop them into viable quantum dot devices and to then use them to couple quantum dots to dopants.

Chapter 4

Gate-based charge sensing of a double quantum dot in a silicon nanowire

In Chapter 1 of this thesis we stressed the importance of finding a material host and qubit architecture which will be a useful platform for a coupled dopant-dot system. In Chapter 2 we discussed silicon as a material that presents multiple benefits for qubit coherence times, in addition to being a semiconductor suitable for both dopant and quantum dot qubits. Within the context of silicon, we would like to focus on a device architecture with the minimum number of control gates possible for the quantum dot to assist with scaling up. We therefore explore a silicon-on-insulator nanowire finFET architecture with very small channels, as well as localised channel doping, as described in Chapter 3. These devices have been shown to have corner states that can function as quantum dots[106], as well as have dopants in the channel[28, 107] through which transport has been measured[108]. They also have the added benefit of being CMOS-foundry fabricated with excellent prospects for scalability.

In this Chapter, we seek to establish these devices as suitable for few-electron quantum dots, as well as work out theories of charge detection and quantum dot behaviour based on our chosen method of charge sensing, gate-based radiofrequency reflectometry (as introduced in Chapter 3). To that end, we present a few-electron double quantum dot established in a nanoscale CMOS silicon transistor. The chapter is divided into two parts. First, we delve into gate-based reflectometry in these quantum dot systems, using it to explore a single quantum dot via its coupling to the lead (Fig. 4.1). Gate based charge sensing based on RF-reflectometry is advantageous in terms of ultimate charge sensitivity[93] as well as for reduction of circuit elements for quantum computation. We show that the coupling of

the dot to the resonator can be used to develop tools valuable for cryogenic measurement and metrology of the qubit environment, such as primary thermometry and the sensing of microwave amplitudes and pulse shapes.

In the second part, we move on to a double-quantum dot system in the silicon nanowire device and present Landau-Zener-Stückelberg (LZS) measurements performed for a single electron charge qubit in silicon. In recent years LZS interferometry has gained prominence as a viable method for all-electrical coherent control of few-electron quantum states. First described for atomic states[109], it has been observed for superconducting quantum point contacts[110], interacting magnetic molecules[111], nitrogen vacancy centres in diamond [112] and ultracold molecular gases[113], among others. In the solid state, it has been used to great effect for the control of semiconductor quantum dots[45, 50, 51, 114], in superconducting qubits[115–117] and in donors in silicon[108]. However, nanodevices suitable for LZS control can be geometrically complicated, with complex lithography requirements making them hard to scale up. As such, it is of interest whether such coherent dynamics of electronic charge states can be observed in standard commercial CMOS transistors. In this experiment, we apply microwaves to the double quantum dot system present in the device and use RF-reflectometry to observe a multi-regime LZS pattern, showing distinct signatures of the single, double, and multiple-passage regimes of LZS interferometry in the same device. We also observe a strong enhancement of the pattern at the points where the electron tunnels out to the leads. The interference pattern is enhanced at these detection points, and strongly suppressed when the microwave excitation is strong enough to drive the electron across both of them, indicating that the state has been collapsed and a quantum superposition no longer exists. We study decoherence effects and present a theory of LZS detected through the quantum capacitance signal of the double quantum dot, and put forward some applications of these multi-regime LZS measurements.

Before we delve into these experiments, we briefly discuss the sample and the measurement setup below. These measurements were carried out at the University of Cambridge, in conjunction with Dr. M. F. González-Zalba, at the Hitachi Cambridge Laboratory.

Sample and setup

Our device is a silicon nanowire transistor, shown in (Fig. 4.2(a,b)), fabricated on a silicon-on-insulator substrate composed of a 145 nm buried oxide layer, a 11 nm thick intrinsic silicon layer, and an 850 μm handle wafer which can be used as a global back

gate. The silicon layer is etched to create a nanowire (200 nm long and 60 nm wide) by means of deep-UV lithography. A 40 nm wide wrap-around top gate is defined using a SiO_2 (0.8 nm)/ HfSiON (1.9 nm) stack for the gate dielectric followed by TiN (5 nm)/poly-Si(50 nm) as the top gate material. The self-aligned source and drain (not represented on the sketch) are formed by ion implantation after the deposition of 20 nm thick Si_3N_4 spacers which prevent dopant diffusion into the channel.

Measurements were performed at the base temperature of a Kelvinox K400 (“wet”) dilution refrigerator (40 mK), details of the measurement and wiring of which can be found in Ref. [89]¹. High sensitivity charge detection[93, 118] is achieved by radiofrequency reflectometry on a tank circuit composed of a surface mounted inductance (390 nH), a parasitic capacitance to ground C_p (~ 1 pF) and the device capacitance between the transistor top gate and the channel. RF-reflectometry is performed close to the resonance frequency (313 MHz) and the reflected signal amplified by a low noise cryogenic amplifier. The signal is further amplified and demodulated at room temperature as shown in Fig. 4.2(a). An on-board bias tee is used to apply both DC and RF voltages on the top gate. Additionally, a fast line terminating at a 50 Ω -matched on-PCB stripline is used to deliver microwaves to the sample. The undoped silicon substrate is activated by flashing a surface mounted blue LED to generate free carriers and can then be used as a back gate[119]. Applying a voltage to the top gate of the fully depleted device creates accumulation, which occurs first at the topmost corners creating a double quantum dot in parallel[106, 107, 120].

4.1 Primary thermometry

Primary thermometry is the measurement of absolute temperature without the need for calibration against an external thermometer. At millikelvin temperatures, Coulomb blockade thermometry (CBT)[92, 121] is popular because it can be readily performed using electronic devices exhibiting transport. However, transport and its measurement are slow, and there are regimes of interest (for example, a quantum dot coupled to only one of the leads) in which electronic transport is not established or possible. Other primary thermometry techniques exist, such as Josephson noise thermometry[122] and shot noise thermometry[123]. However, the former requires a superconducting element, and noise thermometry in gen-

¹Most details of this system are very similar in terms of filtering and anchoring, to the UCL cryogen-free “dry” dilution refrigerator described in Chapter 3. The low-noise-amplifier used here, a key component, is a Quinstar QCA-U350-30H anchored at the 4K plate, providing ~ 40 dB amplification with a nominal 2.8 K noise temperature at 350 MHz.

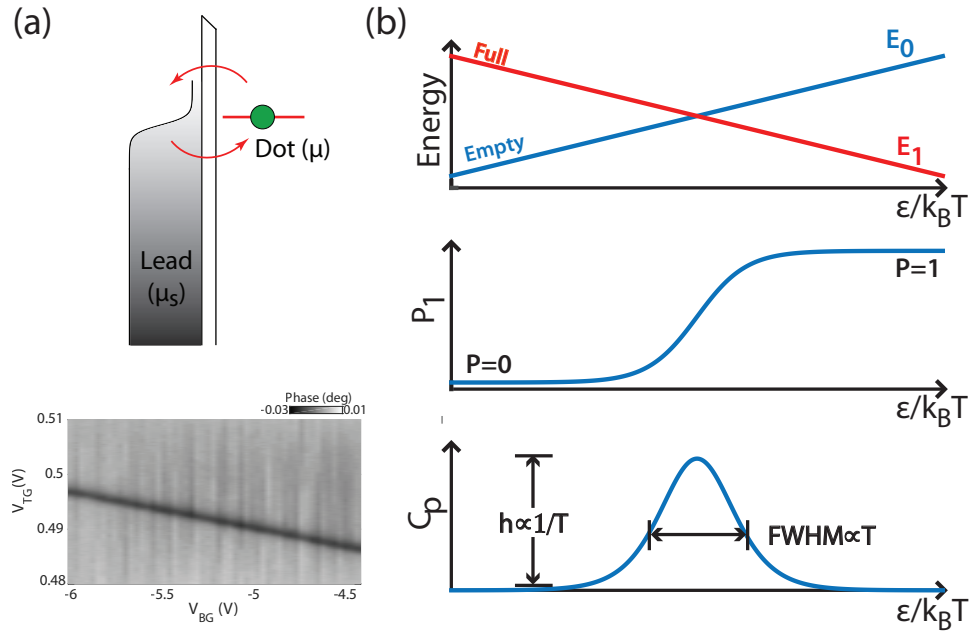


Figure 4.1: (a) Top, schematic energy diagram of the discrete quantum dot level aligned with the temperature-broadened Fermi level of the lead. Bottom, RF phase as a function of top gate and back gate voltages showing a gate-voltage dependent transition (at a mixing chamber temperature of 40 mK and a resonator drive frequency of 313 MHz). (b) Top, energy band diagram. Middle, probability (P_1) of the electron being in the dot. Bottom, the tunnelling capacitance (C_p) peaks at the degeneracy point (the phase response is negative and proportional to C_p).

eral requires extremely sensitive measurement of small voltages or currents (in the \sim pA range) and careful elimination of other sources of noise, such as voltage bias induced self-heating. Charge-sensed thermometry[124], and gate based RF-reflectometry in our sensor in particular, has the advantage of being a fast technique[118, 125] which does not need to pass current through the device, as well as a readily reproducible one. The high-frequency, resonant measurement also makes our sensor insensitive to many typical sources of noise (for example $1/f$ noise). Lastly, like CBT (which has been tested up to 27 T), the RF-reflectometry technique has the advantage of insensitivity to magnetic fields[126].

In this study we are primarily concerned with the dot to lead transition and its applications and will ignore double-dot behaviour for this section. In the last section of this chapter dealing with double quantum dot behaviour, we present the stability diagram and charge assignment of the system. However it is worth mentioning that the system is potentially a self-contained charge or spin qubit in itself, offering the promise of a fast primary thermometer very closely integrated with every qubit in this architecture.

In this and the following section, we consider a dot-to-lead transition (for example, the one shown in Fig. 4.1(a), a close-up of the larger double-dot stability diagram shown later in this Chapter), which can be seen at regular intervals (~ 10 mV) in the phase response of the resonator as we sweep the top gate of the device while holding the back gate at a fixed voltage in the subthreshold regime.

4.1.1 Thermometry

We consider a two level system consisting of the empty and full states of a dot coupled to a lead. The MHz tone applied to the resonator (with quality factor Q) drives this two level system in a cyclical single-state tunneling process between the dot and the lead (Fig. 4.1(a)), well understood in terms of the tunnelling capacitance[93, 97, 127]. As in a previous work[93], considering charge tunneling between the dot levels E_0 (empty) and E_1 (full) and a lead, we see that the levels are aligned at a certain detuning ε_0 . The system is driven around this point by the RF drive, with a frequency ω_0 . We have discussed in Chapter 3 various regimes and the consequent reflectometry peak shape and linewidths, depending on the ratio of ω_0 and Γ_0 , the latter being the constant tunnel rate away from degeneracy. When ω_0 is comparable to Γ_0 , the RF excitation, starting in the ground state at reduced gate voltage n_g^0 with an amplitude of δn_g , moves the system out of equilibrium into the excited state, where it remains until it tunnels inelastically[93]. The excess dissipated energy shows up

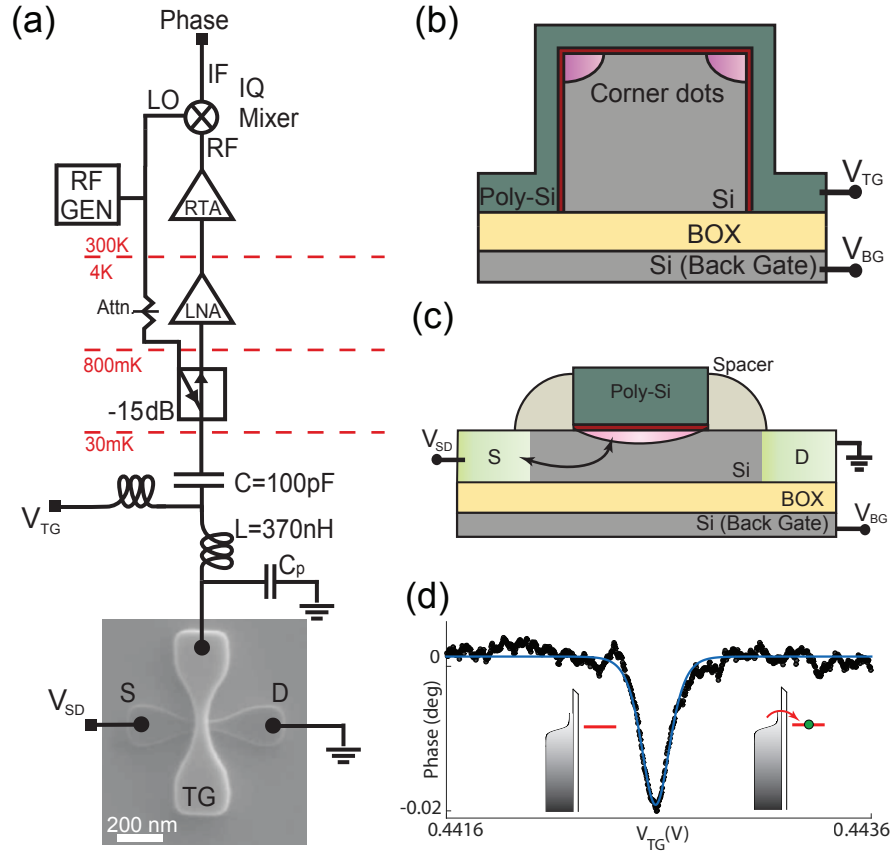


Figure 4.2: (a) RF reflectometry setup from 40 mK to room temperature. Cross sections of the device showing (b) corner quantum dots and wrap-around top gate and (c) from the other axis, source-drain and electron exchange with leads; silicon nitride spacers form the tunnel barriers. (d) Phase response of the resonator across a transition between the dot and the lead, indicating a single electron tunneling event. Data taken at 500 mK and fitted using Eq. 4.5 using $\alpha = 0.86$, and keeping the temperature T as the fit parameter.

as a change in the reflected power from the resonator, while a dispersive signal, manifesting as an additional tunneling capacitance C_t , is detected when electrons tunnel out of phase with the RF cycle. However in the case where $\Gamma_0 \gg \omega_0$, that is, in the regime of a tunnel rate much higher than the RF driving frequency, the effective resistance entering into the complex admittance ($Y = 1/\Delta R + i\omega_0\Delta C$) diverges[95]. Therefore, at high tunnel rates, no power is dissipated and electron tunneling is elastic. In this experiment our dot-to-lead transitions are in this regime, and we will therefore consider this limit. (In the next section, we will show that the fact that we are in the double-passage regime of Landau-Zener interferometry confirms this assumption, and that our tunnel rate is ~ 10 GHz, much higher than our RF drive frequency at 300 MHz.)

The dynamics of the charge tunneling process can be described by a master equation[97]:

$$\dot{P}_0 = \Gamma_- P_1 - \Gamma_+ P_0, \dot{P}_1 = \Gamma_+ P_0 - \Gamma_- P_1 \quad (4.1)$$

which reduces to solving the differential equation

$$\dot{P}_1(t) + \Gamma_0 P_1(t) = \Gamma_+(t) \quad (4.2)$$

due to probability conservation and the fact that $\Gamma_+ + \Gamma_- = \Gamma_0$. Here Γ_+ and Γ_- are the tunneling rates into and out of the dot, while P_0 is the probability of the electron being outside the dot and P_1 is the probability of the electron being in the dot. Because of the rf drive P_1 shows up in the dispersive readout as the tunneling capacitance term:

$$C_t(t) = (e\alpha)^2 \frac{dP_1}{d\varepsilon} \quad (4.3)$$

where α is the gate lever arm, defined as the conversion ratio of the applied gate voltage to the resulting shift in the dot energy levels. This generates a resonator phase shift $\Delta\phi \propto C_t(t)$ and an average phase shift $\langle\Delta\phi\rangle$. We can then arrive at an analytical expression for $\langle\Delta\phi\rangle$ by expanding the tunnel rates in Eq. 4.2 around n_g^0 to the first order of δn_g (an approximation valid for $\delta n_g \ll k_B T/E_C$),

$$\langle\Delta\phi\rangle \simeq -\frac{\pi Q (e\alpha)^2}{C_p} \frac{1}{2k_B T} \frac{1}{\cosh^2(\frac{\Delta E}{2k_B T})} \frac{1}{1 + \omega_0^2/\Gamma_0^2} \quad (4.4)$$

The phase response of the resonator is related to the effective change in the capacitance of the system ΔC as $\Delta\phi \approx -\pi Q \Delta C/C_p$. In our system we consider the high tunnel rate

limit ($\Gamma_0 \gg \omega_0$), and obtain a final equation for the average phase²:

$$\langle \Delta \phi \rangle \simeq -\frac{\pi Q (e\alpha)^2}{C_p} \frac{1}{2k_B T \cosh^2(\frac{\Delta E}{2k_B T})} \quad (4.5)$$

This equation can also be derived by noting that in the high temperature limit, the probability of the electron being in the dot is a function of the thermal energy, and is given by

$$P_1 = \frac{e^{-\frac{\Delta E}{k_B T}}}{2 \cosh(\frac{\Delta E}{k_B T})} \quad (4.6)$$

which leads to the same result for the resonator phase response ϕ . The variation of E , P_1 and C_t with the detuning from the charge degeneracy is shown in Fig. 4.1(b), with the detected phase response being proportional to the inverse of C_t .

This equation is valid in the additional limit where $k_B T > \hbar \Gamma_0$, that is at higher temperatures. The \cosh^{-2} part of Eq. 4.5 can be used to fit the peak in the resonator phase shift around the degeneracy point, where the signal is maximum, to obtain the temperature T from the full width at half maximum (FWHM). From the bottom panel of Fig. 4.1(b) it can be seen that the full width at half maximum (FWHM) and the height of the peak both depend directly on the temperature, and this dependence can be isolated since the other parameters are easy to extract from other measurements. Specifically, the height is difficult to extract directly in terms of temperature, since the quality factor of the resonator is difficult to determine with reasonable accuracy. Therefore, we choose to fit the peak to the \cosh^{-2} part of Eq. 4.5, and extract the FWHM, which will be of the form $3.53k_B T / e\alpha$ [94, 95]. The only unknown parameter in this equation is the gate lever arm α , which can be determined from some other energy scaling in the system, such as a charging energy measurement from Coulomb diamond spectroscopy, or in the subthreshold regime without direct transport (as in our case), a magnetic field energy scaling as described in the following subsection, where we extract a gate lever arm $\alpha = 0.86$. In Fig. 4.2(b) we show a peak in the reflectometry phase response taken at a mixing chamber temperature of 500 mK, measured using a ruthenium oxide (RuO_2) thermometer mounted at the cold finger of the dilution refrigerator, close to the sample. This is a temperature at which we can be sure that we are in the linear regime where the peak FWHM is set by the temperature. Using the FWHM form derived from Eq. 4.5 and our value of α , we obtain a good fit to the peak and obtain a temperature

²For the full analytic calculation, see Supplementary Note 2 of Ref. [93].

of $\sim 480 \pm 66$ mK. This is a primary value and does not need calibration against another thermometer. Some sources for the error in our measurement could be the insufficient precision of the measurement of the energy scaling for the gate lever arm, the fact that the RuO₂ thermometer at the coldfinger is some distance away from the device itself, as well as the fact that at higher temperatures, the peak amplitude becomes smaller and the error on the FWHM increases. In addition, at higher temperatures thermalization of the device can take time, and the electron temperature can consequently vary from the temperature shown by the RuO₂ thermometer.

We now discuss the lower limit set on the thermometer by the lifetime broadening due to the coupling to the leads. As we decrease the temperature, we emerge out of the regime where $k_B T > \hbar\Gamma_0$ and into the regime where the peak is broadened by $\hbar\Gamma_0$ and not by the temperature. As discussed in Chapter 3 and above, in this regime the electron tunneling is elastic and has a purely capacitive response given by

$$C_p = \frac{(\alpha e)^2}{\pi} \frac{\hbar\Gamma_0}{(\hbar\Gamma_0)^2 + (\Delta E)^2} \quad (4.7)$$

Therefore, by fitting to the peak at a point where decreasing the temperature no longer has any effect (in the case of a system with a high tunnel rate), we can extract the tunnel rate of the system. Indeed, at the lowest temperatures (40 mK, shown in Fig. 4.3(a)), we obtain a better fit to the peak using the Lorentzian form (Eq. 4.7) than to the temperature-broadened equation, which fits well for higher temperatures (400 mK and 1 K). From the fit, we obtain a tunnel rate of ~ 14.5 GHz, which matches well with the conclusions drawn from our Landau-Zener experiment in the next section. We see that valuable information about tunnel rates can be extracted from a gate-based reflectometry measurement, in addition to its use for primary thermometry.

In general the lower limit of the primary thermometer is given by the lifetime broadening arising from the leads, and also by the fact that the tunnel rate needs to be larger than the resonator frequency, which is typically in the few hundred MHz range, to avoid excess dissipation. However, the study presented here is used to illustrate the different regimes in which the thermometry and tunnel rate detection can be performed. For a device similar to ours, but intended to be used for thermometry purposes, it would be possible to (a) engineer a dot with suitable tunnel rates to the leads using tunable tunnel barriers as well as (b) within the same device, find a different transition with a lower tunnel rate (the variabil-

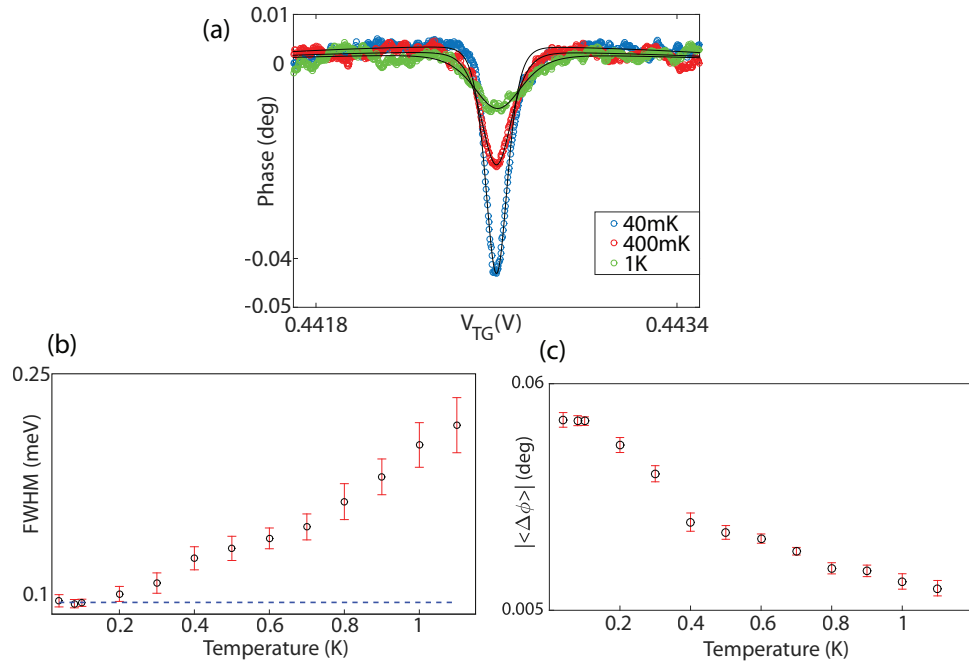


Figure 4.3: Peak shape, FWHM and amplitude with mixing chamber temperature. (a) The phase response of the resonator at three different mixing chamber temperatures, measured using a RuO_2 thermometer mounted at the coldfinger of the dilution fridge. The peak at 40 mK is fitted using Eq. 4.7, while those at 400 mK and 1 K are fitted using Eq. 4.5. (b) and (c) show the extracted FWHM and the amplitudes of the peaks as we vary the temperature. In (b) a linear fit to the saturated FWHM values below 200 mK is used to extract the tunnel rate of the transition.

ity of tunnel rates in the same device, within a large range from 100 MHz to 22 GHz, was demonstrated in Ref. [95] using different transitions of the same dot).

In Fig. 4.3(b) and (c) we present measurements showing the extracted FWHM and height of the peak arising from the phase response of the resonator, with respect to mixing chamber temperature as detected by the external RuO₂ resistance thermometer mounted close to the sample. The trend shown is similar to CBT in quantum dots, where the FWHM of the peak decreases as the mixing chamber temperature is decreased. The trend in peak amplitude is similar. In our devices, as discussed, we use the saturation of the peak's FWHM at low temperature to extract the tunnel rate of the transition, by fitting a line to find the y-axis saturation point ($y = c$), which gives us the FWHM. From the FWHM and amplitude plots, in this case, we can only surmise therefore an electron temperature lower than ~ 260 mK (obtained from the tunnel rate), since if it were higher than this value, the peak width would saturate due to temperature (and not lifetime broadening).

RF drive and lever arms

One last crucial consideration for the kind of lineshape analysis and thermometry we present here is that in practice the device must be carefully set up so that the RF power supplied to the sample is less than the thermal smearing due to $k_B T$. We accomplish this by lowering the RF amplitude and measuring the FWHM until it is no longer dependent on the RF amplitude, as shown in Fig. 4.4(a). In addition, to obtain numerical results from the peak fitting, the gate lever arm α must be obtained. This can be done by looking at an external energy scale of the system, for example the extent of Coulomb diamonds in transport; in our case, we monitor the dot-to-lead transition as we sweep the magnetic field and the shift in the peak towards higher or lower energy gives us a calibration of our gate lever arm in terms of energy, $\alpha = 0.86 \pm 0.2$, as shown in Fig. 4.4(b).

We now turn to a slightly different application of the gate-based reflectometry technique, which is the calibration of microwave amplitudes.

4.2 Microwave sensing

Microwave pulses are yet another control mechanism vital to many qubit architectures[58, 61]. However, due to the difficulties inherent in high-frequency microwave engineering there is often a trial-and-error process required to quantify pulse amplitudes and shapes

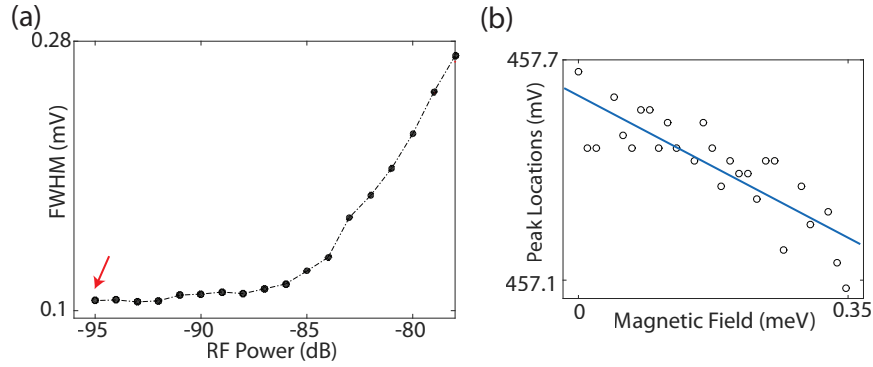


Figure 4.4: RF-drive broadening and gate lever arm calibration. (a) Full-width-at-half-maximum of a resonator phase-detected peak plotted against the estimated RF power reaching the sample (calculated from measurements taken at the RF output port of the dilution fridge using a power meter, see Appendix B). Thermometry measurements are taken where the peak is no longer power-broadened (indicated by the red arrow). (b) Peak position in top gate plotted against magnetic field (in energy units assuming $g = 2$), with linear fit.

reaching the device of interest. Currently, techniques such as Landau-Zener Interferometry can be used to estimate microwave amplitudes by fitting to Bessel functions[43]; however this requires coherent oscillations, a certain regime of driving, and a well-confined few-electron system. In addition, pulse shape tuning is often performed by trial and error or using external, room-temperature instruments, and should be ideally done in-situ at the device location at low temperature. Using gate based reflectometry, in contrast, does not require a special regime or a few-electron double quantum dot, but simply a well-defined charge instability, as found in many nano-electronic devices.

4.2.1 Effect of applying microwaves to peak

To explore the microwave detection properties of the sensor, we apply microwaves to the FET device via an on-PCB coplanar waveguide situated near the device (on the same PCB) at a frequency of 4 GHz, far higher than the RF drive frequency. Fig. 4.5(a) shows that the peak arising from the dot-to-lead transition is consequently reduced in amplitude as well as split into two peaks by the microwave excitation. We show the peak splitting seen for two microwave amplitudes (0.1 V and 0.2 V at source) and notice that the splitting of the peak is proportional to the amplitude generated by our microwave source. This can then give us a value for A , the microwave amplitude reaching the sample.

Applying microwaves to the sample affects the energy levels involved and therefore the probability (P_1) of the electron being in the dot, which depends upon the tunnel rates into and out of the dot. This means we need to extend the undriven thermal equation for $P_1(t)$ (taken to first approximation)[93],

$$P_1 = \frac{\Gamma_+}{\Gamma_- + \Gamma_+} \simeq \frac{1}{1 + e^{\frac{\epsilon_0}{k_B T}}} \quad (4.8)$$

to include the effect of the time-variant, sinusoidal microwave drive, resulting in

$$P_1(t) \simeq \frac{1}{1 + e^{\frac{\epsilon_0 + A \cos(\omega_{MW} t)}{k_B T}}} \quad (4.9)$$

Both in our system and typically, microwave drives are far faster than RF reflectometry drives, which means that $\omega_{MW} \gg \omega_{RF}$, so that the resonator sees an averaged P_1 probability

$$\langle P_1(t) \rangle \simeq \frac{1}{T_{MW}} \int_0^{T_{MW}} \frac{1}{1 + e^{\frac{\epsilon_0 + A \cos(\omega_{MW} t)}{k_B T}}} dt \quad (4.10)$$

However what is detected by the resonator is the dispersive capacitance change $C_t(t)$, which can be calculated as follows:

$$C_t = -(e\alpha)^2 \frac{\delta \langle P_1(t) \rangle}{\delta \epsilon} \quad (4.11)$$

Knowing the other terms in the equation above, the microwave amplitude A can be extracted by comparing the fit of the model above to the peak broadened and split by the microwaves. However, the equation above cannot be fitted directly; it requires numerical simulations which are then fitted iteratively for the extraction of the microwave amplitude.

4.2.2 Simulations

To fit our experimental results and verify our theoretical model, we implement a numerical simulation based on the equations above that attempts to recreate the splitting of the sisyphus peak at various microwave amplitudes³. Fig. 4.5(b) shows the results of this simulation at different microwave amplitudes, based on how much they perturb the top gate

³The simulation program was developed by Dr. Andreas Betz at the Hitachi Cambridge Laboratory.

voltage⁴, parametrized as δn_g , for the bias point $n_g^0 = C_g/eV_{tg}$, with the charge degeneracy occurring at $n_g^0 = 0.5$. With $\delta n_g = 0$, the peak is not split at all, as expected, while with $\delta n_g = 0.01$ and $\delta n_g = 0.02$ (with the latter splitting double that of the former as in the two amplitudes shown in our measurements in Fig. 4.5(a)) we see the peak splits proportionally with the increase in microwave amplitude. The model is in good qualitative agreement with the experiment. The simulations are performed at a temperature of 200 mK and a tunnel rate $\Gamma_0 = 15$ GHz. At higher temperatures, the microwave and temperature effects are decoupled, since the peak splitting remains the same, and can be fit separately, leading to the microwave amplitude probe being useful at higher temperatures as well. Variations in tunnel rates do not affect the splitting, but the overall signal intensity, as expected from Refs. [93, 95]. The effects of temperature and tunnel rate vs microwave frequency can be seen in Appendix B.

Lastly, using our model in a situation where the applied excitation is in the form of a pulse or a sawtooth ramp generates a very different response, as shown in Fig. 4.5(c) and (d), an effect which motivates further experimental work in this area. This can then be used to calibrate other kinds of excitations; an effect especially important in the case of pulsing, for which the peak is sensitive to the pulse sharpness and the model can be used to engineer best pulse frequencies and amplitudes for a given tunnel rate. In addition, the profile of very fast voltage pulses as seen by the qubit is extremely important for qubit manipulation. Applying such a pulse to the device and comparing it with the corresponding model could allow direct comparisons and quantifications of pulse sharpness and amplitude.

In the next section we move on to the study of a double quantum dot system in this device.

4.3 Multi-regime Landau-Zener Stückelberg interferometry in a double quantum dot

In this section, we present a multi-level LZS interferometry study performed in a silicon-transistor-based charge qubit, which is tunnel coupled to a fermionic sea that allows us to characterise the qubit dynamics in the strong driving regime. We discussed LZS interferometry in Chapter 2 and note that in the cases analysed in Ref. [43], the multiple passage

⁴These measurements are taken with the source and drain of the device grounded and there is a single gate.

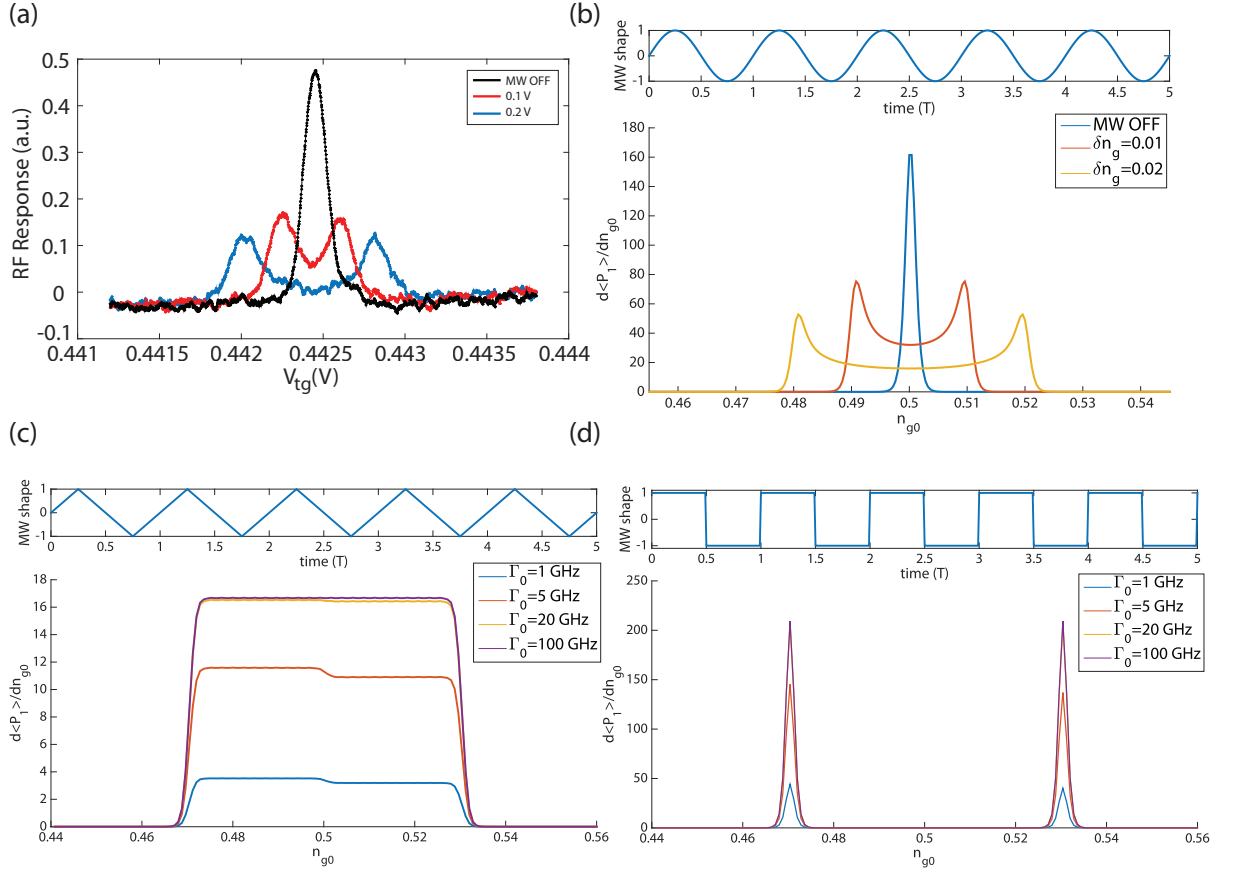


Figure 4.5: Microwave effects and simulations. (a) Microwaves are applied to an on-PCB coplanar waveguide situated near the device, at a frequency of 4 GHz and an amplitude at source of 0.1 V (red trace) and 0.2 V (blue trace) or turned off (black trace). In (b), (c) and (d) we show numerical simulations performed in MATLAB using Eq. 4.11. We plot $\frac{\delta\langle P_1(t) \rangle}{\delta n_{g0}}$ vs n_{g0} for (b) sine, (c) sawtooth, and (d) square excitations (with excitation type shown above the results), at a temperature of 200 mK. In (b) we simulate for the cases where the microwave is off (blue trace), and for an excitation amplitude δn_g at the device of 0.01 (red trace) and 0.02 (yellow trace), with a frequency of 4 GHz, the same as experiment. For (c) and (d), we simulate for different tunnel rates Γ_0 while keeping the microwave frequency at 20 GHz. (In (c) at the two lowest tunnel rates there is a simulation-induced artefact leading to asymmetry around n_{g0} .)

case is typically visible as an interference pattern as shown in Fig. 2.8(c). In Mach-Zehnder interferometry in semiconductors, the double-passage problem has been separately studied and applied as a method of qubit control[50]. However, in the present experiment, the single, double and multiple passage regimes are observable within the same device and at the same drive frequency, and the microwave drive amplitude can be varied to switch between the different regimes. Our measurement is performed by RF reflectometry directly on the gate (rather than using additional charge sensors); this can distinguish between electrons tunnelling between the dots (a phase-conserving effect) and electrons tunnelling off the dot onto the leads (an effect involving relaxation and loss of phase information, analogous to the photon detector in the optical interferometer), two processes which we briefly discuss in the next section before presenting our results.

4.3.1 The quantum capacitance in a two-level system

For the specific two level system we consider here, the double quantum dot (DQD) with a single electron, there is a well-defined TLS with an avoided crossing at zero detuning ($\varepsilon = 0$), given an interdot tunnel coupling Δ . At large detuning, the electron is localised in the left or right dot (we label these dot 1 and dot 2), while at low detuning it is delocalised over the two dots, leading to hybridised ground and excited state energy levels, given by Eq. 2.9. We are interested in the differential capacitance and changes in it, as seen from the top gate, as that is where our resonator is coupled. This should provide us with a formula for the detection of LZS interferometry via gate-based charge-sensing. Following Ref. [46], the differential capacitance can be defined as

$$C_{\text{diff}} = \frac{d(Q_1 + Q_2)}{dV_G} \quad (4.12)$$

where we take into account the sum of the charges Q_1 and Q_2 on the dots due to a certain gate voltage V_G , and we know that

$$\begin{aligned} Q_1 &= C_{G1}(V_G - V_1) \\ Q_1 &= -e\langle n \rangle_1 + (C_{S1} + C_{D1})V_1 - C_M(V_2 - V_1) \end{aligned} \quad (4.13)$$

and so on for the charge on the right dot Q_2 ; with $\langle n \rangle_1$ as the average charge number and V_1 as the gate voltage on the left dot, with the dots coupled with mutual capacitance C_M and the left dot coupled to the source and drain by C_{S1} and C_{D1} , respectively. Noting that

$\langle n \rangle_1 = -\langle n \rangle_2$ when the dots exchange electrons, we can solve this set of linear equations (considering Q for both dots). We define the total capacitance of the dots $C_{\Sigma 1(2)}$ and the lever arms $\alpha_{1(2)} = C_{G1(2)}/C_{\Sigma 1(2)}$. This gives us a differential capacitance

$$C_{\text{diff}} = C_{\text{geom}} + (e\alpha)^2 \frac{d\langle n \rangle}{d\varepsilon}, \quad (4.14)$$

where $C_{\text{geom}} \approx \alpha_1(C_{S1} + C_{D1}) + \alpha_2(C_{S2} + C_{D2})$ includes the static dot capacitance terms, and we define the lever arm for the double quantum dot as $\alpha_- \approx (\alpha_2 - \alpha_1)/2$. The average electron occupation (here for the right dot) can be expressed as a function of the ground and excited state probabilities $Z = P_- - P_+$, which is what we will need for our extension of the Landau-Zener problem:

$$\langle n \rangle = \frac{1}{2} \left(1 + \frac{\varepsilon}{\Delta E} Z \right) \quad (4.15)$$

Noting that ΔE also depends on ε as $E_{\pm}(t) = \pm \frac{1}{2} \sqrt{\Delta^2 + \varepsilon(t)^2}$ and combining Eqs. 4.14 and 4.15, we have our differential capacitance equation,

$$\begin{aligned} C_{\text{diff}} &= C_{\text{geom}} + C_Q(\varepsilon) + C_T(\varepsilon) \\ C_Q &= \frac{(2e\alpha_-)^2}{2} \frac{(\Delta)^2}{(\Delta E)^3} Z \\ C_T &= \frac{(2e\alpha_-)^2}{2} \frac{\varepsilon}{\Delta E} \frac{\delta Z}{\delta \varepsilon} \end{aligned} \quad (4.16)$$

where we have separated out the two contributions parametric on ε . The quantum capacitance C_Q , arising from the curvature of the energy bands and the tunneling capacitance C_T , arising from population redistribution processes such as relaxation (occurring on the same timescale as the resonator, or faster) both need to be considered while analysing the effect of the qubit upon the resonator. In the theoretical analysis of our results we will use this framework for our four-state Landau-Zener experiment. This is essential both in understanding the effect of the resonator (ideally negligible) on the interferometer, as well as in fitting the parameters of our system to extract useful information from the experiment[115, 116]. We now move on to our experimental results.

4.3.2 DC transport measurements

This LZS study is performed in the same device presented in the previous sections, measured with the same setup, as shown in Fig. 4.2(a). However we are now interested in the double quantum dot system instead of a single quantum dot to lead transition. We start by plotting the source-drain DC current I_{SD} of the device in Fig. 4.6(a), as a function of the top gate voltage, V_{TG} , and the back-gate voltage, V_{BG} . These measurements are taken at 35 mK with a source drain bias voltage, $V_{SD} = 1$ mV. At $V_{TG} \approx 0.4 - 0.6$ we observe the transistor turning on. The threshold top gate voltage depends upon the back gate voltage applied and in general for a higher V_{BG} , turn-on occurs at a lower top gate voltage. Near the threshold, we observe oscillatory features in the current indicating Coulomb blockade. This is due to the corner effect explored in Chapter 3 in these finFET devices, that confines electrons onto quantum dots at the topmost corners of the transistor. The dots are well coupled to the source and drain allowing direct transport measurements to be taken in these DC measurements. However, the white square, in Fig. 4.6(a), shows the region where the gate based rf-reflectometry measurements we present are taken. Here no direct transport through the transistor can occur as we are biased well below threshold and as the dots are weakly coupled to the source and drain reservoirs.⁵ The difference in the transport and reflectometry regimes in their sensitivities shows that gate-based reflectometry is a valuable tool for charge-sensing where direct transport is not possible.

4.3.3 Stability diagram and dispersive detection

In Fig. 4.6(b), we see the demodulated phase response of the resonator as a function of the top gate and back gate voltages. The phase response is sensitive to capacitance changes in the system. In the subthreshold regime of the transistor, where direct transport measurements are not sensitive enough, we observe the characteristic stability diagram of two coupled quantum dots, as a function of the top gate and back gate voltages. As is typical in these corner quantum dots which are located at the top corners of the wrap-around top gate [105], the charge transitions are coupled more strongly to the top gate than to the back gate.

RF reflectometry can be used to detect both dissipative and dispersive changes in the system under study. Dissipative processes such as a charge tunneling between a lead and a

⁵In addition, this means that both dots are well centered in the channel and are unlikely to be dopants diffused from the source and drain reservoir.

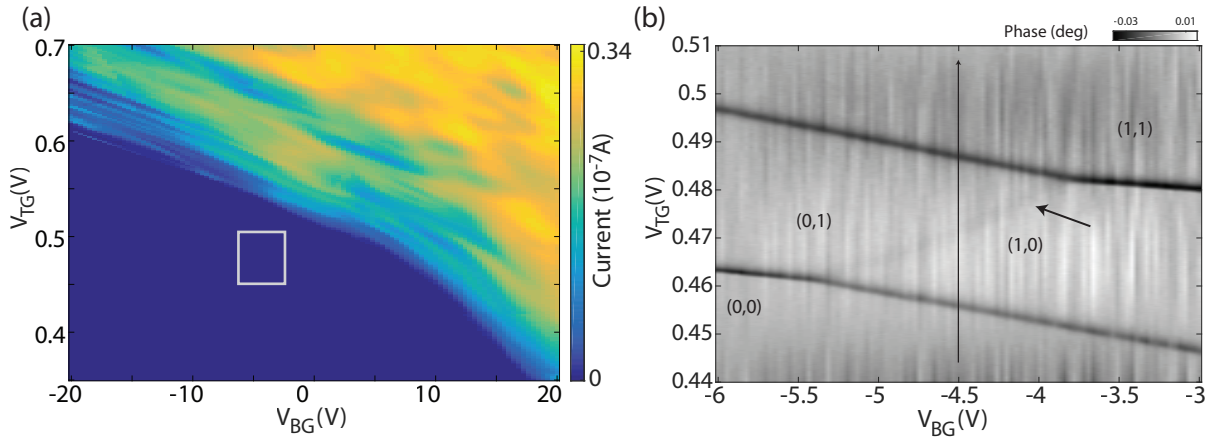


Figure 4.6: Stability diagram in transport and reflectometry. (a) shows the stability diagram of the double quantum dot as a function of the back gate and top gate voltages, with charge assignments marked according to the description in the text. The short black arrow shows the location of the faint interdot charge transition (ICT) line, while the long black arrow shows the cut in back gate voltage at which the Landau-Zener experiment is performed. Panel (b) shows the DC transport characteristics of the device over a larger region, with the white square marking the region in gate space where our measurements are taken.

corner dot can be detected, as we have seen in the previous section (and in Chapter 3). In addition, processes involving thermal excitation and relaxation induce changes in the tunneling capacitance C_T [93, 106, 118]. These changes account for the dot to lead transitions detected in Fig. 4.6(b). The figure also shows an extra coupling ridge, an interdot charge transition (ICT), where an electron tunnels between the two dots, with a white dashed line serving as a guide to the eye. This process, due to the nonzero curvature of the energy bands, contributes to the quantum capacitance C_Q [23, 125]. The ICT itself, shown by the short black arrow in Fig. 4.6(b), is faintly visible due to the fact that the response of the resonator depends on the quantum capacitance, itself dependent on the difference of the lever arms between the two corner dots $\alpha_- = (\alpha_2 - \alpha_1)/2$. These two corner dots have almost equal gate couplings since they are both oriented very similarly to the same top gate, and therefore $2\alpha_- \approx 0.1^6$. (The ICT visibility is clearer in the first few slices of the Landau-Zener pattern in Fig. 4.7, where we show data averaged over a much longer time.)

Using the phase response of the resonator, we assign the electron filling of the system. By lowering the top gate voltage below the value at which we see the coupled double-dot

⁶The approximate value for $2\alpha_-$ is estimated from the fact that the diagonal photon lines in the multiple-passage pattern shown in Fig. 4.7 are spaced by the energy of the 21 GHz microwave photon, such that $2\alpha_- V_{tg} = h\mu$

system, we deplete the dots of electrons. Below this point in top gate voltage we do not see any more dot transitions, leading us to commence our numbering of the charge states in Fig. 4.6(b) from (0,0). However in essence we can assert only that we are at an odd-parity charge transition at the ICT, labelled (0,1) to (1,0)[128]. We will calculate and plot the full four-state energy diagram of the system, in the next section. The long black arrow in Fig. 4.6(a) shows the slice at a back gate voltage value of 4.5 V where we perform the LZS experiment.

4.4 LZS results and discussion

Fig. 4.7 shows the phase response of the resonator as a function of detuning and microwave amplitude. The frequency of the microwave excitation, applied to an on-PCB stripline next to the sample, is $\nu = 21$ GHz, chosen so that we are driving fast enough to perform multiple passages within the charge coherence time T_2 . In Fig. 4.7, at $A_{\text{mw}} = 0$, the interdot charge transition is centered at zero detuning $\varepsilon = 0$, while the dot-to-lead transitions are above and below, as would be expected in the cut taken through the stability diagram along the black line shown in Fig. 4.6(a).

Four distinct regions are visible in the figure (apart from the background baseline of the resonator response where there are no transitions), described below using the symbols superimposed on them in Fig. 4.7:

- **Incoherent driving (blue star):** The regions marked with a blue star in Fig. 4.7 are regions devoid of any interference pattern. This is expected, since in this region the electron is transitioning from the dot to the lead and then back again, which is not a phase-conserving process. This means that every passage will be a single-passage process.
- **Multiple passage (red star):** In this region, we see the characteristic multiple-passage patterns seen in a typical fast-passage Landau-Zener interferometry experiment. Resonant lines appear at equally spaced points $\varepsilon = n\hbar\nu$, where n-photon transitions mediate the charge oscillation between the dots (which can be used to calibrate the gate lever arm α_-). In this region, the electron is being swept back and forth by the microwave drive between the left and right dot.
- **Double passage (green circle):** In this region, at higher microwave driving strength, the multiple-passage interference pattern sharply gives way to a very different fringe

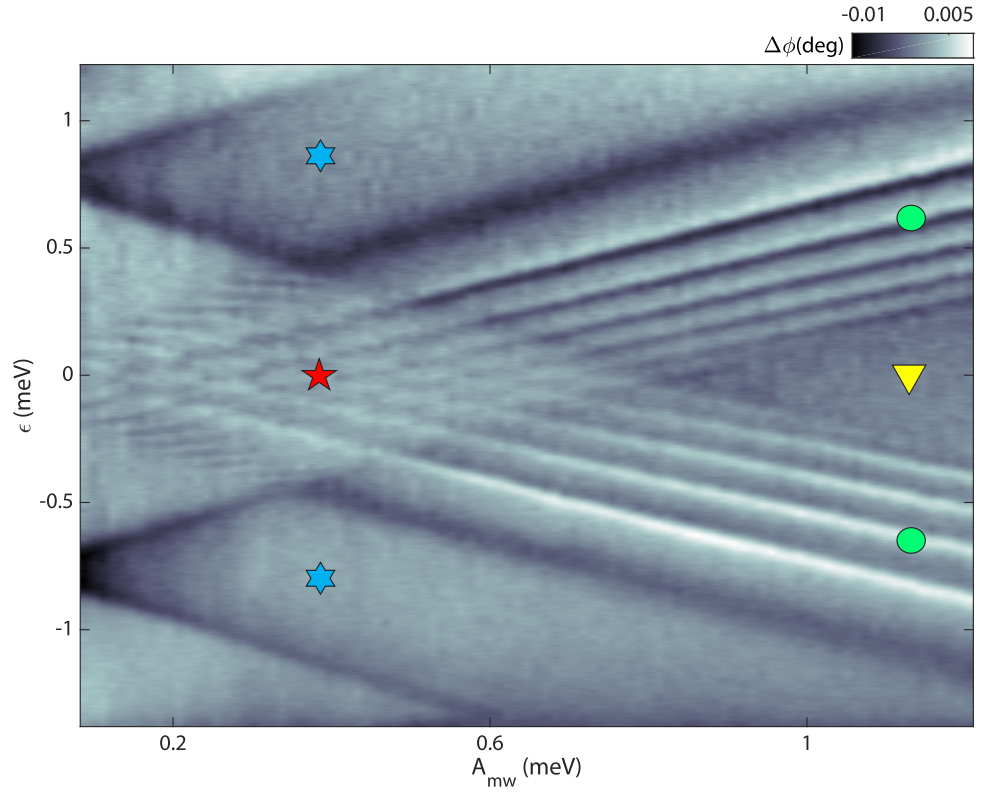


Figure 4.7: (a) Phase response of the resonator $\Delta\phi$ as a function of detuning ε and calibrated microwave amplitude A_{mw} . Symbols indicate the four different regions of the Landau-Zener interferometry patterns as described in the main text.

pattern, where the individual photon lines are no longer visible. In addition, we note that the visibility of the fringes is strongly enhanced, and we discuss the reasons for this enhancement in the next section.

- **Destruction of Interference (yellow triangle):** Lastly, we increase the microwave drive even higher and consider the resulting region, marked by a yellow triangle in Fig. 4.7. Here there is an abrupt loss of the coherent interference pattern. It is also the point where the broadened dot-to-lead transitions overlap.

Before discussing these results in our theoretical framework, we look at the dependence of this multi-regime pattern on the microwave drive frequency and use it to make a first-order estimate of the coherence time of the charge qubit, which we will need for the fit.

4.4.1 Frequency dependence

Our theoretical description considers our gate-based reflectometry setup in the semi-classical limit of a quantum system coupled to a classical resonator, with $h\nu \ll k_B T$, an approach successful for the description of atom-light interactions. For us this requires that characteristic qubit times are much shorter than the period of the resonator, or that $\nu^{-1} \gg h/\Delta, T_1, T_2$. Since the resonator is much slower than the qubit, it sees the stationary value for the occupation probabilities[46]. Our resonator frequency is 313 MHz, with a corresponding period of ~ 3 ns. The full width at half maximum of the quantum capacitance signal lineshape at the ICT gives us a rough measure of the tunnel coupling of the system, which is $\Delta \sim 33 \mu\text{eV}$ or 8 GHz, while from our tunnel rate measurements in the previous section, we know that the tunnel rate of the dot to the lead is very fast, ~ 15 GHz (which is why we are in the double passage regime upon encountering them), and that the “coupling” at these crossings is essentially, zero.

Results

In Section 2.4 we saw that the microwave frequency used to drive the Landau-Zener experiment can have a significant effect on the interference pattern, depending on the qubit timescales. Reducing the manipulation time below the coherence time of the system affects the central multiple-passage pattern first, since at some frequency we shift to an intermediate regime of double-passage where the microwave period approaches T_2 . Subsequently,

with a further lowering of the microwave frequency, we will go into the incoherent single-passage regime, where the electron phase coherence is lost within every passage, such that multiple passages are but an aggregation of single-passages. The electron phase coherence time in our strongly-driven TLS can therefore be studied by performing a microwave frequency dependence of the LZS interferometry pattern (since of course we do not have direct control over the T_2 of the charge qubit). Fig. 4.8 shows the LZS interferometry study performed using three different microwave frequencies (29 GHz, 11 GHz, and 4.72 GHz), where the change in driving frequency leads to differences in the maxima and minima positions since the resonant lines appear at equally spaced points $\varepsilon = nh\nu$. We observe three regimes: the quantum coherent regime in (a), the intermediate driving regime in (b) and the incoherent driving regime in (c). In (a), measured at 29 GHz, successive transitions through the avoided crossing are correlated, and clear interference fringes are visible. This indicates that $\nu^{-1} < T_2$. In (b) we observe fewer clear minima and maxima regions while others are blurred, indicating that ν^{-1} is approaching T_2 and that we are close to the double-passage regime. In (c), Landau-Zener transitions are uncorrelated and we observe no interference pattern, indicating $\nu^{-1} > T_2$. We see that in the enhanced regions, the double-passage interference pattern persists up to 4.72GHz, or ~ 200 ps, and we take this value of T_2 as a first guess for the fit to theory. We use T_1 as a fitting parameter.

As we describe below, we find the best fit of theory to experiment with T_1 and T_2 in the same range, of a few hundred picoseconds, as is common for charge qubits in these architectures[29, 46, 108]. In Chapter 6 we will use a different method to find the T_1 and T_2 of a similar charge qubit. These results indicate that our assumption that all characteristic qubit times are much shorter than the resonator period is accurate.

To develop an explanation for the different regions in our multi-regime LZS experiment, we need to gain a sense of the different energy levels of the system that come into play. For this purpose we now calculate the energy level diagram of this regime of the double quantum dot.

4.4.2 Energy levels of the double quantum dot

We discussed the energy of a double quantum dot system calculated in the constant interaction model in Section 2.2.2, for a single gate, as well as the reduced gate voltage n_g . In the current device, we have a double quantum dot coupled to two gates, which can be represented with a circuit diagram as shown in Fig. 4.9(a). The two gates are the top gate and

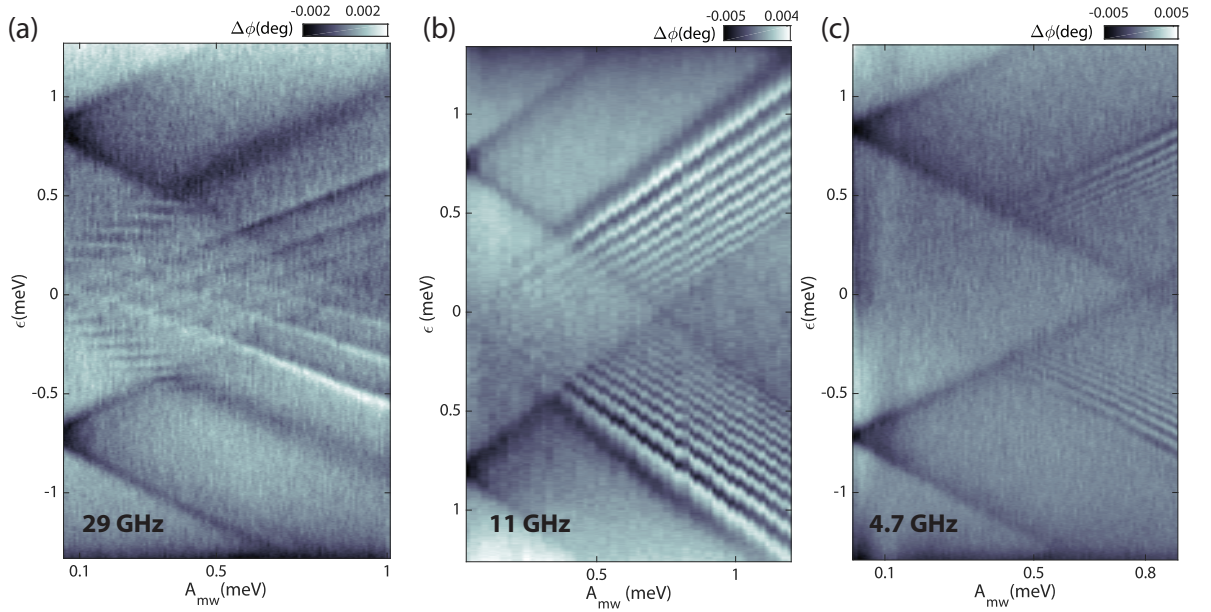


Figure 4.8: Frequency dependence of the LZS interferometry pattern. The phase response of the resonator is shown for a microwave driving frequency of (a) 29 GHz, (b) 11 GHz and (c) 4.72 GHz, with a decreasing visibility of the LZS pattern from left to right.

the back gate, with corresponding applied voltages V_{tg} and V_{bg} , and reduced gate voltages n_{tg} and n_{bg} . Following Eq. 2.4, we now write down the electrochemical levels of quantum dot 1 as a function of N_1 , N_2 and the reduced gate voltages:

$$\mu_1^* = \frac{\mu_1(N_1, N_2)}{E_C} = \left(N_1 + \frac{N_2}{m} - 1/2 \right) - n_{tg} \left(1 + \frac{1 + 2\alpha_-}{m} \right) - n_{bg} \left(1 + \frac{1 - 2\alpha_-}{m} \right), \quad (4.17)$$

where α_- is the asymmetry in the gate couplings, as before, m is the ratio between the total and mutual charging energies, $E_C = E_{C1} = E_{C2} = mE_{Cm}$ (for the purposes of an illustrative energy diagram, we take the charging energies of the two dots, which are typically very similar, to be the same), and we have divided throughout by the constant E_C for the sake of simplification.

We can now calculate the stability diagram of the device (Fig. 4.9(b)) by plotting the pairs of values (n_{tg}, n_{bg}) that satisfy the condition $\mu_{1(2)}^* = 0$ for all of the four charge states. When this condition is fulfilled, the two charge states become degenerate and the double quantum dot system can alternate between the two different charge configurations. Here

we have used $m = 10$, *i.e.*, a ten times lower mutual charging energy as compared to the individual charging energies, as a typical value for semiconductor double quantum dots. To obtain $2\alpha_- = 0.1$, we use the gate voltage spacing of the Landau-Zener photon lines in Fig. 4.7, which gives us an energy scaling as per the equation $dV_{tg} = 2\alpha_- * h\nu$, where ν is the frequency of the applied microwaves[129]. The reduced back gate voltage value where the experiment is performed, at the middle of the ICT line, corresponds to the bias point $n_{bg}^0 = 0.25$.

The energy diagram of the DQD in terms of the reduced gate voltages can now be calculated, essentially taking a cut across the top gate, along the $n_{bg}^0 = 0.25$ line. We plot the total energy of the DQD for $N_1, N_2 = 0, 1$. Fig. 4.9(c) shows a plot of the reduced DQD energies as a function of reduced gate voltage n_{tg} for $m = 10$ and $a = 0.1$ as before, using a tunnel coupling $\Delta_c = E_C/150$.

Fig. 4.9(c) shows the energy diagram with different charge regions as indicated in the measured stability diagram (Fig. 4.6(b)). From the figure we see that the central multiple-passage LZS pattern occurs at an anticrossing that is detected via the quantum capacitance (as described in Fig. 2.5(b) and Section 4.3.1), as the electron is swept back and forth across the anticrossing. At the enhanced regions the electron is driven far enough that it can reach one of the two lower crossings shown in Fig. 4.9(c), where the electron can tunnel out from dot to lead and be replaced by another from the Fermi sea of the lead, so that it can only perform a double passage before tunneling out and being detected. When both tunneling points are reached by the microwave drive strength, the electron tunnels out in each passage across the anticrossing.

4.5 Theoretical description

To interpret our multi-regime interference pattern, we use the LZS and quantum capacitance theory discussed in Section 2.4 and 4.3.1 (extended in conjunction with Dr. S. N. Shevchenko from the Center for Emergent Matter Science, RIKEN, Japan, who also performed simulations of the results). However, we now have to apply it, at least initially, while including all four of the interacting energy levels shown in Fig. 4.9.

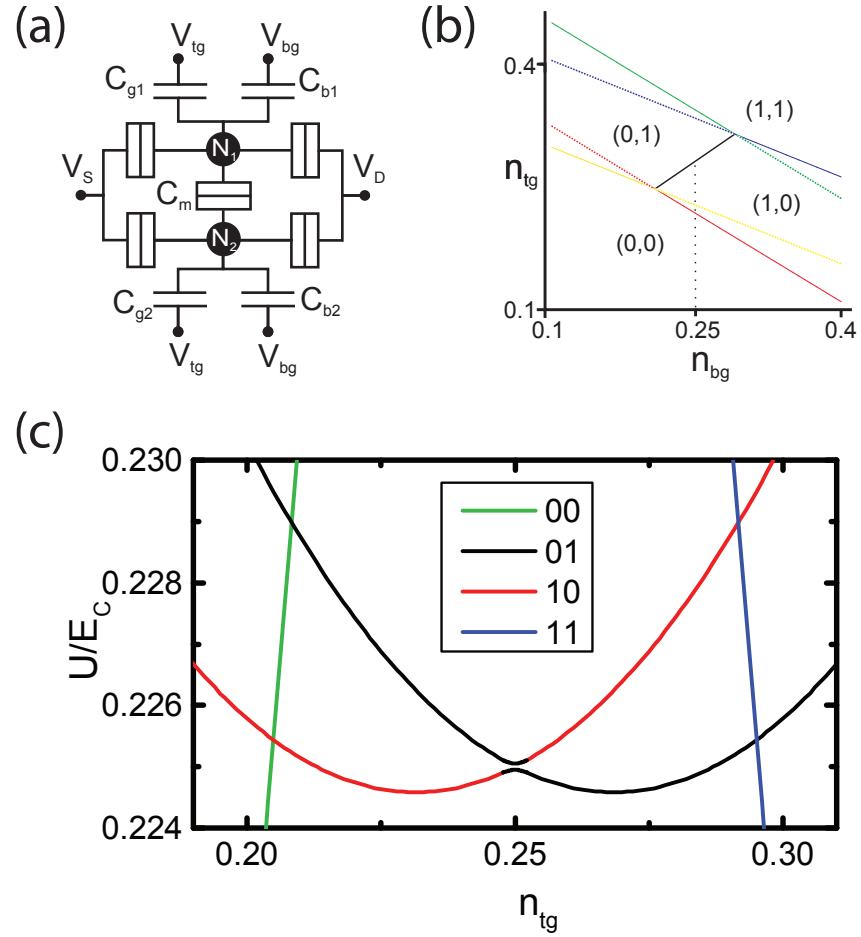


Figure 4.9: Circuit model, stability diagram and energy levels of the double quantum dot. (a) Circuit model of the DQD in parallel. (b) Calculation of the electrochemical potentials with $m = 10$ and $a = 0.1$, forming a charge stability diagram, with lines indicating the fulfilment of the condition $\mu_{1(2)}^* = 0$ for the four charge states. The dotted line shows the cut taken to match the x-axis in panel (c), which shows the energy levels of the DQD plotted as a function of reduced gate voltage and the different charge states: (0,0) in green, (1,1) in blue, (1,0) in red and (0,1) in black, with a tunnel coupling $\Delta = E_C/150$.

The expression for the quantum capacitance of our four-state device can be extrapolated from Eq. 4.14 and Eq. 4.15:

$$\begin{aligned} C_Q &\approx -e \frac{d}{dV_{\text{TG}}} \{ \alpha_1 \langle n_1 \rangle + \alpha_2 \langle n_2 \rangle \} = \\ &= -e \frac{d}{dV_{\text{TG}}} \{ \alpha_- (\langle n_1 \rangle - \langle n_2 \rangle) + \alpha_+ (\langle n_1 \rangle + \langle n_2 \rangle) \}, \end{aligned} \quad (4.18)$$

where we have $\alpha_{\pm} = \frac{\alpha_1 \pm \alpha_2}{2}$ as before. This means our detuning ε should now be expressed as

$$\varepsilon = -e2\alpha_- (V_{\text{TG}} - V_{\text{G0}}). \quad (4.19)$$

We assume⁷ that the charge is counted from 1/2, so that we have

$$\langle n_1 \rangle = \langle \psi | n_1 | \psi \rangle = -\frac{1}{2} (P_{00} + P_{01}) + \frac{1}{2} (P_{10} + P_{11}), \quad (4.20)$$

$$\langle n_2 \rangle = \langle \psi | n_2 | \psi \rangle = -\frac{1}{2} (P_{00} + P_{10}) + \frac{1}{2} (P_{01} + P_{11}). \quad (4.21)$$

The formula for the quantum capacitance for our four-state DQD can then be written as the following

$$C_Q \approx 2(e\alpha_-)^2 \frac{d}{d\varepsilon} \left\{ P_{01} - P_{10} + \frac{\alpha_+}{\alpha_-} (P_{00} - P_{11}) \right\} \quad (4.22)$$

The quantum capacitance can be normalized by $C_{Q0} = 2e^2\alpha_-^2/\Delta$, which is the value that gives the maximal ground-state DQD capacitance. We note that in the particular sub-case of the two-level problem where only the two interdot states ($|01\rangle$ and $|10\rangle$) are relevant, then $P_{00} = P_{11} = 0$ and $P_{01} + P_{10} = 1$, and we obtain the result:

$$C_Q = 4e^2\alpha_-^2 \frac{d}{d\varepsilon} P_{01} \quad (4.23)$$

with P_{01} being the probability of one electron in the right dot, and zero in the left.

We note that the geometrical factor $\alpha_+/\alpha_- \gg 1$ that appears in Eq. 4.22 makes the transitions involving $|00\rangle$ and $|11\rangle$ states result in the enhanced response (in the double-passage regime) as compared to the multiple-passage interdot transitions $|01\rangle \leftrightarrow |10\rangle$.

⁷See Section 2.2.2; an integer charge indicates the single-electron tunneling regime and electron exchange with the leads, *i.e.*, a lifting of Coulomb blockade. Therefore we take ε_0 as 1/2.

We now try to fit this theory to the different sections of the complex interference pattern observed in our experiment, for the measurements carried out at a microwave frequency of 21 GHz, shown in Fig. 4.7.

4.5.1 Standard LZS interferometer: multiple passage

Fig. 4.10 is plotted with Eq. 4.22, with the upper-level occupation probability given by Eq. 2.15. The region described is that denoted by a red star symbol in Fig. 4.7. The simulation generated using the theory is presented on the left⁸, while our measured data is on the right. The parameters used to obtain good agreement with the experiment are as follows⁹: $\Delta = 8.25 \text{ GHz} \cdot h$, $T_2 = 0.25 \text{ ns}$, $T_1 = 5T_2$. A T_1 of 1 ns is similar to other studies in charge qubits in this kind of silicon nanowire system[29, 46]. These short charge relaxation times could be due to low-lying orbital excited states in silicon quantum dots which can result in relaxation times ranging down to picoseconds[130].

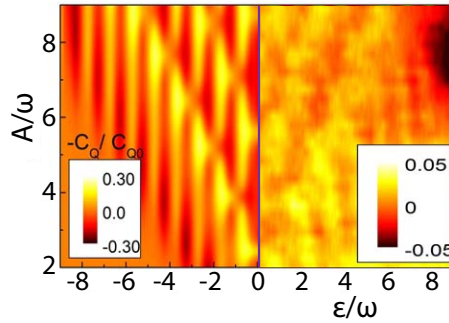


Figure 4.10: The region of the standard multiple-passage regime of LZS interferometry, denoted with the red star in Fig. 4.7. The normalised quantum capacitance C_Q/C_0 is plotted with the simulated pattern on the left, and experimental data on the right.

In this region, looking at the energy diagram of Fig. 4.9, we see a drive that is strong enough to move the electron across the avoided crossing, but that does not bring it close to the two crossings with the other two states $((0,0)$ or $(1,1))$ on either side. In addition, given that we are using a microwave frequency high enough ($> 1/T_2$) to be able to per-

⁸The theoretically simulated lines of high upper diabatic state probability are plotted using a contour plot, with averaging between points.

⁹The tunnel coupling is measured as mentioned in Section 4.4.1 to be $\sim 8 \text{ GHz}$. However the fit is performed to the ICT peak which has a low signal intensity and therefore it is used as a starting value to the simulation and adjusted as a parameter.

form multiple passages across the avoided crossing, we see a characteristic and clear LZS interference pattern, as expected.

4.5.2 MW detection region

The region marked with the blue star is shown in Fig. 4.11 and corresponds to the $|01\rangle \leftrightarrow |11\rangle$ dot-to-lead transitions, if we consider the right section of the energy diagram in Fig. 4.9, for example. We plot the normalised quantum capacitance C_Q/C_0 (Eq. 4.24) with the probability P_{11} given by the single-passage LZS expression (Eq. 2.10) and the tunnel rate as before. This section corresponds to the analysis presented in Section 4.2.1 of this chapter, and the splitting of the peak with increasing microwave amplitude can be used to calibrate microwave amplitudes as before. However, in this Section we are not concerned with these regions since the dot to lead transitions play the role of the measuring device, rather than forming part of the quantum system itself. When the electron tunnels out at these points in detuning to be detected, it is a destructive, classical measurement and we can characterise these as “detectors”, in an analogy to photon detectors as in a Mach-Zehnder experiment.

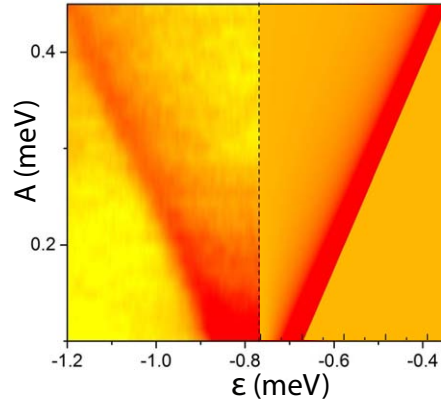


Figure 4.11: The region of the single-passage regime of LZS interferometry, denoted with the blue star in Fig. 4.7. The normalised quantum capacitance C_Q/C_0 is plotted, with the simulated pattern on the right, and experimental data on the left.

4.5.3 Enhanced interferometry: double passage

This region is denoted with the green circle and corresponds to an increased microwave drive A . In this situation, the electron, starting at one end of the avoided crossing, is driven

across the $01 - 10$ transition twice; this is followed by an encounter with the dot-to-lead transition labelled $|11\rangle$ or $|00\rangle$ in Fig. 4.9 (to the right or to the left, respectively). However, at this point the transition rapidly results in a relaxation; for example, to the right, we would obtain the transition $|01\rangle \leftrightarrow |11\rangle$. This indicates that the electron can no longer keep its phase coherence, as it tunnels out at this transition and is replaced by another. We now look at the simulation based on our theory.

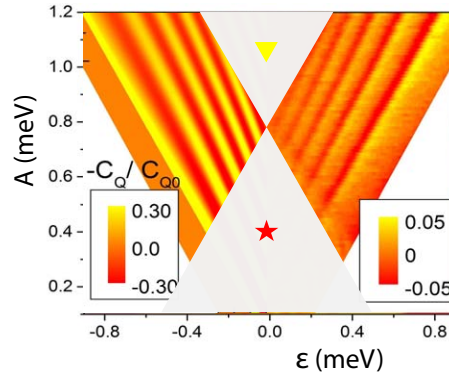


Figure 4.12: The region of the double-passage regime of LZS interferometry, denoted with the green star in Fig. 4.7. The normalised quantum capacitance C_Q/C_0 is plotted, with the simulated pattern on the left, and experimental data on the right. As in the multiple passage case, Δ , T_1 and T_2 are parameters.

Even though several terms enter Eq. (4.22), only the P_{11} -term matters (for example for the $|01\rangle \leftrightarrow |11\rangle$ transition we are considering), due to the large asymmetry factor $\frac{\alpha_+}{\alpha_-} \gg 1$. Owing to the rapid relaxation occurring at this kind of Sisyphus transition, this probability (P_{11}) equals the occupation of the $|01\rangle$ -state after the double passage. Then Eq. (4.22) will simplify to

$$\frac{C_Q}{C_{Q0}} = -\frac{\alpha_+}{\alpha_-} \Delta \frac{d}{d\varepsilon} P_{11} \quad (4.24)$$

with P_{11} given by the double-passage two-level solution presented in Eq. 2.12. With this simplified model, a good quantitative agreement is obtained, as demonstrated in Fig. 4.12. For this we have taken the geometric ratio in the lever arms to be $\frac{\alpha_+}{\alpha_-} = 10$. It is worth noting that the enhancement in the signal in this region is a purely geometric effect to do with the small difference in lever arms between the two coupled dots. However, this kind of small difference in lever arms and the consequent visibility difference between the dot-to-lead transitions and the quantum capacitance is a feature of many gated quantum dot architectures. This is because it is lithographically hard to engineer a double quantum dot

system with a very high asymmetry in dot lever arms without affecting other aspects such as control over the tunnel coupling and/or the need to keep the dots at similar sizes.

4.5.4 The interrupted interferometer

The last region of Fig. 4.7, marked with a yellow triangle, is an area where a sudden loss of the LZS interference pattern is observed as the two broadened dot-to-lead transitions meet each other. In this region, as in the MW-detection regime described in Section 4.5.2, we are also in the incoherent driving regime; however, since we can see the pattern in the multiple-passage region and we are at the same microwave frequency, we can be sure it is not because we are driving too slowly (i.e. $\nu^{-1} < T_2$).

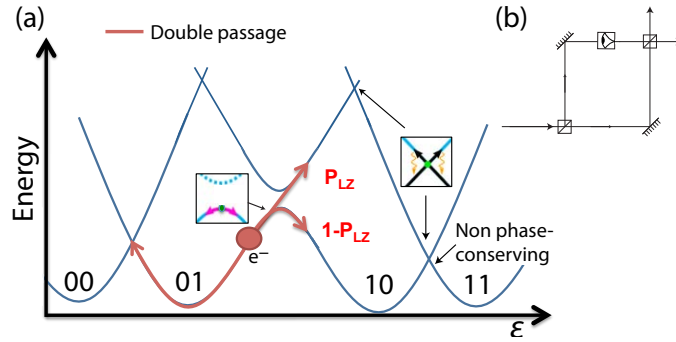


Figure 4.13: (a) Schematic showing LZS interferometry in our four-level DQD system, with P_{LZ} the probability of a LZS transition. The center inset shows the quantum capacitance mechanism behind the signal detected near the anticrossing, while the right inset shows the elastic tunnelling process at the crossings where electron exchange occurs between the dot and the lead. (b) Illustration of a Mach-Zehnder interferometer with a “detector” placed within one of the arms of the interferometer, so that the accumulation of phase is not possible.

To explain this region we take a look at the schematic presented in Fig. 4.13 and see that we are now in the region where the microwave amplitude is higher than all previous regions. This means that with each passage through the avoided crossing, the electron encounters a dot-to-lead transition in detuning, or a “detector” and tunnels out. The electron which tunnels back in is now swept back across the avoided crossing, but encounters the dot-to-lead transition on the other side. Consequently, we see that the phase coherence that leads to Landau-Zener transitions cannot be built up. In Fig. 4.13(b) we show a form of the Mach Zehnder interferometer showed in Fig. 2.7 in Chapter 2, where we have placed the analogous photon detector (the dot-to-lead transition) in the middle of the interferometer

path, after the beam splitter (the avoided crossing), to illustrate that the interferometry is, in a sense, “interrupted”.

4.6 Outlook and conclusion

In summary, in this chapter we have shown that gate based RF-reflectometry can be used to perform fast, sensitive primary thermometry at millikelvin temperatures. We also show that the tunneling capacitance peak responds quantifiably to microwave excitation and that this can potentially be used to calibrate the microwave amplitude arriving at the device. We have been able to develop a theoretical model and simulate qualitatively the effect of the microwaves. Additionally, our sensor is implemented in a nanoscale CMOS silicon architecture which is readily able to be mass-produced both for integration with conventional electronics as well as with current quantum computation schemes.

We have also reported dispersive readout of a double quantum dot in the channel of a commercial CMOS transistor. We read out the charge state of the system in a continuous non-demolition regime by using the dispersive response of a high-frequency resonator, discussed earlier in this chapter, which is coupled to the quantum system via the gate. We use microwaves to perform multiple fast passages through the qubits avoided crossing and we observe the emergence of the LZS interferometry pattern, corresponding well to theoretical predictions and previous experimental work. At stronger drives, however, using a projective measurement to an even-parity charge state, we observe a strong geometrical enhancement of the readout signal. At even stronger drives, we perform a second projective measurement which occurs during the coherent evolution, resulting in a loss of the interference pattern. Using microwave pulses accessing different regimes of the LZS interferometry, instead of a continuous drive this kind of novel multi-regime interference pattern could demonstrate a way to increase the state readout signal of coherent quantum systems, in addition to providing valuable insight into the field of single-electron analogues to optical reflectometry. Potential fine control over the interferometry and the regimes is possible, by using fast pulses to drive back and forth across the avoided crossing, accumulate a fixed amount of phase by waiting, and then pulse just as far as the dot-to-lead crossing to read out the phase with an enhanced signal. Lastly, our results demonstrate a way to integrate qubit control, readout and the exploration of novel physical phenomena with existing large-scale and robust CMOS technology.

In the next chapters we will explore the idea of integrating dopants into this double-quantum dot architecture by performing a spin-dependent transport study on a dopant in silicon, and finally we will present a coupled hybrid dopant-dot system.

Chapter 5

Electrically Detected Magnetic Resonance of Selenium Donors in Silicon

5.1 Introduction: deep double donors in silicon

The previous chapter explored quantum dots in nanodevices in silicon, as well as ways to perform single-electron charge-sensing and qubit control in a scalable architecture. Ultimately, as stated before, we seek to combine this fast, readily tunable and versatile architecture with a spin system that has been proven to have extremely long coherence times; donors in silicon. In this Chapter we employ the sensitive magnetic resonance technique of EDMR (described in Chapter 3) to study a dopant in silicon that has potential for successful integration into nanodevices, in addition to coherence and relaxation times attractive for quantum computation.

As described in Chapter 1, the electron and nuclear spin of phosphorus donors in silicon have been widely studied for qubit applications. These have been manipulated and read out via their integration into electronic devices[6–8] as well as in the bulk[16, 131]. Arsenic and bismuth donors have also been studied in the bulk, but along with phosphorus, these are all “shallow” dopants in silicon, that is, they are relatively close to the conduction band and require little energy to ionise, as shown in Fig. 5.1.

The chalcogens in silicon, however, have not been studied in detail despite having multiple characteristics making them viable as donor-based qubits, as well as useful systems for spintronics. The chalcogens are deep, “double” dopants in silicon; while group V dopants

like phosphorus have a single electron to donate, group VI dopants, such as selenium, have two bound electrons in the neutral state[132].

In this work we study one of this class of dopants, namely selenium, through the sensitive spin-to-charge conversion technique called Electrically Detected Magnetic Resonance (EDMR), first demonstrated in 1972 by Lepine[133]. EDMR has been the frontrunner of device development and integration of dopant spins into single-atom spin qubit devices in silicon, especially for phosphorus. Many aspects of the physics of donor spins, and their interactions with interface defects in silicon were understood through EDMR, as were mechanisms such as spin-dependent tunneling[84] and spin-to-charge conversion, which are essential techniques in the readout of quantum dots[56][41] as well as for phosphorus donor devices. In addition to applications for quantum information mentioned above, EDMR has been instrumental in the study of photovoltaics and disordered materials (such as amorphous-Si:H, notably in the context of solar cells[134]).

Spin dependent transport in silicon is typically understood within the two frameworks of polarization-dependent models and spin-dependent recombination. Within these frameworks, there exist a variety of mechanisms, discussed in Section 5.1.3. However, in the context of donors in silicon, these mechanisms have been identified through experimental studies on the shallow donors only. It is conceivable that due to their double-donor nature and their strong binding energies, deep donors in silicon may give rise to previously unobserved EDMR mechanisms. Our study, performed on a bulk selenium-doped silicon sample using transport measurements, seeks to examine this hypothesis and we are interested in identifying and isolating novel spin-to-charge conversion mechanisms in silicon. We also aim to gain understanding into a possible spin-to-charge conversion mechanism that will lead us to the first chalcogen implanted devices. It is hoped that the study will shed light on spin-dependent transport processes involving a deep, double donor in silicon, which have not been observed before.

5.1.1 State of the art for chalcogens in silicon

The electronic structure of the chalcogens has been investigated[132, 135–140] for almost thirty years now. Electronic structures and ionization energies were determined by Deep Level Transient Spectroscopy (DLTS)[135] and by Fourier Transform Infrared Spectroscopy (FTIR) techniques on p-n diodes[132], while information on the excited states of selenium was obtained through IR optical absorption spectroscopy both in natural[137]

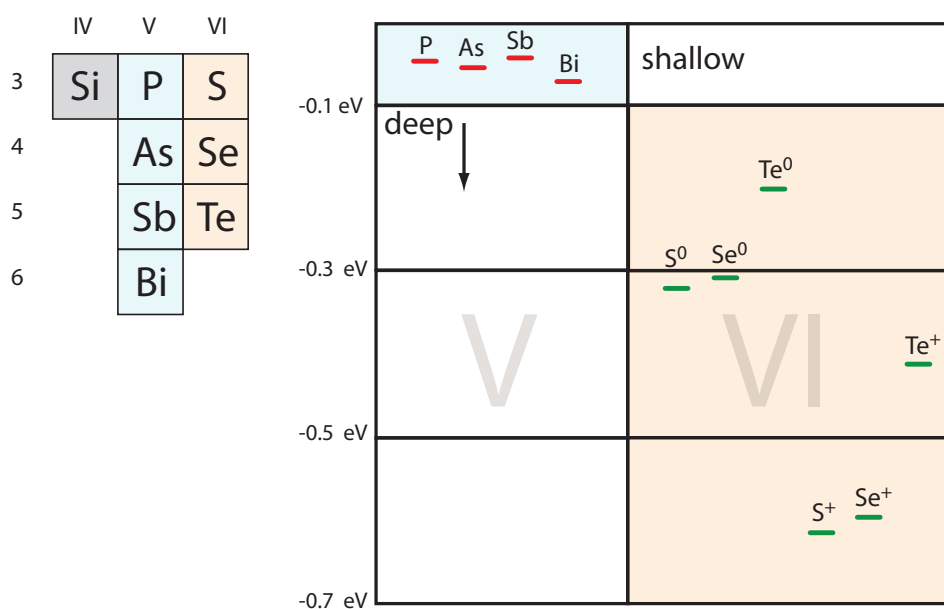


Figure 5.1: Shallow and deep donors in silicon. Left, periodic table showing the position of the chalcogens in silicon. Right, illustration showing the ionization energies of the donors in silicon. For references, see Table 5.1.

and isotopically enriched silicon[140]; the narrow linewidths of the latter demonstrating the possibility of optically resolving the ground state hyperfine coupling. Magnetic resonance experiments were first carried out in 1981 for the Se^+ state[136], yielding a direct measurement of the g-factor and the hyperfine coupling.

More recently, ESR experiments performed using selenium-doped isotopically enriched silicon samples have been able to determine the electron spin relaxation and coherence times of selenium[141], and we are now able to compare with the shallow donors. In this work, the electron spin relaxation times of Se^+ in 28-silicon were demonstrated to be the longest among other donors in the range 5–30 K. Primarily as a result of this increase in T_1 , the electron spin coherence times in Se^+ were shown to be two orders of magnitude longer than group V donors for temperatures above 10 K. At lower temperatures, the coherence times in this work were limited by the high concentration of selenium donors, but are expected to be at least as long as those of phosphorus (and perhaps longer, due to the increased T_1). Lastly, the study showed the possibility of ionising Se^0 to bring it into the ESR active Se^+ state using $4\text{ }\mu\text{m}$ illumination.

A recent proposal[142] has suggested the implantation of selenium dopants in a photonic structure, for an architecture enabling single-spin, single-shot readout at 4K and exploiting the electric-dipole allowed optical transitions available to deep donors. In isotopically purified silicon, these transitions were shown to be spin selective at very low magnetic fields (the Earth's magnetic field, for example) as well as emitting single photons when pumped with near-bandgap light. This could result in a photonic active, long-lived spin qubit, as well as an emitter useful for quantum repeaters, fast optical switches and silicon-based optical sources.

Before proceeding with our results, we provide a few arguments for the further exploration of chalcogen donors in silicon, as well as for their integration into silicon nanodevices.

5.1.2 Selenium donors in silicon: advantages and applications

Group VI elements are of interest for their scientific and technological applications, particularly in the chemical and metallurgical industries, as well as for the interesting properties they exhibit in compound form (for example, bismuth selenide and telluride have been identified as three-dimensional topological insulators). However, as donors in silicon, they are an interesting physical system since they have two additional electrons per site with

respect to the silicon lattice. There are quite a few reasons why they present an attractive prospect for quantum computation as well as for spintronic applications.

- **Binding Energy** In phosphorus, the P^- two-electron state has a very weak binding energy of only 2 meV, and the other shallow donors have similar values. However the neutral selenium donor (Se^0) possesses two bound electrons in a singlet ground state, and has a very high binding energy of 307 meV[137]. Spin readout methods using spin-to-charge conversion often require that the two-electron state on the donor is well bound, and selenium is an ideal candidate for such applications[5, 143].

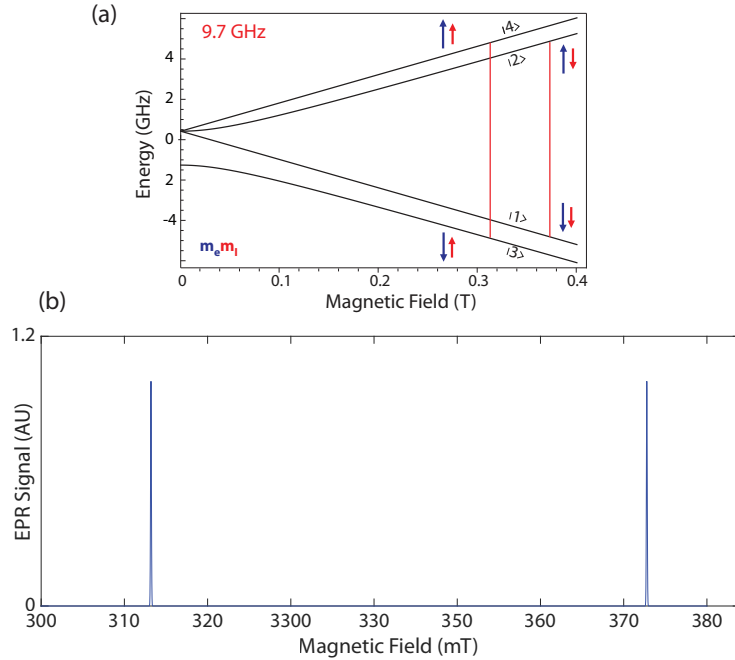


Figure 5.2: Energy levels of ^{77}Se in silicon as a function of magnetic field. Spin resonance allowed transitions shown in (a)[144] and their expected ESR resonance positions for X-band microwave excitation shown in (b). (Calculations performed using the *Easyspin* toolbox for MATLAB.)

- **Ionization Energy** In addition to high binding energies, when compared to the shallow donors, selenium also has a very high ionization energy, as shown in Fig. 5.1 and in Table 5.1. The ionization energy of 593 meV for Se^+ [132] means that it can retain a bound electron even at room temperature, making ESR and spin applications possible at higher temperatures.

- Spin Relaxation** The spin relaxation time T_1 of selenium was predicted (and measured in an earlier work[141], as described in the previous section) to be extremely long due to the large energy separation between the donor ground state and first excited valley state. This energy splitting is an order of magnitude larger in Se^+ than for group V donors in silicon. In ^{31}P , this splitting is small ($\Delta=10.5$ meV)[145], leading to phonon scattering being able to cause relaxation. This causes a rapid drop in T_1 after a certain temperature, where the Raman process switches over to the Orbach process[146][147]. However, since Se has such a large splitting ($\Delta=429$ meV), this effectively removes the Orbach two-phonon spin relaxation mechanism (though its effect on the strength of the Raman process is not fully understood yet), eliminating the sharp drop in T_1 after a certain temperature. Indeed, the T_1 measured in Ref. [141] follows the Raman process for 8 orders of magnitude and a huge range of temperatures. This is particularly useful for reaching higher operating temperatures for qubit or spintronics applications, and is promising for the electron spin coherence time T_2 , since T_1 has been shown to limit T_2 in the shallow donors.

Donor	Group	S	I	E_d (meV)	g	A (MHz)	Reference
^{31}P	V	1/2	1/2	45.6	1.9992	117.53	[131]
^{75}As	V	1/2	3/2	53.8	1.99837	198.35	[148]
^{121}Sb	V	1/2	5/2	42.7	2.0004	186.8	[149]
^{209}Bi	V	1/2	9/2	71.0	2.0003	1475.4	[150]
$^{33}\text{S}^0$	VI	0	3/2	318	2.0054	-	[136]
$^{33}\text{S}^+$	VI	1/2	3/2	612	2.0054	312.4	[136]
$^{77}\text{Se}^0$	VI	0	1/2	307	2.0057	-	[136]
$^{77}\text{Se}^+$	VI	1/2	1/2	589	2.0057	1658.5	[136]
$^{125}\text{Te}^0$	VI	0	1/2	199	2.0023	-	[136]
$^{125}\text{Te}^+$	VI	1/2	1/2	411	2.0023	3491.7	[136]

Table 5.1: Experimental values of ionization energies, g-factors, and hyperfine interactions for shallow and deep donors in silicon.

- Electron Spin Coherence Times** Directly as a result of the increase in the T_1 (which in shallow donors is a limiting factor especially at higher temperatures), the electron spin coherence times in Se^+ were shown to be significantly longer than for group V donors for temperatures above 10 K[141]. This trend should hold for lower temperatures as well, given samples lower in selenium concentration (which was a leading contributor to decoherence in the work referenced).

- Optical Transitions for Spin Readout** One of the limitations for the coherence time of the nuclear spin of a donor (which can be useful for a quantum memory) is the hyperfine interaction. This interaction can be removed, with great enhancement to the nuclear spin coherence time, by optical ionization of the donor electron[151, 152]. In addition, specific hyperfine-split donor-bound exciton transitions can be targeted. In $^{28}\text{Si}:^{77}\text{Se}^+$, under an applied magnetic field, the ground state hyperfine coupling can be spectrally resolved using the $1s(\text{T}_2)\Gamma_7$ absorption transition¹[140]. A tuneable source at $\sim 2.9\ \mu\text{m}$ could therefore be used for fast and efficient hyperpolarization of both electron and nuclear spin. Because the ionisation energies of selenium are much larger than those of the shallow donors, optical sources at the required frequencies ($2\text{--}5\ \mu\text{m}$) are already commercially available, for the optical control and readout of deep donors[144]. As mentioned in the previous section, selenium dopants implanted in a photonic structure have been proposed as an architecture enabling single-spin, single-shot readout at 4K[142].

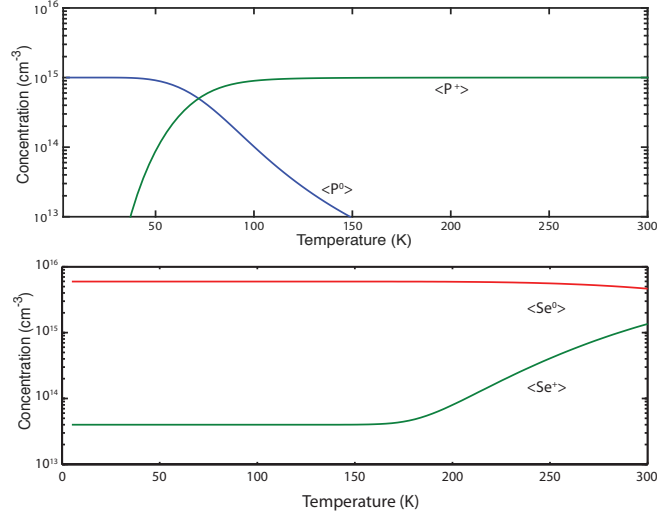


Figure 5.3: Ionization energies and donor species populations with temperature[144]. Top, phosphorus starts ionizing around 45K. Below, selenium concentrations up to room temperature.

¹The $1s(\text{T}_2)$ state is one of the three states into which the six-times degenerate ground state of a donor in silicon splits, due to the tetrahedral symmetry of the crystal (called valley-orbit splitting). This state can further split into the Γ_7 and Γ_8 states due to spin-valley splitting, arising from the electron spin[144].

In addition to these promising characteristics, selenium donors also have some positive features that make them valuable for integration into nanodevices. As discussed in Chapter 1, this thesis is primarily concerned with the development and exploration of a hybrid dopant-dot qubit and/or architecture and selenium is a viable candidate for this avenue of research.

- **Large Hyperfine Constant** The hyperfine constants of shallow and deep donors in silicon are set out in Table 5.1. We immediately notice that selenium has one of the highest hyperfine constants in the table (1.66 GHz), as well as having a nuclear spin-1/2 isotope, ^{77}Se . One of our motivations to explore selenium as a dopant in silicon is for its integration into nanodevices, specifically the hybrid dopant-dot spin qubit in silicon that is the focus of this thesis. Such a qubit, where the dopant is selenium, would have a singlet-triplet mixing dominated by the hyperfine interaction with the nuclear spin localised at the donor site. The electron on the donor would then be detuned by $\delta = AS \cdot \mathbf{I}$, implying, for example, that in the case of phosphorus, with a hyperfine coupling strength of 117 MHz, the $S(1,1)$ - T_0 coherent evolution at a very low exchange coupling could be driven at around 50 MHz[153]. For selenium, with its high hyperfine coupling of 1.66 GHz, the driving frequency could be much higher, in the GHz range (in addition to the relaxation and coherence time improvements mentioned previously).
- **Stark Shift** The large value of Δ for selenium should result in a highly reduced Stark shift[154] when compared to shallow donors. This would be good news for nanodevice integration, since then the electron and nuclear spin coherence of Se^+ would be relatively unaffected by the charge noise that is somewhat unavoidable in gate-controlled nanodevices (despite the large value of the hyperfine coupling).

Lastly, looking at Table 5.1, it is important to observe that there are two other deep, double donors available, selenium's fellow chalcogens sulphur and tellurium. While these may have similar valuable properties to selenium (tellurium in particular has the highest hyperfine constant of all the donors), we choose to focus on selenium. In the case of sulphur, there is no stable nuclear spin-1/2 isotope (and a much lower hyperfine splitting). For tellurium, we find a low solid solubility making it difficult to incorporate into substitutional sites in silicon[155] (additionally, implantation-doped tellurium samples have shown conflicting electronic properties, possibly due to implantation damage and the formation of

complex defects) or into the kind of samples studied in this thesis through ESR, EDMR or other nanodevice techniques. However, further research into these donors may well be fruitful.

5.1.3 Spin-dependent transport mechanisms in silicon

Before discussing our results in their entirety, we look at a brief description of some common spin-dependent transport processes in silicon. EDMR is a versatile technique that can elucidate many spin-dependent processes and spin-to-charge conversion mechanisms in silicon (indeed, sometimes one or more of these may be superimposed or competing). It is worthwhile to note that all these mechanisms have been explored and developed in the context of shallow, single-electron donors in silicon (though some deep levels such as interface traps have been studied). As such, more theoretical work is required to develop a framework for the interpretation of charged, singly-ionised double donors in silicon with very deep energy levels.

We look at broadly two kinds of models; (i) polarization-dependent models such as spin-dependent scattering, tunneling and trapping, where the carrier and paramagnetic defect polarizations influence the signal strength at resonance, and (ii) spin-pair models, which use the concept of local donor-acceptor or donor-defect pairs to mediate spin-dependent recombination. The latter typically gives a higher EDMR signal, and the global carrier polarizations do not have much effect. However, in both these populations, the mechanism involved is similar; under an applied magnetic field B_0 , paramagnetic defects as well as photo-induced carriers will achieve equilibrium populations, resulting a certain value of the steady-state photocurrent. Upon resonant microwave irradiation, the thermal equilibrium population is destroyed as we flip the spin, and the singlet and triplet (or spin up and down) populations are equalised (assuming a saturated transition), giving a different value of the steady state photocurrent and a peak (or dip) in the spectrum. We look at a few EDMR mechanisms in brief below.

Bolometric detection

While not a spin-dependent transport mechanism in the typical sense, bolometric detection, or changes in the conductivity due to resonant heating of the electrons in the sample, must be carefully ruled out as a primary mechanism. For bolometric heating, the sign of the change in resistivity $\Delta\rho$ at resonance is expected to follow the change in resistivity

with temperature $\delta\rho_0/\delta T$ [86, 156]. Since we are operating at cryogenic temperatures, any temperature dependence of the resistivity is caused by changes in the electron temperature, since acoustic phonon scattering should not make a significant difference. In addition, a bolometric effect is expected to be enhanced at higher magnetic fields as the absorbed Zeeman energy on resonance is increased.

Spin dependent trapping

Spin-dependent charge trapping occurs in the presence of paramagnetic traps, for instance shallow donors in silicon at low temperature, which can be in the neutral D^0 state or the doubly occupied D^- state. For phosphorus, with a D^0 ground state having a binding energy of 50meV, and a D^- state with a very small binding energy of $E_b \sim 1 - 2$ meV, there can be no bound triplet states (unless at a very large magnetic field). Therefore, a D^0 state can capture a conduction electron if a donor spin in a triplet configuration with a conduction electron is flipped (say during EDMR), so that they then form a singlet. Trapping of conduction electrons decreases the current at resonance for shallow donors, since there are fewer photocarriers in the conduction band to contribute to the steady-state photocurrent. In the context of deep dopants like selenium, the binding energies are much higher than the shallow donors, and consequently the triplet states should not be forbidden. However, the singlet-triplet capture rates may vary, with a measurable effect on the steady-state current. Currently this process is not well understood for deep, singly-ionised dopants like Se^+ and has not been observed to date, but we expect it to be quite different from the shallow donor case (which have no bound triplet states).

Spin dependent tunneling and hopping

Spin-dependent tunneling is in principle similar to the trapping process, but the electrons tunnel to localized paramagnetic states in a spin-dependent manner[157]. The tunneling probability of a conduction electron to a localised state, or between localised states in the context of spin-dependent hopping between adjacent singly occupied states, is determined by the mutual spin orientation of the two participating spins. In the case of tunneling onto a donor, the polarization of the charge carriers would matter. However for spin-dependent hopping, involving the hopping of conduction electrons from the conduction band tail between donor pairs for instance, the relative spin states of the two dopants would matter, not the conduction electron polarization. The current at resonance is expected to decrease for

tunneling processes, at least in the case of shallow donors, since electrons that can contribute to the photocurrent tunnel to donor states instead. The sign of the change in current can vary for a hopping process; for example, it has been shown to decrease at resonance for interface defects such as P_b centers at high magnetic fields[158].

Spin-dependent scattering

Spin dependent scattering is a process that can occur without direct charge transfer (such as the trapping or tunneling of an electron), since scattering events with paramagnetic centres often have a spin dependence due to the scattering rates depending on the relative spin states. If the singlet or the triplet scattering cross sections are greater, the sample resistivity will change as a result. A detailed calculation in Ref. [159] has shown that the singlet scattering cross section is expected to be greater, leading to an increase in sample resistivity or a resonant decrease in current. However, this contradicts recent experimental results[160][86] and theoretical work exists[161] showing that there can be cases with a higher triplet scattering cross section, which would lead to an increase in photocurrent at resonance. Lastly, since the effect is electron-polarization dependent (for instance, the change in resistivity is proportional to the product of the donor and conduction electron polarizations, for the case of scattering off neutral donors), we expect enhanced signals at higher magnetic fields.

Spin-dependent recombination

Spin dependent recombination was proposed by Kaplan, Solomon and Mott in 1978[162] to explain the discrepancy in EDMR signal amplitudes between the current change of $\sim 10^{-6}$ expected from spin polarization based mechanisms and the current change of $\sim 10^{-2}$ – 10^{-4} detected in many EDMR experiments. Since then, especially for ^{31}P - P_b centre experiments, spin dependent recombination through donor-defect or donor-acceptor pairs has become almost synonymous with EDMR. Here, it is assumed that after the excitation of photocarriers, they recombine through mid-gap states, and singlet pairs recombine much faster than triplet pairs. The pairs do need to be in close proximity to facilitate a weak exchange interaction. Upon resonance, triplet pairs (which are slow to recombine) are converted to singlet pairs, which then recombine very fast, leading to a decrease in the current at resonance (as charge carriers recombine and are depleted). In the KSM picture, global carrier polarizations do not play a role, leading to no polarization (and field) dependence of the EDMR signal.

In the next section, we lay out our experimental findings and draw conclusions to aid the theoretical development of a mechanism explaining spin-dependent transport for the case of the chalcogens in silicon. The potential for a novel EDMR mechanism, due to the deep energy levels of the selenium dopant as well as its additional electron, is also a strong motivation for this work.

5.2 Sample design and measurement Setup

5.2.1 Device design

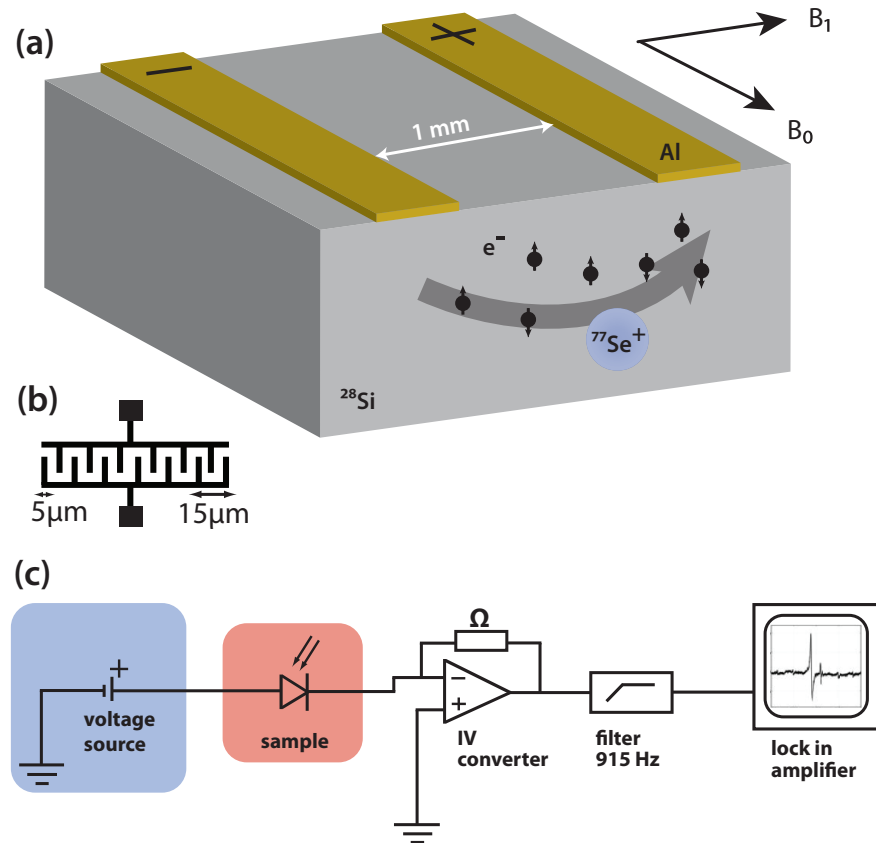


Figure 5.4: Sample and measurement setup. (a) Isotopically purified bulk silicon sample, doped with ^{77}Se and with metal contacts deposited on top. Static (B_0) and microwave-generated (B_1) magnetic field directions also shown. (b) Interdigitated electrodes: dimensions and design. (c) EDMR measurement setup.

Device design for the measurement of spin-dependent transport, and EDMR in general, requires some careful consideration, since we are looking for a small change in current on top of a large background which may itself change gradually with magnetic field (due to the magnetoresistance of doped silicon[163]). Current is typically measured through electrodes deposited on the surface, and EDMR is very sensitive to surface impurities. As such, the sample surface must be kept extremely clean, especially before the contacts are deposited. Other device design constraints involve the shape and size of the contacts. Interdigitated contacts are chosen since they provide an improvement on the EDMR signal intensity by minimising absolute sample resistance and generating stronger local electric fields. The distance between the individual fingers of the contacts also needs to be taken into account since some EDMR mechanisms are length-dependent and will not occur on length scales that are too small. For our contacts, shown in Fig. 5.4(b), we chose an inter-digit distance of $15\mu\text{m}$, based on previous work[86].

Additionally, the bulk silicon sample itself and the dopant concentration needs to be optimised. In our experiment, isotopically purified silicon was used to suppress decoherence arising from the ^{29}Si nuclei (with nuclear spin $1/2$), which occur with 5% natural abundance. In addition, as discussed previously, we are interested in the isotope of selenium with nuclear spin $1/2$, ^{77}Se . We also need an appreciable concentration of Se^+ states, since it possesses a bound spin- $1/2$ electron and is ESR-active (in a previous study on the same sample showing good EPR signal intensities[141], the Se^+ concentration was identified as $\sim 4 \times 10^{13} \text{ cm}^{-3}$, which we should be able to detect through our EDMR experiment). This is achieved by doping with an acceptor, in our case boron.

The selenium doped devices used in this chapter were fabricated on samples prepared by M. Steger at Simon Fraser University[140]. The composition of the isotopically purified starting material was 99.991% ^{28}Si , with residual concentrations of 75 ppm ^{29}Si and 15 ppm ^{30}Si . The boron concentration was $\sim 5 \times 10^{13} \text{ cm}^{-3}$, confirmed by ESR measurements of the selenium spin relaxation T_2 [141]. Selenium was then thermally diffused into the sample by sealing the silicon in an ampoule with the dopant at a temperature of 1000 K. Resistivity measurements were used to determine the concentration of selenium as $\sim 5 \times 10^{15} \text{ cm}^{-3}$. This sample was infused with isotopically enriched selenium, with 97.1% concentration of ^{77}Se , the nuclear spin- $1/2$ isotope.

A schematic of the device used in this experiment is shown in Fig. 5.4(a). Interdigitated contacts (shown in Fig. 5.4(b); each finger is $5\mu\text{m}$ wide, with a spacing of $15\mu\text{m}$ between adjacent fingers, covering a 1 mm by 2 mm area on the sample surface) were fabricated by a

photolithographic lift-off procedure on the ^{28}Si substrate, detailed in Appendix A. Prior to this, the sample was put through a 10 minute deep solvent clean and a piranha etch followed by a plasma ash step to remove all metal, photoresist and organic residue, followed by a 1 minute hydrofluoric acid wet treatment to remove native oxide. After photolithographic pattern development, 200 nm aluminium was deposited for the contacts through thermal evaporation. In EDMR measurements, a “dark current”, or a measurable value of current through the sample while it is not illuminated, is typically associated with surface impurities. In our sample, after the above treatment, the dark current went from a value close to 10% of the off-resonance photocurrent to none (or rather, a value below the noise baseline of the apparatus, $<0.01\%$ of the photocurrent). In addition, an array of lines in the EDMR spectrum typically associated with surface defects, complexes and/or contamination also disappeared completely (see Appendix A), leaving us with a strong selenium signal and a broad resonance centred around $g = 2$.

5.2.2 Measurement setup

Spin-dependent transport measurements require sensitive detection of current and typically require lock-in detection techniques. EDMR was carried out by continuous wave measurements (cw-EDMR) using a Bruker Elexsys spectrometer at X-band (9.7 GHz) around a magnetic field of 0.34 T. The sample was mounted on a PCB and wirebonded with $25\mu\text{m}$ aluminium wire on to each of the two interdigitated contacts. The PCB was then fitted into an EDMR probe fitting into the Bruker spectrometer and lowered to be centered at the static magnetic field, inside a cylindrical microwave resonator with a quality factor tunable up to 20000 (tuned using a screw controlling the matching of the cavity and the amount of microwaves entering it, via the size of the coupling hole) and an inner diameter of 5 mm. The entire resonator was mounted within a liquid helium flow cryostat capable of temperatures down to 4.2 K. The measurement setup is shown in Fig. 5.4(c). The photocurrent required for EDMR was induced by white light generated by a xenon discharge lamp coupled in through a free-space optical window. The sample was biased with a constant voltage source while the current from the sample was passed through an I-V converter and amplifier and a 915 Hz high-pass filter. Finally, using a lock-in amplifier, a component of the Bruker system, the signal from the sample was detected and demodulated. The magnetic field is modulated by the lock-in amplifier modulation frequency, usually in the range 10-100 kHz.

5.3 EDMR spectrum

Different donor species give rise to characteristic EDMR spectra, given by the particular hyperfine coupling of the donor electron to the nuclear spin. In this section, we present the continuous-wave EDMR spectra and lineshape of the $^{28}\text{Si}:^{77}\text{Se}$ device, in the form of the relative change in the current with magnetic field, $\delta(\Delta I/I_0)/\delta B$. The data were taken at 5 K, at a microwave power high enough to saturate the transition (see next section). The EDMR spectrum is presented in Fig. 5.5.

We attribute the broad central resonance signal to either conduction electrons or a P_b center interface defect, based on the g-factor of the line ($\sim g = 2$); it is difficult to narrow it down further without a precise idea of the mechanism due to the breadth of the peak and their very similar g-factors. The other two low and high field resonances, separated by the hyperfine coupling of 59.1 mT, correspond to the $m_I = \pm 1/2$ ^{77}Se transitions. While previous EDMR work does not exist for the chalcogens in silicon, the values obtained for the g-factor (g) and the hyperfine constant (A) of selenium agree well with results obtained through EPR[136][141]. We notice that the only difference between the on- and off-resonance photocurrent is the fact that at resonance, we saturate a selenium hyperfine transition with microwaves (such that spin up and down selenium populations are equal), while off-resonance there is a surplus of a certain spin species. Therefore, the observation of these resonances in the spectrum indicates spin-dependent transport for selenium donors in silicon (to our knowledge the first such measurement for the chalcogens).

A few things can be noted about the spectrum in Fig. 5.5:

- The magnitude of the selenium signals are high, of the order of a 10^{-4} change in current at resonance. Such high signal amplitudes are typically seen (in shallow donors) through mechanisms such as spin-dependent recombination involving dopants paired with P_b centers[86].
- The central resonance is very broad (~ 5 mT), compared to the EDMR resonance from the selenium (~ 400 μT); which is itself far broader than corresponding EPR measurements from the same isotopically purified sample (~ 5 μT for hyperfine-split selenium resonances)[141], indicating a different decoherence mechanism or a different subset of donors.
- The phase of the broad resonance centred around $g = 2$ is opposite to that of each of the selenium signals, an effect consistent over a wide range of temperatures, mi-

crowave powers and over low and high modulation frequencies. This implies a correspondingly opposite change in current at resonance; i.e. if one of them increases at resonance, the other decreases. (This is because the lock-in detection phase is related to the sign of the change in current at resonance. While the absolute phase is hard to measure, the two derivative peaks in the spectrum show opposite phase under all measurement conditions, indicating opposite signs of the change in current.)

We will discuss these observations in a later section.

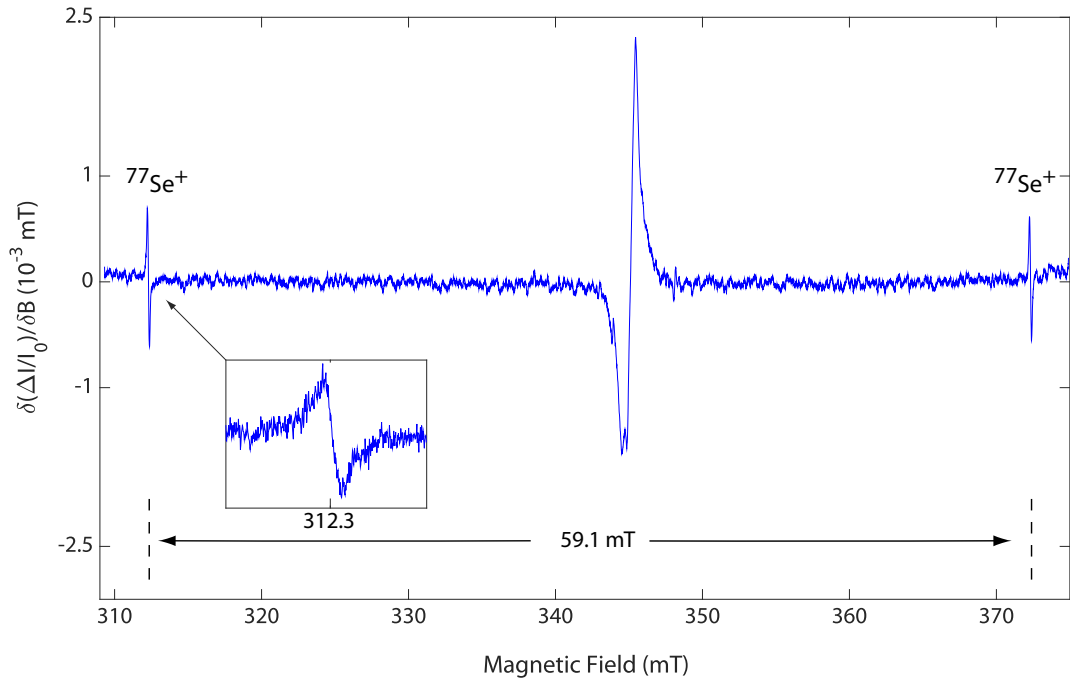


Figure 5.5: EDMR spectrum of 28-Si: ^{77}Se device measured at a temperature of 5K and at saturated microwave power. The ^{77}Se donor hyperfine-split resonances are separated by 59.1 mT, as indicated.

5.4 Temperature and power dependence of the EDMR signal

5.4.1 Microwave power

We can make a meaningful comparison of our EDMR signal intensities to literature only when we have calibrated them correctly. For this reason, the polarizations due to absorp-

tion at resonance (p) have to be equal, and this is most easily achieved by measurements at full saturation, so that $p \rightarrow 0$. In this regime, the microwave power is sufficiently high such that the induced spin state transitions occur on a much faster timescale than the natural relaxation rates. Then the spin up and spin down populations become equal; this is called the saturated state. The EDMR spectra and other measurements presented in this chapter are taken at saturation. We achieve this by increasing the microwave power until the EDMR signal intensity remains constant (Fig. 5.6(a)), indicating that the spin up and down populations are equal.

A clear difference between conventional EPR and EDMR is the dependence of the signal intensity on the microwave power[86][164]. A conventional EPR spectrum will have a maximum signal intensity at a relatively low microwave power, as we see in the selenium EPR measurement in Fig. 5.6(b), followed by the signal dropping off again as the microwave power (P_{mw}) is further increased. This behaviour follows the law

$$S_{\text{EPR}} \propto (1 + (\frac{1}{4})\gamma^2 B_1^2 T_1 T_2)^{-3/2} (P_{\text{mw}})^{1/2} \quad (5.1)$$

while at high microwave powers, an inverse relation $S_{\text{EPR}} \propto (P_{\text{mw}})^{-1}$ is observed. In contrast, for the EDMR power dependence, we have a high and constant signal reached at saturation, as per the equation below:

$$S_{\text{EDMR}} = C \frac{\beta P_{\text{mw}}}{1 + \beta P_{\text{mw}}} \quad (5.2)$$

where β and C are parameters, with C the saturation value at high P_{mw} . These predictions are borne out in our experiment (the blue line in Fig. 5.6(a) is a fit to Eq. 5.2, while the one in Fig. 5.6(b) is a fit to Eq. 5.1), and throughout, we report EDMR signal intensities that are maximised at saturation.

5.4.2 Linewidth and coherence time

EDMR lineshapes contain information about the spin relaxation times of the paramagnetic species involved[83]. With inhomogeneous broadening, the cw-EPR linewidth exhibits a Gaussian lineshape and provides information about T_2^* only, while for intrinsic homogeneous line broadening, Lorentzian functions fit well and the intrinsic T_2 can be extracted. The principle is similar for EDMR lineshapes, and a peak to peak linewidth can be calculated using the Bloch equations in the rotating frame[83], which give us the polarization in

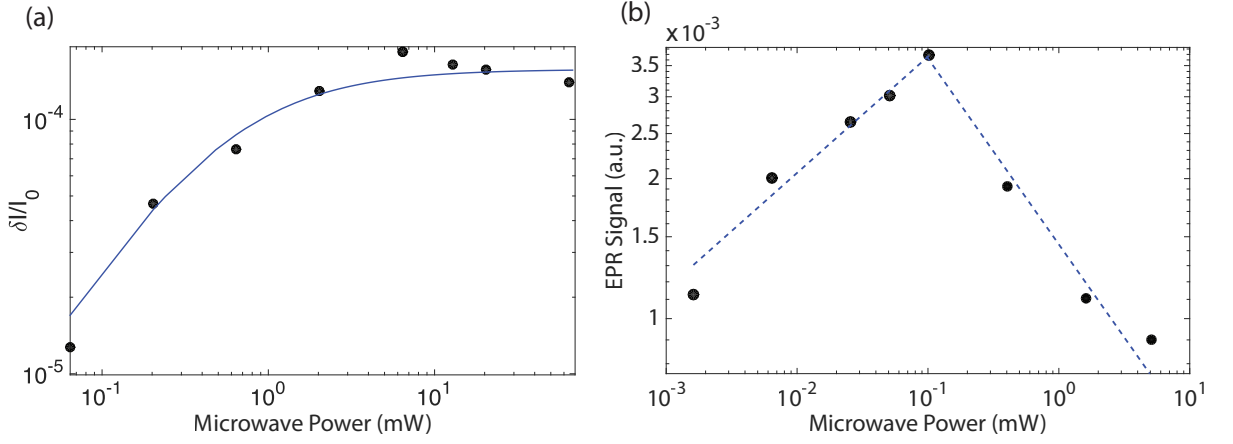


Figure 5.6: Power dependence of the EDMR and ESR resonances. (a) The power dependence of the EDMR signal with a fit (blue line) to Eq. 5.2. (b) The power dependence of the EPR signal; the blue dashed line is a fit to Eq. 5.1 up to the saturation point (at a microwave power of 0.1 mW), with the higher microwave power points fit to the inverse relation $S_{\text{EPR}} \propto (P_{\text{mw}})^{-1}$ as described in the main text.

terms of the magnetization. Combined with the fact that the EDMR signal is a change in current of the form[86]:

$$\frac{\Delta I}{I_0} = \frac{cp_c}{p_0} \left[\left(\frac{1 + \gamma^2 T_2^2 (B_0 - B)^2}{1 + \gamma^2 T_2^2 (B_0 - B)^2 + \gamma^2 B_1^2 T_1 T_2} \right)^2 - 1 \right] \quad (5.3)$$

where c is a constant representing the polarization-dependence of the carrier resistivity, and p_c is the thermal equilibrium polarization of the carriers, we can take the derivative with respect to B to obtain the measured EDMR lineshape. The peak-to-peak lineshape then becomes:

$$\Delta B_{\text{pp}} = \frac{1}{3} \frac{1}{\gamma T_2} [-12 + 18\gamma^2 B_1^2 T_1 T_2 + 6\sqrt{16 + (3\gamma^2 B_1^2 T_1 T_2)^2}]^{\frac{1}{2}} \quad (5.4)$$

In the limit of zero microwave power, when $B_1 \rightarrow 0$, this gives us:

$$\Delta B_{\text{pp}} = \sqrt{\frac{4}{3}} \frac{1}{\gamma T_2} \quad (5.5)$$

This equation for a homogeneously broadened line is derived within the confines of Lepine's original polarization model[133] making it a crude measure of T_2 for resonances arising from more complex mechanisms (in such a case, pulsed-EDMR for a direct mea-

surement of the coherence time is conclusive). However, it is a useful order-of-magnitude estimate of the coherence time of the spins involved.

To satisfy the microwave power conditions such that Eq. 5.5 is valid, we must measure our EDMR signal at a low enough microwave power that the linewidth is not broadened by the microwaves. For this purpose we plot the peak to peak linewidths of the selenium signal as a function of microwave power in Fig. 5.7(a), at the lowest temperature measured, 4.3K. We measure at the low power of 2 mW, indicated in the figure. The resonance peak at this low microwave power has a reduced signal intensity, and is shown in Fig. 5.7(b). The peak is better fit with a Lorentzian lineshape, indicating homogeneous broadening, which is a measure of T_2 . Using our Lorentzian fitted linewidth in Eq. 5.5, we extract a coherence time of ≈ 170 ns for the ^{77}Se donors, similar to coherence times extracted for ^{31}P donors in MOSFETs through EDMR (~ 100 ns)[86]. This is a reduction of over five orders of magnitude from the bulk measurements[141]. In MOSFETs this reduction was explained by scattering with conduction electrons, exacerbated by strong gate-generated electric fields in the \hat{z} -direction, leading to fluctuating Rashba fields which contribute to T_2 . In our device, it is not fully clear what lies behind this short coherence time; some possible origins could be interface effects (if we are looking at a subset of donors close to the interface), donor-acceptor proximity, or donor-donor pair formation. We will discuss these in a later section. Further studies performed through pulsed EDMR could provide direct measurements of the coherence time through a spin echo sequence. In previous measurements using a Carr-Purcell refocusing sequence, a coherence time of $2\ \mu\text{s}$ was observed for ^{31}P donors in the bulk[165].

5.4.3 Temperature and modulation frequency

Fig. 5.8(a) shows the temperature dependence of the saturated selenium EDMR signal intensity from the $^{28}\text{Si}^{77}\text{Se}$ device. The signal intensity decreases with increasing temperature, more rapidly than for the central resonance, which is shown in Fig. 5.8(b). The solid lines in Fig. 5.8(a,b) are fits to spin polarization models; for spin-dependent trapping and a few other spin-polarization dependent mechanisms, it is expected that the temperature dependence of the selenium EDMR signal follows that of the spin polarization[86]. In a spin polarization model of the kind originally proposed by Lepine[133], under an applied magnetic field B the paramagnetic defects and photocarriers will achieve their respective thermal equilibrium spin polarizations p_d and p_c , and the change in photocurrent at resonance is

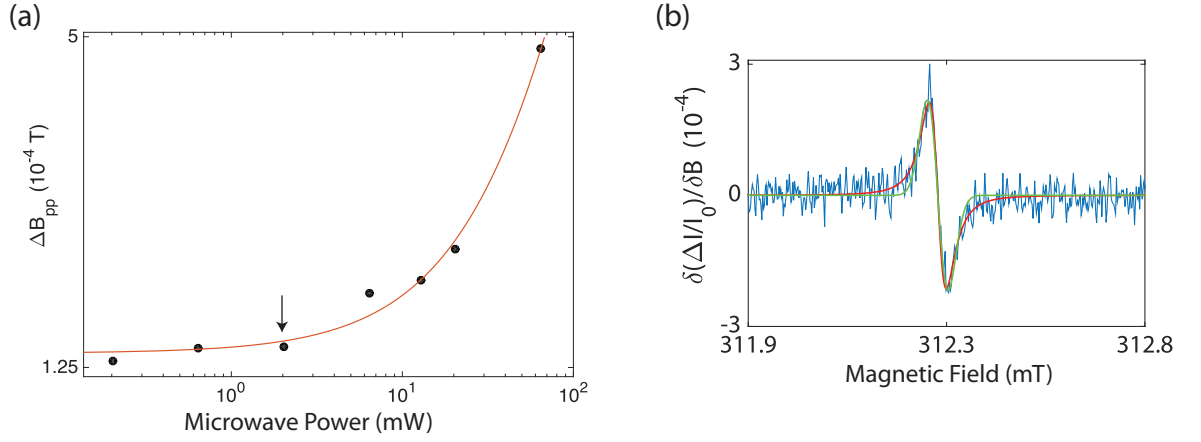


Figure 5.7: (a) Microwave power dependence of the peak to peak linewidth of the 28-Si:⁷⁷Se device measured at 5K. (b) EDMR spectrum showing peak-to-peak linewidth of the selenium resonance line at the low microwave power indicated in (a). The red line is a derivative Lorentzian fit, while the green line is a derivative Gaussian fit.

then due to the destruction of this thermal equilibrium polarization, so that $\Delta I/I_0 \approx p_d p_c$. For the donor, the thermal equilibrium spin polarization is given by

$$p_d = \tanh\left(\frac{g\mu_B B}{k_B T}\right) \quad (5.6)$$

and therefore an expression of the form, with a as a fitting parameter:

$$\frac{\Delta I}{I_0} = a \tanh\left(\frac{g\mu_B B}{k_B T}\right) \quad (5.7)$$

is used to fit the blue solid line, since at X-band, $B \approx 0.35$ T and g , μ_B and k_B are known. The red solid line is a fit to a similar form, but to the square of the spin polarization (as in Lepine's expression) in the above fit equation, as a crude model that takes into account the spin polarization of the conduction electrons as well[166]. The fit to either of these models is not ideal, but we note that the temperature dependence of the EDMR signal can be much more complicated than a simple spin polarization interpretation. The T_1 lifetimes of the donor electron as well as the conduction electrons can play a significant role and can scale differently with temperature. In addition, in the context of a spin-pair type model, the fraction of singlets and triplets in the system can change depending on the differing T_1 lifetimes, and the generation and recombination rates at different temperatures. In Sec-

tion 5.6.1, we present a spin-dependent trapping mechanism that relies on spin-dependent recapture rates; these may also vary with a particular dependence on temperature.

Additionally, we note that the temperature dependence of the central line deviates strongly from the spin polarization curves and decreases much more slowly than that of the selenium resonance, indicating a difference in mechanism and origin.

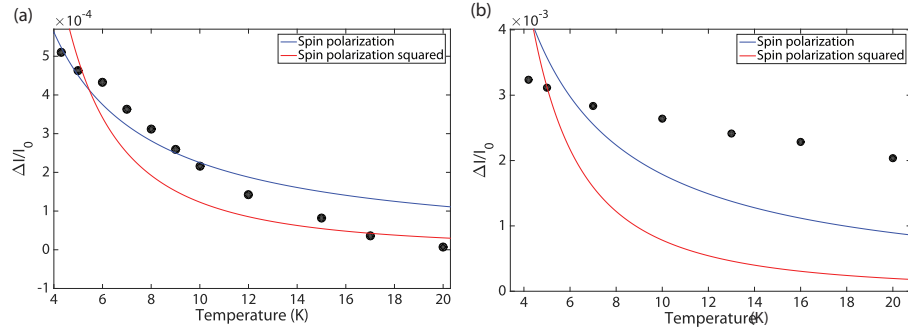


Figure 5.8: Temperature dependence of the EDMR signal for (a) the selenium and (b) the central resonance peaks. The solid lines in (a) are fits to Eq. 5.6 (blue) and its squared form (red).

We note that the temperature dependence of the EDMR signal can be much more complicated than a simple spin polarization interpretation. The T_1 lifetimes of the donor electron as well as the conduction electrons can play a significant role and can scale differently with temperature. In addition, in the context of a spin-pair type model, the fraction of singlets and triplets in the system can change depending on the differing T_1 lifetimes, and the generation and recombination rates at different temperatures.

Lastly, cw-EDMR is typically carried out using a lock-in detection technique called field modulation. Here the magnetic field is modulated at a certain frequency f_{mod} , and the resulting signal demodulated before detection. The modulation frequency therefore needs to be chosen to be much slower than any transient effects or spin dynamics from the device. If f_{mod} is slower than the T_1 and T_2 times of the excited electron spin, we are compliant with the slow adiabatic passage condition[167]. On the other hand, a higher frequency can correspond to a decrease of $1/f$ noise, while if it is too high, the RC delay of the probe and device can cut off the signal; making some optimization necessary. The Bruker Elexsys allows a range of frequencies from 0.5–100 kHz. For the experiments in this Chapter, a modulation frequency of 20 kHz was used after signal optimization. If the modulation frequency is too fast compared to the system dynamics, modulation-related artefacts can be introduced. To rule out such an artefact being responsible for the opposite

phase of the selenium and central resonances, we perform a modulation frequency study. Fig. 5.9 shows the selenium and central resonances taken at modulation frequencies of 5 kHz, 20 kHz and 50 kHz, with no change in the relative phase between the two. In the frequency range allowed by the Elexsys, we did not observe any change in this relative phase, and this, combined with the linewidth-extracted T_2 of 170 ns ($\ll 1/f_{\text{mod}}$) in the previous section, leads us to conclude that our measurements are in the low-frequency limit and consequently, f_{mod} should not affect the signal.

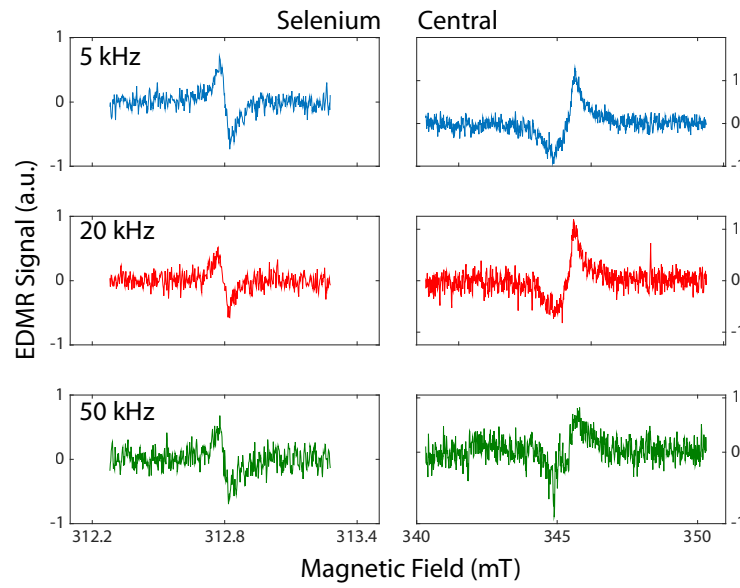


Figure 5.9: Temperature dependence of the EDMR signal for (a) the selenium and (b) the central resonance peaks.

5.5 Effects of laser and broad-wavelength illumination

Apart from the usual control parameters of temperature, microwave and field modulation, one way to study EDMR and identify its mechanism is to explore different illumination sources to generate the photocurrent in the silicon. Previous studies[168] have explored the variation in EDMR signals with white halogen light and lasers of different wavelengths; these variations were attributed to the fact that the optical penetration depth into silicon is strongly wavelength dependent at cryogenic temperatures.

5.5.1 Halogen light and laser illumination

In our experiment, Fig. 5.10 shows the EDMR spectrum under halogen lamp light as well as 1047 nm above-bandgap laser light. There are two things we note here.

The first is the increase in the signal intensity from the central defect resonance as we go from halogen to laser light. An increase in signal intensity in going from halogen to laser light was also observed in Ref. [168]. In addition, they observed that the magnitude of the donor resonance signal decreased, while that of the central resonance increased. In our case, the donor resonance signal disappears as we go from halogen light to laser light, and our central resonance at $g = 2$ increases in magnitude. As hypothesised in the reference, this could indicate that additional defect-defect interactions are able to come in to play when the selenium donors are not contributing, i.e. that the mechanisms are competing. However in general it is hard to make a quantitative prediction from cw-EDMR signal strengths with different photocurrent sources, in part because of the many rate constants involved such as different pair generation, recombination/tunneling rates, and T_1 lifetimes.

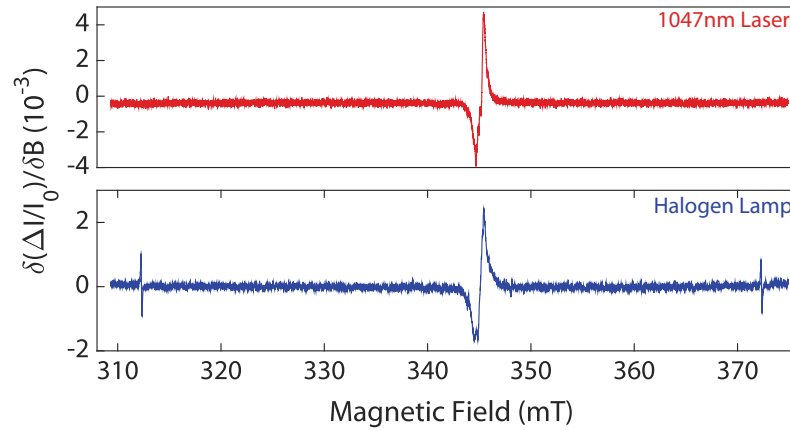


Figure 5.10: Effect of white light and laser illumination on the EDMR spectrum. Top, with 1047 nm laser light, selenium resonances are no longer visible. Bottom, EDMR spectrum observed with white light from a halogen lamp.

The second feature of Fig. 5.10 is the complete disappearance of the selenium resonances, an effect consistent at different laser powers as well as different microwave powers, modulation frequencies, and temperatures. One possible reason could be that this is because the selenium dopants we see are ones close enough to an acceptor such that they are able to donate an electron to the acceptor (boron) in order to be in the ESR-active Se^+ state. As shown in Ref. [141], the donor-acceptor (D-A) recombination dynamics show that

immediately after a laser pulse is applied to the sample, the Se^+ concentration (as determined from T_1 measurements) becomes zero. This is because, as shown in Fig. 5.12, the generation of electron hole pairs in the conduction and valence bands brings both the donor and the acceptor into the neutral state. This effect could penetrate deeper into the bulk for the laser, while for the lamp there would still be donor-acceptor pairs left to contribute to the signal. However further research into the timescales involved is necessary.

Lastly, the fact that the central line resonance is still present when the selenium high and low field lines are not under different illumination sources confirms our previous observation that the selenium and central resonances are unrelated and arise from different mechanisms altogether.

5.5.2 Current at resonance

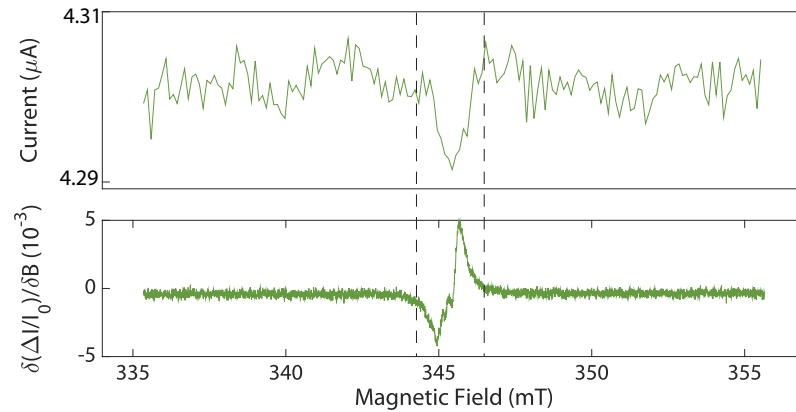


Figure 5.11: Change in photocurrent as we sweep through the central resonance line under 1047 nm laser light. Top, current measured through an amplifier and voltmeter as magnetic field is swept across the transition seen on the bottom.

Lastly, we repeat the experiment that gives us the maximum EDMR signal intensity. This occurs at the central resonance under laser illumination, and we monitor the steady-state current through an IV converter, amplifier, and voltmeter, as this transition is swept. Fig. 5.11 shows that the current decreases at resonance for the central defect line. This implies that when we sweep across the selenium transitions (which are of opposite phase to the central line), the current increases at resonance. It is worth emphasizing that this is a

steady-state current, and should be interpreted as such; for a time-resolved picture, pulsed EDMR and careful monitoring of the current transients after the pulse should be used.

In the next section, we lay out our experimental findings and draw conclusions to aid the theoretical development of a mechanism explaining the spin-dependent transport of the double donors in silicon.

5.6 Analysis

In this section we first summarize our experimental findings. First of all, we report the first observation, to our knowledge, of spin-dependent transport for a deep donor in silicon. We measure this effect through EDMR and find a few interesting features in the spectra and in its dependence on various parameters.

First of all, the EDMR spectrum presented in Fig. 5.5 has a high signal amplitude ($\Delta I/I \approx 10^{-4}$) for the selenium hyperfine-split resonance peaks, and an even higher one ($\Delta I/I \approx 10^{-3}$) for the central resonance at $g = 2$. The width of the central peak is very broad (~ 5 mT), and that of the selenium peaks is two orders of magnitude broader than the ESR linewidth measured from the same sample. By fitting a Lorentzian to the linewidth, we find an approximate value of $T_2 \approx 170$ ns for the spin coherence time of the donors involved in the spin-dependent transport process (five orders of magnitude lower than the bulk ESR value). Finally, the spectrum shows that the phase (and therefore the current change at resonance) of the central line is consistently opposite to that of the selenium transitions.

The power dependence of the EDMR signal is consistent with previous measurements of EDMR from shallow donors, and we are able to saturate the EDMR transition by applying enough microwave power (all results are reported in this regime). The contrast with the behaviour of the EPR signal is also consistent with literature.

The temperature dependence of the EDMR signal (for the selenium and the central resonance) shows a decrease with increasing temperature, and the selenium resonance shows a far stronger fit to spin polarization models than the central resonance.

We also perform the experiment with above band gap laser illumination (1047 nm) in addition to the broadband white-light halogen lamp typically used in cw-EDMR. This experiment produces the interesting result that the central line is undiminished in intensity (indeed, the intensity increases) while the selenium resonances completely disappear, over a wide range of laser powers and even with all other factors, including the photocurrent, held constant.

Lastly, we observe that the photocurrent decreases at resonance for the central defect line, which implies that the photocurrent increases at resonance when we sweep across the selenium transitions (which are of opposite phase to the central line).

Selenium resonances and the central resonance

As a result of the experimental findings above, we conclude that the central defect resonance and the selenium resonances are not linked to each other nor part of the same spin-dependent process. We conclude this from the following facts: (a) the phases of the two signals are opposite for all experimental parameters, and (b) the central resonance occurs through a process which is roughly unchanged, except somewhat in intensity, by moving from a broadband white light source to above band gap illumination using a 1047 nm laser while the selenium resonances disappear (showing both that a different mechanism is at play and that the central line is produced without being dependent on the selenium spin state). P_b -only mechanisms such as spin dependent hopping have been proposed in situations where spin dependent recombination is not dominant (at high magnetic fields, for instance)[158] or where a suitable donor-defect recombination mechanism may not exist. We are concerned here with the mechanism of the spin dependent signal observed from the deep donor, and we discuss this in the next section.

5.6.1 Mechanisms

The above experimental results are typically of great value in determining the spin-dependent transport mechanism operating for shallow donors in silicon. However, in the case of deep, double donors in silicon, we lack a rigorous theoretical framework for the evaluation of our results, and we also lack previous results in literature to compare against. We may perhaps only be able to eliminate some mechanisms through comparison with EDMR features seen when shallow donors are involved, and hazard a guess at the operating mechanism. With these caveats, we go through the mechanisms presented in Section 5.1.3 below.

Bolometric heating

We are able to rule out bolometric heating for a few reasons. First, sample heating due to the resonant ESR absorption of energy is considered to be negligible for phosphorus

concentrations in the $\sim 10^{15} \text{ cm}^{-3}$ range[169]. In our sample, the total doping concentration of selenium is $\sim 5 \times 10^{15} \text{ cm}^{-3}$ and the concentration of ESR-active single-ionised Se^+ species is expected to be the same as the acceptor concentration, which is $\sim 5 \times 10^{13} \text{ cm}^{-3}$. In addition, as discussed in the previous section, the sign of the change in resistivity $\Delta\rho$ at resonance is expected to follow the change in resistivity with temperature $\delta\rho_0/\delta T$ for bolometric heating. However, in our samples while the resistivity decreases at resonance ($\Delta\rho/\rho_0 < 0$), the resistivity increases with increasing temperature ($\delta\rho_0/\delta T > 0$) in the narrow range of temperatures 5–20 K. A bolometric effect is also expected to be enhanced at higher magnetic fields as the absorbed Zeeman energy on resonance is increased; we do not see a difference in the selenium high and low field lines, which differ by 59.1 mT. Lastly, for a bolometric effect, the illumination source used to generate photocarriers (if photocurrents and other parameters are kept constant) should not influence the EDMR signal, while we see a strong difference between laser and broadband light. However, we cannot rule out a bolometric mechanism for the central resonance.

Spin dependent scattering

As discussed in the previous section, scattering of conduction electrons from a donor spin can have a spin dependence from the different singlet triplet scattering cross sections. In addition, despite theoretical calculations to the contrary, resistivity decreases at resonance (i.e. an increase in current) have been reported, matching our experimental result. However, the difference in scattering cross sections between singlet and triplet 2DEG-donor spin pairs are typically quite small and EDMR signal strengths in the 10^{-6} range are expected, whereas ours are about two orders of magnitude higher. Also, a conduction electron signal of the same phase as the selenium signal would conventionally be expected from a scattering mechanism, which we do not see.

Spin dependent recombination

Spin dependent recombination (SDR) is expected to yield EDMR signal intensities in the high range ($\Delta I/I \approx 10^{-2} - 10^{-4}$) that we measure, due to highly different recombination rates for the singlet and triplet configurations of the donor-defect or donor-acceptor pairs. However, it is associated strongly with photocurrent quenching, which contradicts our current findings. However, there are studies involving less-studied defect pairs such as the oxygen vacancy center (OV^-) in conjunction with phosphorus, which have observed a cur-

rent enhancement at resonance[170]. This is explained by the fact that the OV^- could either emit an electron into the conduction band or capture a hole from the valence band, and the former process would lead to an enhancement of the current. The monitoring of dark current transients at resonance (through pulsed EDMR, for instance) could be a way to explore this mechanism for our results, as in the referenced study. However, for a spin

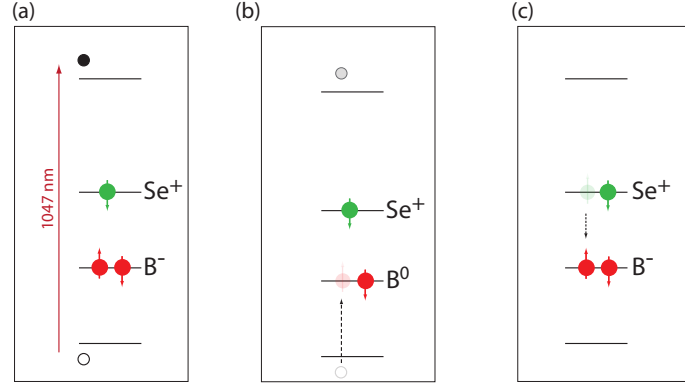


Figure 5.12: Spin dependent Donor-Acceptor Recombination of selenium donors with boron acceptors. (a) Above-bandgap illumination generates photocarriers. (b) Boron accepts a hole from the valence band to form B^0 . (c) Selenium can now accept an electron from the conduction band, which will subsequently return to the acceptor, such that the donor returns to the Se^+ state. Figure adapted from Ref. [144].

dependent recombination process, we would expect to see a resonance of the same phase arising from the defect center spin as well, such as a P_b center. On the other hand for the case of EDMR arising from donor-acceptor recombination, we do have a spin-pair partner for the selenium, which is the compensating acceptor boron. We know that the Se^+ species, which are ESR active, are able to be in the singly ionised state by virtue of being spatially close to a boron acceptor, to which they are able to donate an electron. Therefore, this is by default a spin pair in proximity. Boron is also an acceptor like the OV^- center, and can emit an electron into the conduction band or capture a hole from the valence band. Lastly, boron is very difficult to observe in ESR due to its extremely broad resonance, and extant ESR studies have measured boron only through careful zero-strain processing of samples[164]. Boron resonances have not been observed through EDMR. In our samples, the combination of a fabrication process involving the deposition of strain-inducing interdigitated metal electrodes, as well as PCB mounting using GE varnish, most probably precludes the observation of boron even through ESR. As expected, in our experiment a boron resonance was not observed across almost the entire magnetic field range of the spectrometer (0.8 T), but

this can by no means rule out boron as the other component of the spin pair. The decrease in the selenium EDMR signal strength as we increase the temperature could be caused by the fact that boron typically has a short T_1 which decreases rapidly with temperature.

Lastly, for a typical spin-dependent recombination mechanism as described in literature, there is a pair formation between the donor and the acceptor where the photogenerated electrons and holes are captured by the defect pairs (i.e. an electron by the selenium and a hole by the boron). The pair can then recombine, with triplet recombination much slower than singlet, leading to a spin permutation asymmetry observable through EDMR. Therefore, it is clear that a critical spin-selective process that differentiates between the singlet and triplet states of the pair is required for SDR. The donor and acceptor species in our case are shown in Fig. 5.12. Here, if the Se^+ donor state captures an electron, it leads to a neutral Se^0 state such that there is no spin selectivity between the triplet and the singlet. However, in part (b) of the figure we see that if the boron first accepts a hole from the valence band, we now have a spin pair composed of the Se^+ and B^0 states, and there is now a spin-selective pathway, which leads to faster recombination in the case of a singlet being formed.

Spin dependent hopping

We consider here another possible mechanism, that of spin-dependent hopping. This process is not fully understood in a general sense since it requires a detailed analysis of the particular spin system under observation, to formulate a theory and predict experimental behaviour. Spin dependent hopping requires two singly occupied electron sites in close proximity, for example a pair of singly ionised Se^+ close to each other. Different processes can occur between the two sites, of which one or more has to be spin-dependent. The model is therefore similar to a spin pair model like spin dependent recombination, except that in this case a spin dependent dissociation (and not recombination) destroys the pair, influencing transport rates and not the charge carrier density. Charge carriers do not annihilate during transport, in contrast to recombination; and so spin-dependent processes have to be described in terms of mobility changes. There are models of spin dependent hopping as well as experiments describing a current increase at resonance, however the transport, dynamics and hopping rate all depend on the specific pair.

For our experiment, this process is intriguing since we only see a selenium signal without a corresponding pair (and with a signal intensity higher than typical spin-dependent scattering processes), and a hopping model is possible with two selenium donors in prox-

imity. In addition, spin dependent hopping can lead to current increases at resonance, though a specific prediction for the case of a pair of deep double donors does not exist. The hopping model might also explain the broad resonance and reduced coherence times of the EDMR species as compared to ESR data, since this is expected for paired donors close to each other. Lastly, similar to SDR, this model also does not depend on a large conduction electron polarization.

Indisputable experimental evidence of this kind of spin-dependent transport process would be EDMR signals obtained under dark conditions. In the absence of excess charge carriers, recombination does not exist and can be ruled out. A pulsed EDMR experiment where the dark current after the pulse is monitored would be useful.

Spin dependent trapping

We now consider a final possible EDMR mechanism. We mentioned earlier in this Chapter that spin dependent trapping in shallow donors occurs due to the fact that bound triplet states do not exist, such that a conduction electron can be trapped into a singlet configuration but not a triplet. But for deep donors like selenium in silicon, unlike the P^- case for a shallow donor like phosphorus, the two-electron charge state Se^0 is indeed bound, and quite deeply (~ 307 meV), as shown in Fig. 5.1. In our case, the new mechanism we propose relies on the difference in the capture rates of the singlet and triplet states, formed by a conduction electron and the electron on the selenium atom in its Se^+ state.

Off-resonance, the spin ensemble can have a different singlet/triplet content under constant illumination, due to differing recombination probabilities and T_1 lifetimes. At resonance with the transition saturated with high microwave power, however, a random distribution of singlets and triplets is created. Depending on the electron capture rates for the singlet and triplet configurations, then, there can be an appreciable difference in the steady-state current at resonance. If a certain species traps more conduction electrons, then due to the reduction in its population at resonance (where the populations are equalised), there will be more conduction electrons available and hence a resonant increase in the photocurrent, as we observe.

We present a simple rate-equation model below, where the photocurrent is determined by the density of photoexcited electrons, $I \propto n(t)$. In this simplified picture of a trapping mechanism, there is a constant photocarrier generation rate k_g due to the halogen illumina-

tion, and a constant recapture rate dependent on the dopant population, given by $k_c n_d(t)$

$$\frac{dn}{dt} = k_g - k_c n_d(t) \quad (5.8)$$

with k_c the capture rate and n_d the dopant population. The steady-state conduction electron population (and a proportional photocurrent) is given by

$$n_{ss} = \frac{k_g}{k_c} \quad (5.9)$$

We now assume that the capture rate is spin-dependent, so that we have

$$\frac{dn}{dt} = k_g - k_s p_s - k_t p_t \quad (5.10)$$

where k_s and k_t are the capture rates into the singlet and triplet configurations respectively, while p_s and p_t are the probabilities of projection into the singlet and triplet states for the selenium donor. For microwaves at resonance (with the transition saturated), $p_s = p_t = 1/2$. This will then give us the steady state electron number

$$n_{ss} = \frac{k_g}{k_s p_s + k_t p_t} \quad (5.11)$$

We are interested in the number of electrons in the steady states both on- and off-resonance, as this is proportional to the difference in the currents we measure. Defining the polarization of the carriers as the fractional difference between the spin-up and spin-down populations, we have:

$$p = \frac{n_{\uparrow} - n_{\downarrow}}{n_{\uparrow} + n_{\downarrow}}, \quad (5.12)$$

both for the donor and the conduction electrons. For the triplet state $p_t = p_{\uparrow\uparrow} + p_{\downarrow\downarrow}$ we have

$$p_t = \frac{(1 + p_{Se})(1 + p_{ce}) + (1 - p_{Se})(1 - p_{ce})}{4} = \frac{1 + p_{Se}p_{ce}}{2} \quad (5.13)$$

and similarly, $p_s = \frac{1-p_{Se}p_{ce}}{2}$ for the singlet state, where in both cases we have used the expressions

$$\begin{aligned} p_{\downarrow\downarrow} &= \frac{(1+p_{Se})(1+p_{ce})}{4} \\ p_{\uparrow\uparrow} &= \frac{(1-p_{Se})(1-p_{ce})}{4} \end{aligned} \quad (5.14)$$

and where p_{Se} and p_{ce} are the spin polarizations of the donor and the conduction electrons, respectively.

For a simple calculation of the steady state difference in the capture rates k_s and k_t , therefore, we can consider the change in the number of electrons to be zero. We also take into account that the spin up and down populations of the selenium become equal at resonance for a saturated transition, leading to zero polarization. This gives us

$$n_{ss}(\text{sat}) = \frac{2k_g}{k_s - k_t} \quad (5.15)$$

when the system is on resonance, using $p_{Se} = 0$. Off-resonance, however, there is a difference in the spin-up and down populations of the selenium and the differing populations need to be taken into account. For the off-resonance steady state, therefore, we have

$$n_{ss} = \frac{2k_g}{k_s(1-p_{Se}p_{ce}) + k_t(1+p_{Se}p_{ce})} \quad (5.16)$$

We can then obtain a ratio between the two steady-state conduction electron number values

$$\frac{n_{ss}(\text{sat})}{n_{ss}} = 1 + p_{Se}p_{ce}\left(1 - \frac{2k_s}{k_s + k_t}\right) \quad (5.17)$$

and therefore for our EDMR signal strength (the ratio of the current on and off resonance $\Delta I/I_0$), in terms of the capture rates:

$$\frac{\Delta I}{I_0} = \frac{n_{ss}(\text{sat}) - n_{ss}}{n_{ss}} = p_{Se}p_{ce}\left(\frac{k_t - k_s}{k_t + k_s}\right) \quad (5.18)$$

We can now estimate the difference in singlet and triplet capture rates required by our model to match the experimental results:

$$\frac{k_t}{k_s} = \frac{1+c}{1-c} \quad (5.19)$$

where $c = \frac{\Delta I/I_0}{p_{\text{Se}} p_{\text{ce}}}$. We calculate the donor spin polarisation p_{Se} using Eq. 5.6 to be $\sim 5.5\%$. For the conduction electron polarization, as in the temperature dependence study (Section 5.4.3), we assume the same form as the donor spin polarization (a valid assumption when the donor spins are in spin-lattice equilibrium, and also applicable when they are not if the capture rates are faster than the spin-lattice relaxation[166]). This level of polarization of the donor and conduction electrons will then result in a required difference in the singlet and triplet capture rates of 6%, i. e. a k_t/k_s ratio of around ~ 1.06 . While we are not aware of direct measurements of capture rate differences for donors in silicon (which may partly be because in the more intensively studied shallow donors, the triplet state is not bound and therefore this EDMR mechanism does not exist), in other systems singlet-triplet capture rates can differ significantly. For instance, for deep trapping of conduction electrons in F-center (or colour center) defects in crystals, the range of k_s/k_t was found to be 4.4–38[171] (noting that here the singlet capture rate is faster). Theoretical calculations of these capture rates will be a valuable resource in verifying our spin-dependent trapping mechanism.

5.6.2 Results and further work

In this chapter we presented the first observation, to our knowledge, of spin-dependent transport in a deep donor in silicon. Electrically detected magnetic resonance was used to explore the spin dependent transport mechanism in such devices. Temperature, microwave power, steady-state current monitoring and different illumination sources were used to elucidate the features of the selenium resonances. The high signal strengths, reproducible features, and clear trends with temperature and illumination are all valuable pieces of information and we look forward to a theoretical analysis that can pinpoint a mechanism for the spin-dependent transport and spin-to-charge conversion we observe. In the previous section, we have laid out a few mechanisms that are typically seen in silicon EDMR measurements and analysed our findings in each context. We have also presented a new EDMR mechanism possible in deep donors but not in their shallow counterparts; spin-dependent trapping based on differing capture rates between the singlet and triplet configurations of the donor and conduction electron spins.

Further work would be useful to verify the transport mechanism and explore further the spin physics of deep donors in silicon, for spintronics and quantum information applications. We hope to integrate selenium donors into single-dopant devices such as the ones

described in the next chapter and the EDMR results reported here are a valuable first step in the understanding of deep donor physics in devices.

Some further measurements to perform would be, first, a careful monitoring of the current transient at resonance, especially in the dark. This is a possible way to rule out recombination in favour of spin-dependent transport processes. Secondly, using a few different illumination sources, such as lasers of different wavelengths (above-gap and sub-gap), would be useful to determine the energy levels involved. EDMR studies carried out in lower concentration samples would have fewer Se^+ pairs in close proximity and this could reduce the signal strength if spin-dependent hopping were the underlying mechanism, yielding valuable information. High-magnetic fields (for instance, W-band EDMR)[156][86] have in the past shown interesting variations in mechanism for the shallow donors and will also provide enhanced spectral resolution. Lastly, pulsed EDMR has been invaluable in studying the shallow donors in silicon, and the coherence and relaxation times of the subset of donors involved in spin-dependent transport. This would be welcome information in the case of the deep donors as well in the context of device integration; it would shed light on their behaviour in the presence of electric fields and whether they retain their extremely long ESR relaxation and coherence times.

Recent work also mentions the intriguing possibility of using the illumination sequence developed in Ref. [141] (1047 nm + 4 m) to study the nuclear spin properties of neutral selenium ($^{77}\text{Se}^0$), a technique which requires the observation of EDMR. Our EDMR results are the first steps towards such a process, which could be used to exploit the nuclear spin coherence time of neutral selenium (expected to be much longer even than Se^+) by a sequence consisting of manipulation followed by neutralization to preserve coherence.

Chapter 6

A Hybrid Dopant-Dot Double Quantum Dot in Silicon

In this Chapter, we bring together the work presented in earlier chapters on quantum dot and dopant systems as well as the techniques developed to measure them. In Chapter 1, we discussed the motivations behind the study of a coupled system consisting of quantum dots and dopants in silicon. We noted the long coherence times of dopant electron and nuclear spins and their potential as quantum memories, and mentioned quantum computation architectures consisting of quantum dots as processing units and spin buses to carry information. The common basic link between these proposals is a coherent coupling between a dopant and a quantum dot, in a scalable, compact architecture. In addition, there is scientific value in the previously unexplored physics of the coupling between a natural atom (a phosphorus donor) and an artificial atom (the quantum dot).

We now present measurements taken on a silicon nanowire transistor of the kind explored as a quantum dot architecture in Chapter 4. The device presented here was designed and fabricated by the TOLOP project partners at CEA-Leti and measured at UCL at the base temperature of our dilution fridge, as described in Chapter 3. We show now that given a version of the devices presented in Chapter 4, with the channel implanted at a dose corresponding to a few dopants in the channel, we are able to measure a coupled double quantum dot system made up of a single phosphorus atom and a corner quantum dot. This is to our knowledge the first such measurement¹.

¹Recently, in a gate-defined metal-oxide-semiconductor quantum dot with a dopant implanted nearby, nuclear-spin driven singlet-triplet rotations were reported[30].

6.1 Device and measurement setup

The device under measurement (shown in Fig. 6.1) was fabricated at CEA-LETI, from an SOI substrate with a 145 nm buried oxide and a silicon layer doped with phosphorus at a concentration of $5 \times 10^{17} \text{cm}^{-3}$, with the fabrication process described in more detail in Section 3.5. This doped silicon layer is etched to create a 200 nm long and 30 nm wide nanowire using deep-UV lithography. A 30 nm wide wrap-around top gate is defined using an $\text{SiO}_2(0.8 \text{ nm})/\text{HfSiON}(1.9 \text{ nm})$ stack for the gate dielectric followed by $\text{TiN}(5 \text{ nm})/\text{poly-Si}(50 \text{ nm})$ as the top gate material (the number of dopants expected for this size of channel is about five). The source and drain are self aligned and formed by ion implantation after the deposition of 20 nm long Si_3N_4 spacers.

We employ RF gate-based sensing as well as microwave spectroscopy for measurement; the measurement setup is elaborated in Section 3.3 and shown in part in Fig. 6.1(b). In addition to the DC and RF lines connected via bias tee to the top gate, the undoped silicon substrate is used as a back gate after activation using a surface-mounted blue LED to generate free carriers. Our setup includes a microwave antenna located a few mm above the sample.

6.2 Double quantum dot behaviour

Double-dot stability diagram

As discussed in Section 3.3, RF gate-based sensing can detect two types of responses; (a) dissipative, or a change of resistance occurring, say, due to a charge tunnelling from a localized state to a lead[93] and (b) dispersive, or a change of quantum capacitance due to a charge tunnelling between two quantum dots[23, 125]. Fig. 6.2 shows the device charge stability diagram as a function of top gate (V_{tg}) and back gate voltages (V_{bg}), detected via RF reflectometry. It shows a set of charge transitions with a small dependence on V_{bg} , corresponding to single charges tunnelling from the source or drain to quantum dots localized below the top gate. We attribute these charge transitions to the so-called corner quantum dots, known to be formed in the top corners of these nanowires where the electric field is maximum [105] and discussed extensively in previous chapters. These dots have relatively large charging energies, $E_c \sim 18 \text{ meV}$, and a strong top gate lever arm, $\alpha_{\text{tg}} \sim 0.85$, similar to what has been reported elsewhere [93, 105], deduced from the extent of measured Coloumb diamonds. One single transition however, indicated with a black arrow

in Fig. 6.2, is more coupled to the back-gate than the other charge transitions, indicating a localized state situated deeper in the channel.

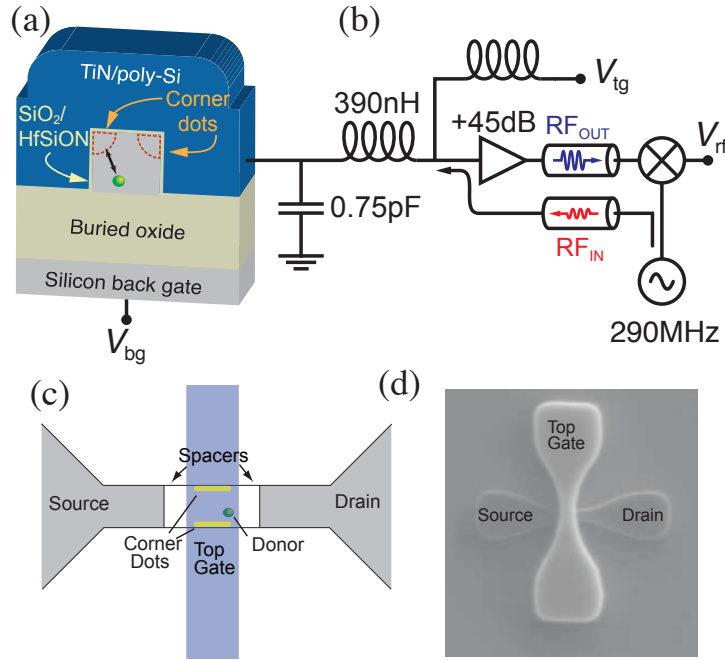


Figure 6.1: (a) Quantum dots localized in the corners of a silicon nanowire FET device with a donor shown deeper in the channel. (b) Simplified RF reflectometry setup. (c) Top view, schematic of the device showing the source and drain as well as the nitride spacers that act as tunnel barriers between the dots and the source and drain. (d) Top view, SEM image of a similar device showing the top gate orientation on top of the channel.

Subthreshold resonances like these are commonly attributed to single donors located in the channel [108, 172]. In this sample as well, the impurity state is close to the conduction band edge and very close to threshold (650 mV), as expected for phosphorus atoms in silicon [173]. We can also place it far below the surface, using the back gate/top gate ratio, which eliminates interface charge traps and electron puddles. In addition, at these channel sizes (30 nm wide, 30 nm long, 11 nm thick silicon), the number of bulk defects intrinsic to the nanowire is typically a few orders of magnitude lower than the average number of dopants that were deliberately implanted (about 5 dopants in this size of channel). Significantly, such subthreshold signatures were not observed in any of the undoped devices (see Ref. [93, 106] as well as Chapter 4); however, doped devices we have measured

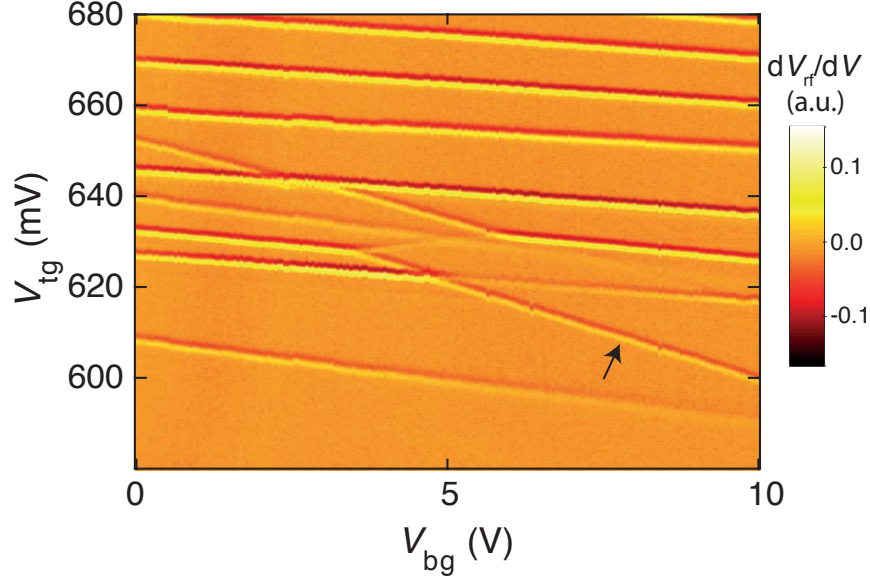


Figure 6.2: The Gaussian filtered derivative of the demodulated resonator response as a function of V_{tg} and V_{bg} (charge stability diagram). The black arrow indicates a charge transition attributed to a phosphorus atom in the bulk of the nanowire.

regularly show such subthreshold resonances², as do similar doped devices measured by different research groups, as well as collaborators[108, 172](see also Appendix B for other measurements).

Quantum dot charge assignment

To correctly assign the electron filling of the DQD system to the transitions observed in the charge stability diagram, we turn to the phase response of our resonator. We can extract the phase response of the device from the I and Q channels. Fig. 6.3 shows the charge stability diagram of the donor-dot system, with the phase response data plotted on the right. The signal intensity in a single channel does not vary enough to allow us to differentiate between the systems under study. However, the phase response data shows a strong variation in intensity between the different quantum dots in the channel, most probably due to differences in tunnel rates, as described in Section 3.3. The degree of visibility of its resonances in the phase response should be characteristic of a particular quantum dot, since it is related to the proportion of its signal in the dissipative versus dispersive regimes (at

²Depending on channel length, about one in three doped devices will show such subthreshold resonances that are deeper in the channel and coupled more to the back gate, as opposed to those from corner dots.

least over a small number of transitions and a small change in gate voltage). Using this method of discrimination, we are able to isolate three sets of lines in Fig. 6.3(b); a corner dot uncoupled to the donor (blue dotted line), a corner dot that couples to the donor (red dotted line) as well as the donor charge transition (green dotted line). Later measurements confirm this charge assignment and we will discuss this in more detail in Section 6.5. We note, however, that while the charge assignment in the stability diagram commences from zero electrons for clarity (at a point in top gate voltage below which we do not see any more dot transitions), in essence we can assert only that we are at an even parity transition at the interdot charge transition (ICT).

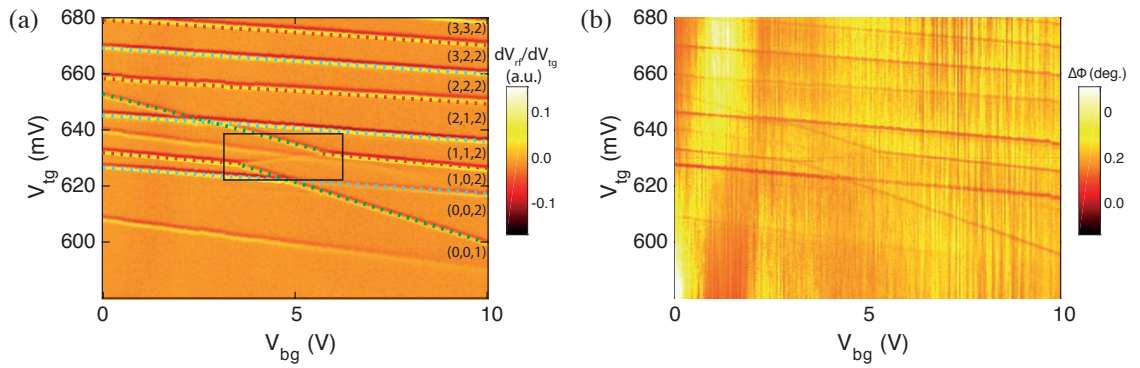


Figure 6.3: (a) Numerical derivative, filtered, of the amplitude response as a function of V_{tg} and V_{bg} . The last digit of the charge assignment corresponds to the donor atom (green dotted line), the second digit to the coupled corner dot (red dotted line) and the first digit to the uncoupled corner dot (blue dotted line). The unassigned transitions are attributed to another donor in the channel, while the black box encloses the region of interest. (b) Phase response of the coupled dot-donor system as a function of V_{tg} and V_{bg} . The visibility of the phase response allows discrimination between the two corner dots.

Dopant charge assignment

Fig. 6.4 shows the magnetic field dependence of the ICT at $\epsilon = 0$ (black star) as well as of the dopant line (green star). The interdot quantum capacitance signal has a strong magnetic field dependence, explored in Section 6.5.

The amplitude of the dopant line does not diminish under field, but it exhibits a gradual shift towards higher top gate voltages. In general from this we can infer the spin polarity of the tunneling electrons: a shift towards higher top gate voltage, or higher energy, indicates tunneling of spin-up electrons. Here it indicates that the Zeeman energy increases the donor

chemical potential. In our system, as studied previously[28, 173], this shift towards higher energy is consistent with a D^- state, in which electrons form a two-electron singlet. Finally, the $D^+:D^0$ charge transition of the donor is not visible in our system. This may be explained by a small tunnel rate between the donor and the reservoir. Indeed, the $D^+:D^0$ is deeper below the conduction band than the $D^0:D^-$, and as a result, the tunnel barrier between the reservoir and the donor is more opaque[28]. Due to the fact that our RF reflectometry technique is most sensitive to charges tunneling at a frequency comparable to the excitation (and higher, for the phase response)[93], we are unlikely to see the $D^+:D^0$ charge transition if the tunnel rate is too low.

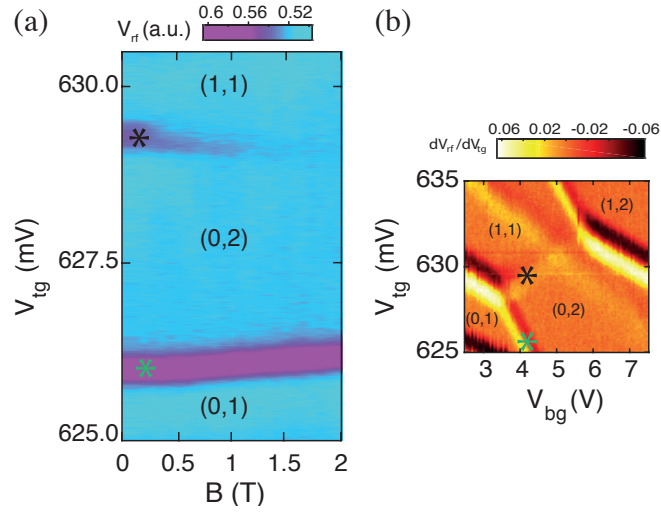


Figure 6.4: (a) Resonator response as a function of V_{tg} and magnetic field B , and (b) of V_{tg} and V_{bg} . The charge transition of interest, for the donor, is labelled with a green star in (a) and (b).

Interdot charge transition

Lastly, focusing on the small region in Fig. 6.5(a), we see the classic signature of a double quantum dot: the presence of a ridge at the intersection between the donor and dot charge transitions. A close-up of the coupling ridge is shown in Fig. 6.5(a), with our inferred donor/dot charge occupancies added. From our previous charge assignments, we can now label all the regions of charge stability. The signal at the ICT can be modelled as a quantum capacitance, as in Ref. [23]. We recall from Section 2.3 (as Fig. 6.5(b) shows) that when the energy levels of the donor and the corner dot are brought into resonance the coupling between the donor and dot lead to bonding and antibonding molecular orbitals, with

the quantum capacitance directly proportional to the curvature of the eigenenergies with respect to detuning. We find

$$C_q = -(e\alpha)^2 \frac{\partial^2 E}{\partial \epsilon^2}, \quad (6.1)$$

where α is the coupling between the resonator and the double quantum dot, E the eigenenergies and ϵ the detuning energy. The quantum capacitance is then maximum for $\epsilon = 0$, where the curvature of the eigenenergies is maximum. It is worth noting that the sign for the response from the bonding and antibonding at the same detuning is equal and opposite (see Fig. 6.6(b)); which offers us a way to monitor population transfer between the two states. If we are able to resonantly populate the excited state, our signal should reduce strongly.

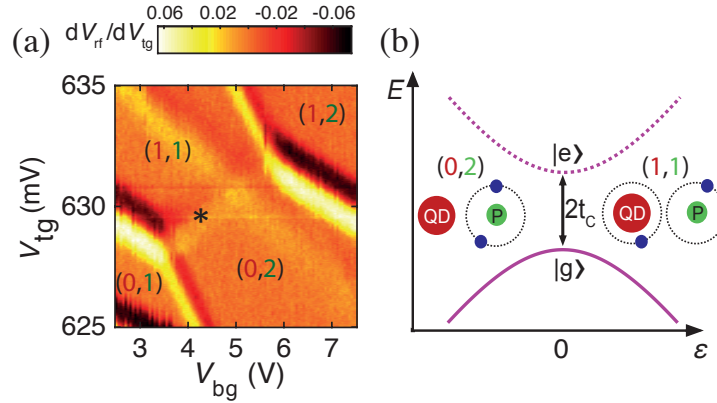


Figure 6.5: (a) A close-up of the charge stability diagram shows the charge transition between a corner dot and a donor, with charge occupancies labeled as (corner dot, donor). There is an unrelated and non-interacting transition that cuts through the ICT. The * indicates the avoided level crossing sketched in (b), which shows the energy levels of the hybrid double quantum dot, where the quantum dot and the P atom form bonding, $|g\rangle$, and antibonding $|e\rangle$ states when the detuning ϵ is near zero. For simplicity, spin effects are omitted here and will be discussed later. For $|\epsilon| \gg 0$, the double dot has ionic-type wavefunctions where the charges are localized on the dot or donor.

6.3 Microwave spectroscopy

We now characterize this coupling by performing microwave spectroscopy using our local antenna coupled to the top gate. The dependence of the RF-reflectometry signal amplitude (A) with microwave frequency is shown in Fig. 6.6(a), normalised against the signal

amplitude with no microwaves applied (A_0). The microwave excitation causes a fraction of the ground-state population to be promoted to the excited state, reducing the averaged quantum capacitance. The maximum change of signal should occur when the microwave frequency matches the tunnel splitting. Sweeping the frequency of our microwave antenna, we find this point to be $\nu = 5.5$ GHz. From this we extract $\Delta = 2t_c = 5.5$ GHz. Fitting this transition with a Gaussian lineshape, we obtain a charge dephasing time of $T_2^* \sim 200$ ps, similar to other measurements in double-donor systems in the same type of nanowire system ([108]).

The tunnel splitting could in principle be tuned in more evolved device designs based on the same architecture, for example with the top gate split to form two gates in a facing geometry[108]. The T_2^* can be improved by going to lower temperature (if it is limited by charge relaxation) or by improving the charge stability of the device (if it is charge noise limited). The charge noise explanation is more likely, since the ~ 20 nm wide nitride spacers are suspected to be a source of charge noise as they bear a large trapped charge density[174]. However, we look at the charge relaxation in the next section.

Microwave spectroscopy power dependence

We now look at the power dependence of the microwave spectroscopy experiment described above. Figure 6.6(c) and (d) show the interdot charge transition under a continuous microwave excitation of 5 GHz as a function of microwave power and gate detuning, ε .

In a two level system, Landau-Zener-Stückelberg (LZS) interferometry theory provides us with the respective slow passage ($A\nu \lesssim \Delta^2$) and fast passage ($A\nu \gg \Delta^2$) conditions, where A is the driving amplitude, ν is the frequency, and Δ is the energy splitting between the excited and ground states, as described in Section 2.4. As we vary the power we supply to the microwave antenna, we are varying the driving amplitude A , which in turn takes us from the slow to fast passage regime. This, as shown in Figure 6.6, gives rise to the expected squared Bessel function behaviour at zero detuning for multiple passage, as theoretically investigated in Ref. [43]. The MW driving tunes the charge polarisation as:

$$P_g - P_e = J_0^2(a) \quad (6.2)$$

where $J_0^2(a)$ is the square of the 0-th order Bessel function evaluated at $a = eV_{ac}/h\nu$. We send microwaves through an antenna close to the sample, which then modulates the top gate voltage by V_{ac} . Our data, while fitting well to the Bessel function, also allows us to

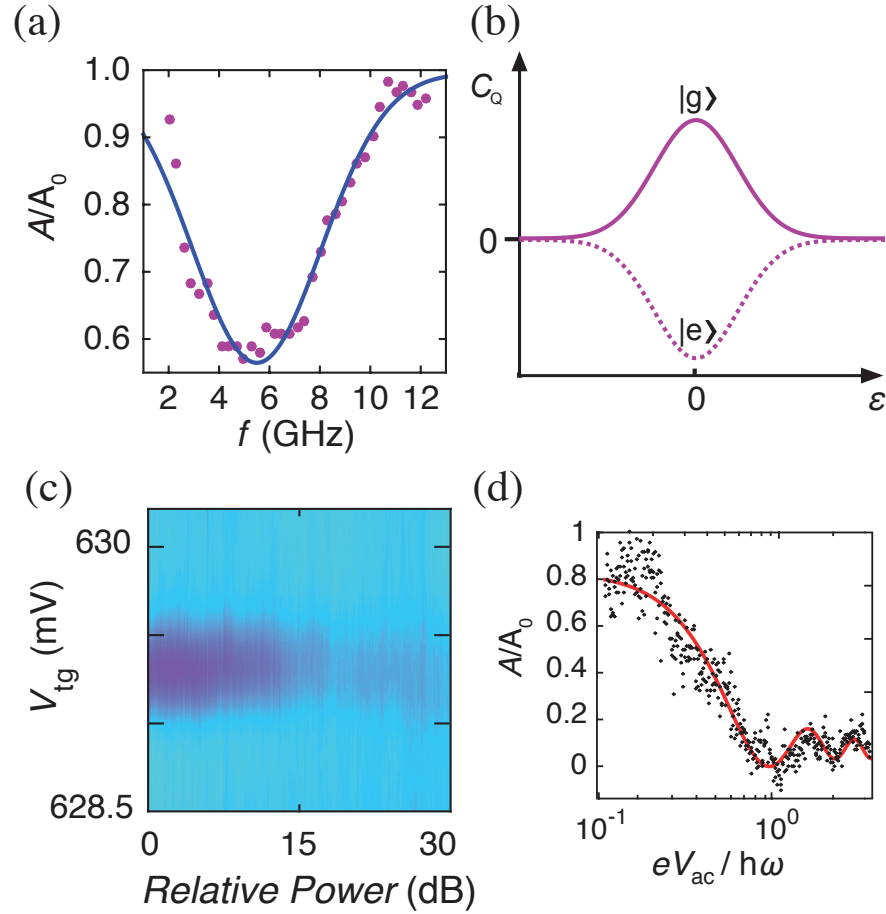


Figure 6.6: (a) Monitoring the interdot charge transition as a function of applied microwave frequency shows a reduction in signal amplitude upon resonance with the $|g\rangle:|e\rangle$ transition, since these states have opposite values of quantum capacitance as shown in (b). (c) Resonator response as a function of V_{tg} and the relative microwave power broadcasted by the antenna. (d) Amplitude of the interdot charge transition as a function of the microwave amplitude. Equation (6.2) is used to fit the data.

calibrate the power arriving at the sample by measuring the distance between the zeros of J_0^2 , occurring at $eV_{ac}/h\omega$, given by $a_1 = 2.4$ and $a_2 = 5.5$. Figure 6.6(d) shows the calibrated result.

While we do see a characteristic power dependence at detuning $\epsilon = 0$, no higher order photon assisted tunneling has been observed in the high frequency limit ($hf > 2t_c$). This can be explained by considering spin effects in the double dot at the (0,2) to (1,1) transition: for negative detuning, the ground state is the singlet S(0,2) while the excited state is a mixture of triplet states (T_0 , T_- and T_+) and singlet S(1,1). As a result, a microwave induced transition between these two states requires a spin-flip process ($\Delta m = 1$). Hence, in the absence of spin orbit coupling[175], or a particular electron-phonon interaction[176], microwave photon absorption is forbidden. This observation of the suppression of higher order tunneling is further evidence in support of the charge assignment in Section 6.2. We now move on to measuring the relaxation time of our charge qubit.

6.4 Charge relaxation

We expect a longer charge relaxation time in Si than in GaAs (where $T_1 \sim 10$ ns) due to the absence of piezoelectric coupling[77]. However, expecting a relaxation time for this charge qubit that is still fast compared to our demodulator and amplifier bandwidth (about a few MHz), we use a method developed in Ref. [41] instead of a transient measurement. To measure the charge relaxation time, we use microwave excitation to populate the excited charge state (the antibonding state in Fig. 6.5(b)) and measure how fast it decays to the ground state.

Measurement method

In this method (explained in Ref. [52], simulations from which are shown in Fig. 6.7), the microwaves are chopped at some frequency $1/\tau$ with a 50% duty cycle, while time averaging the signal amplitude at the ICT. In the first half of the pulse cycle, in the experiment referenced in Fig. 6.7, microwaves saturate the (1,0) to (0,1) transition such that an average population $P(1,0)$ of 0.5 is seen. The microwave excitation is then turned off, such that during the second half of the cycle there is charge relaxation, with $P(1,0)$ approaching 1 on a timescale set by T_1 (assuming $T \ll h\nu/k_B$). Simulations of $P(1,0)$ as a function of

time for $\tau = 1\mu s$ are shown in Fig. 6.7 for three realistic values of T_1 . Given T_1 , varying τ should produce a similar result.

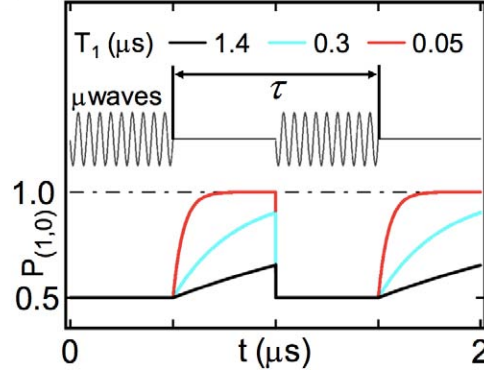


Figure 6.7: Pulse sequence used to measure T_1 and simulated qubit response. $P(1, 0) = 0.5$ when resonant microwaves drive transitions between $|g\rangle$ and $|e\rangle$, and approaches 1 on a timescale set by T_1 when the microwaves are turned off. Simulations from Ref. [52].

Results

In our experiment, we define the charge polarization as $P = P_g - P_e$, with P_g and P_e the ground and excited state populations. When $\tau \ll T_1$, or for very short periods, the signal amplitude is close to the saturation value (P_{sat}) throughout the cycle since the system has no time to relax to the ground state. In contrast when $\tau \gg T_1$, the signal is an equal time average of thermal and saturated ($\langle P \rangle \approx 1/2(P_{\text{sat}} + P_{\text{th}})$). This is because the polarization is, to a good approximation, at saturation, P_{sat} , during the first part of the cycle (microwave on) and at thermal equilibrium, P_{th} , during the second part (microwave off). Charge relaxation takes the system between these two extremes, with a signal strongly dependent on τ when $\tau \sim T_1$. Expressing $\langle P \rangle$ as a function of τ , we get

$$\begin{aligned} \langle P \rangle &= \frac{P_{\text{sat}}}{2} + \frac{1}{\tau} \int_0^{\tau/2} P_{\text{th}} - (P_{\text{th}} - P_{\text{sat}})e^{-\tau/T_1} dt \\ &= \frac{(P_{\text{sat}} + P_{\text{th}})}{2} - \frac{(P_{\text{sat}} - P_{\text{th}})}{\tau} [T_1 e^{-\tau/T_1}]_0^{\tau/2} \end{aligned} \quad (6.3)$$

which gives us the final equation for $\langle P \rangle$:

$$\langle P \rangle = \frac{(P_{\text{sat}} + P_{\text{th}})}{2} + (P_{\text{sat}} - P_{\text{th}}) \frac{T_1(1 - e^{-\tau/2T_1})}{\tau}. \quad (6.4)$$

Here the normalised amplitude A/A_0 at the ICT is directly proportional to $\langle P \rangle / P_{\text{th}}$ (A_0 being the amplitude in the absence of MW excitation); thus, $P_{\text{sat}}/P_{\text{th}}$ is obtained from the ICT signal under continuous microwave excitation in Fig. 6.7 (light blue curve). The figure also shows the ICT under microwave excitation chopped with 100 ns and 100 μ s time periods. As expected, the signal amplitude is greater when the charge has more time to relax.

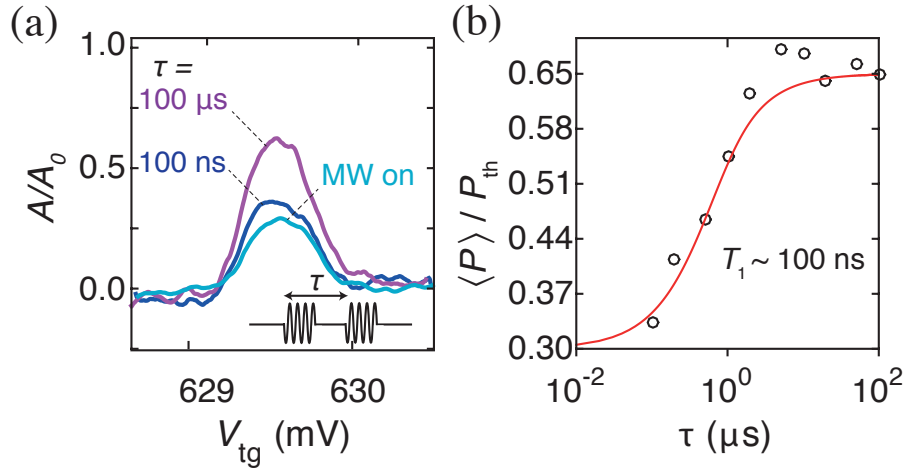


Figure 6.8: (a) ICT under continuous MW (light blue), chopped MW at 10 MHz (dark blue) and 10 kHz (purple). (b) Renormalized average charge state population difference as a function of the chopping period τ , fitted using Eq. 6.4 with T_1 as the fitting parameter.

Fig. 6.8(b) shows the time averaged polarisation recorded for different values of τ and is fitted using Eq. 6.4 to give a charge relaxation time $T_1 \sim 100$ ns.

This result confirms that our coherence time T_2^* is not limited by charge relaxation, since $T_1 \gg T_2^*$. Moreover, the phonon-induced dephasing rate in silicon is expected to be in the MHz range[177]. Therefore, background charge fluctuations or noise in the gate voltages are assumed to be the main dephasing sources as they induce fluctuations in both tunnel coupling and detuning energy. Earlier studies have found charge relaxation tunable over orders of magnitude in silicon by tuning the voltages controlling the tunnel coupling, with a longer characteristic relaxation time (up to 45 μ s) corresponding to larger interdot barrier heights[52]. Given more complex samples with independent tuning of the dots (for example, samples identical to ours but with the top gate split into two face-to-face halves[108]) which will also enable tuning of the tunnel coupling via the back gate, we might be able to reach longer charge relaxation times. However, we are particularly inter-

ested in the novel spin system available to us in this coupled dopant-dot hybrid qubit, and for now we move on to explore the spin degree of freedom.

6.5 Spin blockade

We now discuss the spin-related phenomena observed at the ICT and show that it is indeed of even parity. Fig. 6.9(b) shows the energy level diagram of the system near the (1,1) to (0,2) transition in the presence of a magnetic field. The magnetic field shifts the triplet T-state lower in energy so that it starts to become the ground state instead of the singlet. As in previous measurements shown in this section, a quantum capacitance measurement can be used to exploit the difference in bandstructure (energy versus gate voltage relation) of the singlet and triplet states. At $\epsilon = 0$, as the magnetic field is increased, the population of the singlet state decreases while the population of the T₋ triplet state increases (and eventually dominates for $g\mu_B B \gg k_B T$). As the triplet state has a linear detuning dependence, it has a zero quantum capacitance signature. Therefore, when it becomes the ground state at finite magnetic field, it does not contribute to the RF-reflectometry signal at the ICT. This allows for the observation of Pauli spin blockade.

Fig. 6.9(a), indeed, shows the RF signal at the ICT disappearing with increasing magnetic field (as seen in other systems, notably GaAs double quantum dots[128]). Above 1.2 T it has completely vanished. A similar response has been observed in an InAs double quantum dot coupled to an RF resonator [128], including the shift in the maximum amplitude position observed at low fields, see Fig. 6.9(a) and (c), and has been theoretically investigated in Ref. [96].

The shift in the maximum amplitude position can be understood by considering the intersection of the singlet and T₋ states at the detuning value ϵ_{ST} , which shifts with magnetic field as shown in Fig. 6.9. For $\epsilon < \epsilon_{ST}$, there is a singlet ground state and the quantum capacitance has a finite value (however, this decreases for more negative ϵ_{ST}). For $\epsilon > \epsilon_{ST}$ there is a T₋ ground state and the quantum capacitance vanishes. The asymmetric line-shape observed is a sign, therefore, that the system has a significant population following the ground state, even at the S:T₋ intersection. We understand this by the presence of an avoided level crossing at this intersection, combined with the fact that our measurements are inherently multipassage ones.

The mixing between these two states is generally induced by the magnetic field gradient created by the nuclear spin bath[178]. In contrast, in this silicon hybrid double dot, the

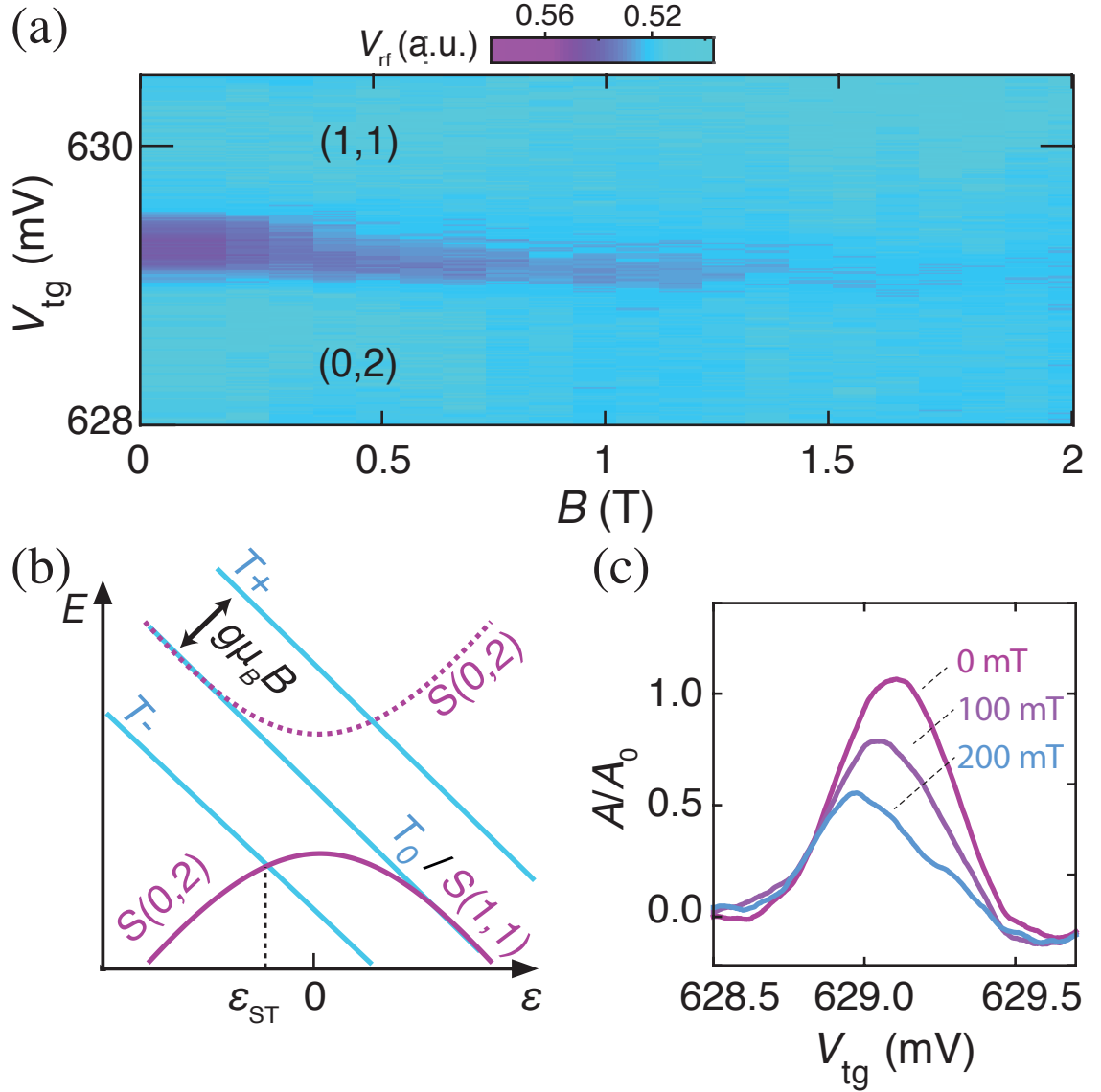


Figure 6.9: (a) The quantum capacitance signature of the interdot charge transition (ICT) become strongly suppressed with increasing magnetic field, as the T_- triplet state becomes the ground state, as shown in (b) the energy level diagram near the (1,1) to (0,2) transition in the presence of a magnetic field. ϵ_{ST} denotes the value at which the singlet and T_- states intersect, and is responsible for the shift and asymmetry observed in (c), the ICT measured at 0 mT, 100 mT and 200 mT.

mixing should be dominated by the hyperfine interaction with the nuclear spin localized at the donor site. As a result, neglecting the Overhauser field created by the ^{29}Si , the electron located on the donor is detuned by $\delta = A\mathbf{S} \cdot \mathbf{I}$ where A is the hyperfine coupling constant, \mathbf{S} the electron spin and \mathbf{I} the donor nuclear spin. We will discuss this mixing and its consequences in a later section.

6.6 Conclusions

To conclude, we have presented a hybrid double-dot system consisting of a phosphorus atom and a corner quantum dot in a foundry-fabricated nanoscale silicon transistor. First, this hybrid qubit is scalable by virtue of its implementation in an industry-compatible fabrication platform. Secondly, the measurement of the double quantum dot is accomplished wholly by the technique of gate-based reflectometry, which simplifies device fabrication and scaling up immensely, since a separate charge sensor quantum dot is not required. We have shown that both charge and spin effects in the system can be probed using this technique, and in particular have measured coherence (T_2^*) and relaxation times for the charge qubit formed using microwave spectroscopy techniques.

Finally, the observation of spin blockade opens up ground for the exploration of spin effects in this novel, hybrid system as well as for a new kind of singlet-triplet qubit with spin dynamics possibly governed by the donor nuclear spin. This is hinted at by the avoided level crossing formed by the mixing of the singlet and T_- states which we attribute to the hyperfine coupling of the electron with the nuclear spin of the phosphorus atom. We discussed before that the electron on the donor is detuned by the $\delta = A\mathbf{S} \cdot \mathbf{I}$ where A is the hyperfine coupling constant, which for phosphorus is 117 MHz. Therefore the S(1,1)- T_0 coherent evolution at a very low exchange coupling could be driven at ~ 50 MHz. In the case of bismuth, $I = 9/2$ and $A = 1.48$ GHz, the driving frequency should be even higher ranging from 300 MHz up to 3 GHz depending on the nuclear spin state. Similarly, for selenium, the dopant explored in the previous Chapter 5, the hyperfine constant is similarly large, $A = 1.66$ GHz.

Finally, exploiting the interdot exchange coupling would allow a SWAP operation between the corner dot and the donor atom spin state and, eventually, its storage in the donor nuclear spin using electronuclear double-resonance (ENDOR) techniques. This would take us one step closer to the qubit implementation mentioned at the beginning of the thesis

which enables the donor nuclear spin, with its extremely high coherence times, to be used as a quantum memory.

6.7 Methods for coherent control

While we have presented spin effects in this hybrid dopant-dot system, ultimately the goal is to develop a coherent coupling that we can manipulate using microwaves, and use for the transfer of information between the dopant and the dot. For this, the first step would be to perform electron spin resonance or ESR. In the previous section we saw that the quantum capacitance signal has a finite curvature for the singlet state, and is flat in detuning for the triplet state. This translates to a situation where the singlet gives us, via our coupled resonator, a strong signal at the ICT when we are in the singlet state, and no signal when we are in the T_- triplet. This then provides us with a natural way of discrimination between these two spin states of the system and we would like to be able to coherently evolve, or even pulse between these two states.

As we have presented previously, in this system we were equipped with a static magnetic field (used to bring the hybrid double-dot into spin blockade) as well as a microwave antenna, built originally as a quarter-wave antenna for 20 GHz. In principle, this provides us with a B_1 magnetic field orthogonal to B_0 , making ESR possible according to the principles outlined in Chapter 3. However, in practice we were severely limited by the distance of our antenna from the sample (a few mm) which meant that we were unable to apply the microwave powers required to generate a magnetic field high enough to flip the spin, without heating up the dilution fridge. At moderate powers (at which the fridge temperature was stable at a mixing chamber temperature lower than our measured electron temperature), we measured the amplitude of the RF signal with the double quantum dot in blockade, while applying microwaves at the frequency of the antenna, measured using a network analyser to be ~ 19.4 GHz. Both methods of performing cw-ESR, i.e. sweeping the magnetic field with the microwave frequency held constant, as well as sweeping the microwave frequency with the field held constant, were employed. Our best-case results, after extensive signal filtering and measurements taken over long timescales (spanning a day or so), are shown in Fig 6.10. In both cases, we saw a weak signal at points in field and frequency separated by the hyperfine splitting of phosphorus (117 MHz in frequency and 4.2 mT in field). While we stress that these measurements were inconclusive due to the high noise in the measurement (as well as due to the fact that frequency vs magnetic field scans showing a

linear relationship could not be taken due to the long timescales needed to average each data point), they nevertheless were an encouraging motivation to improve our ESR setup to explore the spin system further. We therefore present the development of an on-chip waveguide, to be used for both continuous wave as well as pulsed ESR experiments, and eventually coherent control of the hybrid double quantum dot system. .

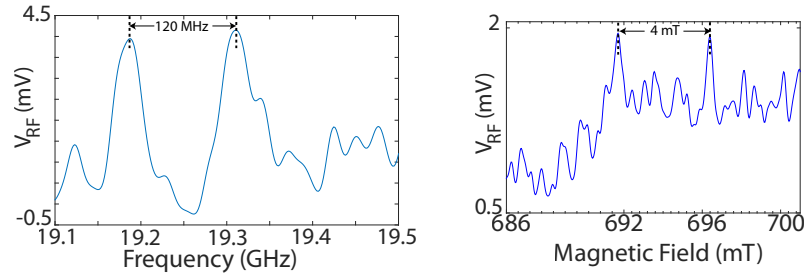


Figure 6.10: Gaussian filtered resonator response at the interdot charge transition. Left, microwave antenna frequency is swept while magnetic field is held at 690 mT. Right, magnetic field is swept while microwave frequency is held constant at 19.4 GHz. Approximate peak-to-peak distances are indicated by arrows. (For ^{31}P , the hyperfine splitting is 117 Mhz in frequency and 4.2 mT in magnetic field.)

ESR using a coplanar waveguide

Magnetic resonance is an important technique for spin manipulation in nanodevices for weak spin-orbit materials such as silicon (and with a negligible nuclear spin field in the case of ^{28}Si), where Electron Dipole Spin Resonance (EDSR) is not possible. This has been accomplished in the past using coplanar nanoscale transmission lines in purpose-built devices in silicon [7, 179]. Integrating such charge-sensitive devices with broadband GHz excitations involves careful minimization of the electric field while maximising the magnetic field at the spin, and is not trivial. Here we present a nanoscale coplanar waveguide (CPW) which is designed to be used for charge sensitive nanodevices as well as to be used along with the sensitive readout technique of RF-reflectometry at millikelvin temperatures. The waveguide also has unique challenges as it needs to be designed to add on to devices which are manufactured in a silicon industry-compatible foundry (it could possibly be incorporated into future devices).

The CPW described above was designed and modelled in CST Microwave Studio, a full-3D electromagnetic and microwave simulation software, following previous work [179]. (A CPW based design connected to the on-PCB CPW was chosen since a

coplanar stripline-to-waveguide (CPS-CPW) balun was unfeasible with the space constraints of the system). The fabrication of this CPW and a discussion of the modelling of the structure are discussed in Appendices A and B, respectively. In essence, so as to avoid shorting with the bond pads of the device, a thin layer of hydrogen silsesquioxane (HSQ, ~ 100 nm) is spun on and then baked to convert it to silicon oxide. Above this insulating layer, an aluminium CPW is deposited. Bonds to the device pads are made through the HSQ (layers this thin can easily be bonded through, locally)³. These samples have been tested at millikelvin temperatures; however their measurement lies beyond the scope of this thesis. Concerns about the HSQ oxide layer creating charge noise or problems for RF-reflectometry based readout have proven unfounded, since RF measurements on these devices do not show such effects.

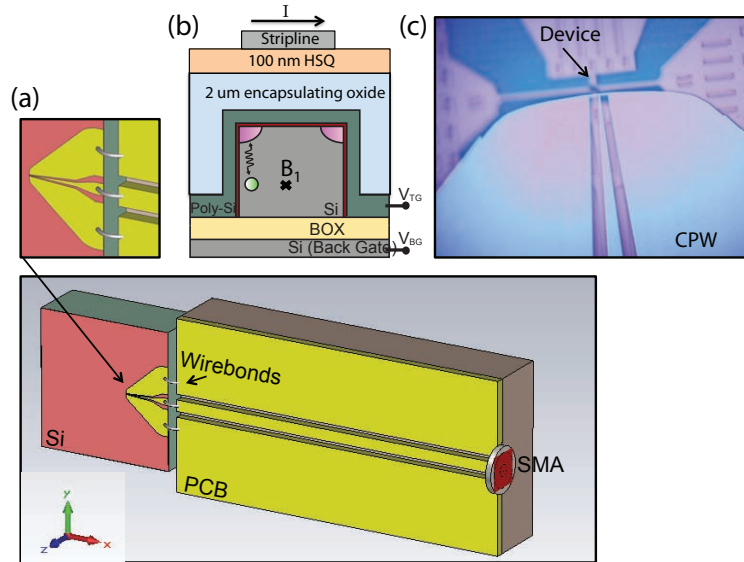


Figure 6.11: (a) CST model, (b) Design schematic with device and (c) optical microscope image of a fully-fabricated coplanar waveguide for ESR measurements, on a silicon fin-FET device.

An optical image of a finished sample is shown in Fig. 6.11(c). While the B_1 magnetic fields from the striplines themselves have not been measured yet, the electric fields (despite being minimized at the device location in the design) are stronger than those from microwaves with similar powers sent through a far-away on-PCB stripline, which is an optimistic outlook for getting sufficient amounts of power (and consequently, a large enough

³While wirebonding through the HSQ was a concern, these devices show the same currents and turn-on behaviour at mK as exhibited by devices where there is no HSQ layer to bond through.

oscillating magnetic field) to the spins in the sample. In future, given encouraging results, similar coplanar waveguides (or even micromagnets to provide a field gradient) could be integrated into the silicon foundry fabrication protocol, ensuring a way of qubit control in a highly-scalable silicon architecture.

Operation as a singlet triplet qubit

Lastly, in the previous section, we presented another method of coherent control and spin qubit formation, motivated by the observation of a singlet-triplet ($S(1,1)-T_0$) avoided crossing where the hyperfine coupling of the dopant nuclear spin could provide a magnetic field gradient to drive coherent spin rotations[153]. For this kind of system, we would not need an ESR microwave antenna, but simply fast voltage pulses to drive the transition as in a typical singlet-triplet qubit (EDSR)[66] as described in Section 2.5.2. This approach merits consideration of the RF-reflectometry drive which at the moment is always on during qubit operation and readout. This is quite a large drive, chosen for signal-to-noise reasons (typically -85 dBm at the sample, though we have been able to go as low as -96 dBm) and can have the effect of moving us over the entire transition in detuning, whereas we would like to probe the ($S(1,1)-T_0$) avoided crossing which has a very small extent in detuning, and requires a finer probe than this strong drive. The effect of the RF drive can possibly be mitigated in a few ways. First, the drive amplitude could be reduced to much lower values, something that is possible by further engineering our RF-circuit and our cryogenic amplifiers, as well as reducing the noise in the measurement setup; or perhaps even by utilising quantum-limited amplifiers such as a Josephson parametric amplifier (JPA). Secondly, qubit parameters such as the tunnel coupling could perhaps be tuned for a larger ($S(1,1)-T_0$) avoided crossing in a different device geometry. Lastly, a fast (sub-nanosecond) switch for the RF drive could be used to turn off the RF-drive during a pulse sequence, followed by turning it on for fast measurements taken at the zero detuning point (or elsewhere, depending on the measurement protocol). This, combined with a reduced RF drive, could result in a viable hybrid dopant-dot singlet-triplet spin qubit.

Chapter 7

Conclusion and Outlook

In this Chapter, we summarize the work presented in this thesis in terms of the main achievements in the development of dopant-dot qubits, and identify future directions for the arenas of research presented. We give suggestions for improving the existing manipulation, readout and charge sensing techniques as well as the coherence properties of quantum dot and dopant spins in CMOS-compatible qubits, in the context of developing a scalable quantum computing architecture.

The main advancements presented in this thesis have been fourfold:

Gate-based reflectometry

In this thesis we have extensively used the technique of gate-based reflectometry for charge sensing of our few-electron quantum dots. This technique has recently gained a lot of popularity and is especially suited to our edge-state quantum dots which have a very strong coupling to the top gate, and hence to the resonator. In Chapter 4 we presented measurements which have developed this technique further for metrology applications and along with those in Chapter 6, have shown its applicability for the control and readout techniques used for few-electron charge and spin qubits in silicon.

Firstly, in Chapter 4 we showed that similar to Coulomb blockade peaks for transport measurements, the dot-to-lead transition resonances detected through gate-based reflectometry can be used to perform nanoscale thermometry, without the need for external thermometers and integrated into a silicon-CMOS architecture. We also showed that the behaviour of the resonance at low temperatures can also be used to extract tunnel rates of the quantum dot involved, which is valuable information for qubit tuning and control. Sec-

ondly, we performed microwave measurements on the dot-to-lead resonance and showed that these can be used to calibrate the amount of microwave power arriving at the sample. We developed a theory to simulate the peak splitting, and found that this method of microwave calibration has potential to be used for pulse shape calibration as well.

Lastly, in Chapter 4 and 6 we showed that sensitive measurements of the charge and spin state of a double quantum dot can be performed using this gate-based charge sensor. We showed that the charge stability diagram of edge-state quantum dots as well as hybrid dopant-dot systems can be measured with high bandwidth. The detection of Landau-Zener interferometry in multiple regimes through gate based reflectometry was demonstrated, as well as Pauli spin blockade, both well established and essential techniques for the read-out and control of charge and spin qubits in quantum dots. This is a significant advance since gate-based reflectometry can enable us to construct complex and close-packed qubit structures without the need for external charge sensors.

CMOS foundry-based quantum dot architecture

Spin qubits in silicon have recently been shown to have excellent coherence characteristics and prospects for scalability[6–8, 17, 18]. Spin qubits in silicon, established mainly in the planar-MOS process, have been proposed and also experimentally demonstrated in academic laboratories, some of them high-fidelity qubits close to satisfying error correction conditions. However, all of these approaches rely on external charge sensors of the same scale as the device, as well as external, coplanar micromagnets or striplines for qubit control.

In this thesis, we have made some first steps to show that similar high-fidelity spin qubits can be manufactured in silicon using industry-standard CMOS processes within a large-scale nanofabrication facility with fabrication methods essentially identical to that of the consumer electronics industry. In Chapters 4 and 6, we have shown that our approach, based on a single, versatile building block (the wrap-around gate on SOI) can be implemented in various configurations to form single and double quantum dots as well as a hybrid dopant-dot system. Some of the qubits that can be built using this basic scheme, with the wrap-around gate divided into two facing control gates, are shown in Fig. 7.1. This building block can also be extended in the second dimension using nanowires facing each other in close proximity. Furthermore, this kind of system can harbour low temperature peripheral electronics, sharing the same CMOS technology and manufactured at the same

time, leading to close integration and alignment of device and control electronics on the same chip. Lastly, the scaling of qubits is only possible when they show minimal variability, very reduced complexity of their control/readout gate and charge sensing structure. During the course of this thesis, many measurements were performed on many different devices and we have observed that these CMOS structures are extremely reliable and robust to measure, with almost every nanoscale cooled-down device showing edge-state quantum dots, with charging energies consistently in the range of low tens of meV.

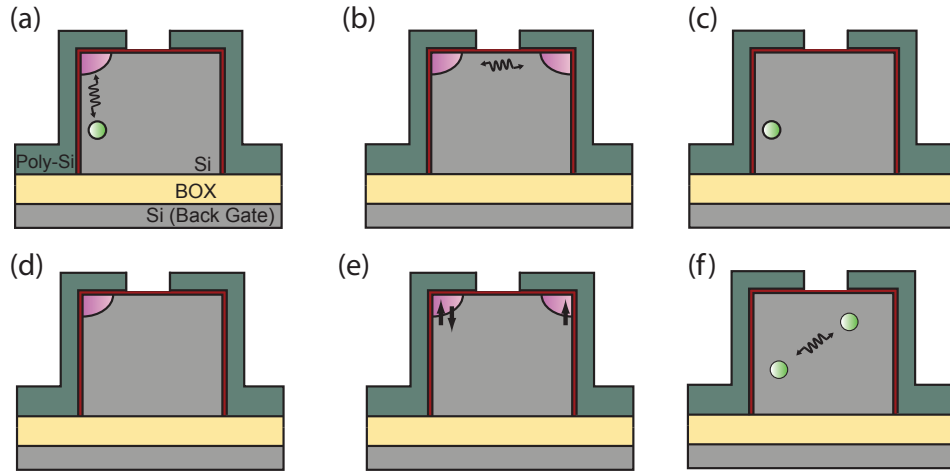


Figure 7.1: Qubit configurations for silicon nanowire finFETs. (a) A hybrid dopant-corner dot system as described in Chapter 6, (b) A double-quantum dot system made up of corner dots, (c) A spin qubit consisting of the spin states of a single dopant, (d) A single-dot spin qubit where the other corner dot can be used as a charge sensor, (e) A charge-spin hybrid qubit as described in Ref. [180] and (f) Two dopants coupled to each other in the transistor channel as in Ref. [108].

Deep dopants in silicon

In Chapter 5 of this thesis we have focused on another goal of hybrid dopant-dot architecture development, which is to identify which dopants are optimum for such a qubit. We mentioned before that phosphorus and the other shallow donors have energies that are located close to the conduction band in silicon, and this leads to low ionisation temperatures and electric fields, both of which are conditions present in nanoscale electrically gated devices. We have therefore explored the deep dopants in silicon (in particular the dopant selenium) which have not been studied extensively despite their strong binding en-

ergies and very high ionization temperatures and fields. Selenium also possesses a strong hyperfine constant, leading it to be suitable for a dopant-dot hybrid qubit driven in the singlet triplet regime by the hyperfine gradient from the nuclear spin of the dopant. In this chapter we have explored this dopant using the tool of electrically detected magnetic resonance (EDMR), and showed the first observation of spin-dependent transport through a deep dopant in selenium. An additional but equally strong motivation for this experiment is in the context of EDMR, where the chalcogens in silicon, by virtue of their deep and double donor nature, are expected to give rise to previously unknown EDMR mechanisms. Indeed, our study yields observations that cannot be adequately explained by EDMR mechanisms commonly used to describe spin dependent transport through shallow donors. We have therefore presented a model of a new mechanism, that of spin dependent trapping based on a difference in singlet-triplet capture rates; a mechanism that is not possible in shallow donors since they lack bound triplet states. In future, the further exploration of EDMR in the chalcogens as well as the integration of selenium dopants into devices are expected to be exciting avenues for research.

Hybrid dopant-dot qubit

In Chapter 6 we put together the gate-based reflectometry technique and CMOS-SOI foundry architecture described above to show a coupling between a single donor and an edge-state quantum dot in a nanowire transistor, and to establish that these two objects behave as a double quantum dot. We explored the coupled system as a charge qubit, measuring the relevant coherence and relaxation times, as well as the tunnel coupling. Finally, we presented a way to differentiate between the singlet and triplet spin states of the coupled qubit and demonstrated Pauli spin blockade, a crucial first step towards a hybrid dopant-dot spin qubit. We also showed progress towards coherent control, involving the design and fabrication of a stripline for controlling spin rotations. While this system is undoubtedly interesting for the purposes of quantum information, it also offers a novel platform for looking at the unexplored physics of an asymmetrical double quantum dot made up of an engineered artificial structure and a natural implanted atom, the latter having the additional degree of freedom of the nuclear spin.

Other advances developed during the course of this thesis have been the design of a flexible device platform in silicon MOS as a testbed for devices with more complicated gate structures, as well as the development of a versatile and low-noise millikelvin temperature

dilution fridge setup suitable for transport and gate based reflectometry measurements in few-electron quantum dots.

7.1 Outlook and future work

A few perspectives emerging out of the current work, and the direction in which further experiments can be taken, are outlined below.

Electron spin resonance

Coherent control of the hybrid spin qubit is a logical next step after the demonstration of spin blockade. Using the stripline design presented which is suitable for these silicon foundry-made devices, experiments are possible that can use ESR to flip the electron spin and hence lift the Pauli spin blockade shown in Chapter 6, recovering the signal at the ICT. Once this is established, pulsed ESR measurements can be performed to achieve coherent control[58].

Charge noise

In our experiments, the measured dephasing rate is close to the tunnel splitting, limiting the fidelity of coherent charge transfer to mediate spin information (the CTAP protocol mentioned in Section 1.4). Since in our system $T_1 \gg T_2$, charge coherence is not limited by phonon coupling. Background charge noise in the gate voltages or charge fluctuations in the sample itself should be the main dephasing sources. The T_2 measured for the quantum dot and dopant-dot systems in this thesis (measured in two different low-temperature systems at different universities) are both similar, in the ~ 200 ps range, and they are also similar to other measurements in these silicon nanowire transistors[108], leading us to believe the charge noise identified is a feature of the device architecture or fabrication process. This could be somewhat mitigated by removal of the nitride spacers in the device, known to bear a large trapped charge density.

Tunability

Currently the device tunnel couplings presented in this thesis are not electrostatically tunable, since there is only one gate which functions as a top gate. The tunnel coupling might

be tunable in a different architecture, for instance one with an extra top gate (such as in the device similar to ours, but with two facing-gates, used in Ref. [108]).

Spin blockade

The asymmetry in our demonstration of Pauli spin blockade for the dopant-dot hybrid qubit (Chapter 6) indicates a hybrid singlet-triplet spin qubit. In such a qubit, mixing between the $S - T_-$ states is generally induced by the nuclear spin bath's magnetic field gradient. As we have discussed previously, in this hybrid double dot the mixing should be dominated by the hyperfine interaction with the nuclear spin localized at the donor site. The time evolution of such a singlet-triplet qubit should then be governed by the donor nuclear spin, enabling controlled rotation gates using NMR excitation. In the case of phosphorus, the $S(1,1) - T_0$ coherent evolution at very low exchange coupling could be driven at ~ 20 MHz, with an even higher frequency possible for bismuth or selenium.

Isotopic purification

The key factor behind the very long spin coherence times obtained in silicon is isotopic purification. Using SOI wafers with a ^{28}Si -rich device layer, grown by means of a chemical vapor deposition (CVD) process, is possible in the foundry at CEA-Leti, where these devices were made. While obtaining isotopically purified silane required for the CVD process is a hurdle, such a development could result in an extremely scalable qubit with coherence times unparalleled in the solid state.

Nuclear spin memory

Long-term, the nuclear spin of the dopant that is essentially a bonus addition to our hybrid spin qubit is a useful resource for a long-lived quantum memory; it has been shown through ensemble measurements to have an (ionised) coherence time of 39 minutes at room temperature [151]. Exploiting the hybrid qubit's interdot exchange coupling would allow a SWAP operation between the quantum dot and the donor atom spin state. Eventually this state could be stored in the donor nucleus using electro-nuclear double resonance (ENDOR) techniques. Finally, a potential further application could be the creation of spin buses with quantum dot chains to mediate quantum information stored in these long-lived donor qubits over long distances [22].

The results in this thesis represent some first steps towards a scalable hybrid dopant-dot architecture implemented in silicon and fabricated using industry compatible techniques. I have shown that our chosen silicon nanowire finFET architecture is a versatile platform for the measurement of quantum dots using the technique of gate-based charge-sensing, which allows close proximity to the quantum dot and accurate charge sensing without sacrificing ease of fabrication. I have also shown that the nano-transistor channel is also a viable host for a coupled dopant-dot system behaving like a double quantum dot. With the observation of Pauli spin blockade and the promise of electron spin resonance in this hybrid quantum dot, the outlook on the coherent control of the spin system is bright. Further efforts to fabricate more controllable systems that retain versatility, for example devices with split-gates for tunable tunnel couplings and independent control of dots, promise to be very fruitful in the future. In addition, the incorporation of more exotic dopants such as selenium into silicon devices might also be an intriguing avenue of research.

Appendix A

Fabrication Listings

Silicon MOS devices

Table A.1: Silicon MOS fabrication process flow

Step	Step Details
	SiO₂ Protective Layer
1	15 mins 1000°C dry oxidation, target 20nm
	Electron Beam Alignment Marks
2	Dehydration, 210°C, 20min
3	HMDS prime
4	Spin ZEP520A, 3370rpm, 180s
5	Hot plate, 180°C, 180s
6	Exposure
7	Develop ZED-N50, 2min, rinse HPLC-IPA, 2min
8	RIE Poly-Si etch (SF ₆ :18, O ₂ :13.5)
Continued on next page.	

Table A.1 – Silicon MOS fabrication process flow continued

Step	Step Details
	Scribe and Wafer Clean
9	Scribe into 4 quadrants, A-D
10	10min FNA (fuming nitric acid)
11	60s HF 20:1, target etch 23 nm
12	10min 45°C RCA1
13	30s HF 20:1
14	10min 45°C RCA2
15	30s HF 20:1
	Channel Stopper Implant through Mask Oxide
16	Mask oxide: dry oxidation 950°C, 10hrs
17	Mask clean: manual Acetone and IPA
18	Lithography: Step 2-3
19	Spin S1813, 5000rpm, 30s
20	Hot plate, 115°C, 1min
21	Exposure
22	Develop, MF319 for 45s, rinse DI water 45s
23	RIE O ₂ plasma ash (descum), 30s
24	Mask oxide etch: 20:1 BHF, 6min30s, target 160nm+overetch
25	Channel stopper implant, Boron, University of Surrey
	Post Implantation Wafer Clean
26	Plasma ash 15min
27	10min FNA
28	HF 20:1, 4min20s etch, target 130nm
29	Fresh HF 20:1, 2 min etch, target 30nm+overetch
Continued on next page.	

Table A.1 – Silicon MOS fabrication process flow continued

Step	Step Details
30	Steps 12-15
	Field Oxide Growth and Etch for Ohmics
31	Wet oxidation 950°C, 42min30s, target 150nm
32	Ohmics lithography: Steps 17-22, with ohmics mask
33	Field oxide etch: 20:1 BHF, upto ~30nm SiO ₂ for protective layer
	Ohmic Regions
34	Ohmics n+ implant, Phosphorus, University of Surrey
35	Wafer clean: Steps 10-15
	Active Regions and Gate Oxide
36	Active region lithography: Steps 17-22, with active regions mask
37	Active region etch: 20:1 BHF, time based on ohmics etch
38	Wafer Clean: Steps 10, 12-15
39	Gate oxide: dry oxidation, 950°C, 5min, 5slm O ₂ , target 8-9nm
	Ohmic Contacts
40	Ohmic contacts lithography: Steps 17-22, with ohmic contacts mask
41	HF etch 20:1 BHF, 50% overetch
42	Thermal evaporation Al(Si) 100nm, rate 1Å/s
43	60°C pressurised NMP liftoff, NMP bath overnight
44	Sample clean, acetone and IPA
	Test Structures
45	Test structure lithography: Steps 17-22 with test structure mask
46	RIE O ₂ plasma ash (descum), 30s
47	Thermal evaporation Al(Si) 100nm, rate 0.4Å/s
48	Liftoff: Steps 43-44
Continued on next page.	

Table A.1 – Silicon MOS fabrication process flow continued

Step	Step Details
	Contact Anneal
49	Forming gas anneal, 20 min, 400°C (after electron beam layers, if device chip)
50	Room temperature test structure measurements (skip if device chip)
	Electron Beam Layer 1
51	Lithography: Positive EBL resist, process depends on design
52	Expose Layer 1: JEOL 100kV electron beam tool
53	Metallization and liftoff: Steps 47-48, 30nm Al(Si)
54	Aluminium Oxide Growth: hot plate 150°C, 10min
	Electron Beam Layer 2
55	Lithography, exposure, metallization, liftoff: Steps 51-53

CEA-Leti devices, post-processing and stripline fabrication

Table A.2: CEA-Leti die, postprocessing and stripline fabrication

Step	Step Details
	Cleave and clean die
1	Apply thick layer of photoresist for protection, hard bake
2	Cleave into 5×5mm chips centering devices of interest
3	30 minutes before spinning, take HSQ 6% out of cold storage to warm up
4	Clean protective resist: 15min acetone
5	Rinse in IPA, 2min
6	N ₂ blow dry, inspect
	Insulation layer
Continued on next page.	

Table A.2 – Stripline fabrication process flow continued

Step	Step Details
7	Apply HSQ to cover chip
8	Spin 1min at 3000rpm, no ramp
9	Bake 1hr at 300°C on clean glass slide, cool 5min
	Spin resist
10	Apply PMMA A4 to cover
11	Spin 2s at 500rpm, 45s at 2000rpm
12	Bake at 180°C, 5min
	Charging Layer and exposure
13	Thermal evaporator: 7-10nm Al, 1Å/s
14	Load into Raith E-Line with metal clamp touching charging layer
15	Expose pattern. Align to images taken of test die earlier, stay on row numbers only
	Metallization
16	Remove charging layer: 45s MF-26A (TMAH developer). Make sure all Al is gone.
17	Rinse in IPA 30s
18	N ₂ blow dry, inspect stripline short carefully under optical microscope
19	Thermal evaporator: 150nm Al, 0.5Å/s
20	Liftoff: overnight in acetone, heat to 60°C if possible for 2hrs
21	Can sonicate in 5s bursts (¡30s total) at low power, followed by inspection.
22	Rinse in IPA 30s
23	N ₂ blow dry, inspect

EDMR Device Fabrication

EDMR measurements are very sensitive to surface impurities, so any fabrication must take place using ultra-clean tools, glassware and evaporator chambers. To illustrate the importance of this surface treatment, spectra before and after a thorough and careful surface cleaning are shown in Fig. A.1.

Table A.3: EDMR interdigitated contact fabrication

Step	Step Details
Cleaning procedures	
1	10 minute clean acetone
2	2 minute rinse IPA
3	N ₂ blow dry
4	10 minute piranha etch (fresh, bubbling H ₂ O ₂ and H ₂ SO ₄ 1:3)
5	Rinse in DI water, 3 times
6	N ₂ blow dry
7	RIE O ₂ plasma ash, 5min
8	60s BHF 20:1 to remove possibly contaminated native oxide
9	Rinse in DI water 3 times, N ₂ blow dry
Lithography and Metallization	
10	Apply S1818 photoresist to cover, spin 5000rpm, 30s
11	Expose in Quintel mask aligner largest 5 × 15 μm finger design that fits on chip
12	Develop in MF-319, IPA rinse
13	Thermal evaporation: 200 nm Al, 0.5 Å/s

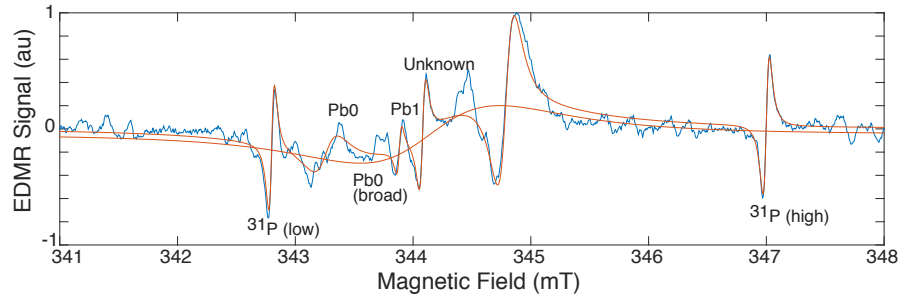


Figure A.1: A test EDMR spectrum taken prior to surface treatment. Dangling bonds at the surface (some identified as P_b centers due to their g-factors) as well as unknown resonances were seen, which were eliminated by intensive surface treatment; compare with Fig. 5.5.

Appendix B

Measurement Notes

Measurement of foundry-fabricated silicon devices

We have explained the basics of the gate-based reflectometry measurements used in this thesis in Chapter 3. In this section, we describe sequentially how to efficiently use the setup described to measure a double quantum dot and attain a suitable level of charge sensitivity. We also present some considerations for improvement.

Identification of samples

Foundry-fabricated devices are typically far more robust and reliable across a large wafer than those made in university research cleanrooms. However, some considerations are:

- Avoid dies from the very edge of a wafer; these tend to have the worst of the typical variations across wafers, even foundry-fabricated ones.
- Avoid channels that are very small, if looking for double quantum dot systems. These dots tend to be extremely well coupled to each other, and to have very similar lever arms to the top gate, leading to an almost invisible quantum capacitance signal at the interdot charge transition. However, with a tunable coupling, or more than one gate, these could be useful devices to measure. Samples in the range of 40 nm to 60 nm are typically interesting.
- If a probe able to work at 4 K that is equipped with an RF setup is available for quick testing, this is invaluable for identifying a sample with a good dopant-dot or double quantum dot system before cooling down in a dilution refrigerator.

Wirebonding

Wirebonding is a little trickier for SOI devices, especially those with very small bond pads made for automatic and accurate wirebonding in large foundries. These typically have very small gaps between devices, and the bond pads themselves can be effectively even smaller if a stripline is added that partially extends over them. A few tricks are:

- When bonding, bond to the source and drain of the device first, and then the gate(s).
- A small $15\ \mu\text{m} \times 15\ \mu\text{m}$ bonder wedge, with $15\ \mu\text{m}$ diameter Al bond wire, has been found to work much better for these devices, increasing the post-bonding yield dramatically.
- Make sure to ground the pins carefully, together and to ground, when transferring to the dilution fridge, and check for shorts between the leads/gates and the stripline, if using.

Testing of samples

These samples can be tested at room temperature, which is an immense bonus, since they do not require a full fridge cooldown cycle before one can find out that whether the device is working or not. A simple and quick procedure to follow for this would be:

- Load the sample with the source connected to a small bias ($\sim 1\ \text{mV}$) and the drain connected to your current amplifier and digital multimeter of choice (this setup is useful for later DC measurements as well) and connect a voltage source to the gate.
- Apply a voltage, in $0.1\ \text{mV}$ increments, to the gate. The source-drain current should then show turn-on around $0.2\text{--}0.6\ \text{V}$ typically. Don't exceed $1\ \text{V}$ on the gate since this can blow the sample.
- If the device turns on, it will most likely show double quantum dot behaviour at low temperature and is worth cooling down.
- If the device is doped and has a lower threshold than others of the same channel size, this has been found to indicate a higher chance of finding a dopant in the channel.
- For making observations of the above sort, it is highly advisable to keep a log of channel size, turn-on voltage, low-temperature behaviour, and other observations about measured devices.

- The back gate can now be connected to another voltage source and ± 5 V applied to it. No LED illumination is required now, at room temperature. The back gate should have a small effect on the source-drain current around turn-on, but this typically intensifies much more at low temperature.

Setup

The sequence of measurements should involve DC measurements followed by setting up and moving to the RF charge sensing measurements. We assume that the sample is now at base temperature in a dilution fridge, around 30 mK. Note that this method of taking RF measurements is just one of many, and is specific to the setting up process for quick feedback and optimization (and not for sensitive or time-resolved qubit operation).

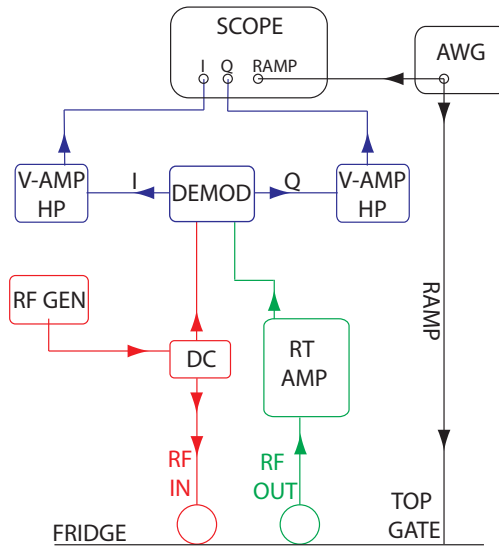


Figure B.1: Room temperature RF setup. A simplified setup for setting up a gate-based RF-reflectometry measurement. The IQ demodulation card is denoted “DEMOM” while the directional coupler is “DC” and the voltage amplifiers used to amplify the I and Q channels after demodulation are labelled “V AMP” as well as “HP” to indicate that a high pass filter is recommended.

- Using the testing setup mentioned earlier, take a two-dimensional map of the source-drain current, for back-gate (between ± 20 V) and top-gate (for $\sim \pm 0.4$ V around threshold). Sub-threshold features in transport could indicate the presence of dopants, as well as quantum dot to lead transitions.

- For changing the back gate, an LED needs to be turned on. This can be flashed for 2 seconds, or kept on if just tuning up the device (this has been found to be disruptive for some devices, but not for others). Remember that the biasing of this LED will be different from that at room temperature. When the LED is correctly on and working, the fridge should heat up by a few millikelvin.
- Connect the resonator lines (connected via a bias tee to the top gate of the device) to a Vector Network Analyser. You should see a resonance around the resonant frequency (350 MHz for our setup), in transmission mode (S_{21}). Record the resonance while sweeping the back gate (with the blue LED biased on), since the resonance depends on the back gate position. The resonator driving frequency will need to be set to the correct value based on where in back gate space we are measuring.
- Set up the instruments as shown in Fig. B.1 and apply a low power of 5 dBm at the resonance frequency (measured on the VNA previously), for the back gate voltage you are at. Do not connect to the IQ demodulator card (or mixer) yet since these can be damaged at too high a power, or to the fridge ports.
- Using a handheld power sensor (Rohde and Schwarz make a good one), check the power going into the fridge reflectometry port, and after calculating the power reaching the sample (based on the attenuation inside the fridge), connect to the fridge port. Then including the amplifier into your calculations, check the power coming out of the fridge. If all is well, check the power that will go into the IQ demodulator card or mixer; this should be within the optimum range specified by the manufacturer. Finally, connect everything according to Fig. B.1.
- Change the gate voltages so that you are at the first interesting feature in gate space, as seen on the DC measurement. If changing the back gate, make sure to change the resonator drive frequency you are using accordingly.
- Using the arbitrary waveform generator, apply a ramp to the top gate (a slow ramp of 33 Hz, driving around 100 mV around the feature identified in DC transport, is a good starting value; the best frequency is a matter of trial and error). Trigger an oscilloscope with this ramp and connect the amplified IQ signals coming from the voltage amplifiers in Fig. B.1 to two oscilloscope channels, using AC coupling.

- If you've done the steps before correctly and everything is well, you should now immediately see clear resonances on the oscilloscope. Factors that can be tuned are the resonant frequency, the resonator drive, and the addition of room temperature attenuation. A good starting measurement is a gate stability diagram.

Other dopant-dot devices measured and results

In this section we present two other doped foundry-fabricated devices in which dopant signatures were seen. Fig. B.1(a) shows a device measured by our collaborators at the University of New South Wales, Australia¹. This device was doped with phosphorus donors, but had a wider and larger channel ($240\text{ nm} \times 100\text{ nm} \times 10\text{ nm}$). A tank circuit with a resonant frequency of 671 MHz was connected to the top gate, a small AC excitation was applied to the drain at frequency of 1.1 kHz and the amplitude of the resonant side band (671.0011 MHz) was measured as a function of top gate and back gate using a spectrum analyzer. The presence of numerous charge transitions in the figure can be attributed to the larger number of dopants in the channel compared to the device presented in Chapter 6. The left panel of Fig. B.1(a) shows a close-up of the stability diagram where a donor-based interdot charge transition is visible, similar to our observations. Fig. B.1(b) shows a doped device with a smaller channel ($30\text{ nm} \times 40\text{ nm}$), measured by me at the Center for Quantum Devices, University of Copenhagen. In this device as well, signature subthreshold resonances indicative of dopants, coupled much more to the back gate, were seen, though fewer in number due to the much smaller channel. This device harboured dopants which were not sufficiently tunnel coupled to the corner dot whose transitions it intersected with; this kind of system provides a major motivation for the movement to devices with the top gate split into two as mentioned before, since then the tunnel coupling could be controlled for the establishment of a dopant-dot qubit using this kind of transition. Since many doped devices show dopant transitions, but coupled to various extents with the corner quantum, the tuning of this coupling could be of great help to form a consistent architecture of dopant-dot qubits.

These additional measurements indicate the flexibility of these devices and the range of measurement setups in various laboratories in which they have been found to yield measurable corner quantum dots, as well as donor-dot couplings.

¹The data shown was taken by Dr. Takeshi Kobayashi.

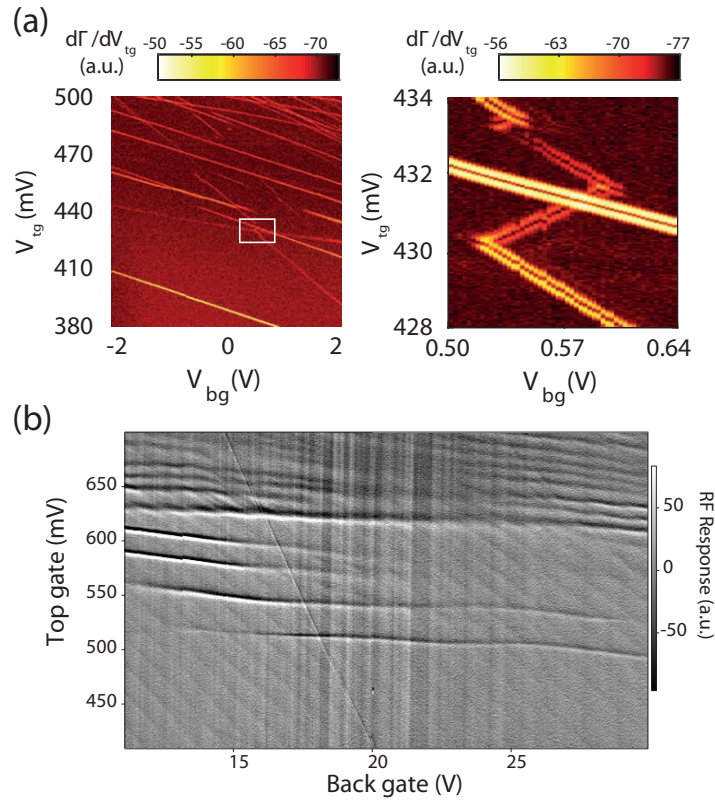


Figure B.2: Additional dopant-dot device measurements. Panel (a) has a top gate versus back gate stability diagram on the left, with a close-up onto the dopant-dot crossing on the right. There is an unrelated transition that cuts through the interdot charge transition. Panel (b) shows a stability diagram from a different device, with a non-interacting dopant transition visible on the left side of the image.

Microwave Simulations

In Chapter 4 we presented results on the microwave response of a quantum dot-to-lead transition arising in the channel of a nanowire transistor such as the ones discussed above. Simulation results were presented for microwave shapes applied to the top gate in the form of a sine wave, a square pulse and a ramp. In this Section we show simulations for the sine wave form of microwave when applied to the top gate of such a device, and detected through RF-reflectometry, but for different (a) temperatures and (b) tunnel rates to the lead. This is shown in Fig. B.3. For the temperature variation in panel (a), we see that the temperature does not affect the splitting of the peak but the peak height and sharpness, leading us to construe that the microwave and temperature measurements can be decoupled and independently useful at higher temperature. For the tunnel rates, it can be seen that the signal intensity follows the trend shown in earlier studies[93, 95] where increasing tunnel rates lead to an increase in the signal strength. However, this does not seem to influence the splitting of the peak either, but only the individual peak heights.

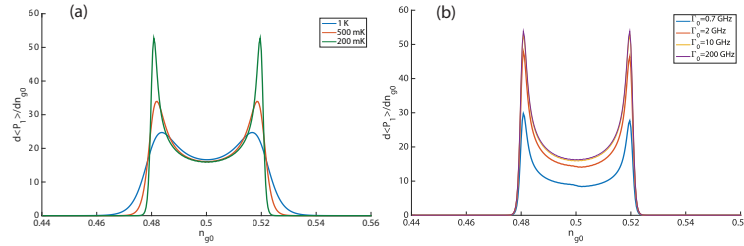


Figure B.3: Microwave simulations for a dot-to-lead transition performed at 4 GHz under (a) elevated temperatures and (b) differing tunnel rates. The splitting of the transition due to the sine-wave shaped microwave excitation is decoupled from these two parameters.

Stripline Modelling

In this section we describe the process of modelling a nanoscale stripline that is compatible with the foundry-fabricated design used in this thesis. The critical task here is to design a structure which maximises the electric field at the spin location while minimising the electric field seen by the device, which could affect charge sensing measurements. For

this purpose, we follow previous work by J. P. Dehollain et al. [179], where four different designs of nanoscale transmission lines were compared².

Choice of Design: The two main contenders were (a) the on-PCB coplanar waveguide with an on-chip coplanar waveguide terminated by a short, and (b) an on-chip CPW-CPS balun (for balancing the transition) design developed by the team behind the work. While both these designs had similar transmission characteristics with minimal stray reflections, the latter design had the advantage that the current (and hence the field strength) was not halved at the spin location. For our purposes, and for compatibility with the foundry-fabricated devices described above (where the dies have devices spaced very closely together), we chose the former design due to space constraints. In addition the design has the widest range of operating frequencies and the lowest insertion loss, since there are no mode conversions[179]. This type of design was used by Fuchs et al. [112] to drive the ESR of a nitrogen-vacancy centre in diamond.

Impedance Matching: The CPW will have to be impedance-matched to the coaxial cable that delivers the microwave. For 50Ω matching, the characteristic impedance of planar transmission lines needs to be taken into account; this is typically a function of the width and thickness of the metal strips, the gap between coplanar strips and the thickness of the dielectric. These parameters were tweaked and modelled in TX-Line, a transmission line calculator from Applied Wave Research, including the PCB characteristics (Rogers 4003C laminate).

Modelling: The software used to model the CPW was CST Microwave Studio, a full-3D microwave engineering software that can be used to model the electric and magnetic fields from the stripline as well. Using this software, we were able to model the whole structure, including the chip and the PCB, as well as the bond wires and the SMA connector delivering the input power, as shown in Chapter 6.

Solver and Meshing: Within CST, the finite integration method (FIM) in the frequency domain was used (repeated to obtain broadband results), with tetrahedral meshing. Subdivided meshes were used to increase the mesh detail near the crucial nanoscale short of the CPW, while the mesh was left less detailed elsewhere.

Probes and Fields: Electric and magnetic field probes were placed in a grid around the stripline to determine the best position to align with the device. Since our stripline is located above the sample (as is the case in Koppens et al. [58], the first demonstration

²Improvements to my initial design and meshing were made by Simon Schaal.

of single-spin ESR in a quantum dot), there is more flexibility compared with Ref. [179] where the device geometry only left a particular coplanar position for the CPS.

Transmission and Fields: Our results and field distributions are shown in Fig. B.4, (we assume 1 mW at the input port, taking into account the attenuation in our dilution fridge). The transmission of the design is excellent, with the simulations showing that the fully-CPW structure shows near-ideal behaviour, with $S_{11} \approx 0$ dB from 0 to 40 GHz, as found in Ref. [179] (where it was also found that this design radiated the smallest electric field at the spin location). Field strengths for our design are shown in Fig. B.4 as well. We see that the field strength decreases strongly with distance from the central pin, which confirms the importance of lowering the level of encapsulation of these foundry-fabricated devices. However, with a field intensity in the high μ T range, we hope to be able to observe cw-ESR from our dopant-dot devices.

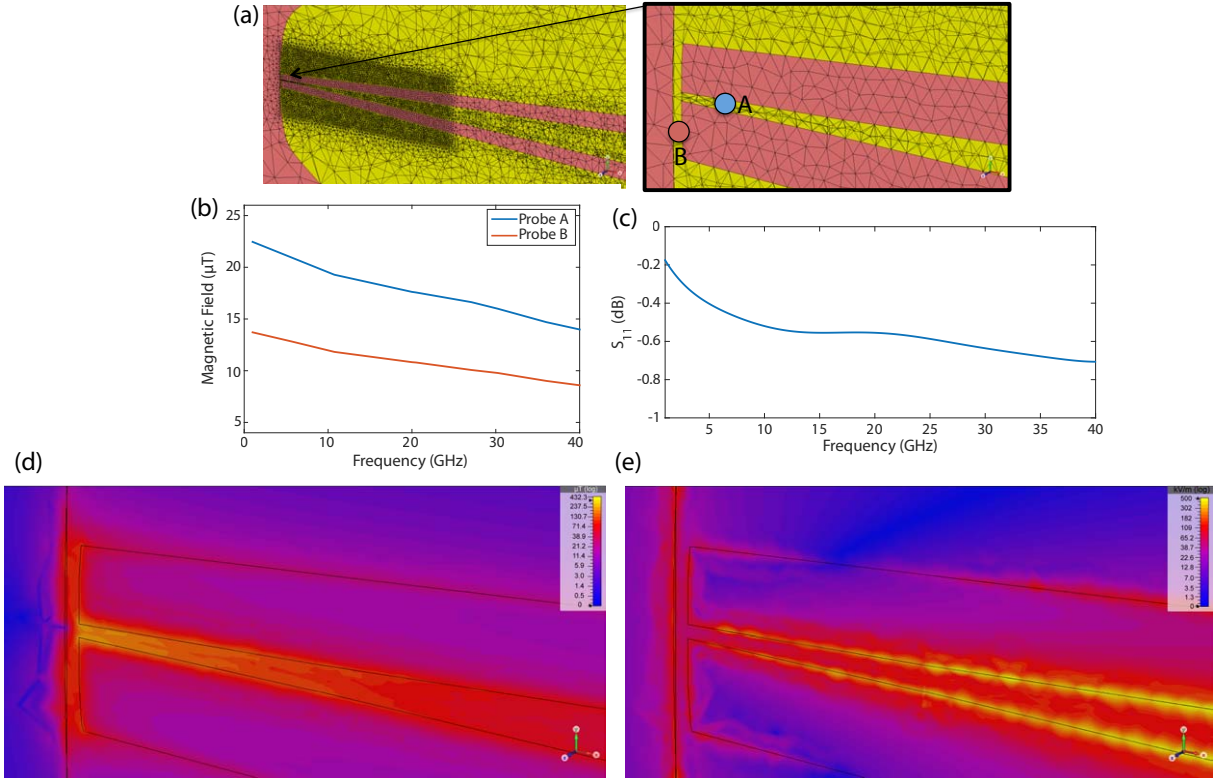


Figure B.4: Coplanar waveguide model, with simulations performed in CST. (a) shows the fine meshing near the critical short of the CPW, while the zoomed-in picture on the right shows the locations of two points where we probe the magnetic field ($2\text{ }\mu\text{m}$ below the surface, due to the device encapsulation). (b) shows the magnetic field intensity in μT at the two field locations shown in (a), labelled as probe A (blue) and B (red). The field is stronger at the location of probe A. (c) shows the reflections in the modelled CPW, with $S_{11} \approx 0\text{ dB}$ from 0 to 40 GHz. (d) and (e) show respectively the simulated magnetic and electric field strengths at the surface.

Bibliography

- [1] International technology roadmap for semiconductors, <http://www.itrs.net> (2009).
- [2] P. Shor, Algorithms for quantum computation: discrete logarithms and factoring, *Proceedings, 35th annual symposium on foundations of computer science* (1994).
- [3] R. P. Feynman, Simulating physics with computers, *International Journal of Theoretical Physics* **21**, 467 (1982).
- [4] D. P. DiVincenzo, The physical implementation of quantum computation, *Fortschr. Phys.* **48**, 711 (2000).
- [5] B. Kane, A silicon-based nuclear spin quantum computer, *Nature* **393**, 133 (1998).
- [6] A. Morello, J. J. Pla, F. A. Zwanenburg, K. W. Chan, and K. Y. Tan, Single-shot readout of an electron spin in silicon, *Nature* **467**, 687 (2010).
- [7] J. J. Pla, K. Y. Tan, J. P. Dehollain, W. H. Lim, J. J. L. Morton, D. N. Jamieson, A. S. Dzurak, and A. Morello, A single-atom electron spin qubit in silicon, *Nature* **489**, 541 (2012).
- [8] J. J. Pla, K. Y. Tan, J. P. Dehollain, W. H. Lim, J. J. L. Morton, F. A. Zwanenburg, D. N. Jamieson, A. S. Dzurak, and A. Morello, High-fidelity readout and control of a nuclear spin qubit in silicon, *Nature* **496**, 334 (2013).
- [9] J. T. Muhonen, J. P. Dehollain, A. Laucht, F. E. Hudson, R. Kalra, T. Sekiguchi, K. Itoh, D. N. Jamieson, J. C. McCallum, A. S. Dzurak, et al., Storing quantum information for 30 seconds in a nanoelectronic device, *Nature Nanotechnology* **9**, 986 (2013).
- [10] J. van Donkelaar, C. Yang, A. Alves, J. McCallum, C. Hougaard, B. Johnson, F. Hudson, A. S. Dzurak, A. Morello, D. Spemann, et al., Single atom devices by ion implantation, *Journal of Physics: Condensed Matter* **27**, 15 (2015).
- [11] M. Fuechsle, J. Miwa, S. Mahapatra, H. Ryu, S. Lee, O. Warschkow, L. C. L. Hollenberg, G. Klimeck, and M. Y. Simmons, A single-atom transistor, *Nature Nanotechnology* **7**, 242 (2012).

- [12] F. Bradbury, A. Tyryshkin, G. Sabouret, J. Bokor, T. Schenkel, and S. A. Lyon, Stark tuning of donor electron spins in silicon, *Physical Review Letters* **97**, 176404 (2006).
- [13] G. Wolfowicz, M. Urdampilleta, M. L. W. Thewalt, H. Riemann, N. V. Abrosimov, P. Becker, H.-J. Pohl, and J. J. L. Morton, Conditional control of donor nuclear spins in silicon using Stark shifts, *Physical Review Letters* **113**, 157601 (2014).
- [14] A. Laucht, J. T. Muhonen, F. A. Mohiyaddin, R. Kalra, J. P. Dehollain, S. Freer, F. E. Hudson, M. Veldhorst, R. Rahman, G. Klimeck, et al., Electrically controlling single-spin qubits in a continuous microwave field, *Science Advances* **1**, 1500022 (2015).
- [15] B. Koiller, X. Hu, and S. D. Sarma, Exchange in silicon-based quantum computer architecture, *Physical Review Letters* **88**, 027903 (2002).
- [16] J. J. L. Morton, A. M. Tyryshkin, R. M. Brown, S. Shankar, B. W. Lovett, A. Ardavan, T. Schenkel, E. E. Haller, J. W. Ager, and S. A. Lyon, Solid state quantum memory using the ^{31}P nuclear spin, *Nature* **455**, 1085 (2008).
- [17] M. Veldorst, J. Hwang, C. Yang, A. Leenstra, B. de Ronde, J. Dehollain, J. Muhonen, F. Hudson, K. Itoh, A. Morello, et al., An addressable quantum dot qubit with fault-tolerant control fidelity, *Nature Nanotechnology* **9**, 981 (2014).
- [18] M. Veldorst, C. Yang, J. Hwang, W. Huang, J. Dehollain, J. Muhonen, S. Simmons, A. Laucht, F. Hudson, K. Itoh, et al., A two qubit logic gate in silicon, *Nature* **526**, 410 (2015).
- [19] T. Schenkel, C. C. Lo, C. D. Weis, J. Bokor, A. M. Tyryshkin, and S. A. Lyon, in *Single-Atom Nanoelectronics*, edited by E. Prati and T. Shinada (Taylor and Francis Group, 2013), p. 255.
- [20] D. Loss and D. P. DiVincenzo, Quantum computation with quantum dots, *Physical Review A* **57**, 120 (1998).
- [21] D. M. Zajac, T. M. Hazard, X. Mi, E. Nielsen, and J. R. Petta, Scalable gate architecture for a one-dimensional array of semiconductor spin qubits, *Phys. Rev. Applied* **6**, 054013 (2016).
- [22] M. Friesen, A. Biswas, X. Hu, and D. Lidar, Efficient multiqubit entanglement via a spin bus, *Physical Review Letters* **98**, 1 (2007).
- [23] K. D. Petersson, C. G. Smith, D. Anderson, P. Atkinson, G. A. C. Jones, and D. A. Ritchie, Charge and spin state readout of a double quantum dot coupled to a resonator., *Nano letters* **10**, 2789 (2010).

- [24] A. D. Greentree, J. H. Cole, A. R. Hamilton, and L. C. L. Hollenberg, Coherent electronic transfer in quantum dot systems using adiabatic passage, *Physical Review B* **70**, 235317 (2004).
- [25] R. Rahman, R. P. Muller, J. E. Levy, M. S. Carroll, G. Klimeck, A. D. Greentree, and L. C. L. Hollenberg, Coherent electron transport by adiabatic passage in an imperfect donor chain, *Physical Review B* **82**, 1 (2010).
- [26] T. A. Baart, M. Shafiei, T. Fujita, C. Reichl, W. Wegscheider, and L. M. K. Vandersypen, Single-spin ccd, *Nature Nanotechnology* **11**, 330 (2016).
- [27] M. F. González-Zalba, D. Heiss, and A. J. Ferguson, A hybrid double-dot in silicon, *New Journal of Physics* **14**, 023050 (2012).
- [28] H. Sellier, G. P. Lansbergen, J. Caro, and S. Rogge, Transport spectroscopy of a single dopant in a gated silicon nanowire, *Physical Review Letters* **97**, 206805 (2006).
- [29] M. Urdampilleta, A. Chatterjee, C. C. Lo, T. Kobayashi, J. Mansir, S. Barraud, A. C. Betz, S. Rogge, M. F. González-Zalba, and J. J. Morton, Charge dynamics and spin blockade in a hybrid double quantum dot in silicon, *Physical Review X* **5**, 031024 (2015).
- [30] P. Harvey-Collard, N. T. Jacobson, M. Rudolph, J. Dominguez, G. A. Ten Eyck, J. R. Wendt, T. Pluym, J. K. Gamble, M. P. Lilly, M. Pioro-Ladrière, et al., Nuclear-driven electron spin rotations in a single donor coupled to a silicon quantum dot, *arXiv:1512.01606v1* (2015).
- [31] R. Hanson, L. P. Kouwenhoven, J. R. Petta, S. Tarucha, and L. M. K. Vandersypen, Spins in few-electron quantum dots, *Reviews of Modern Physics* **79**, 1217 (2007).
- [32] L. Hofstetter, S. Csonka, J. Nygård, and C. Schönenberger, Cooper pair splitter realized in a two-quantum-dot Y-junction, *Nature* **461**, 960 (2009).
- [33] F. Pei, E. A. Laird, G. A. Steele, and L. P. Kouwenhoven, Valley-spin blockade and spin resonance in carbon nanotubes, *Nature Nanotechnology* **7**, 630 (2012).
- [34] J. Baugh, Y. Kitamura, K. Ono, and S. Tarucha, Large nuclear Overhauser fields detected in vertically coupled double quantum dots, *Physical Review Letters* **99**, 096804 (2007).
- [35] D. Schroer, S. Ludwig, J. P. Kotthaus, K. Eberl, and W. Wegscheider, *Research Reports: Quantum dots as quantum bits* (L. M. Universitat Meunchen, Meunchen, 2004).
- [36] W. G. Van der Wiel, S. de Franceschi, J. M. Elzerman, T. Fujisawa, S. Tarucha, and L. P. Kouwenhoven, Electron transport through double quantum dots, *Reviews of Modern Physics* **75**, 1 (2002).

- [37] L. P. Kouwenhoven, D. G. Austing, and S. Tarucha, Few-electron quantum dots, *Reports on Progress in Physics* **64**, 701 (2001).
- [38] T. Fujisawa, T. Hayashi, and S. Sasaki, Time-dependent single-electron transport through quantum dots, *Reports on Progress in Physics* **69**, 759 (2006).
- [39] T. Hayashi, T. Fujisawa, H. D. Cheong, Y. H. Jeong, and Y. Hirayama, Coherent manipulation of electronic states in a double quantum dot, *Physical Review Letters* **91**, 226804 (2003).
- [40] T. H. Oosterkamp, T. Fujisawa, and W. G. Van der Wiel, Microwave spectroscopy of a quantum-dot molecule, *Nature* **395**, 873 (1998).
- [41] J. R. Petta, A. C. Johnson, C. M. Marcus, M. P. Hanson, and A. C. Gossard, Manipulation of a single charge in a double quantum dot, *Physical Review Letters* **93**, 186802 (2004).
- [42] K. W. Lehnert, K. Bladh, L. F. Spietz, D. Gunnarsson, D. I. Schuster, P. Delsing, and R. J. Schoelkopf, Measurement of the excited-state lifetime of a microelectronic circuit, *Physical Review Letters* **90**, 027002 (2003).
- [43] S. N. Shevchenko, S. Ashab, and F. Nori, Landau–Zener–Stückelberg interferometry, *Physics Reports* **492**, 1 (2010).
- [44] B. Damski and W. H. Zurek, Adiabatic-impulse approximation for avoided level crossings: from phase-transition dynamics to Landau–Zener evolutions and back again, *Physical Review A* **73**, 063405 (2006).
- [45] J. Stehlik, M. Z. Maialle, M. H. Degani, and J. R. Petta, Role of multilevel Landau–Zener interference in extreme harmonic generation, *Phys. Rev. B* **94**, 075307 (2016).
- [46] M. F. González-Zalba, S. N. Shevchenko, S. Barraud, J. R. Johansson, A. J. Ferguson, F. Nori, and A. C. Betz, Gate-sensing coherent charge oscillations in a silicon field-effect transistor, *Nano Letters* **16**, 1614 (2016).
- [47] L. D. Landau and E. M. Lifshitz, *Quantum Mechanics: Non-Relativistic Theory* (Pergamon Press, Oxford, 1977).
- [48] L. D. Landau, A theory of energy transfer on collisions, *Physikalische Zeitschrift der Sowjetunion* **1**, 88 (1932).
- [49] E. C. G. Stückelberg, Theory of inelastic collisions between atoms, *Helvetica Physica Acta* **5**, 369 (1932).
- [50] J. R. Petta, H. Lu, and A. C. Gossard, A coherent beam splitter for electronic spin states, *Science* **327**, 669 (2010).

- [51] K. D. Petersson, J. R. Petta, H. Lu, and A. C. Gossard, Quantum coherence in a one-electron semiconductor charge qubit, *Physical Review Letters* **105**, 246804 (2010).
- [52] K. Wang, *Few-electron Qubits in Silicon Quantum Electronic Devices* (PhD Thesis: Princeton University, Princeton, 2014).
- [53] Y. Nakamura, Y. A. Pashkin, and J. S. Tsai, Coherent control of macroscopic quantum states in a single-Cooper-pair box, *Nature* **398**, 786 (1999).
- [54] D. Rugar, R. Budakian, H. J. Mamin, and B. W. Chui, Single spin detection by magnetic resonance force microscopy, *Nature* **430**, 329 (2004).
- [55] M. S. Grinolds, P. Maletinsky, S. Hong, M. D. Lukin, R. L. Walsworth, and A. Yacoby, Quantum control of proximal spins using nanoscale magnetic resonance imaging, *Nature Physics* **7**, 687 (2011).
- [56] J. M. Elzerman, R. Hanson, L. H. Willems van Beveren, B. Witkamp, L. M. K. Vandersypen, and L. P. Kouwenhoven, Single-shot read-out of an individual electron spin in a quantum dot, *Nature* **430**, 431 (2004).
- [57] A. C. Johnson, J. R. Petta, C. M. Marcus, M. P. Hanson, and A. C. Gossard, Singlet-triplet spin blockade and charge sensing in a few-electron double quantum dot, *Physical Review B* **72**, 165308 (2005).
- [58] F. H. L. Koppens, C. Buizert, K. J. Tielrooij, I. T. Vink, K. C. Nowack, T. Meunier, L. P. Kouwenhoven, and L. M. K. Vandersypen, Driven coherent oscillations of a single electron spin in a quantum dot, *Nature* **442**, 766 (2006).
- [59] K. C. Nowack, F. H. L. Koppens, Y. V. Nazarov, and L. M. K. Vandersypen, Coherent control of a single electron spin with electric fields, *Science* **318**, 1430 (2007).
- [60] M. Pioro-Ladrière, T. Obata, Y. Tokura, Y. S. Shin, and T. Kubo, Electrically driven single-electron spin resonance in a slanting Zeeman field, *Nature Physics* **4**, 776 (2008).
- [61] E. Kawakami, P. Scarlino, D. R. Ward, F. R. Braakman, D. E. Savage, M. G. Lagally, M. Friesen, S. N. Coppersmith, M. A. Eriksson, and L. M. K. Vandersypen, Electrical control of a long-lived spin qubit in a Si/SiGe quantum dot, *Nature Nanotechnology* **9**, 666 (2014).
- [62] E. A. Laird, C. Barthel, E. I. Rashba, C. M. Marcus, M. P. Hanson, and A. C. Gossard, Hyperfine-mediated gate-driven electron spin resonance, *Physical Review Letters* **99**, 246601 (2007).

- [63] T. Meunier, I. T. Vink, L. H. W. van Beveren, K. J. Tielrooij, R. Hanson, F. H. L. Koppens, H. P. Tranitz, W. Wegscheider, L. P. Kouwenhoven, and L. M. K. Vandersypen, Experimental signature of phonon-mediated spin relaxation in a two-electron quantum dot, *Physical Review Letters* **98**, 126601 (2007).
- [64] J. Levy, Universal quantum computation with spin-1/2 Pairs and Heisenberg exchange, *Physical Review Letters* **89**, 147902 (2002).
- [65] M. Schroer, *Charge and Spin Manipulation in InAs Nanowires* (PhD Thesis: Princeton University, Princeton, 2012).
- [66] J. R. Petta, A. C. Johnson, J. M. Taylor, E. A. Laird, A. Yacoby, M. D. Lukin, C. M. Marcus, M. P. Hanson, and A. C. Gossard, Coherent manipulation of coupled electron spins in semiconductor quantum dots, *Science* **309**, 2180 (2005).
- [67] J. R. Petta, J. M. Taylor, A. C. Johnson, A. Yacoby, M. D. Lukin, C. M. Marcus, M. P. Hanson, and A. C. Gossard, Dynamic nuclear polarization with single electron spins, *Physical Review Letters* **100**, 067601 (2008).
- [68] D. J. Reilly, J. M. Taylor, J. R. Petta, C. M. Marcus, M. P. Hanson, and A. C. Gossard, Suppressing spin qubit dephasing by nuclear state preparation, *Science* **321**, 817 (2008).
- [69] E. A. Laird, J. M. Taylor, D. P. DiVincenzo, C. M. Marcus, M. P. Hanson, and A. C. Gossard, Coherent spin manipulation in an exchange-only qubit, *Physical Review B* **82**, 075403 (2010).
- [70] D. P. DiVincenzo, D. Bacon, J. Kempe, and G. Burkard, Universal quantum computation with the exchange interaction, *Nature* **408**, 339 (2000).
- [71] J. Könemann, R. J. Haug, D. K. Maude, V. I. Fal'ko, and B. L. Altshuler, Spin-orbit coupling and anisotropy of spin splitting in quantum dots, *Physical Review Letters* **94**, 226404 (2005).
- [72] R. Winkler, *Spin-orbit coupling effects in two-dimensional electron and hole systems*, vol. 191 of *Springer Tracts in Modern Physics* (Springer Science & Business Media, Berlin, 2003).
- [73] J. D. Jackson, *Classical electrodynamics* (John Wiley & Sons, New York, 1975).
- [74] G. Dresselhaus, Spin-orbit coupling effects in zinc blende structures, *Physical Review* **100**, 580 (1955).
- [75] E. I. Rashba, Properties of semiconductors with an extremum loop, *Soviet Physics Solid State* **2**, 1109 (1960).

- [76] T. Ihn, *Semiconductor Nanostructures: Quantum states and electronic transport* (Oxford University Press, Oxford, 2010).
- [77] M. Raith, P. Stano, and J. Fabian, Theory of spin relaxation in two-electron laterally coupled Si/SiGe quantum dots, *Physical Review B* **86**, 205321 (2012).
- [78] C. J. Wellard, L. C. L. Hollenberg, F. Parisoli, L. M. Kettle, H. S. Goan, J. A. L. McIntosh, and D. N. Jamieson, Electron exchange coupling for single-donor solid-state spin qubits, *Physical Review B* **68**, 195209 (2003).
- [79] G. Wolfowicz, A. M. Tyryshkin, R. E. George, H. Riemann, N. V. Abrosimov, P. Becker, H.-J. Pohl, M. L. W. Thewalt, S. Lyon, and J. J. L. Morton, Atomic clock transitions in silicon-based spin qubits, *Nature Nanotechnology* **8**, 561 (2013).
- [80] J. M. Luttinger and W. Kohn, Motion of electrons and holes in perturbed periodic fields, *Physical Review* **97**, 869 (1955).
- [81] M. Taniguchi and S. Narita, D-state in silicon, *Solid State Comm.* **20**, 131 (1976).
- [82] G. P. Lansbergen, R. Rahman, J. Verduijn, G. C. Tettamanzi, N. Collaert, S. Biesemans, G. Klimeck, L. C. L. Hollenberg, and S. Rogge, Lifetime-enhanced transport in silicon due to spin and valley blockade, *Physical Review Letters* **107**, 136602 (2011).
- [83] C. Poole and H. A. Farach, *Handbook of electron spin resonance* (Springer-Verlag, New York, 1999).
- [84] M. Xiao, I. Martin, E. Yablonovitch, and H. W. Jiang, Electrical detection of the spin resonance of a single electron in a silicon field-effect transistor, *Nature* **430**, 435 (2004).
- [85] D. R. McCamey, H. Huebl, M. S. Brandt, W. D. Hutchison, J. C. McCallum, R. G. Clark, and A. R. Hamilton, Electrically detected magnetic resonance in ion-implanted Si:P nanostructures, *Applied Physics Letters* **89**, 182115 (2006).
- [86] C. C. Lo, *Electrical Detection of Spin-Dependent Transport in Silicon* (PhD Thesis: University of California at Berkeley, Berkeley, 2011).
- [87] A. C. Johnson, *Charge Sensing and Spin Dynamics in GaAs Quantum Dots* (PhD Thesis: Harvard University, Cambridge, 2005).
- [88] L. Di Carlo, *Mesoscopic Electronics Beyond DC Transport* (PhD Thesis: Harvard University, Cambridge, 2007).
- [89] M. F. González-Zalba, *Single donor detection in silicon nanostructures* (PhD Thesis: University of Cambridge, Cambridge, 2012).

- [90] F. Mueller, R. N. Schouten, M. Brauns, T. Gang, W. H. Lim, N. S. Lai, A. S. Dzurak, W. G. van der Wiel, and F. A. Zwanenburg, Printed circuit board metal powder filters for low electron temperatures, *Review of Scientific Instruments* **84**, 044706 (2013).
- [91] R. Kalra, A. Laucht, J. P. Dehollain, D. Bar, S. Freer, S. Simmons, J. T. Muhonen, and A. Morello, Vibration-induced electrical noise in a cryogen-free dilution refrigerator: characterization, mitigation, and impact on qubit coherence, *arXiv:1603.03146v2* (2016).
- [92] J. P. Pekola, K. P. Hirvi, J. P. Kauppinen, and M. A. Paalanen, Thermometry by arrays of tunnel junctions, *Physical Review Letters* **73**, 2903 (1994).
- [93] M. F. González-Zalba, S. Barraud, A. J. Ferguson, and A. C. Betz, Probing the limits of gate-based charge sensing, *Nature Communications* **6**, 6084 (2015).
- [94] J. C. Frake, S. Kano, C. Ciccarelli, J. Griffiths, M. Sakamoto, T. Teranishi, Y. Majima, C. G. Smith, and M. R. Buitelaar, Radio-frequency capacitance spectroscopy of metallic nanoparticles, *Scientific Reports* **5**, 10858 (2015).
- [95] M. G. House, T. Kobayashi, B. Weber, S. J. Hile, T. F. Watson, J. van der Heijden, S. Rogge, and M. Y. Simmons, Radio frequency measurements of tunnel couplings and singlet–triplet spin states in Si:P quantum dots, *Nature Communications* **6**, 8848 (2015).
- [96] A. Cottet, C. Mora, and T. Kontos, Mesoscopic admittance of a double quantum dot, *Physical Review B* **83**, 121311 (2011).
- [97] F. Persson, C. Wilson, M. Sandberg, and P. Delsing, Fast readout of a single cooper-pair box using its quantum capacitance, *Physical Review B* **82**, 134533 (2010).
- [98] S. Hellmüller, M. Pikulski, T. Müller, B. Küng, G. Puebla-Hellmann, A. Wallraff, M. Beck, K. Ensslin, and T. Ihn, Optimization of sample-chip design for stub-matched radio-frequency reflectometry measurements, *Applied Physics Letters* **101**, 042112 (2012).
- [99] S. M. Sze, *VLSI technology* (McGraw-Hill, New York, 1988).
- [100] B. E. Deal, Standardized terminology for oxide charges associated with thermally oxidized silicon, *Journal of The Electrochemical Society* **127**, 979 (1980).
- [101] A. Stirling, A. Pasquarello, J. C. Charlier, and R. Car, Dangling bond defects at Si-SiO₂ interfaces: atomic structure of the Pb1 center, *Physical Review Letters* **85**, 2773 (2000).
- [102] A. Rossi, T. Tanttu, F. E. Hudson, Y. Sun, M. Möttönen, and A. S. Dzurak, Silicon metal-oxide-semiconductor quantum dots for single-electron pumping, *Journal of Visualized Experiments* **100**, 52852 (2015).

- [103] A. Dzurak, One- and two-qubit logic using silicon-MOS quantum dots, *APS March Meeting Abstracts* **61**, 2 (2016).
- [104] M. F. González-Zalba and TOLOP Project Partners, Final report: Towards low power information and communication technologies, (2016).
- [105] B. Voisin, V.-H. Nguyen, J. Renard, X. Jehl, S. Barraud, F. Triozon, M. Vinet, I. Duchemin, Y.-M. Niquet, S. de Franceschi, et al., Few-electron edge-state quantum dots in a silicon nanowire field-effect transistor, *Nano Letters* **14**, 2094 (2014).
- [106] A. C. Betz, R. Wacquez, M. Vinet, X. Jehl, A. L. Saraiva, M. Sanquer, A. J. Ferguson, and M. F. González-Zalba, Dispersively detected Pauli spin-blockade in a silicon nanowire field-effect transistor, *Nano Letters* **15**, 4622 (2015).
- [107] H. Sellier, G. P. Lansbergen, J. Caro, S. Rogge, N. Collaert, I. Ferain, M. Jurczak, and S. Biesemans, Subthreshold channels at the edges of nanoscale triple-gate silicon transistors, *Applied Physics Letters* **90**, 073502 (2007).
- [108] E. Dupont-Ferrier, B. Roche, B. Voisin, X. Jehl, R. Wacquez, M. Vinet, M. Sanquer, and S. De Franceschi, Coherent coupling of two dopants in a silicon nanowire probed by Landau-Zener-Stückelberg interferometry, *Physical Review Letters* **110**, 136802 (2013).
- [109] M. S. Child, *Molecular Collision Theory* (Academic Press, London, 1974).
- [110] L. Y. Gorelik, N. I. Lundin, V. S. Shumeiko, R. I. Shekhter, and M. Jonson, Superconducting single-mode contact as a microwave-activated quantum interferometer, *Physical Review Letters* **81**, 2538 (1998).
- [111] W. Wernsdorfer, R. Sessoli, A. Caneschi, D. Gatteschi, and A. Cornia, Nonadiabatic Landau-Zener tunneling in Fe₈ molecular nanomagnets, *Europhysics Letters* **50**, 552 (2000).
- [112] G. D. Fuchs, V. V. Dobrovitski, D. M. Toyli, F. J. Heremans, and D. D. Awschalom, Gigahertz dynamics of a strongly driven single quantum spin, *Science* **326**, 1520 (2009).
- [113] M. Mark, T. Kraemer, P. Waldburger, J. Herbig, C. Chin, H.-C. Nägerl, and R. Grimm, Stückelberg Interferometry with ultracold molecules, *Physical Review Letters* **99**, 113201 (2007).
- [114] H. Ribeiro and G. Burkard, Nuclear state preparation via Landau-Zener-Stückelberg transitions in double quantum dots, *Physical Review Letters* **102**, 216802 (2009).
- [115] W. D. Oliver, Y. Yu, J. C. Lee, K. K. Berggren, L. S. Levitov, and T. P. Orlando, Mach-Zehnder interferometry in a strongly driven superconducting qubit, *Science* **310**, 1653 (2005).

- [116] M. Sillanpää, T. Lehtinen, A. Paila, Y. Makhlin, and P. Hakonen, Continuous-time monitoring of Landau-Zener interference in a Cooper-pair box, *Physical Review Letters* **96**, 187002 (2006).
- [117] C. M. Wilson, T. Duty, F. Persson, M. Sandberg, G. Johansson, and P. Delsing, Coherence times of dressed states of a superconducting qubit under extreme driving, *Physical Review Letters* **98**, 257003 (2007).
- [118] J. I. Colless, A. C. Mahoney, J. M. Hornibrook, A. C. Doherty, H. Lu, A. C. Gossard, and D. J. Reilly, Dispersive readout of a few-electron double quantum dot with fast RF-gate sensors, *Physical Review Letters* **110**, 046805 (2013).
- [119] B. Roche, B. Voisin, X. Jehl, R. Wacquez, M. Sanquer, M. Vinet, V. Deshpande, and B. Previtali, A tunable, dual mode field-effect or single electron transistor, *Applied Physics Letters* **100**, 032107 (2012).
- [120] B. Voisin, V.-H. Nguyen, J. Renard, X. Jehl, S. Barraud, F. Triozon, M. Vinet, I. Duchemin, Y.-M. Niquet, S. de Franceschi, et al., Few-electron edge-state quantum dots in a silicon nanowire field-effect transistor, *Nano Letters* **14**, 2094 (2014).
- [121] T. Bergsten, T. Claeson, and P. Delsing, A fast, primary Coulomb blockade thermometer, *Applied Physics Letters* **78**, 1264 (2014).
- [122] R. A. Kamper and J. E. Zimmerman, Noise thermometry with the Josephson effect, *Journal of Applied Physics* **42**, 132 (1971).
- [123] L. Spietz, K. W. Lehnert, I. Siddiqi, and R. J. Schoelkopf, Primary electronic thermometry using the shot noise of a tunnel junction, *Science* **300**, 1929 (2003).
- [124] A. Mavalankar, S. J. Chorley, J. Griffiths, G. A. C. Jones, I. Farrer, D. A. Ritchie, and C. G. Smith, A non-invasive electron thermometer based on charge sensing of a quantum dot, *Applied Physics Letters* **103**, 133116 (2013).
- [125] S. J. Chorley, J. Wabnig, Z. V. Penfold-Fitch, K. D. Petersson, J. Frake, C. G. Smith, and M. R. Buitelaar, Measuring the complex admittance of a carbon nanotube double quantum dot, *Physical Review Letters* **108**, 036802 (2012).
- [126] J. P. Pekola, J. J. Toppari, J. P. Kauppinen, K. M. Kinnunen, A. J. Manninen, and A. G. M. Jansen, Coulomb blockade-based nanothermometry in strong magnetic fields, *Journal of Applied Physics* **83**, 5582 (1998).
- [127] R. Ashoori, H. Stormer, J. Weiner, L. Pfeiffer, S. Pearton, K. Baldwin, and K. West, Single-electron capacitance spectroscopy of discrete quantum levels, *Physical Review Letters* **68**, 3088 (1992).
- [128] M. D. Schroer, M. Jung, K. D. Petersson, and J. R. Petta, Radio frequency charge parity meter, *Physical Review Letters* **109**, 166804 (2012).

- [129] A. Mavalankar, T. Pei, E. M. Gauger, J. H. Warner, G. A. D. Briggs, and E. A. Laird, Photon-assisted tunneling and charge dephasing in a carbon nanotube double quantum dot, *Physical Review B* **93**, 235428 (2016).
- [130] C. Tahan and R. Joynt, Relaxation of excited spin, orbital, and valley qubit states in ideal silicon quantum dots, *Physical Review B* **89**, 075302 (2014).
- [131] A. M. Tyryshkin, S. A. Lyon, A. V. Astashkin, and A. M. Raitsimring, Electron spin relaxation times of phosphorus donors in silicon, *Physical Review B* **68**, 193207 (2003).
- [132] H. G. Grimmeiss, E. Janzen, and K. Larsson, Multivalley spin splitting of 1s states for sulfur, selenium, and tellurium donors in silicon, *Physical Review B* **25**, 2627 (1982).
- [133] D. J. Lepine, Spin-dependent recombination on silicon surface, *Physical Review B* **6**, 436 (1972).
- [134] D. E. Carlson and C. R. Wronski, Amorphous silicon solar cell, *Applied Physical Letters* **28**, 671 (1976).
- [135] H. G. Grimmeiss, E. Janzen, and B. Skarstam, Electronic properties of selenium-doped silicon, *Journal of Applied Physics* **51**, 3740 (1980).
- [136] H. G. Grimmeiss, E. Janzen, H. Ennen, O. Schirmer, J. Schneider, R. Wörner, C. Holm, E. Sirtl, and P. Wagner, Tellurium donors in silicon, *Physical Review B* **24**, 4571 (1981).
- [137] E. Janzen, R. Stedman, G. Grossmann, and H. G. Grimmeiss, High-resolution studies of sulfur- and selenium-related donor centers in silicon, *Physical Review B* **29**, 1907 (1984).
- [138] P. T. Huy, C. A. J. Ammerlaan, T. Gregorkiewicz, and D. T. Don, Hydrogen passivation of the selenium double donor in silicon: a study by magnetic resonance, *Physical Review B* **61**, 7448 (2000).
- [139] R. E. Peale, K. Muro, A. J. Sievers, and F. S. Ham, Zeeman splitting of double-donor spin-triplet levels in silicon, *Physical Review B* **37**, 10829 (1988).
- [140] M. Steger, A. Yang, M. L. W. Thewalt, M. Cardona, H. Riemann, N. V. Abrosimov, M. F. Churbanov, A. V. Gusev, A. D. Bulanov, I. D. Kovalev, et al., High-resolution absorption spectroscopy of the deep impurities S and Se in 28-Si revealing the 77-Se hyperfine splitting, *Physical Review B* **80**, 115204 (2009).
- [141] R. Lo Nardo, G. Wolfowicz, S. Simmons, A. M. Tyryshkin, H. Riemann, N. V. Abrosimov, P. Becker, H.-J. Pohl, M. Steger, S. A. Lyon, et al., Spin relaxation and donor-acceptor recombination of Se⁺ in 28-silicon, *Phys. Rev. B* **92**, 165201 (2015).

- [142] K. J. Morse, R. J. S. Abraham, H. Riemann, N. V. Abrosimov, P. Becker, H.-J. Pohl, M. L. W. Thewalt, and S. Simmons, A photonic platform for donor spin qubits in silicon, *arXiv:1606.03488v1* (2016).
- [143] M. J. Calderon, B. Koiller, and S. Das Sarma, Proposal for electron spin relaxation measurements using double-donor excited states in Si quantum computer architectures, *Physical Review B* **75**, 161304 (2007).
- [144] R. Lo Nardo, *Charge state manipulation of silicon-based donor spin qubits* (PhD Thesis: Oxford University, Oxford, 2015).
- [145] T. G. Castner, Raman spin-lattice relaxation of shallow donors in silicon, *Physical Review* **130**, 58 (1963).
- [146] R. Orbach, On the theory of spin-lattice relaxation in paramagnetic salts, *Proceedings of the Physical Society* **77**, 821 (1961).
- [147] T. G. Castner, Orbach spin-lattice relaxation of shallow donors in silicon, *Physical Review* **155**, 816 (1967).
- [148] D. K. Wilson and G. Feher, Electron spin resonance experiments on donors in silicon, *Physical Review* **124**, 1068 (1961).
- [149] R. C. Fletcher, W. A. Yager, G. L. Pearson, and F. R. Merritt, Hyperfine splitting in spin resonance of group V donors in silicon, *Physical Review* **95**, 844 (1954).
- [150] G. Wolfowicz, S. Simmons, A. M. Tyryshkin, R. E. George, H. Riemann, N. V. Abrosimov, P. Becker, H.-J. Pohl, S. A. Lyon, M. L. W. Thewalt, et al., Decoherence mechanisms of 209-Bi donor electron spins in isotopically pure 28-Si, *Physical Review B* **86**, 245301 (2012).
- [151] K. Saeedi, S. Simmons, J. Z. Salvail, P. Dluhy, H. Riemann, N. V. Abrosimov, P. Becker, H.-J. Pohl, J. J. L. Morton, and M. L. W. Thewalt, Room-temperature quantum bit storage exceeding 39 minutes using ionized donors in silicon-28, *Science* **342**, 830 (2013).
- [152] L. Dreher, F. Hoehne, M. Stutzmann, and M. S. Brandt, Nuclear spins of ionized phosphorus donors in silicon, *Physical Review Letters* **108**, 027602 (2012).
- [153] R. Kalra, A. Laucht, C. D. Hill, and A. Morello, Robust two-qubit gates for donors in silicon controlled by hyperfine interactions, *Physical Review X* **4**, 021044 (2014).
- [154] G. Pica, G. Wolfowicz, M. Urdampilleta, M. L. W. Thewalt, H. Riemann, N. V. Abrosimov, P. Becker, H.-J. Pohl, J. J. L. Morton, R. N. Bhatt, et al., Hyperfine stark effect of shallow donors in silicon, *Physical Review B* **90**, 195204 (2014).

- [155] H. G. Grimmeiss and E. Janzen, in *Deep Centers in Semiconductors*, edited by S. T. Pantelides (CRC Press, 1992), pp. 87–176.
- [156] V. Lang, C. C. Lo, R. E. George, S. A. Lyon, J. Bokor, T. Schenkel, A. Ardavan, and J. J. L. Morton, Electrically detected magnetic resonance in a W-band microwave cavity, *Review of Scientific Instruments* **82**, 3 (2011).
- [157] C. Michel, *Theoretical Studies of Spin Dependent Transport Phenomena* (PhD Thesis: Universitat Marburg, Marburg, 2007).
- [158] D. R. McCamey, G. W. Morley, H. A. Seipel, L. C. Brunel, J. Van Tol, and C. Boehme, Spin-dependent processes at the crystalline Si-SiO₂ interface at high magnetic fields, *Physical Review B* **78**, 045303 (2008).
- [159] R. de Sousa, C. C. Lo, and J. Bokor, Spin-dependent scattering in a silicon transistor, *Physical Review B* **80**, 045320 (2009).
- [160] R. N. Ghosh and R. H. Silsbee, Spin-spin scattering in a silicon two-dimensional electron gas, *Physical Review B* **46**, 12508 (1992).
- [161] K. C. Kwong, J. Callaway, N. Y. Du, and R. A. LaViolette, Elastic scattering of electrons by neutral donor impurities in silicon, *Phys. Rev. B* **43**, 1576 (1991).
- [162] D. Kaplan, I. Solomon, and N. F. Mott, Explanation of the large spin-dependent recombination effect in semiconductors, *Le Journal de Physique* **39**, 51 (1978).
- [163] A. F. da Silva, A. Levine, Z. S. Momtaz, H. Boudinov, and B. E. Sernelius, Magnetoresistance of doped silicon, *Physical Review B* **91**, 214414 (2015).
- [164] J. M. Spaeth, in *Identification of Defects in Semiconductors*, edited by M. Stavola (Elsevier, 1998), pp. 45–92.
- [165] H. Huebl, F. Hoehne, B. Grolik, A. R. Steger, M. Stutzmann, and M. S. Brandt, Spin echoes in the charge transport through phosphorus donors in silicon, *Phys. Rev. Lett.* **100**, 177602 (2008).
- [166] A. Honig, Nuclear impurity scattering and impurity Zeeman spectroscopy in semiconductors using highly spin-polarized carriers, *Physical Review Letters* **17**, 186 (1966).
- [167] M. Weger, Passage effects in a paramagnetic resonance experiment, *Bell System Technical Journal* **39**, 1013 (1960).
- [168] L. Zhu, K. J. van Schooten, M. L. Guy, and C. Ramanathan, Optical dependence of electrically-detected magnetic resonance in lightly-doped Si:P devices, *arXiv:1608.04441* (2016).

- [169] G. W. Morley, D. R. McCamey, H. A. Seipel, L. C. Brunel, J. Van Tol, and C. Boehme, Long-lived spin coherence in silicon with an electrical spin trap readout, *Physical Review Letters* **101**, 207602 (2008).
- [170] D. P. Franke, F. Hoehne, L. S. Vlasenko, K. M. Itoh, and M. S. Brandt, Spin-dependent recombination involving oxygen-vacancy complexes in silicon, *Physical Review B* **89**, 195207 (2014).
- [171] F. C. Brown, in *Point Defects in Solids*, edited by J. H. Crawford and L. M. Slifkin (Springer US, 1972), pp. 491–549.
- [172] J. Verduijn, M. Vinet, and S. Rogge, Radio-frequency dispersive detection of donor atoms in a field-effect transistor, *Applied Physics Letters* **104**, 102107 (2014).
- [173] K. Y. Tan, K. W. Chan, M. Möttönen, A. Morello, C. Yang, J. Van Donkelaar, A. Alves, J. M. Pirkkalainen, D. N. Jamieson, R. G. Clark, et al., Transport Spectroscopy of single phosphorus donors in a silicon nanoscale transistor, *Nano Letters* **10**, 11 (2010).
- [174] T. Itakura and Y. Tokura, Dephasing due to background charge fluctuations, *Physical Review B* **67**, 195320 (2003).
- [175] L. Schreiber, F. Braakman, T. Meunier, V. Calado, J. Danon, J. Taylor, W. Wegscheider, and L. M. K. Vandersypen, Coupling artificial molecular spin states by photon-assisted tunnelling, *Nature Communications* **2**, 556 (2011).
- [176] J. I. Colless, X. G. Croot, T. M. Stace, A. C. Doherty, S. D. Barrett, H. Lu, A. C. Gossard, and D. J. Reilly, Raman phonon emission in a driven double quantum dot, *Nature Communications* **5**, 3716 (2014).
- [177] Z. Shi, C. B. Simmons, D. R. Ward, J. R. Prance, R. T. Mohr, T. S. Koh, J. K. Gamble, X. Wu, D. E. Savage, M. G. Lagally, et al., Coherent quantum oscillations and echo measurements of a Si charge qubit, *Physical Review B* **88**, 075416 (2013).
- [178] S. Foletti, H. Bluhm, D. Mahalu, V. Umansky, and A. Yacoby, Universal quantum control of two-electron spin quantum bits using dynamic nuclear polarization, *Nature Physics* **5**, 903 (2010).
- [179] J. P. Dehollain, J. J. Pla, E. Siew, K. Y. Tan, A. S. Dzurak, and A. Morello, Nanoscale broadband transmission lines for spin qubit control, *Nanotechnology* **24**, 015202 (2013).
- [180] D. Kim, Z. Shi, C. B. Simmons, D. R. Ward, J. R. Prance, T. S. Koh, J. K. Gamble, D. E. Savage, M. G. Lagally, M. Friesen, et al., Quantum control and process tomography of a semiconductor quantum dot hybrid qubit, *Nature* **511**, 70 (2014).